CHARACTERIZATION AND CHRONOLOGY OF REFRACTORY INCLUSIONS (CAIs) IN THE CV3 CHONDRITE NWA 4502

by

Marian Selorm Sapah

A thesis submitted in fulfilment of the requirements for the degree of Doctor of Philosophy.

The Australian National University

August 2015

STATEMENT OF ORIGINALITY

This is to certify that to the best of my knowledge, the content of this thesis is my own work. This thesis has not been submitted for any degree in this or any other university. The intellectual content of this thesis is the product of my own work. All assistance and collaborations received in analytical work as well as information derived from published and unpublished work of others has been duly acknowledged in the text and list of references.

Marian Selorm Sapah

6th August, 2015

DEDICATION

To Christian, Elizabeth, Charles, Emmanuella and Benjamin with much love and appreciation

ACKNOWLEDGEMENTS

I would like to express my deepest gratitude to my immediate supervisors Trevor Ireland and Yuri Amelin. Without their consistent help, support and patient guidance, this thesis would not have been possible. Thank you to Trevor for taking a chance on me and giving me a second shot at a PhD and to Yuri for the opportunity to take on this project. Scholarship provided by The ANU throughout the course of my research and the facilities, logistics and funding at RSES is greatly appreciated.

I am also grateful to members of my advisory panel and collaborators; Alexander N. Krot for his analytical contributions, funding and hospitability during my visit to the Hawai'i Institute of Geophysics and Planetology, University of Hawai'i at Manoa, Claudine Stirling and Qing-Zhu Yin for their analytical contributions and stimulating discussions and Marc Norman for encouragement and helpful discussions.

This project would not have run as well as it did without technical support. For this, thanks are due Trevor Ireland, Peter Holden, Peter Lanc, Janaina Avila, John Foster and Ben Jenkins, for all their work maintaining the SHRIMPS and Yuri Amelin, Vickie Bennet and Sonja Zink for the upkeep of the SPIDE^{2}R lab. Janaina, I appreciate the time and patience you spared to get me acquainted with SHRIMP SI and helping to produce a well formatted thesis. To my colleagues, office mates and lab mates, thank you for your company, helpful discussions and sharing.

Throughout my program I have received help, advice, encouragement and moral support from many thoughtful people within and outside RSES. Notable among these are Frances Jenner, Daniel Asiedu, Vickie Bennett, Daniela Rubbato, Bjorn Mysen, Maree Coldrick, and Robyn Petch. I would like to specially mention Josephine Magro who apart from her administrative and moral support, I am very grateful for her kindness and friendship.

The love and support of my family back home in Ghana has given me the strength and will to complete this PhD. I would like to express my profound love and appreciation (however inadequate) to my parents, Christian and Elizabeth, my siblings, Charles, Emmanuella and Benjamin whose absolute confidence in me and many sacrifices on my behalf has brought me this far.

ABSTRACT

In this thesis I report the petrographic, elemental and isotopic (oxygen, Al-Mg, Rb-Sr and uranium) compositions as well as U-Pb ages of five coarse-grained igneous inclusions (Type A CAIs *1* and *4a*, Type B CAIs *5*, *6* and *7*) from the CV chondrite North West Africa (NWA) 4502 the second largest CV chondrite so far after Allende.

At a mineralogical level, NWA 4502 is rather pristine. In comparison with CAIs from Allende and other CV chondrites, CAIs from the NWA 4502 show many similarities with CAIs from other CV3 chondrites. However, all studied NWA 4502 CAI types have low levels of secondary hydrothermal alteration, thermal and shock metamorphism that affected CAIs in other CV chondrites. Even though NWA 4502 shows pristine parent-body characteristics, complexities discovered in some of the isotope systems especially Rb-Sr indicate significant imprint of terrestrial weathering. Acid leached residues of NWA 4502 CAI fractions yield a Pb-Pb age (4567.40 ± 0.27 Ma) and initial $^{87}Sr/^{86}Sr$ (0.698886 ± 0.000026) and an average initial $^{26}Al/^{27}Al$ ($4.90 \pm 1.51 \times 10^{-5}$) ratio consistent with values reported for Allende and Efremovka CAIs inspite of the differences in secondary processes between these CV chondrites. This leads to the conclusion that secondary processing did not bias the U-Pb isotopic ages of these CV CAIs.

The evaluation of three acid leaching procedures aimed at removing weathering products and terrestrial contamination has shown that U-Pb dating of CAIs using the most radiogenic material can be achieved using mild acid leaching methods on coarse grained pyroxene and melilite-rich fractions.

This study enabled us to expand the population of well characterized CV CAIs and provided an insight to better understanding the influence of secondary processes on isotopic systems and the chronology of CAIs.

TABLE OF CONTENT

LIST OF FIGURES

LIST OF TABLES

CHAPTER 1

INTRODUCTION AND OVERVIEW

1.1. TIME SCALE OF FORMATION FOR THE EARLY SOLAR SYSTEM

Over the years, many studies have been carried out in an effort to answer the question, how and when did the solar system form? Compared to the study of the rocks delivered by space missions, one of the cheapest and easiest ways of getting information regarding the early stages of the solar system development is the study of meteorites. Our solar system evolved through several stages from a nebular cloud to a protoplanetary disk to a planetary system. Developments in isotopic dating techniques allow us to establish the sequence and duration of the early solar system processes with greater precision and accuracy, and to constrain the temporal relationships between solar system formation events.

Patterson et al. (1955) first estimated the age of the Earth to be about 4.5 Ga using U-Pb dating. Hf-W isotopic studies of lunar rocks by Lee et al. (1997) give an approximate age of the moon as 4.5 Ga. Houdek and Gough (2011) estimated the formation of the solar system begun some 4.6 Ga ago based on asteroseismic calibration of solar models. However, more reliable U-Pb age determinations of CAIs in meteorites (e.g., Amelin et al., 2002; Jacobsen et al., 2008; Amelin et al., 2010; Connelly et al., 2012) give an age of about 4.567 billion years to define the age of the solar system.

The prevailing hypothesis based on increasing knowledge and understanding of the physical and chemical properties of the solar system, suggests that the collapse of an interstellar molecular cloud (nebula gas) made up of hydrogen, helium and other products of earlier generations of stars, formed our solar system through condensation of mineral grains, accretion and the growth

of planetesimals and planets within a period of a 10 Ma after the formation of the Sun (Woolfson, 1993; Kleine et al., 2002; Montmerle et al., 2006; Scott, 2007; Rollinson, 2009; Williams, 2010). Clumps of material condensed in the molecular cloud collapse by gravitational force to form a proto-sun. Due to the conservation of angular momentum, the collapsing matter formed an accretionary (protoplanetary) disk from which gas and dust accreted onto the proto-Sun in the centre. While most of the material of the disk was accreted onto the Sun, some of the dust through heating and rapid cooling create the first solids, which accreted to form planetesimals, and these subsequently grew into planetary embryos and planets. During the collapse of the molecular cloud, most of the presolar material is altered or destroyed by heating but isotopic evidence has shown that some may survive and are preserved in meteorites (Huss, 1988; Weidenschilling and Ruzmaikina, 1994; Fegley Jr, 1999 and references therein).

Important constraints on the physical and chemical processes in the solar nebula for the first 10 Ma are obtained from some of the most primitive objects in the solar system, i.e., chondritic meteorites. Meteorites can be divided into two major groups, undifferentiated and differentiated. Undifferentiated meteorites, also known as chondrites are primitive objects that have endured no large-scale melting and planetary differentiation and thus most likely represent the composition of the solar nebula at the time of their formation. Chondrites are made up of components of silicate spherules called chondrules and high-temperature condensates called Calcium-Aluminium-rich Inclusions (CAIs) that formed in the cooling protoplanetary disk. These are embedded in matrix (an assemblage of minerals that did not undergo high-temperature processing). Accretion of the earliest condensates represented by chondrules and CAIs within chondritic meteorites was accompanied by early chemical differentiation in the disk (Lord III, 1965; Papanastassiou and Wasserburg, 1969; Grossman, 1972; Gray et al., 1973; Wood, 2004; Scott, 2007). Due to their refractory nature and old absolute age of ~4567 Ma (Amelin et al., 2010; Connelly et al., 2012), CAIs are thought to be the first solids that formed in the cooling disk and thus define the age of the solar system.

The accretion of planetesimals, planetary embryos and planets from nebular dust and the earliest condensates was subsequently followed by planetary differentiation processes. Differentiated meteorites are derived from parent bodies that experienced differentiation into a core, a mantle and a crust due to heating and melting of an initially homogeneous planetesimal or asteroidal parent body. Parent bodies of differentiated achondrites such as howardites, eucrites, diogenites, (HED meteorites) and angrites have experienced extensive (planetary-scale) melting and differentiation, such that their bulk compositions are significantly different from those of

chondrites. Primitive achondrites on the other hand, are meteorites with igneous texture and mineralogy that were heated to the point of melting but never experienced large-scale differentiation. Their parent bodies have not experienced planetary-scale differentiation, and in many cases retain near-chondritic bulk compositions (e.g. brachinites, acapulcoites, lodranites, and winonaites).

1.2 CHONDRITES AND REFRACTORY Ca-Al-RICH INCLUSIONS (CAIs)

A range of complex processes occurred during the evolution of the early solar system. Evidence of such processes is recorded in meteorites and their components such as CAIs. CAIs can be described as clasts within chondritic meteorites with unique chemical and mineralogical characteristics that distinguish them from all other chondritic components. Their structures and compositions retain a component of presolar nucleosynthetic origin, and they record a complex post formation history, which includes repeated melting and secondary alteration, both in nebula and on asteroidal parent bodies (MacPherson et al., 2005; Krot and Bizzarro, 2009). As such, CAIs provide direct clues as to the processes and environments that existed during the nebula phase of our solar system.

CAIs were first described in 1968 from the Vigarano meteorite (Christophe Michel-Lévy, 1968). CAIs primarily have a high abundance of refractory elements and occur especially in carbonaceous chondrites (Scott and Krot, 2003; Scott and Krot, 2005; Scott, 2007; Hezel et al., 2008). Hezel et al. (2008) presented a complete list of CAI modal abundances in carbonaceous chondrites including (in area%): CV: 2.98, CM: 1.21, Acfer 094: 1.12, CO: 0.99, CK/CV (Ningqiang and Dar al Gani 055): 0.77, CK: 0.2, CR: 0.12 and CB: 0.1 obtained from a combination of previously reported CAI modal abundances and their our own data set (Figure 1.1).

CAIs usually occur as “white” inclusions with sizes ranging from <1mm to ~2cm (e.g., Figure 1.2). They can be completely spherical in shape but are also commonly irregularly shaped. The primary mineralogy of CAIs has been shown to correspond to the predicted sequence of condensation of the first phases condensing from a hot gas of solar composition (Lord III, 1965; Larimer, 1967; Grossman, 1972; Yoneda and Grossman, 1995). They are made up mainly of Ca-Al-Ti silicates and oxides such as melilite (gehlenite $Ca_2Al(Si,Al)_2O_7$ - akermanite $Ca_2MgSi_2O_7$ solid solution), pyroxene (Al-Ti diopside $Ca(Mg,Ti,Al)(Al,Si)_2O_6$), spinel ($MgAl_2O_4$) and anorthite ($CaAl_2Si_2O_8$). Hibonite ($CaAl_{12}O_{19}$) and perovskite ($CaTiO_3$) usually occur as accessory phases.

The origin of CAIs is not yet clearly understood. Their mineralogy and refractory trace-element abundances including rare earth elements are consistent with a gas-solid condensation origin. Lord III (1965) and Grossman (1972) showed that the high-temperature minerals abundant in CAIs would be the first condensates in a cooling solar nebula. Rare earth element chemistry of CAIs shows large variations that suggest that they formed by volatility-controlled processes such as evaporation and condensation in the solar nebula (Grossman, 1972; Kornacki and Fegley, 1986). Other studies (Blander and Fuchs, 1975; Mason and Taylor, 1982b; Kornacki and Fegley, 1984) have suggested the crystallization of CAI phases from melt or formation of CAIs from melting of dust aggregates.

CAIs have experienced various degrees of alteration. This is evident in the occurrence of secondary minerals such as sodalite, nepheline, grossular and other phyllosilicates in CAIs. This is particularly true for CAIs from the CV chondrite group e.g., Allende (Allen et al., 1978; Krot et al., 1998; Ford and Brearley, 2007a; Ford and Brearley, 2008; Krot et al., 2010). Even though CAIs have been altered, they still provide useful information about the processes and conditions that were present in the solar nebula where they formed.

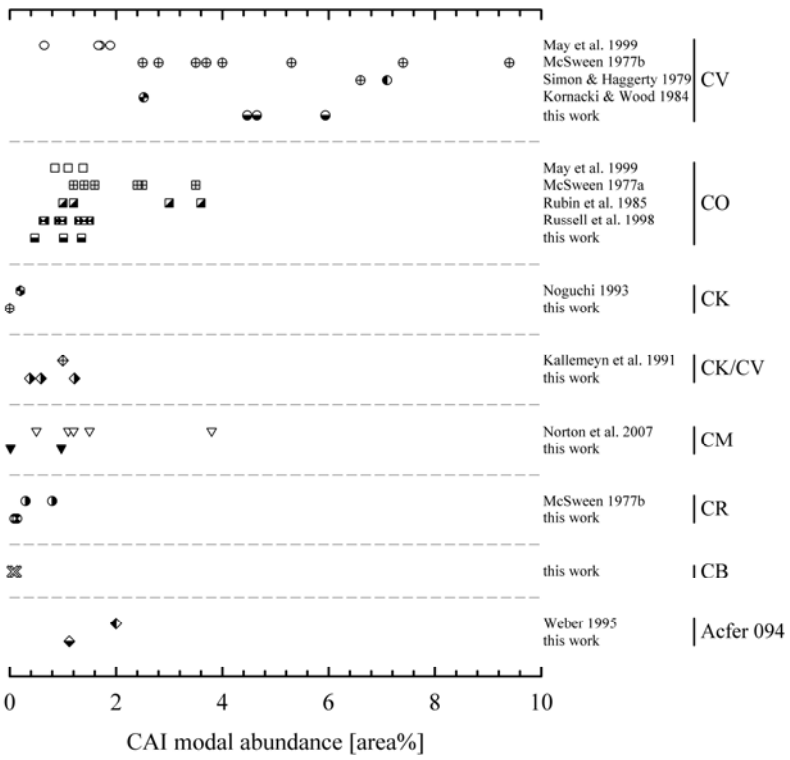

Figure 1.1: A compilation of literature data of CAI modal abundances for carbonaceous chondrites (Hezel et al., 2008).

CAIs have been described in other carbonaceous chondrites such as CM chondrites (Macdougall and Goswami, 1981; MacPherson et al., 1983; Ireland, 1990), CK chondrites (Greenwood et al., 2003; Greenwood et al., 2004; Devouard et al., 2006; Greenwood et al., 2010; Chaumard et al., 2014), CR chondrites (Aléon et al., 2002), CO chondrites (Davis, 1985; Greenwood et al., 1992; Kojima et al., 1995; Itoh et al., 2004) and the CB/CH-like chondrite Ishyevo (Krot et al., 2008). However, our understanding and classification of CAIs has been primarily based on studies of large CV chondrites, especially Allende (Total known weight ~2000 kg) and Efremovka (Total known weight ~21 kg). These CV chondrites contain numerous CAIs, including many large ones suitable for comprehensive geochemical and isotopic analysis. Because of the large sizes and relative ease of study, the CV CAIs became the most extensively studied group of CAIs and one of the main sources of knowledge of the nebular stage of our solar system. In addition, within the population of objects sampled in CV chondrites, one type of CAI composed mainly of pyroxene, melilite, spinel and anorthite known as Type B (Grossman, 1975) became more prominent than others. Not only are they large, but being igneous objects they can be treated as initially homogeneous isotopic systems, and this is a critical factor for the interpretation of short- and long-lived radioisotope systems (Kita et al., 2005). Type B CAIs thus became an important part of understanding the earliest history of the solar system.

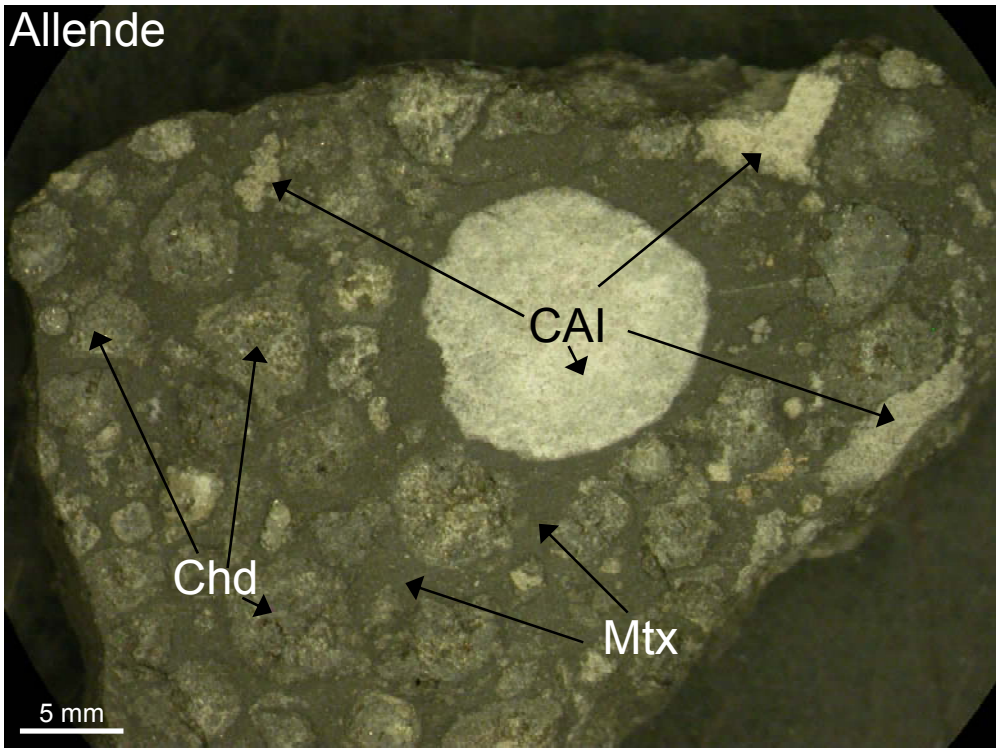

Figure 1.2: Image of the cut surface of a piece of Allende meteorite, showing Calcium-Aluminium rich Inclusions (CAI), Chondrules (Chd) and Matrix (Mtx).

1.2.1. CAI petrography and classification

CAIs are classified based mainly on their petrography (texture and mineralogy) and chemistry (major elements, trace elements and isotopic compositions). Classification of CAIs based on each set of characteristics has lead to a sometimes conflicting nomenclature system for CAIs. Studies have shown that trace-element fractionation patterns are largely decoupled from major element chemistry, and isotopic signatures are largely decoupled from both. As such, Three main types of CAIs have been recognized so far based on mineralogy, bulk major element composition and petrographic features mainly of Allende CAIs (Grossman, 1975; MacPherson and Grossman, 1979; Grossman, 1980; MacPherson et al., 1988).

1) Type A inclusions; composed mainly of 80-85 % melilite, 15-20 % spinel, 5-2 % hibonite, 1-2 % perovskite, and <1 % rhonite $Ca_2(Mg, Fe\ Ti)_6(O_2(Si\ Al)_6O_{18})$.

2) Type B inclusions; now known to occur only in CV3 chondrites consisting of 5-20 % melilite, 35-60 % Al-Ti-rich pyroxene, 15-30 % spinel, and 5-25 % anorthite.

3) Type C inclusions; made up of 30-60 % anorthite, 10-35 % calcic pyroxene, 2-35 % spinel, and 5-20 % melilite, and have distinctive ophitic and poikilitic textures.

Type A inclusions are further distinguished as "compact" or "fluffy" based on differences in shape and internal textures (MacPherson and Grossman, 1979; Grossman, 1980; MacPherson and Grossman, 1984; Beckett and Stolper, 1994; Simon et al., 1999). Compact Type A CAIs (CTA) are coarse grained, spheroidal in shape. Fluffy Type A (FTA) CAIs on the other hand, are fine grained, and irregularly shaped with aggregate structures. CTA CAIs have melilite ranging in composition from $Åk_{10\text{-}70}$ while FTA CAIs have aluminium-rich melilite ($Åk_{0\text{-}35}$) (MacPherson and Grossman, 1984). The preferred interpretation for the origins of Type A CAIs is that they formed by gas-solid condensation processes. Fluffy Type A inclusions generally do not show evidence that they have been melted. However, studies have shown some compact Type A inclusions experienced partial melting (Beckett and Stolper, 1994; Simon et al., 1999).

Type B inclusions are also further subdivided into Type B1, which have a monomineralic melilite mantle surrounding a core of pyroxene, anorthite and spinel, and Type B2, which lack a melilite rich mantle and generally resemble the core of Type B1 CAIs. Type B3 inclusions also known as Fosterite-bearing Type B (FoB), contain fosterite crystals as an essential phase in addition to the typical Type B composition of pyroxene, spinel and melilite. Anorthite is usually minor or absent in Type B3 CAIs (Wark and Lovering, 1982; Wark, 1987). Type B inclusions appear to have an igneous origin with mineral, chemical, and experimental petrologic studies indicating solidification from partial melts.

Type C CAIs are coarse-grained, anorthite-rich inclusions. They were initially described as intermediate between Type A and B CAIs. Grossman (1975) coined the term "intermediate" or Type I to describe an inclusion that differed from Type A and B CAIs having an anorthite-rich (50 %) and melilite-free compositions. Wark and Lovering (1978) also used the term "intermediate" or Type I to describe inclusions that contain ~50 % anorthite, but are melilite-bearing. Such inclusions have since been shown to be an independent type, with distinctive chemical and mineralogical compositions and named Type C. They have been recognized in CV (Wark, 1987; Beckett and Grossman, 1988; Krot et al., 2005), CR (Aléon et al., 2002) and CO (Itoh et al., 2004) chondrites. The distinctive ophitic and poikilitic textures of Type C inclusions are indicative of igneous origin.

AOAs are a class of refractory objects originally recognized in the CV chondrite Allende by Grossman and Steele (1976). AOAs are genetically related to CAIs and occur in most carbonaceous chondrite groups (Krot et al., 2004). They are the least refractory of the refractory inclusions and contain olivine (Fo_{64}-Fo_{99}) which brings them chemically closer to magnesian chondrules than other refractory inclusions.

1.2.2. Trace element classification and condensation processes

The trace element classification of CAIs is based mainly on studies of Allende refractory inclusions (Grossman, 1973; Martin and Mason, 1974; Grossman and Ganapathy, 1976; Mason and Martin, 1977; Mason and Taylor, 1982b). The REE patterns in inclusions have been divided into five main groups; Group I, II, III, V, and VI (Figure 1.3). A sixth REE pattern (Group IV) applies mainly to ferromagnesian objects such as AOAs and chondrules. This pattern is as relatively unfractionated at levels 2-4x CI (Mason and Martin, 1977; Mason and Taylor, 1982b).

Trace element patterns of CAIs generally show enrichment in the most refractory elements such as the lithophile elements scandium, yttrium, zirconium, hafnium, and the rare earth elements (REEs), and depletion in volatile elements (e.g., alkalis such as rubidium, cesium, sodium, potassium, and lithium) relative to REE abundances in CI chondrite (solar composition). The overall enrichment in elements is by a factor of 10 to 100 relative to CI chondrite (Grossman, 1980; Ireland et al., 1988a) suggesting that the CAIs represent the first 10 % to 1 % (respectively) of condensable material from the solar gas.

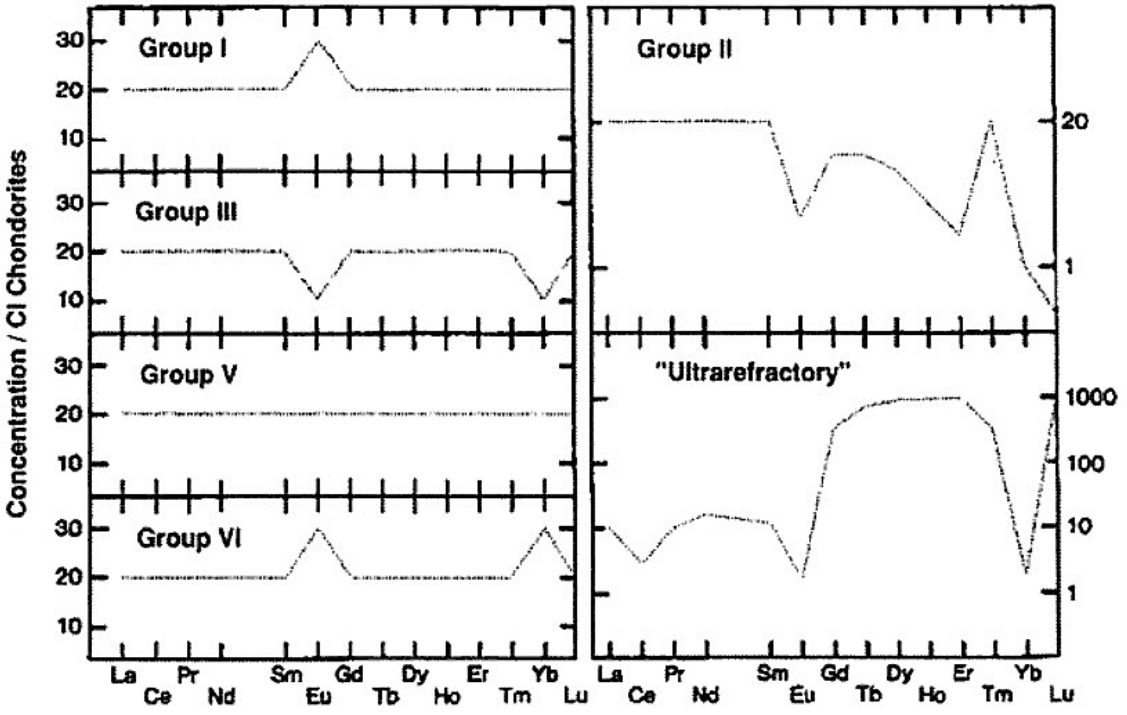

Figure 1.3: An illustration of REE patterns in CV CAIs showing the main groups (after MacPherson et al., 1988; in Hutchison, 2004). REE abundances are normalized to REE abundances in CI chondrite (Anders and Ebihara, 1982). Note there is considerable variation in enrichment factors measured in CAIs.

Unlike terrestrial samples whose REE abundances are largely controlled by solid-liquid fractionation occurring during igneous and metarmorphic processes, the REE abundances in CAIs are more complex and are likely to reflect other processes as well. Group I, III, V, and VI show generally unfractionated REE patterns relative to CI chondrite and are distinguished based on the enrichments and depletions in the more volatile REEs, europium and ytterbium. Group I patterns have unfractionated abundances relative to CI except for a positive Eu anomaly. Group III patterns have unfractionated abundances relative to CI except for negative Eu and Yb anomalies. Group V patterns have unfractionated abundances relative to CI with no anomalies in Eu and Yb, and Group VI patterns have unfractionated abundances except for positive Eu and Yb anomalies. The invariable (REEs in their CI-chondrite proportions relative to each other) enrichment of most of the REEs in these patterns indicates total condensation at high temperatures. Eu is commonly fractionated between Ca-bearing minerals during crystallisation owing to the similar size of Eu^{2+} and Ca^{2+} but the variable Yb anomalies cannot be due to igneous fractionation. Rather it would appear that the REE patterns are established by near-

complete condensation from a gas of solar composition. The depletion of Eu and Yb is explained by their volatility which allows them to only partially condense when the CAI formed (Boynton, 1975; Davis and Grossman, 1979; Ireland et al., 1988a).

.The Group II pattern first identified by Tanaka and Masuda (1973) is quite different. In this pattern, REEs are highly fractionated from one another with depletions in both the most refractory (heavy REEs except ytterbium) and most volatile (europium and ytterbium) REEs. Boynton (1975) interpreted this pattern as resulting from fractional condensation where a component containing the most refractory REEs is removed by condensation and the remaining gas has condensed all remaining REEs except europium and ytterbium. This interpretation is further supported by the abundance of Tm, which appears to have the same volatility as the light REE, although this behaviour is not expressly predicted from thermodynamic data. The Group II REE pattern is frequently observed among fine-grained spinel-rich CAIs from CV chondrites, but has been found to also occur in hibonite grains and spinel-hibonite inclusions in CM chondrites (Ireland et al., 1988a; Ireland, 1990; Ireland and Fegley, 2000) .

A source of the Group II REE pattern through condensation also means there could be a complementary pattern known as the ultrarefractory pattern preserved in CAIs. The ultrarefractory REE pattern was first described in a Murchison inclusion by Boynton et al. (1980). The ultrarefractory fractionated pattern has enrichments in the heavy rare earth elements (Gd-Tm, Lu) that are depleted in the Group II pattern. Depletions in the less refractory elements (viz., Eu & Yb) are also considered to be a signature of this highest-temperature condensate because they remain in the gas phase throughout. In subsequent studies, a few CAIs with the ultrarefractory patterns have been described in CM (Hinton et al., 1988; Ireland, 1990; Simon et al., 1996), CO (Palme et al., 1982; Davis, 1984; Davis, 1991), CH (Weber et al., 1995) and CV (El Goresy et al., 2002) chondrites, and interestingly, this pattern has not been found from Allende.

Other studies such as Ireland and Fegley (2000) have considered that the preservation of Group II and ultrarefractory patterns occur as a chemical memory of condensation and evaporation of precursor grains and that the CAIs are not themselves direct condensates.

1.2.3. Isotopic anomalies in CAIs

Variations in the isotopic compositions of elements can be caused by several mechanisms. The variations due to radioactive decay and mass dependent fractionation are common in both terrestrial and extraterrestrial rocks. Cosmogenic anomalies caused by irradiation are also common. Isotopic variations observed in primitive objects such as meteorites that cannot be explained by radioactive decay, mass dependent fractionation and irradiation are usually referred to as isotope abundance anomalies (isotopic anomalies) and are usually interpreted as nucleosynthetic or possibly being caused by mass-independent fractionation. These anomalies are more common in CAIs than in other materials. The description of isotopic variations in elements among early solar system materials yields important insights into the stellar environment and formation of the solar system, and about initial isotopic ratios relevant to early solar system chronology.

The discoveries of anomalous isotopic ratios in oxygen (Clayton et al., 1973) and small but significant anomalous isotopic ratios in elements such as Ca, Ti, Mn, Fe, Ni, Zn and Cr in CAIs (e.g., Wasserburg et al., 1977a; Heydegger et al., 1979; Lee, 1979; Ireland et al., 1985; Wasserburg and Arnould, 1987; Lee, 1988) prompted the notion of incomplete mixing of different nucleosynthetic sites in the solar system. At the time of these discoveries, the solar system was widely regarded as having initially been homogenous due to the general consistency of isotope ratios found in Earth, Moon, Sun and meteorites. The topic of isotopic anomalies was reviewed by several authors at the time, including (Reynolds, 1967; Clayton, 1978; Podosek, 1978; Clayton et al., 1988).

Of particular interest were anomalies in the Fe-group elements and especially Ti. The abundance of ^{50}Ti was found to be elevated in CAIs by around 1 ‰ (Heydegger et al., 1979), and even more diverse in CAIs that show fractionation and unidentified nuclear isotope properties (FUN inclusions) (Wark and Wasserburg, 1980; Niemeyer and Lugmair, 1981; Niemeyer and Lugmair, 1984). This anomaly was inferred to represent material from near the mass cut of a supernova, and this interpretation is supported by the discovery of ^{26}Mg excesses correlated with Al/Mg that were ascribed to the presence of short-lived ^{26}Al (Lee et al., 1976; Lee et al., 1977). But it was the discovery of excess ^{16}O in CAIs that changed our view of the solar system (Clayton et al., 1973).

The abundance of oxygen in the solar system and terrestrial planets, its presence in both gaseous and solid phases makes oxygen isotopes particularly important tracers of various fractionation

processes in the solar nebula. Oxygen is the third most abundant element in the solar system and the most abundant in rocky planets and other rocky bodies such as asteroids. ^{16}O is the major isotope of oxygen therefore anomalies in ^{16}O represent a large mass fraction of a CAI that is anomalous with respect to the terrestrial abundances if the source of these anomalies is a nucleosynthetic component. CAI being enriched in ^{16}O was quite consistent with a supernova source (Clayton et al., 1973). However, the case for a nucleosynthetic source has always been somewhat problematic because of the lack of a similar isotope trend in other elements and the mass of material that must be incorporated into the solar system from the supernova source but such a large ^{16}O-rich reservoir was not found (Clayton, 1993a).

Other sources of this anomalous behaviour have been sought, and in particular, chemical fractionations that could cause anomalous isotope ratios. For instance, the Earth's stratosphere has anomalous oxygen isotope ratios because of isotopically asymmetric reactions between molecular oxygen (O_2) and ozone (O_3). These cause an overabundance of ^{17}O and ^{18}O in ozone. Studies have pointed towards the mechanism of molecular symmetry to be responsible for the oxygen isotope fractionation in CAIs (Thiemens and Heidenreich, 1983; Heidenreich III and Thiemens, 1986; Mauersberger et al., 1993; Gao and Marcus, 2002; Marcus, 2004). Navon and Wasserburg (1985) proposed shielding in O_2 as a possible explanation for oxygen isotopic anomalies in meteorites and other studies such as Bally and Langer (1982) and van Dishoeck and Black (1988) considered self shielding in the ultraviolet photodissociation of carbon monoxide (CO) which is in line with the current paradigm based on inner solar system photochemical dissociation of CO and self shielding (Clayton, 2002; Lyons and Young, 2005). Figure 1.3 illustrates photodissociation of CO and self shielding. This interpretation is supported by the discovery of a difference in the ^{16}O abundance in the Sun inferred from captured solar wind versus Earth, Moon, Mars and bulk meteorites (McKeegan et al., 2011).

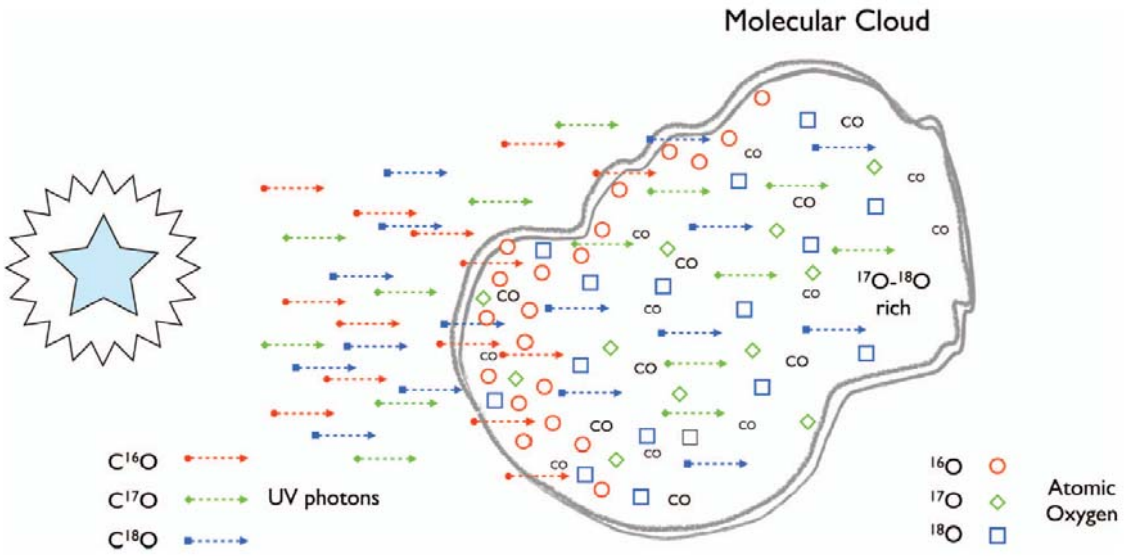

Figure 1.4: A schematic diagram illustrating photodissociation and self shielding in a molecular cloud (Ireland, 2012). The interaction between UV photons from nearby stars and CO molecules results in photodissociation occurs with the breaking of CO molecules. Self shielding occurs as the photons become progressively depleted according to the abundances of the CO Isotopologues. The high abundance of ^{16}O means that these photons are quickly depleted while photons that can dissociate C^{17}O and C^{18}O can proceed deeper into the cloud. Here they release atomic ^{17}O and ^{18}O, which can react with hydrogen to form water ice. Residual CO in the cores of molecular clouds will also become ^{16}O-rich relative to the initial composition.

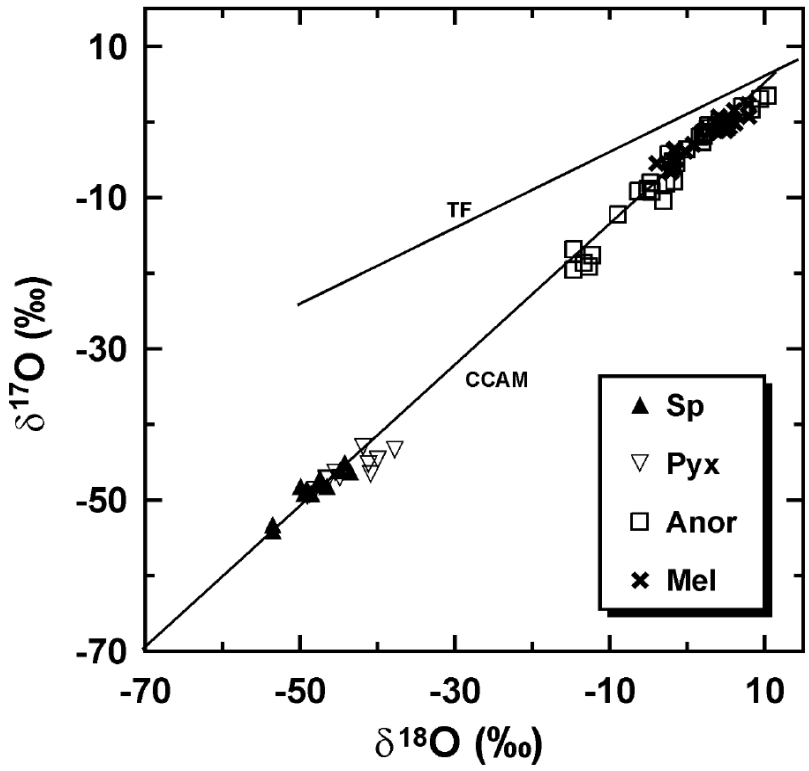

Figure 1.5: A three-isotope plot for oxygen in a single Type B Allende CAI (MacPherson et al., 2005). Spinel and pyroxene are highly enriched in ^{16}O, whereas anorthite and melilite are not. TF: Terrestrial Fractionation Line; CCAM: Carbonaceous Chondrite Anhydrous Minerals line.

Oxygen isotopic compositions are normally represented in Delta (δ) units and plotted on three-isotope diagrams (Figure 1.5). δ units represent deviations in per mil (‰) of the $^{17}O/^{16}O$ and $^{18}O/^{16}O$ ratios from Standard Mean Ocean Water (SMOW) with $^{17}O/^{16}O = 0.0003829$ (Li et al., 1988) and $^{18}O/^{16}O = 0.0020052$ (Baertschi, 1976). Plotted on a three-isotope diagram of $\delta^{18}O$ against $\delta^{17}O$, compositions of nearly all terrestrial samples plot along a single line of slope 0.52 called the terrestrial fractionation line (TFL). This line is as a result of mass-dependent fractionation from chemical and physical processes that fractionate the oxygen isotopes based on the differences in their masses. The slope of the TFL has been found to somewhat be dependent on analytical conditions and minerals analysed and the values of 0.524 to 0.526 are typical (e.g., Greenwood et al., 2005; Rumble et al., 2007). Extraterrestrial materials, including chondrites and their components on the other hand, have oxygen isotopic compositions that

deviate from the TFL. The oxygen isotope composition can be expressed as the deviation from the TFL as Δ^{17}O where $\Delta^{17}O = \delta^{17}O - 0.52\delta^{18}O$.

This reflects non-mass dependent fractionation by processes that occurred prior to the accretion of these bodies in the protoplanetary disk. Chondrite components such as CAIs and chondrules usually plot along a line of slope ~1 and show a large range of Δ^{17}O, from < -20 ‰ to +5 ‰ (Clayton et al., 1973; Clayton, 1993a; Aléon et al., 2002; Itoh et al., 2004). This line of slope ~1 known as the Carbonaceous Chondrite Anhydrous Mineral (CCAM) is defined by CAIs from the CV3 chondrite Allende (Clayton et al., 1973). Figure 1.5 shows different minerals in CAIs preserve different Δ^{17}O. Spinel and pyroxene have large Δ^{17}O deviation while melilite and anorthite are generally closer to terrestrial values. This is interpreted as a result of gas phase resetting. The CAI composition given by spinel and pyroxene are close to solar wind composition (McKeegan et al., 2011).

1.3. CAI CHRONOLOGY

The sequence of important events in the early evolution of the solar system including the formation of CAIs and chondrules as well as the accretion and subsequent differentiation of meteorite parent bodies can be determined by applying short- and long-lived chronometers to meteorites and their components. Table 1.1 shows a list of short and long-lived radionuclides.

Short-lived radionuclides with half-lives <450 Ma are useful for relative chronology and those with half-lives <10 Ma provide tight constraints on early solar system timescales. Long-lived, existing radionuclides are used for absolute dating. The short-lived Al-Mg and long-lived U-Pb and Rb-Sr radionuclide chronometers are the focus of this study.

Table 1.1: List of short and long-lived radioactive nuclides and their half-lives. Modified after Kita et al. (2005).

Short-lived Nucleus	Half-life (Ma)	Long-lived Nucleus	Half-life (Ga)
^{26}Al-^{26}Mg	0.7	^{40}K-^{40}Ar	1.25
^{10}Be-^{10}B	1.51	^{87}Rb-^{87}Sr	48.8
^{41}Ca-^{41}K	0.1	^{147}Sm-^{143}Nd	106
^{36}Cl-^{36}S	0.3	^{187}Re-^{187}Os	41.6
^{60}Fe-^{60}Ni	1.5	^{232}Th-^{208}Pb	13.9
^{182}Hf-^{182}W	9	^{235}U-^{207}Pb	0.704
^{129}I-^{129}Xe	15.7	^{238}U-^{206}Pb	4.468
^{53}Mn-^{53}Cr	3.7		
^{92}Nb-^{92}Zr	35		
^{107}Pd-^{107}Ag	6.5		
^{244}Pu-^{232}Th	81		
^{146}Sm-^{142}Nd	103		
^{97}Tc-^{97}Mo	2.6		

1.3.1. Short-lived radionuclides

Al-Mg dating system

The discovery of live ^{26}Al in Allende CAIs (Gray and Compston, 1974) evident from the presence of its daughter product ^{26}Mg lead to the subsequent development of the Al-Mg chronometer (Lee et al., 1976). The Al-Mg chronometer is particularly useful in CAIs because they are refractory and contain abundant Al relative to Mg.

^{26}Al decays to ^{26}Mg $^{26}Al \rightarrow ^{26} Mg + \beta^{+} + \upsilon_{e}$ with a half-life of 0.705Ma (Norris et al., 1983). The main principle of this dating method is identifying the deviation, i.e. excess ^{26}Mg (^{26}Mg*), from the natural abundance of ^{26}Mg in comparison with the ratios of the stable isotopes of aluminium and magnesium (^{26}Mg/^{24}Mg and ^{27}Al/^{24}Mg). ^{26}Mg* is found by comparing the ^{26}Mg/^{24}Mg ratio (normalised for mass dependent fractionation) to that of terrestrial Mg with a fractionation correction based on ^{25}Mg/^{24}Mg in other solar system materials. ^{26}Al-^{26}Mg dating is based on the assumption that ^{26}Al is homogeneously distributed in the protoplanetary disk where CAIs and chondrules probably formed (MacPherson et al., 1995). If this assumption is correct, and ^{26}Mg* is obtained from the *in situ* decay of ^{26}Al, then a plot of ^{26}Mg/^{24}Mg against ^{27}Al/^{24}Mg

for two or more samples should define a line whose slope is the $^{26}Al/^{27}Al$ ratio at the time the Al-Mg system closed (Figure 1.6). The difference between the initial $^{26}Al/^{27}Al$ ratio of an unknown sample and the canonical $^{26}Al/^{27}Al$ ratio (the solar system initial $^{26}Al/^{27}Al$ ratio based on measured abundances of $^{26}Mg^*$ in CAIs) corresponds to the relative formation age of the unknown.

$$\Delta T = \frac{1}{\lambda} \times \ln \left[\frac{\left(\frac{^{26}Al}{^{27}Al} \right)_i}{\left(\frac{^{26}Al}{^{27}Al} \right)} \right] \quad \text{.....1}$$

Where ΔT is the difference in time, λ is the ^{26}Al decay constant and *i* is the solar system initial $^{26}Al/^{27}Al$ ratio.

The ^{26}Al-^{26}Mg chronometer gives an estimate of the time period for formation of extraterrestrial objects of only few million years. As above, this provides a relative age based on the solar system initial $^{26}Al/^{27}Al$ ratio. To convert relative ages from the ^{26}Al-^{26}Mg chronometer into absolute ages requires calibration with ages of CAIs from absolute chronometers such as U-Pb.

Figure 1.7 shows an example of the evolution of $^{26}Al/^{27}Al$ with time illustrating the ability to date objects isolated from an evolving reservoir. Figure 1.8 shows examples of Al-Mg internal isochron diagrams.

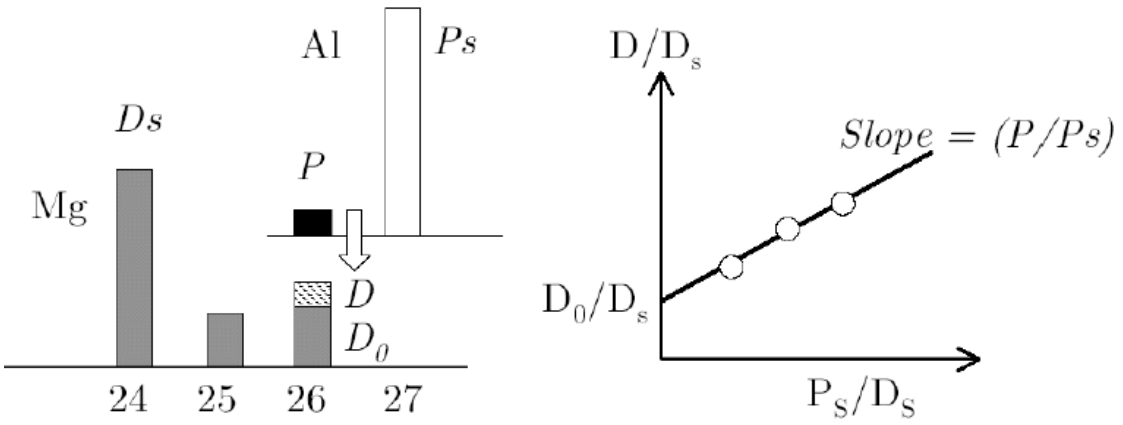

Figure 1.6: An illustration from Kita et al. (2005) of an isochron diagram for ^{26}Al decay to ^{26}Mg. P = parent nuclide, Ps = stable parent isotope, D = nuclide, Ds = stable isotope of daughter nuclide and D_0 = non radiogenic daughter nuclide.

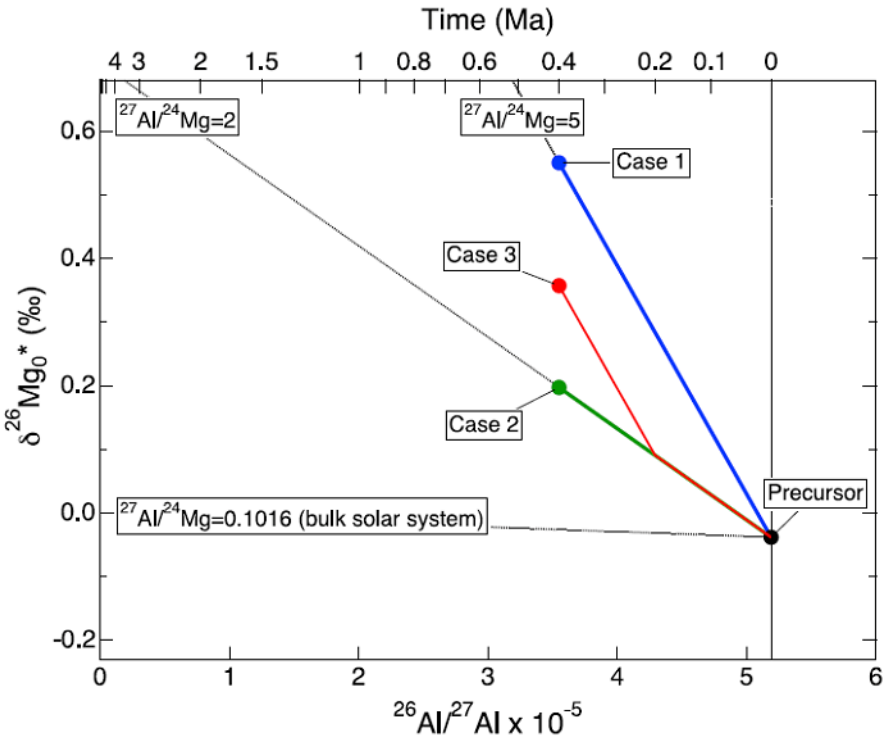

Figure 1.7: Magnesium isotopic evolution diagram from MacPherson et al. (2012) showing the effects of Mg/Al fractionation in CAIs at different times. The figure shows evolution paths for three cases. (1) fractionation event when the precursor to the CAI formed, $^{26}Al/^{27}Al = 5.23\times10^{-5}$; (2) fractionation event when the CAI last melted, $^{26}Al/^{27}Al = 3.58\times10^{-5}$; or, (3) fractionation

event 200,000 years before the final melting event, $^{26}Al/^{27}Al = 4.33\times10^{-5}$. The nearly horizontal line describes magnesium isotopic evolution of the bulk Solar System, which connects the Earth ($^{26}Al/^{27}Al = 0$, $\delta^{26}Mg^*_0 = 0$ ‰) and the early Solar System value ($^{26}Al/^{27}Al = 5.23\times10^{-5}$, $\delta^{26}Mg^*_0 = -0.038$ ‰) and has $^{27}Al/^{24}Mg = 0.1016$. Also shown are isotopic evolution lines for reservoirs with $^{27}Al/^{24}Mg$ ratios of 2 and 5.

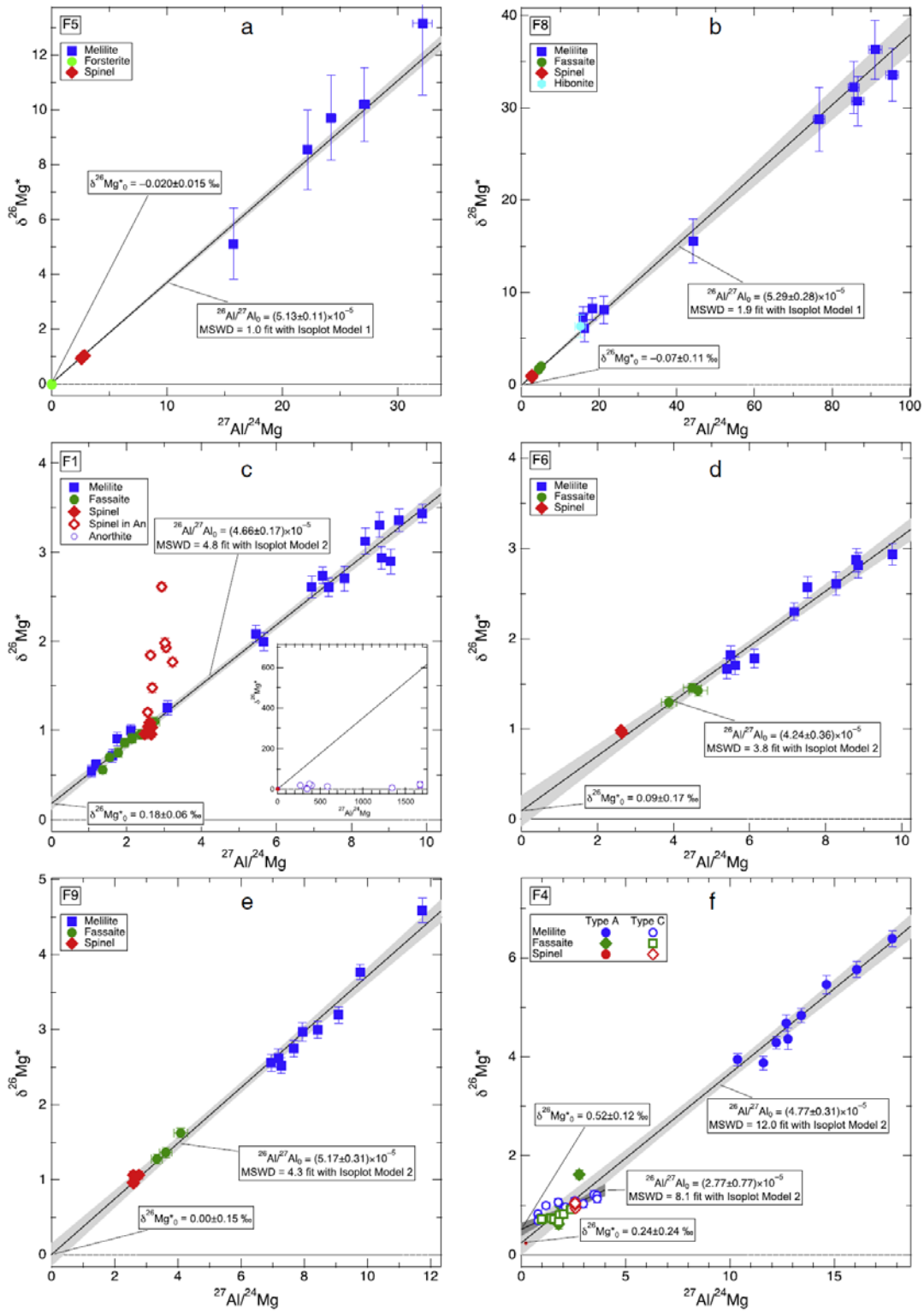

Figure 1.8: Al-Mg internal isochron diagrams (MacPherson et al., 2012) for *in situ* SIMS analysis on (a) an amoeboid olivine aggregate, (b) a fluffy Type A CAI, (c) a Type B CAI, (d, e) compact Type A CAIs, and (f) a complex remelted CAI.

1.3.2. Long-lived radionuclides

Rb-Sr dating system

The ^{87}Rb-^{87}Sr system has a long half-life parent isotope ^{87}Rb allowing for absolute age determinations. However, Rb is a volatile element and so is of low abundance in CAIs. Notwithstanding the low Rb abundance, Sr isotope evolution can still provide firm time constraints based on fractionation away from a reservoir with solar composition.

The long-lived ^{87}Rb-^{87}Sr isotope system has been used for chronology and tracing processes in the early solar system (Papanastassiou and Wasserburg, 1969; Gray et al., 1973; Podosek et al., 1991; Halliday and Porcelli, 2001; Moynier et al., 2010; Moynier et al., 2012; Hans et al., 2013; Paton et al., 2013). Strontium has four stable isotopes: ^{84}Sr (0.56 %), ^{86}Sr (9.86 %), ^{87}Sr (7.00 %), and ^{88}Sr (82.58 %). The major isotopes ^{86}Sr, ^{87}Sr, and ^{88}Sr are all principally made by the same nucleosynthetic process, the slow neutron capture process (*s*-process). Small fractions of ^{87}Sr and ^{88}Sr are also formed by the rapid neutron capture process (*r*-process). ^{84}Sr on the other hand is a proton-rich nuclide purportedly made by the photodissociation of nuclides (*p*-process).

In addition to the primordial (nucleosynthetic) source of ^{87}Sr, it is also produced by the radioactive decay of the unstable ^{87}Rb isotope. $^{87}Rb \rightarrow {}^{87}Sr + e^{-}$ with a half life of 48.8Ga (Neumann and Huster, 1974).

The growth of radiogenic ^{87}Sr is described as:

$$^{87}Sr = {}^{87}Sr_i + {}^{87}Rb\left(e^{\lambda t} - 1\right) \quad \text{..... 2}$$

Where $^{87}Sr_i$ is the initial amount of ^{87}Sr in the sample, λ is the decay constant of ^{87}Rb and *t* is the time since formation of the sample.

Normalizing all concentrations in Equation 2 with that of a reference isotope, in this case, ^{86}Sr, which is stable and not produced by decay yields:

$$\frac{^{87}Sr}{^{86}Sr} = \left(\frac{^{87}Sr}{^{86}Sr}\right)_i + \frac{^{87}Rb}{^{86}Sr}\left(e^{\lambda t} - 1\right) \quad \text{.....3}$$

The slope of the regression line defined by $^{87}Rb/^{86}Sr$ and $^{87}Sr/^{86}Sr$ ratios plotted on an isochron diagram defines the age of the sample and the y intercept defines the initial strontium composition. Two chronometers can be used based on the decay of ^{87}Rb: a Rb-Sr isochron (absolute) chronometer (Figure 1.9) and an Initial $^{87}Sr/^{86}Sr$ (relative) chronometer (Figure 1.10).

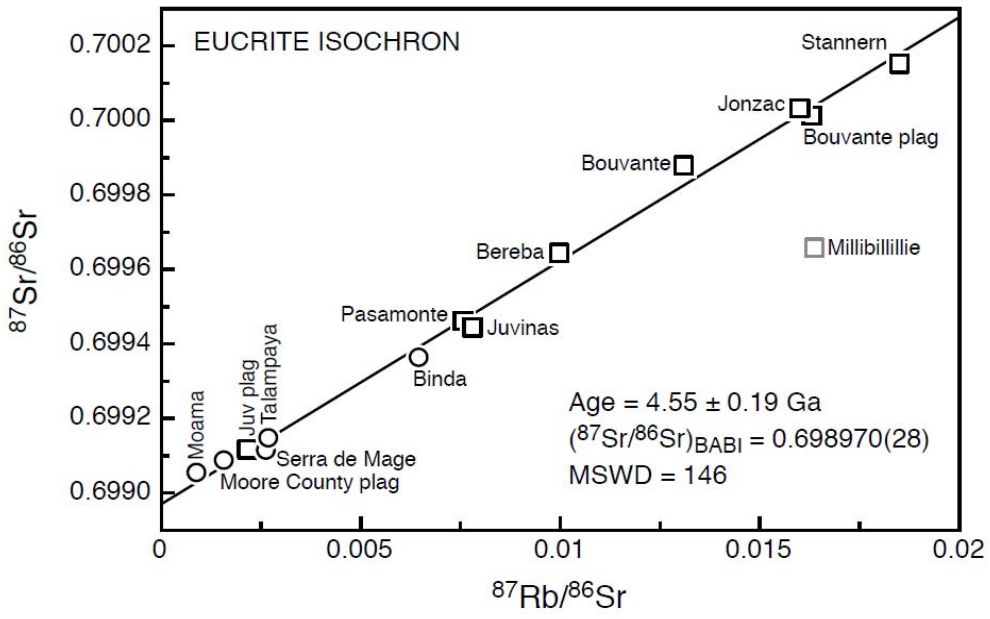

Figure 1.9: Rb-Sr isochron diagram showing data for eucrites (Hans et al., 2013). All data except Millbillillie plot along a correlation line with an age of 4.55 Ga (using a ^{87}Rb decay constant of 1.393×10^{-11} a^{-1}; (Nebel et al., 2011). $(^{87}Sr/^{86}Sr)_{BABI}$ defines the initial Sr isotope composition of the eucrite parent body.

A Rb-Sr isochron requires a high Rb/Sr ratio. This dating method is sensitive to disturbance and its precision is controlled mainly by the Rb/Sr ratio. With the low Rb abundance in CAIs, direct dating based on a Rb-Sr isochron is not practical. The initial $^{87}Sr/^{86}Sr$ dating method on the other hand requires a low Rb/Sr ratio. This method is considered relatively insensitive to disturbance if no Rb is added. Ages obtained by this method are model dependent because they require the determination of an initial $^{87}Sr/^{86}Sr$ of the solar system, and the assumption of association with a chondritic Rb/Sr. Figure 1.10 from Halliday and Porcelli (2001) illustrates how Rb-Sr model ages can be calculated.

The first assumes that objects formed from material that separated from a solar nebula with their current Rb/Sr ratio (Figure 1.10a). The assumption for this model is that objects are depleted in Rb because of incomplete condensation of moderately volatile elements in the nebula at the time of separation. The time of separation of the Sr from the nebula defined by the Rb-Sr model age must predate full condensation of the moderately volatile elements in the nebula and provide a minimum life span of the solar nebula (Gray et al., 1973; Wasserburg et al., 1977b; Podosek et al., 1991; Lugmair and Galer, 1992; Hans et al., 2013). This model provides a limit on the formation age of the object, because the solar nebula is thought to represent the most extreme Rb-Sr reservoir in which the increase in Sr isotopic composition can be accomplished.

Alternatively, Rb-Sr ages can be calculated by considering a model that assumes that accretion of differentiated objects was achieved by collisions between solid bodies that were already variably depleted in volatiles by early events in the solar nebula which (Figure 1.10b). That is, early Sr isotopic evolution occurred, at least in part, in Rb-Sr environments similar to those represented by chondrites, and within early planetesimals. With good independent constraints on the age of the object, the time-integrated Rb-Sr of its precursor material can be calculated from the initial Sr isotopic composition.

CAIs being the oldest objects in the solar system therefore have a unique place in solar system history in tying down the initial $^{87}Sr/^{86}Sr$. In evaluating the Sr isotope characteristics of CAIs we can test the system for closure. In addition, most Sr isotope analyses of CAIs reported in literature were carried out a long time ago and with modern methods we can achieve nearly an order of magnitude greater precision.

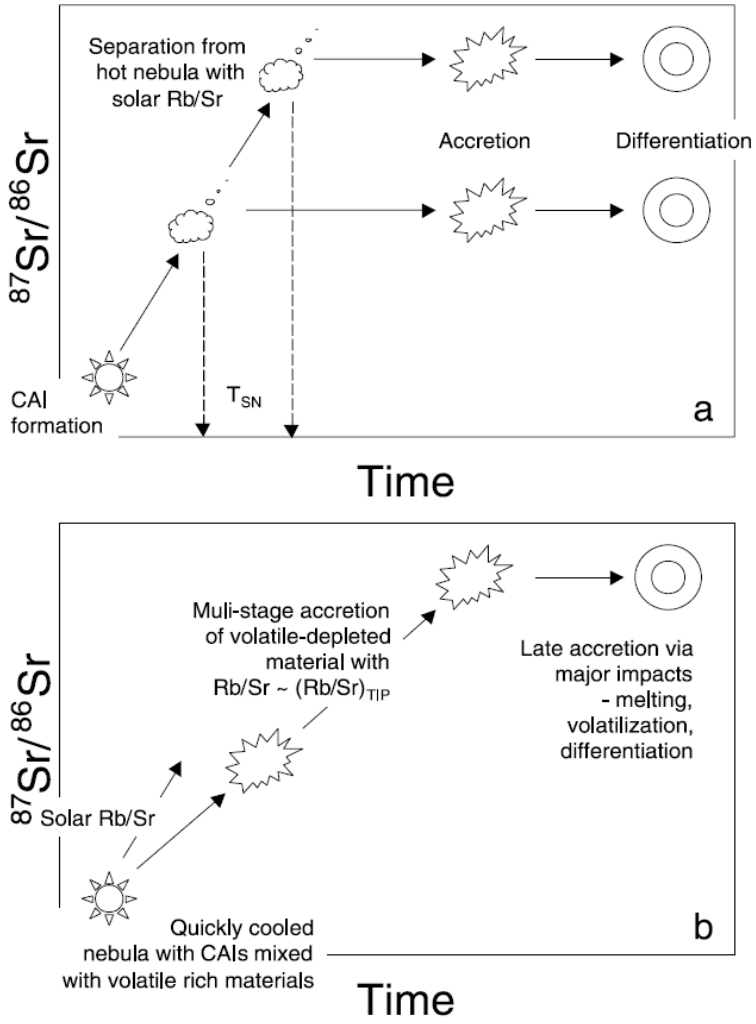

Figure 1.10: Schematic illustration from Halliday and Porcelli (2001) of the concept of defining a) the time of separation from a hot solar nebula (T_{SN}). Initial $^{87}Sr/^{86}Sr$ of the solar nebula evolution is defined by CAI. b) the time-integrated Rb/Sr from Sr isotope data. $(Rb/Sr)_{TIP}$ = time-integrated precursor ratio.

U-Pb dating system

U-Pb dating is another long-lived isotope system, but in this case the parent (U) is refractory and the daughter (Pb) is volatile. As such it offers a much better prospect of direct dating of CAIs because at the temperatures required to melt CAIs, any initial Pb will be lost. The U-Th-Pb dating method is based on the radioactive isotopes of uranium and thorium, decaying to different isotopes of lead. ^{238}U (99.2742 %) decays to ^{206}Pb and ^{235}U (0.7204 %) decays to ^{207}Pb

with half-lives of 4.468 Ga, and 704 Ma respectively (Jaffey et al., 1971) and ^{232}Th (100 %) decays to ^{208}Pb with a half-life of 14.1 Ga (Le Roux and Glendenin, 1963). The parent isotopes decay through a sequence of alpha and beta decays that results in a series of intermediate daughter isotopes, and then finally to the stable isotope of Pb. The decay chains are summarized in Figure 1.11.

The U-Th-Pb system leads to the following equations:

$$\left(\frac{^{206}Pb}{^{204}Pb}\right)=\left(\frac{^{206}Pb}{^{204}Pb}\right)_0+\left(\frac{^{238}U}{^{204}Pb}\right)\left(e^{\lambda_{238}t}-1\right) \quad \text{.....4}$$

$$\left(\frac{^{207}Pb}{^{204}Pb}\right)=\left(\frac{^{207}Pb}{^{204}Pb}\right)_0+\left(\frac{^{235}U}{^{204}Pb}\right)\left(e^{\lambda_{235}t}-1\right) \quad \text{.....5}$$

$$\left(\frac{^{208}Pb}{^{204}Pb}\right)=\left(\frac{^{208}Pb}{^{204}Pb}\right)_0+\left(\frac{^{232}Th}{^{204}Pb}\right)\left(e^{\lambda_{232}t}-1\right) \quad \text{.....6}$$

Where the 0 indicates the ratio of the isotopic composition of Pb when the system closed, *t* is the time since the system closed, and λ_{238}, λ_{235} and λ_{232} are the decay constants of ^{238}U, ^{235}U, and ^{232}Th. Dividing equation 5 by equation 4 for the dual U-Pb decay system (^{238}U → ^{206}Pb and ^{235}U → ^{207}Pb) yields a fourth equation:

$$\frac{\left(\frac{^{207}Pb}{^{204}Pb}\right)-\left(\frac{^{207}Pb}{^{204}Pb}\right)_0}{\left(\frac{^{206}Pb}{^{204}Pb}\right)-\left(\frac{^{206}Pb}{^{204}Pb}\right)_0}=\left(\frac{^{235}U}{^{238}U}\right)\frac{\left(e^{\lambda_{235}t}-1\right)}{\left(e^{\lambda_{238}t}-1\right)}=\left(\frac{^{207}Pb}{^{206}Pb}\right)^* \quad \text{.....7}$$

Where * refers to radiogenic ^{207}Pb/^{206}Pb.

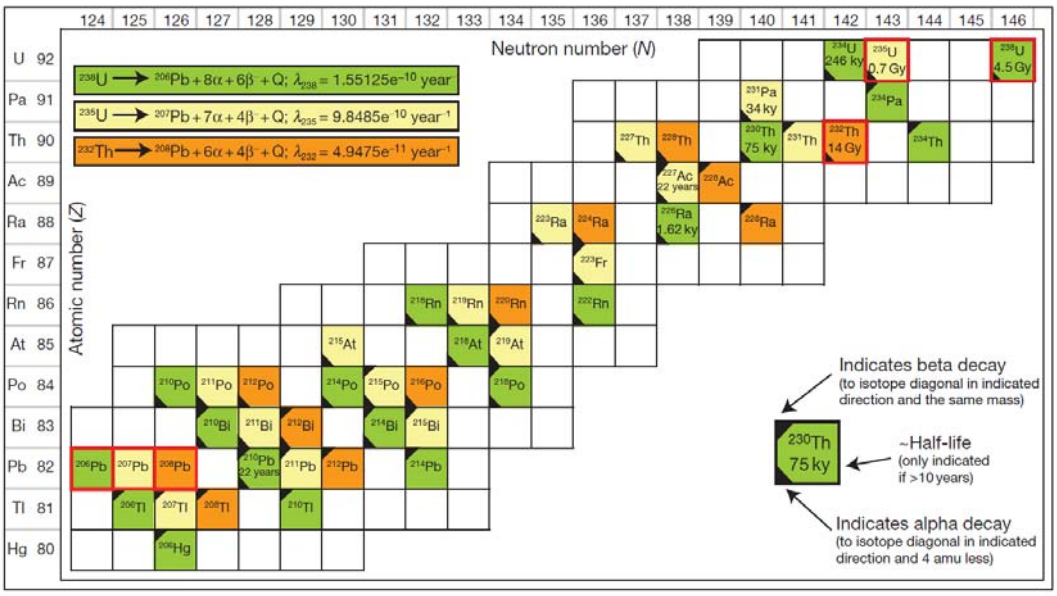

Figure 1.11: A diagram from Schoene (2014), showing the U-Th-Pb decay chains. Each isotope occurring in a given decay chain is colour-coded to its parent isotope, which are outlined in red, as are the stable daughter isotopes of Pb.

All the four equations above, allow for the calculation of dates in U-Th-Pb geochronology. This information can be represented graphically in a number of ways. While the same information can be pulled from any of these graphical depictions, different diagrams have been used as convenient ways of displaying different types of data. Equations 4-6 can be used to create traditional isochron plots that are used widely in many geochronometric systems. Notable among them are the coupled use of both decay schemes in the "concordia diagram" (Wetherill, 1956) (a plot of analytical points relative to a locus of identical $^{206}Pb/^{238}U$ and $^{207}Pb/^{235}U$ dates). Other versions of the concordia diagram have been used in the U-Th-Pb system by placing any two (or more) of the four usable clocks onto axes (e.g., Steiger and Wasserburg, 1966; Villeneuve et al., 2000; Searle et al., 2007). However, the most popular alternative to the Wetherill diagram is the Tera-Wasserburg (T-W) concordia diagram, an inverse form of the Wetherill concordia diagram which places $^{238}U/^{206}Pb$ and $^{207}Pb/^{206}Pb$ on the x- and y-axes, respectively (Tera and Wasserburg, 1972a; Tera and Wasserburg, 1972b). An illustration of the Wetherill and T-W concordia diagrams is shown in Figure 1.12.

Equation 7 allows for the construction of a Pb-Pb isochron diagram in $^{206}Pb/^{204}Pb$-$^{207}Pb/^{204}Pb$ space known as Holmes-Houtermans diagram (Holmes, 1946; Houtermans, 1946). Age can be

calculated by linear regression in $^{206}Pb/^{204}Pb$-$^{207}Pb/^{204}Pb$ space, or if initial Pb is negligible, then the measured $(^{207}Pb/^{206}Pb)^*$ can be used to directly calculate a Pb-Pb date.

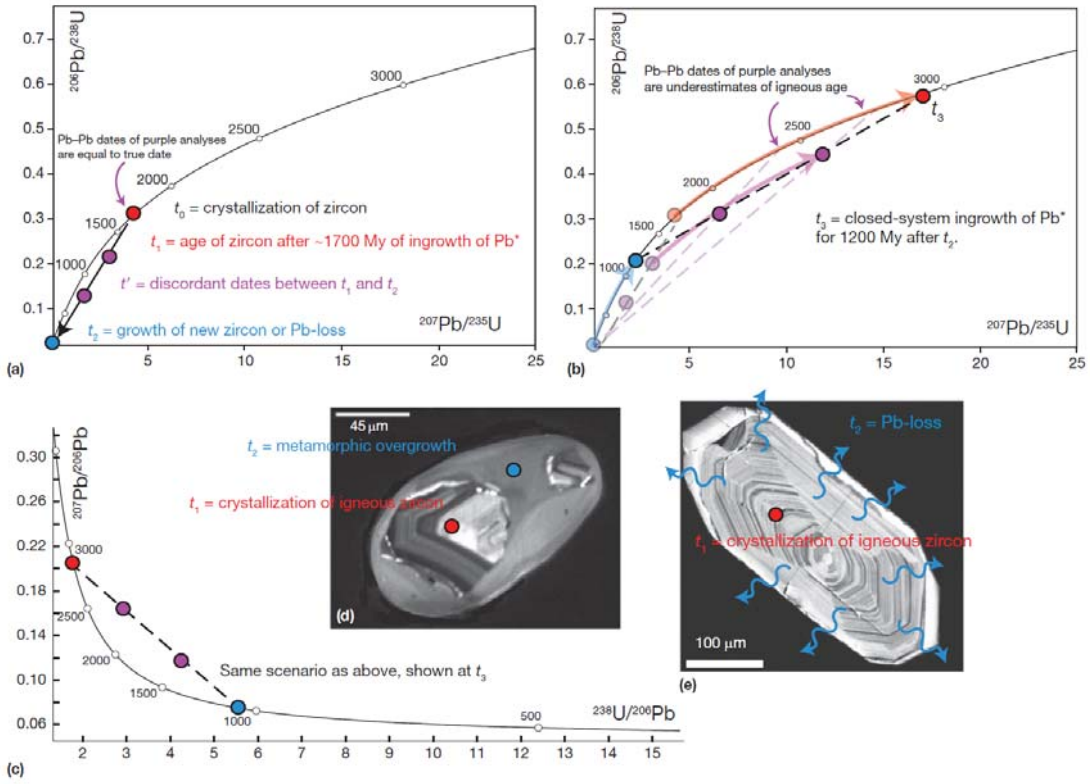

Figure 1.12: Examples of (a, b) Wetherill concordia diagram and (c) the Tera-Wasserburg (T-W) diagram from Schoene (2014) illustrating zircon growth history. (d, e) Illustrate the scenario in (a) and (b) as would possibly be recorded in the event of metamorphism and Pb loss respectively.

Another form of the T-W diagram introduced in Tera et al. (1974) and more often used in modern meteorite geochronology employs a modification of the Pb-Pb isochron by plotting $^{204}Pb/^{206}Pb$ versus $^{207}Pb/^{206}Pb$ (Figure 1.13). This approach in combination with modern analytical techniques, allows very precise calculation of $^{207}Pb/^{206}Pb^*$, which is weighted toward samples that are the least sensitive to Pb_c (nonradiogenic (or common) Pb introduced during laboratory work or naturally prior to sampling) (e.g., Amelin et al., 2002; Baker et al., 2005;

Bouvier et al., 2007; Connelly et al., 2008; Wadhwa et al., 2009; Amelin et al., 2010; Connelly et al., 2012).

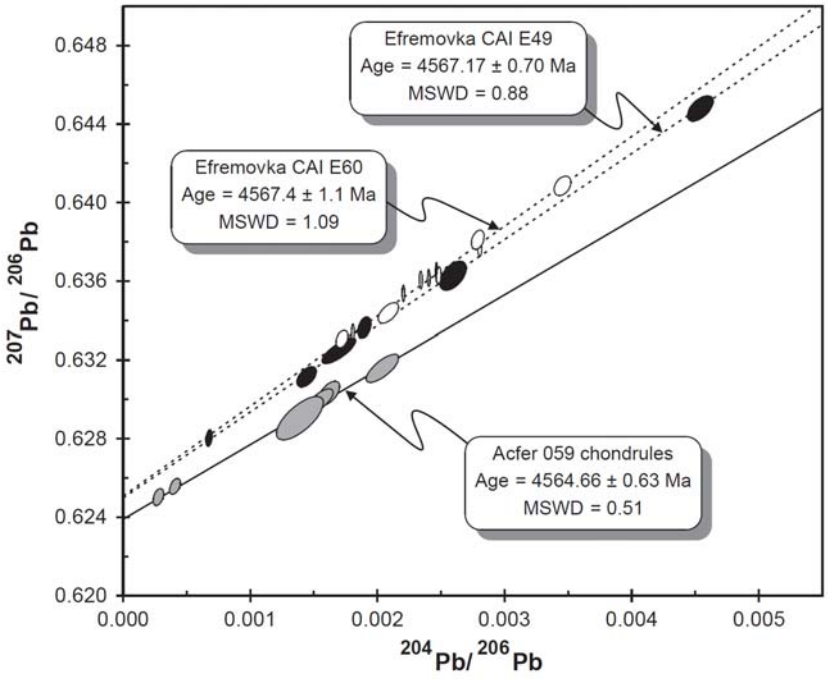

Figure 1.13: A $^{207}Pb/^{206}Pb$ vs $^{204}Pb/^{206}Pb$ isochron plot for acid-washed chondrules from the CR chondrite Acfer 059 (solid line), and acid-washed fractions from the Efremovka CAIs (dashed lines) (Amelin et al., 2002).

As shown in Equation 7, the Pb-Pb isochron method requires the designation of the $^{238}U/^{235}U$ ratio. Until recently, the modern $^{238}U/^{235}U$ ratio in meteoritic material has been assumed to be invariant and taken as 137.88 (Steiger and Jäger, 1977; Chen and Wasserburg, 1980). However, Brennecka et al. (2010) demonstrated that this assumption is invalid with measured values in CAIs of the Allende meteorite ranging from 137.409 ± 0.039 and 137.885 ± 0.009. If variability in $^{238}U/^{235}U$ is not addressed, it causes discrepant ages and thereby increases uncertainties in calculated CAI ages. As a result, reliable CAI ages require a measured modern $^{235}U/^{238}U$ ratio. If the sample behaved as a closed system then the difference between the present and initial ratios of $^{207}Pb/^{204}Pb$ versus $^{206}Pb/^{204}Pb$ should produce a straight line with a slope defining time since formation.

For some time, CAIs have been regarded as the oldest known objects that formed from the early solar nebula (Papanastassiou and Wasserburg, 1969; Gray et al., 1973; Chen and Tilton, 1976; Tatsumoto et al., 1976; Chen and Wasserburg, 1981). Subsequent work has refined this age. Recent Pb-Pb dates of CAIs from the reduced CV chondrite Efremovka gave a consistent age of 4567.3 ± 0.16 Ma (Connelly et al., 2012). CAIs in chondrites are the first solids to form in the protoplanetary disk hence the age of CAIs is considered the age of the Solar System.

1.4. SECONDARY PROCESSING

Most groups of chondritic meteorites experienced varying degrees of secondary processing such as melting, shock metamorphism, thermal metamorphism and aqueous alteration in the solar nebula and or in the asteroidal environment (Scott and Jones, 1990; Scott et al., 1992; Rubin and Krot, 1996; Brearley, 2003; Krot et al., 2006a). The results of these secondary alteration processes include but are not limited to melt veins, strained mineral grains, fractures, brecciation, alkali and iron enrichment, and the formation of secondary hydrous and anhydrous minerals.

Secondary alteration processes have been shown to significantly modify the primary nebular signatures in chondritic components of most chondrite groups (e.g., CV chondrites, (Krot et al., 1995); CK chondrites, (Geiger and Bischoff, 1995); CO chondrites, (Brearley, 1993); ordinary chondrites, (McSween Jr and Labotka, 1993); and Rumuruti type chondrites, (Kallemeyn et al., 1996).

CV carbonaceous chondrites are divided into the reduced (CVred), oxidized Allende-like (CVoxA) and oxidized Bali-like (CVoxB) subgroups based primarily on their complex alteration history (McSween Jr, 1977; Weisberg and Prinz, 1998). The CVoxB chondrites (e.g., Kaba, Bali) experienced aqueous alteration resulting in replacement of primary minerals in chondrules, CAIs, and AOAs by secondary phyllosilicates, magnetite, Fe, Ni-sulfides, Fe, Ni-carbides, fayalite, and andradite. Their matrices largely consist of secondary minerals, including Ca, Fe-pyroxene and andradite, fayalite and ferrous olivine, and abundant phyllosilicates. The CVoxA chondrites (e.g., Allende), are more extensively altered than the CVoxB, but contain very minor phyllosilicates and are enriched in alkalis and iron. Chondrules, matrices and CAIs in the CVoxA chondrites contain secondary nepheline, sodalite, Ca, Fe-pyroxenes, andradite, Fe, Ni-sulfides, magnetite, Ni-rich metal, and ferrous olivine. Alkali-iron enrichment products are

found surrounding primary minerals, and these typically embay primary minerals, fill cross-cutting veins and are located in cavities within CAIs (Figure 1.14a-d).

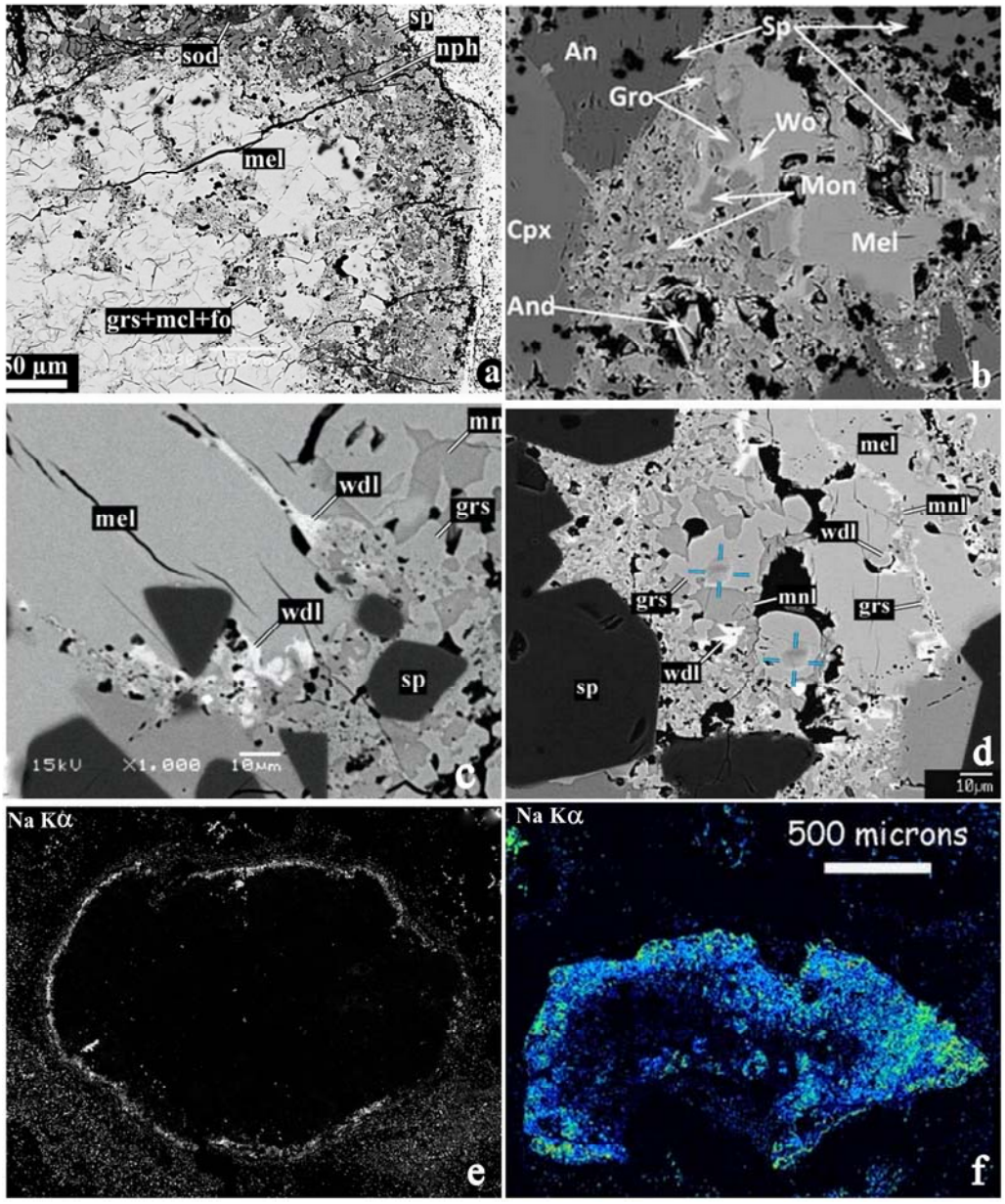

Figure 1.14: BSE images and Na (Kα) maps showing secondary alteration products in Allende CAIs. (a) Type B/C CAI 6-1-72 (Krot et al., 2007), (b) Fosterite bearing Type B CAI SJ101 (Petaev and Jacobsen, 2009), (c) Type B CAI AJEF (Jacobsen et al., 2011) and (d) Type B CAI TS34 (Krot et al., 2010) (e) Na (Kα) map of CAI 6-1-72. The CAI periphery has secondary nepheline and sodalite. (f) Na (Kα) of a Type A CAI (Ford and Brearley, 2007b) characterized

by enhanced Na content due to the presence of nepheline and sodalite alteration products. grs:grossular, and:andradite, fo:fosterite, wdl:wadalite, mnl/mon:monticellite, wo:wollastonite, sod:sodalite, and nph:nepheline.

Whether the alkali-iron alteration was produced by reaction with gaseous H_2O in the solar nebula or by aqueous alteration in parent bodies has been widely debated. Some workers believe the alteration took place in a nebula setting (Grossman and Steele, 1976; Wark, 1981; Fagan et al., 2007) because the sequence of alteration is compatible with equilibration with a cooling, oxidised solar nebula gas (Hashimoto and Grossman, 1987). Wark (1981), also argued for pre-accretionary alteration because of the presence of alkali-rich halos in the meteorite matrix surrounding some CAIs.

Sodium mapping of Allende CAIs (Figure 1.12e, f) shows that sodium is more abundant in accretionary rims suggesting CAIs became alkali-rich prior to incorporation in the parent body. Veins cross-cutting CAIs typically do not extend into the meteorite matrix, indicating they did not form *in situ*. The shape of secondary mineral grains such as well-formed wollastonite whiskers, nepheline needles, and grossular in CAI cavities are indicative of condensation from a vapour, and therefore most likely in the nebula.

An alternative viewpoint argues that the alteration of CV CAIs can be explained by a parent body process of alteration by alkaline-rich fluids followed by dehydration (Krot et al., 1995). This process is postulated to have affected the more oxidised CV meteorites, such as Allende, more than the other CVs, a conclusion also reached by some other studies (e.g., McSween Jr, 1977; Greenwood et al., 1994b; Keller et al., 1994; Ford and Brearley, 2007b; Ford and Brearley, 2010). According to this model, CV chondrites experienced fluid-assisted thermal metamorphism to various degrees, which resulted in mobilization of Ca, Si, Fe, Mg, Mn, Na, and S, and replacement of primary phases in chondrules, matrices and CAIs by secondary minerals.

The CVred chondrites such as Efremovka experienced alteration similar to that of CVoxA, but to a lesser degree.

Scott et al. (1992) carried out a detailed study of shock effects in carbonaceous chondrites using optical microscopy of thin sections and found that carbonaceous chondrites can be assigned to four shock stages, Sl to S4, largely based on shock effects in olivine. The least shocked chondrite groups are CM and CO (S1 to S3). The majority (up to 90 %) of their members

studied are classified as shock stage S1. The most strongly shocked groups are CK and CV (S1 to S4) and >50 % of their members studied are classified between shock stage S2 to S3. Allende contains negligible amounts of shocked material (S1). This is supported by Transmission Electron Microscopy (TEM) studies of Allende (Ashworth and Barber, 1975). Efremovka on the other hand is on the other extreme of the scale with a shock stage of S4.

Many meteorite samples that are being studied to further our understanding of the environment of the early solar system are finds (recovered mostly from hot and cold deserts after a terrestrial residence time). This means they have had some interaction with their terrestrial environments resulting in the alteration of primary features (e.g., rust and oxidation of metal, hydration and carbonation). Knowledge of terrestrial weathering is essential to accurately interpret the pre-terrestrial history of meteorites. Calcium and Mg sulfate veins in CI chondrites were first interpreted as evidence of a late-stage oxidation event in the CI parent body, or fluid transport on the parent asteroid, but have been latterly interpreted as having formed during terrestrial residence (Gounelle and Zolensky, 2001). Terrestrial weathering can have a profound effect on the chemistry of these meteorites (Lee and Bland, 2004; Bland et al., 2006; Hammond et al., 2008). However, limited studies have been carried out regarding distinguishing terrestrial and pre-terrestrial alteration in meteorites especially on carbonaceous chondrites.

Iron-57 Mössbauer spectroscopic analysis and X-ray diffraction has been used with ordinary chondrites as a reference to track the effects of terrestrial weathering in meteorites. The degree of terrestrial weathering in ordinary chondrites can be quantitatively measured using ^{57}Fe Mössbauer spectroscopy to determine the proportions of oxidized Fe (Fe^0, Fe^{2+}, Fe^{3+}) in terrestrial alteration products (metal, sulphides and silicates) of weathered chondrites. This is measured in relation to the known amounts of Fe oxides in newly fallen ordinary chondrites (Bland et al., 1996; Bland et al., 1998b; Bland et al., 2006). In CV chondrites for example, X-ray diffraction for Allende indicates minimal terrestrial alteration (Bland et al., 2004) and ^{57}Fe Mössbauer spectra shows no Fe^{3+} component (Hoffman et al., 2001). However, Axtell (meteorite Find) shows abundant Fe^{3+}-bearing phyllosilicates (Hoffman et al., 2000; Hoffman and Seifu, 2000), with similar Mössbauer parameters to terrestrial weathered ordinary chondrites (Bland et al., 1998a).

1.5. THE PURPOSE OF STUDY

Most of the CAIs described so far are from the large and abundant CV chondrites Allende and Efremovka. The properties of their CAIs (size, variety and abundance) make them a rich source of knowledge concerning the timing, processes and environments of the nebula stage of our solar system.

Allende CAIs however, are known to have experienced variable but often extensive alteration resulting in the replacement of primary minerals by secondary minerals such as grossular, monticellite, wollastonite, anorthite, forsterite, nepheline, sodalite, hedenbergite, andradite, ferroan olivine etc (Meeker et al., 1983; Simon et al., 1999; Brearley and Krot, 2013) and disturbance of their internal isotope systems (Podosek et al., 1991; Papanastassiou et al., 2005). While the extent of hydrothermal alteration in Efremovka is smaller than that of Allende, the former also experienced thermal metamorphism and is moderately shocked (S4) (Scott et al., 1992; Krot et al., 1998). The environment (nebular or asteroidal) and timing of secondary alteration is still debated (Krot et al., 1995; Krot et al., 1998; MacPherson et al., 2005; Fagan et al., 2007; Ford and Brearley, 2007b; Ushikubo et al., 2007; Ford and Brearley, 2008; Krot et al., 2010; Brearley and Krot, 2013).

The effects of secondary processing: parent-body metamorphism and aqueous alteration, impacts, and terrestrial weathering, experienced by their host meteorites, which can influence the U-Pb isotope systematics in CAIs and hence the apparent age as well as acid leaching processes applied to remove non-radiogenic Pb (chondritic and terrestrial) (Amelin and Krot, 2007; Connelly and Bizzarro, 2009) is not well understood.

In recent developments of analytical techniques for the dating of CAIs, progressive dissolution during sample preparation is becoming increasingly popular. This technique is useful in removing non-radiogenic Pb and allows for high-precision dating of CAIs by increasing the spread of the data on the Pb-Pb isochron (Connelly et al., 2008; Connelly and Bizzarro, 2009; Bouvier and Wadhwa, 2010). However, it involves aggressive acid leaching (concentrated acids, high temperature with prolonged heating and ultrasonification) which may differentially attack different mineral phases and thereby induce fractionation of radiogenic Pb isotopes.

Fractionation of radiogenic Pb isotopes induced by acid leaching has been hypothesised by Amelin et al. (2009), observed by Amelin et al. (2010) and acknowledged in other studies (e.g., Connelly et al., 2008; Connelly and Bizzarro, 2009; Bouvier and Wadhwa, 2010). It is an effect

that can produce inaccurate Pb isotopic dates even in highly radiogenic U-Pb systems. This requires further study and detailed monitoring of the effects of leaching steps on rocks and minerals by complete U-Pb analysis and chemical analysis of step leachates.

Since no known meteorite is completely free from secondary processes, the only way to obtain reliable ages of CAIs is to compare the dates for the CAIs from various CV chondrites that were influenced by different secondary processes to various degrees. It is therefore important to extend the population of well-characterized CV CAIs by studying inclusions from different CV chondrites, less altered (or at altered differently than Allende). In an effort to achieve this, we initiated a study of five large refractory inclusions from a CV chondrite NWA 4502 recovered from the deserts of North West Africa, Algeria in 2006.

North West Africa (NWA) 4502 is now the second largest (total known weight >100kg) CV chondrite after Allende, and contains abundant CAIs, some of which are large and suitable for a comprehensive geochemical and isotopic study. Also, preliminary examinations show that this meteorite may have been less affected by secondary alteration than Allende and other CV chondrites. This makes NWA 4502 a promising candidate for establishing CAI chronology, resolving age discrepancies, and understanding the effects of metamorphism, alteration, and shock on the isotopic systems in CAIs.

The first objective of this study is to characterize CAIs from NWA 4502. This includes detailed petrographic, mineralogical and isotopic description of the CAIs. This will help to extend the number of well-characterized CV CAIs. The results and interpretations are presented in Chapter 2. The goal of Chapter 3 is to report isotopic data (Oxygen, Al-Mg, Rb-Sr and Uranium) obtained for NWA 4502 CAIs. A major aim of this study is to investigate the effects of acid leaching processes on U-Pb systems of NWA 4502 CAIs through a comparison between mild and aggressive acid leaching procedures. The results and interpretations together with U-Pb ages are presented in Chapter 4. The rather pristine nature of NWA 4502 CAIs compared to CAIs from Allende and Efremovka lead to a major emphasis of this study to answer the question regarding the influence of secondary processes on isotopic systems and chronology of CAIs. The concluding chapter discusses the characteristics and age of NWA 4502 CAIs in relation to other CV CAIs and attempts to tie together the results of previous chapters and other studies on the broad issue of better understanding the history of the early solar system.

CHAPTER 2

PETROLOGY AND GEOCHEMISTRY OF NWA 4502 CAIS

2.1. INTRODUCTION

The petrography and mineral chemistry of refractory inclusions in NWA 4502 are described in this chapter.

Before the beginning of this study, the NWA 4502 meteorite was only provisionally classified (without approval by the Meteorite Nomenclature Committee), had no official name, and a very basic petrographic description by T. Bunch and J. Wittke at Northern Arizona University which was only enough to designate it a CV chondrite. For the purposes of this study and subsequent data publication I classified this meteorite under the supervision of A.N. Krot of the University of Hawaii at Manoa for publication in the Meteoritical Bulletin (Sapah and Krot, 2013). More details on basic information for the classification of NWA 4502 can be found on the Meteoritical Bulletin database. Figure 2.1 presents the extract from Meteoritical Bulletin database.

There is more than 100 kg of this carbonaceous chondrite in the form of dark stones with little or no fusion crust but have smooth surfaces and varnish from desert polishing. The largest piece found so far is 22.75 kg. There are several pieces under different NWA numbers therefore the total known weight may be more. Being a meteorite find which has been in the desert environment for some time, effects of terrestrial weathering in the form of rust or oxidation can be seen on surfaces of hand specimens.

Date:	Dec 2005
Mass (g):	>100000
Pieces:	Many
Class:	CV3
Shock stage:	S2
Weathering grade:	W1
Fayalite (mol%):	12.4 (1.6-50.7, N=45)
Ferrosilite (mol%):	3.5 (0.7-19.3, N=33)
Wollastonite (mol%):	9.3 (0.7-50.9, N=33)
Classifier:	M. Sapah, ANU, and A. Krot, UHaw
Type spec mass (g):	284.6
Type spec location:	ASU
Main mass:	Eric Olsen meteorites
Comments:	Submitted by Marian S. Sapah

Northwest Africa 4502 (NWA 4502)
Algeria
Found: Dec 2005
Classification: Carbonaceous chondrite (CV3)
History: Purchased In 2006 by A. Aaronson.
Physical characteristics: More than 100 kg of dark stones with smooth, desert-polished surfaces. The largest piece is 22.75 kg
Petrography: (T. Bunch and J. Wittke, *NAU*) Well-defined chondrules, chondrule fragments, and refractory inclusions set in a slightly weathered matrix. CAIs are represented by Type A (a few are very large, up to 32 mm in diameter) and Type C are common, as are AOAs. Type B CAIs are low in abundance however, melilite mantled (Type B1) and fosterite bearing type B CAIs are present. Modal analyses (vol. %): chondrules = 48; CAIs and AOAs = 14; matrix = 38.
Geochemistry: (M. S. Sapah, ANU, and A. N. Krot, *UHaw*) The meteorite matrix consists of small crystals of ferroan olivine, sulfides, magnetite, Ni-rich metal, tiny nepheline crystals, and small irregularly shaped regions of Ca,Fe-rich silicates (pyroxenes ± andradite). Matrix olivine has Fa_{48-54} and ferrosillite and wollastonite contents of matrix pyroxenes are 11-19% and 46-49% respectively. Fayalite content of chondrule olivine is Fa_{2-39}, and ferrosillite and wollasonite contents of chondrule pyroxenes are 1-2%.
Classification: (M. S. Sapah and A. N. Krot) Carbonaceous chondrite (CV3). The sample is CV oxidized. The degree of shock is S2 and the weathering degree is W1.
Specimens: >83 kg *Aaronson*, 35 kg Eric Olson, 2.9 kg *ANU*, 284.6 g *ASU*, and 26 g *NAU*.

Figure 2.1: Classification of NWA 4502. Extract from the Meteoritical bulletin database.

NWA 4502 consists of well-defined chondrules, chondrule fragments, and refractory inclusions, all in a slightly weathered matrix. The CAIs studied in this project are extracted from pieces of NWA 4502 (total weight 2.9 kg) in the Australian National University (ANU) meteorite collection examples of which are shown in Figure 2.2. The CAI population extracted so far from this collection is represented by all the main types: Type A, Type B among which melilite mantled Type B1 and fosterite bearing (FoB) Type B CAIs are present, and Type C CAIs.

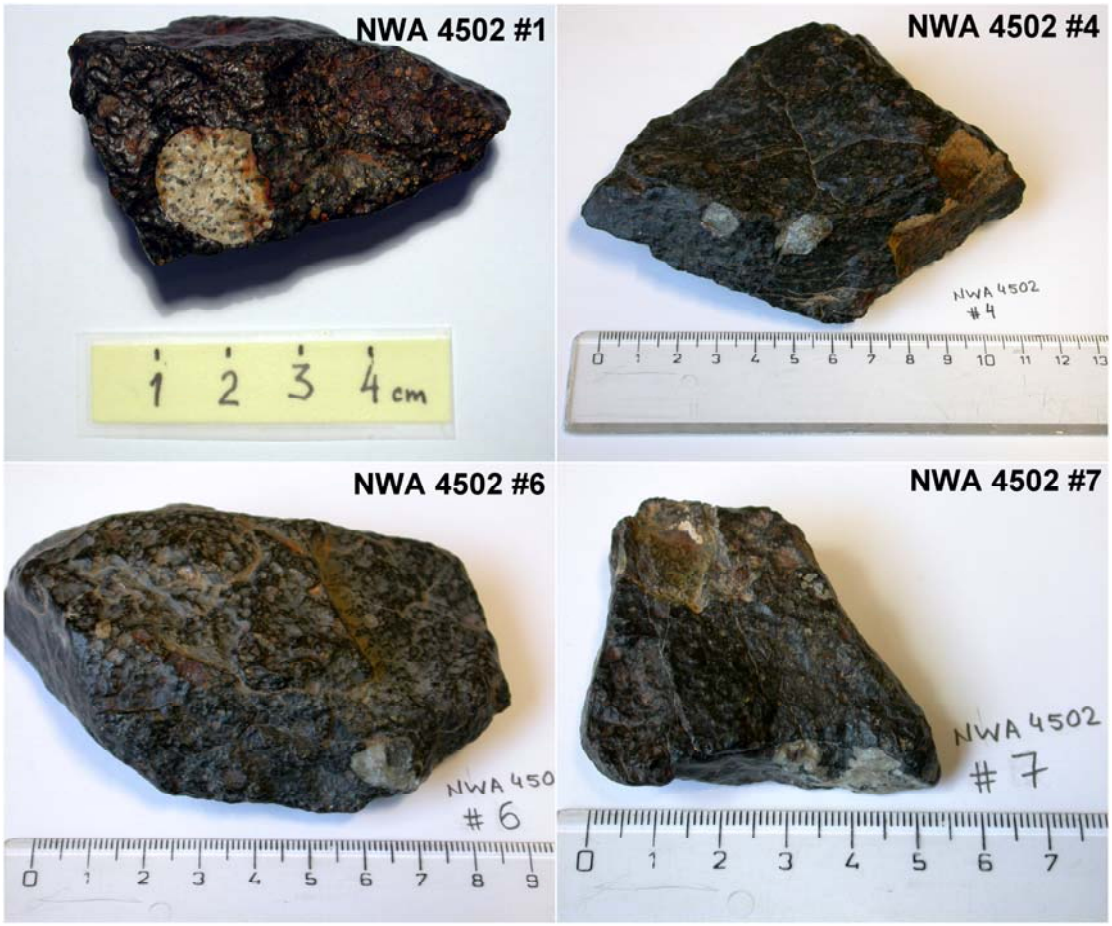

Figure 2.2: Specimens of NWA 4502 in the Australian National University collection from which CAIs were extracted for this study.

2.2. METHODS

Five CAIs were extracted from different specimens of NWA 4502 by precision cutting using a 0.1 mm diamond blade into 1-2 mm thick slices. The names given to these CAIs consists of the number of the specimen in the ANU set of specimens of this meteorite, followed by the letter (a, b, etc.) if more than one CAI were extracted from the same stone. The CAIs selected for this study were denoted *1*, *4a*, *5*, *6*, and *7*. Representative CAIs extracted from the middle portions of each specimen were mounted in epoxy and polished for petrographic and other non-destructive *in situ* analysis. CAI fragments (whole rock) and mineral fractions (separated and unseparated) recovered after disaggregation (separation from matrix and removal of rust),

cleaning and mineral separation from coarse crushed CAI fragments were processed for destructive chemical analysis.

2.2.1. Imaging and element compositions by SEM and EPMA

The mineralogy and petrology of the CAIs and the host meteorite were studied using backscattered electron (BSE) imaging, X-ray elemental mapping, and quantitative analyses with the University of Hawai'i JEOL JXA-8900 Field-Emission Electron Microprobe (EPMA) and the Research School of Earth Science, ANU JEOL JSM-6610A Scanning Electron Microscope (SEM). Both instruments are equipped with a Thermo Electron Energy Dispersive Spectrometer (EDS). The instruments were operated with 15 kV accelerating voltage and 1-2 nA beam current. Element X-ray area maps having a spatial resolution of 7-10 μm per pixel were acquired. The CAIs were mapped for Na, Mg, Al, Si, K, Ca, Ti, Cr, Mn and Fe (Kα) X-rays. Combined false colour elemental maps of Mg, Ca, and Al (Mg: red, Ca: green, Al: blue) were made using a RGB-colour scheme and the commercial software package ENVI (ENvironment for Visualizing Images) for visual presentation of CAI mineralogy. Inclusions characterised in the combined X-ray maps were subsequently studied in the BSE mode. Quantitative analysis of mineral compositions was determined with a 15 kV accelerating voltage, with 10–20 nA beam current and ~1-2 μm beam size, using well characterized in-house silicate and oxide standards (olivine-fosterite, corundum-spinel, augite-pyroxene, plagioclase-anorthite, melilite and, hibonite, and sphene glass-perovskite). Counting times on both peak and background were 10 s for Na and K and 30 s for all other elements. Modal mineralogy of CAIs was obtained using *Image J*, a Java Image Processing and Analysis software package.

2.2.2. Trace element compositions by LA-ICP-MS

In situ trace element analysis of mineral separates from NWA 4502 CAIs was carried out with a single collector Agilent 7700 series ICP-MS coupled to the ANU-designed HelEx ablation cell system at the Research School of Earth Sciences, Australian National University. Samples consist predominantly of melilite, pyroxene, spinel, anorthite, and hibonite. Individual mineral grain sizes were between 100-275 μm. Mineral grains on polished resin mounts were ablated with a Lambda Physik COMPex 110 excimer laser (λ = 193 nm) with a 47 μm spot size. In some cases more than one spot was analysed on one grain. Each analysis consists of 30 s of background measurement and 40 s of sample ablation. NIST standard SRM-612 was used as the

external calibration sample for trace elements. Reference element concentrations were preferred values from the GeoRem database. Multiple analyses of NIST standard SRM 614 were carried out to check the accuracy and precision of the analyses and the results are consistent with NIST reported values and values from Kurosawa et al., 2002 within analytical error. The analysed spots on mineral grains were examined by SEM after analysis to verify the mineralogy of the phases analysed.

2.3. MATRIX AND CHONDRULE DESCRIPTIONS

NWA 4502 is composed of ca. 48 % chondrules and chondrule fragments, 14 % refractory inclusions, and 38 % slightly weathered matrix (weathering grade 1). It is an oxidized CV3 chondrite with a matrix/chondrule ratio of 0.8. The compact matrix consists of rare secondary alteration products such as fine-grained (1-3 μm) ferroan olivine, Fe, Ni-sulphides, magnetite, Ni-rich metal, tiny nepheline crystals, and small irregularly-shaped regions of Ca, Fe-rich silicates (Figure 2.3), all characteristic of the CV oxidized Allende-like subgroup.

Olivine crystals in matrix show intermediate compositions ($Fo_{46-50,}$ $Fa_{47-53,}$ and Ca-$Ol_{0.4-2.1}$) while matrix pyroxenes are Ca-rich (clinopyroxene) and have $En_{32-42,}$ Fs_{12-19} and Wo_{47-49} compositions.

Most chondrules in NWA 4502 are mainly type 1 (FeO-poor; Olivine Fa <10) and have porphyritic textures. They occur as Porphyritic Olivine Pyroxene (POP), Granular Olivine Pyroxene (GOP), Porphyritic Olivine (PO) and Porphyritic Pyroxene (PP) chondrules (Figures 2.4-6). Chondrule olivine is forsteritic in composition ($Fo_{91-99.5}$, $Fa_{0.2-9}$ and Ca-$Ol_{0.3-0.5}$), and pyroxenes are mainly enstatite (En_{98}, $Fs_{0.9-1.4}$ and $Wo_{0.9-1.2}$). The major element compositions of major mineral phases in the matrix and chondrules of NWA 4502 are summarised in Tables 2.1 and 2.2 and plotted in Figure 2.7.

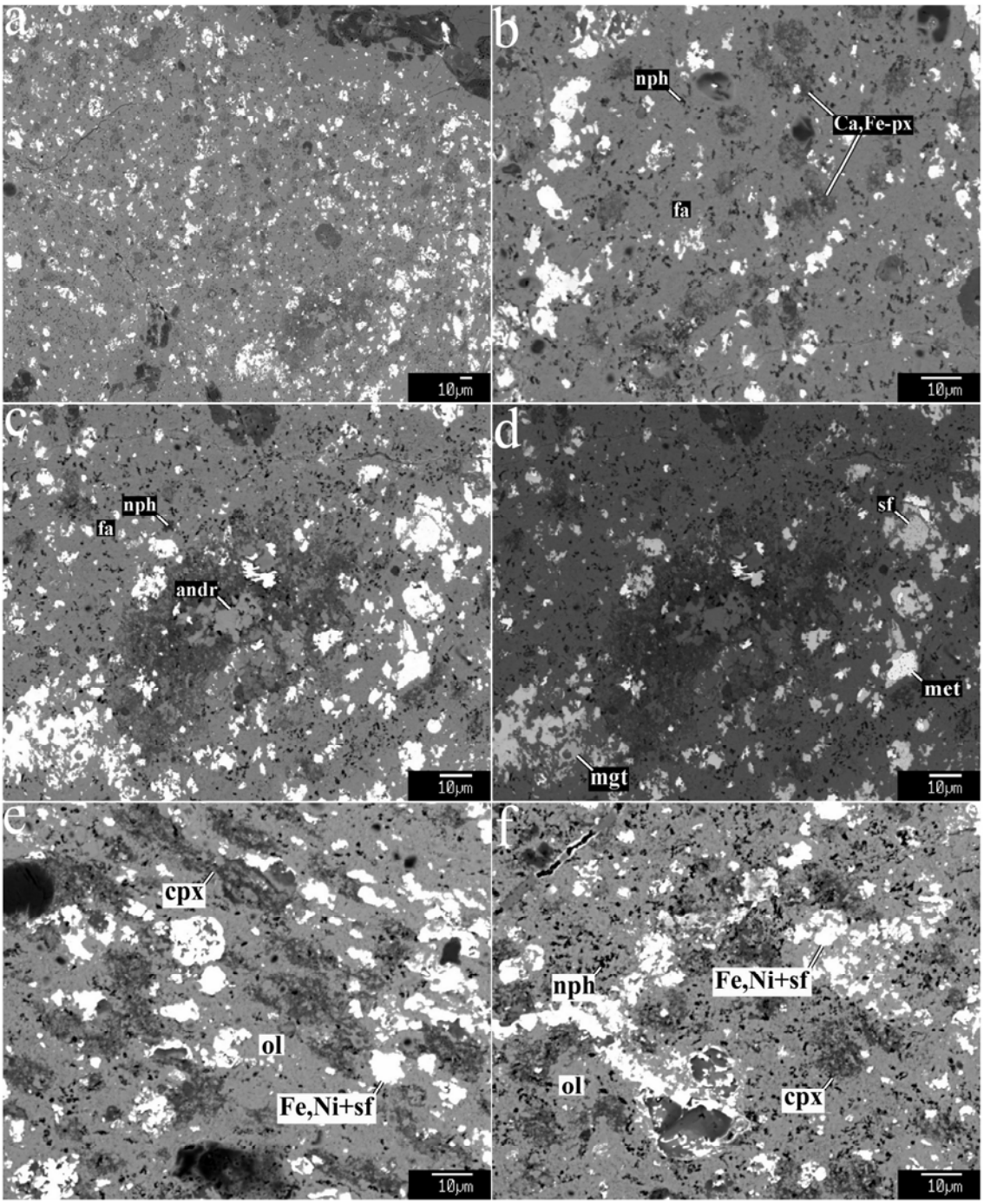

Figure 2.3: BSE images (a-f) of NWA 4502 matrix composed of Fe-rich olivine, Ca-rich pyroxene, andradite, magnetite, Fe, Ni-sulfides, Fe,Ni metal, nepheline crystals, and Ca, Fe-rich silicates. Andr: andradite, cpx: Ca pyroxene, fa: fayalite, Fe-Ni+sf: Iron-nickel sulphides, met: Fe-Ni metal, nph: nephiline, ol: olivine.

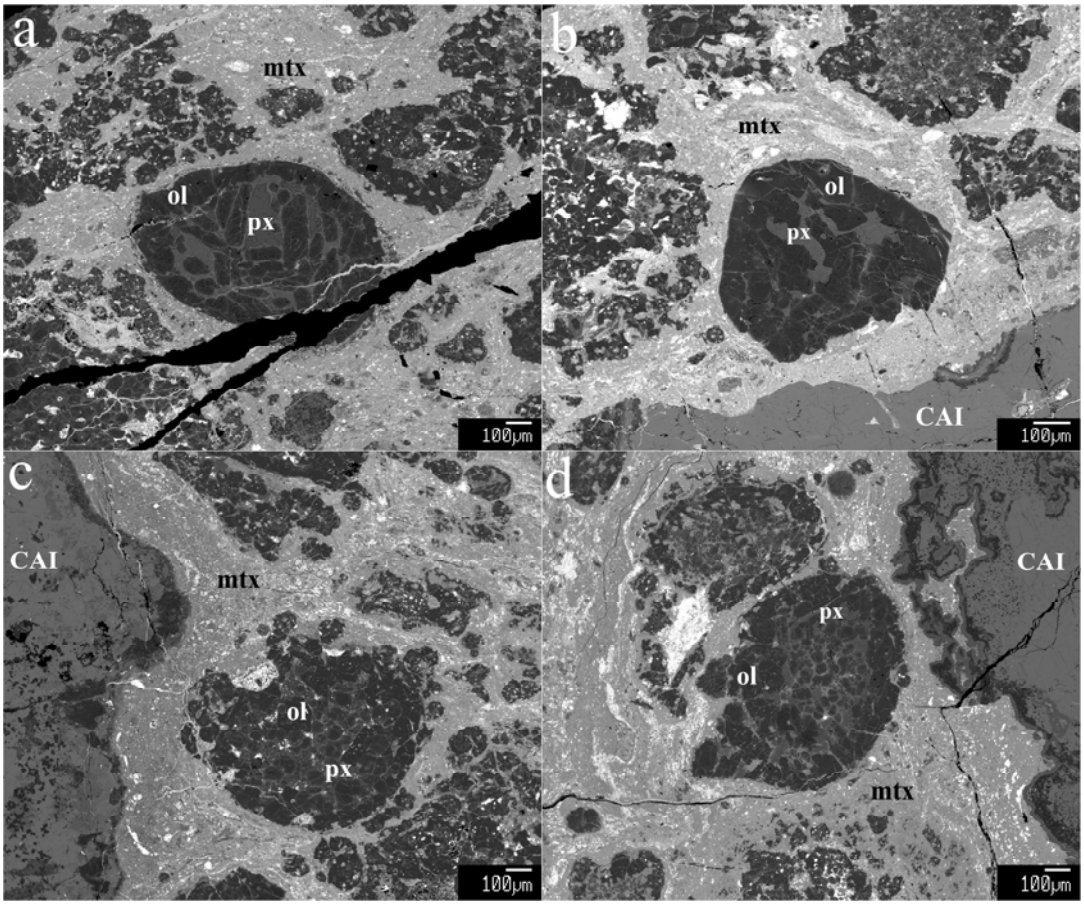

Figure 2.4: BSE images (a, b) of Porphyritic Olivine Pyroxene (POP) chondrules, (c, d) Granular Olivine Pyroxene (GOP) chondrules. px: low-Ca pyroxene, ol: FeO-poor olivine, mtx: matrix.

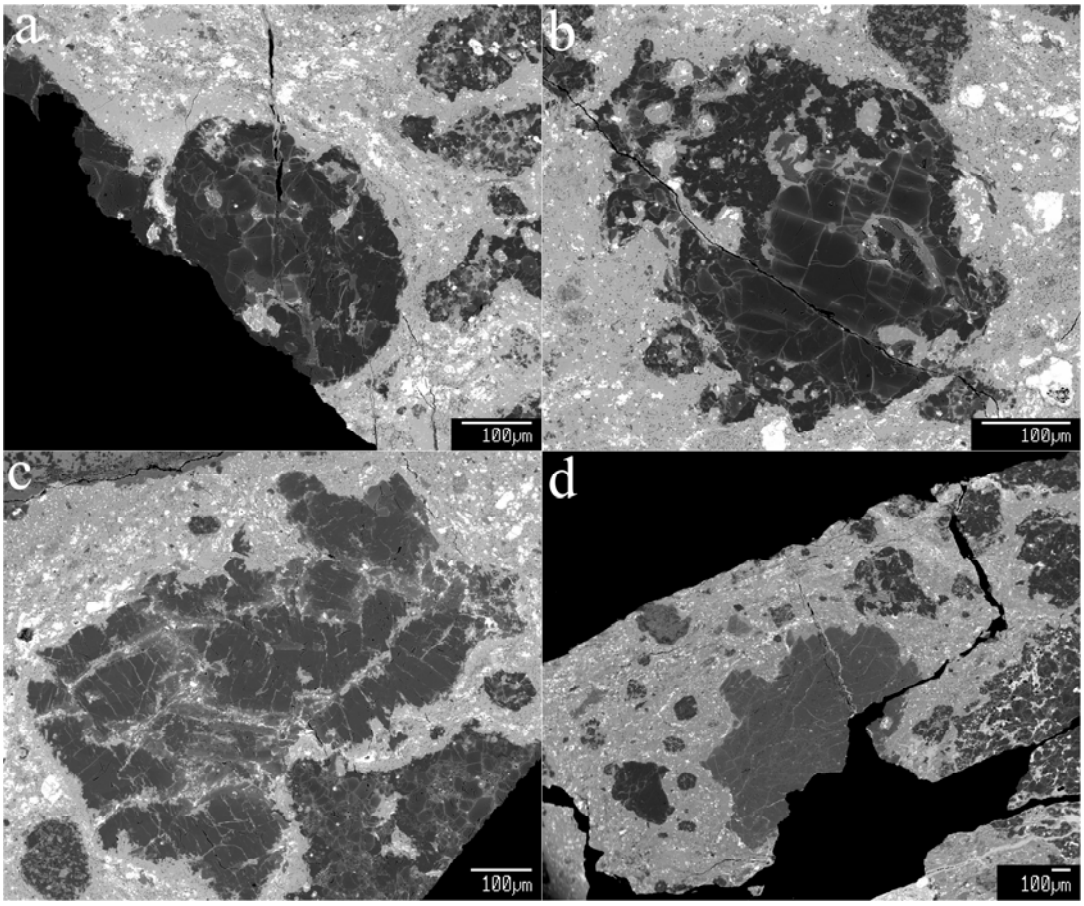

Figure 2.5: BSE images of Porphyritic Olivine (PO) chondrules, (a, b) FeO-poor olivine (type I) chondrules and (c, d) olivine aggregates.

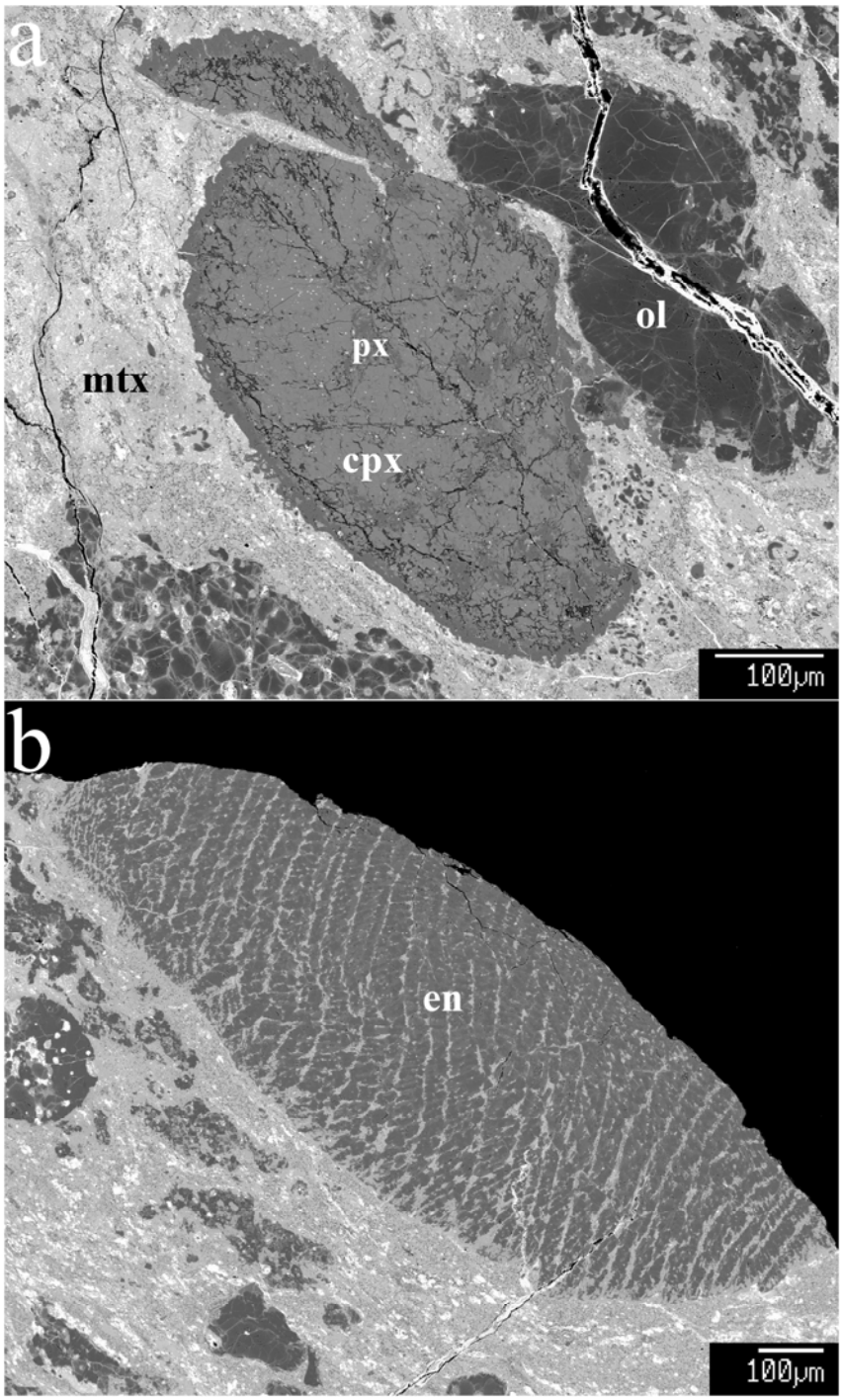

Figure 2.6: BSE images of pyroxene chondrules. (a) chondrule composed mainly of high-Ca pyroxene (cpx) with smaller grains of low-Ca pyroxene (px) in the core and forming a rim layer around the chondrule, (b) chondrule composed of enstatite (en). The enstatite crystals appear to have emanated from a point in the chondrule.

Table 2.1: Major element composition of Olivine and Pyroxene in matrix.

	Olivine					Pyroxene				
Oxide	1	2	3	4	5	1	2	3	4	5
SiO_2	34.98	35.11	34.10	33.99	34.16	52.72	53.05	52.04	52.98	52.73
TiO_2	0.01	0.00	0.06	0.01	0.00	0.01	0.00	0.02	0.01	0.02
Al_2O_3	0.48	0.15	1.88	0.12	0.14	0.77	0.47	1.25	1.12	1.05
Cr_2O_3	0.26	0.07	0.20	0.15	0.07	0.03	0.02	0.03	0.02	0.34
FeO	38.48	39.49	39.90	42.82	42.70	10.94	12.07	11.19	10.24	7.28
MnO	0.28	0.29	0.33	0.36	0.29	0.08	0.11	0.05	0.03	0.07
MgO	23.11	23.04	21.75	20.81	20.60	12.12	11.33	11.78	12.87	14.68
CaO	1.35	0.62	0.48	0.34	0.26	23.85	23.67	22.71	23.48	22.80
Na_2O	0.09	0.03	0.20	0.21	0.10	0.10	0.06	0.16	0.12	0.07
K_2O	nd	nd	0.02	nd	nd	nd	nd	nd	nd	nd
Total	99.0	98.8	98.9	98.8	98.3	100.6	100.8	99.2	100.9	99.0

nd-not detected

Table 2.2: Major element composition of Olivine and Pyroxene in chondrules.

	Olivine					Pyroxene						
Oxide\Chd	1	2	3	4	5	1	2	3	4	5	6	7
SiO_2	40.83	41.11	40.88	41.34	41.37	38.36	58.40	57.70	58.13	58.51	58.79	45.27
TiO_2	0.04	0.04	0.01	0.03	0.01	0.01	0.21	0.22	0.23	0.16	0.13	1.27
Al_2O_3	0.12	0.11	0.01	0.08	0.03	0.07	1.03	1.38	1.09	0.83	0.79	14.46
Cr_2O_3	0.22	0.15	0.06	0.14	0.09	0.13	0.52	0.59	0.47	0.46	0.51	0.45
FeO	4.20	4.84	7.34	4.81	6.64	20.32	0.88	0.78	0.96	0.57	0.91	0.39
MnO	0.09	0.11	0.14	0.06	0.11	0.18	0.10	0.08	0.06	0.05	0.05	0.01
MgO	53.58	52.97	51.40	52.95	52.23	39.14	38.95	37.94	38.32	39.04	38.73	14.98
CaO	0.31	0.27	0.22	0.21	0.19	0.21	0.58	0.54	0.59	0.45	0.46	21.94
Na_2O	0.01	nd	0.01	nd	nd	0.03	nd	nd	nd	nd	nd	0.01
K_2O	nd	nd	nd	nd	nd	nd	nd	nd	nd	nd	nd	nd
Total	99.40	99.61	100.08	99.62	100.67	98.46	100.68	99.23	99.86	100.08	100.37	98.8
n	16	5	5	6	3	6	3	6	5	6	3	5

nd-not detected

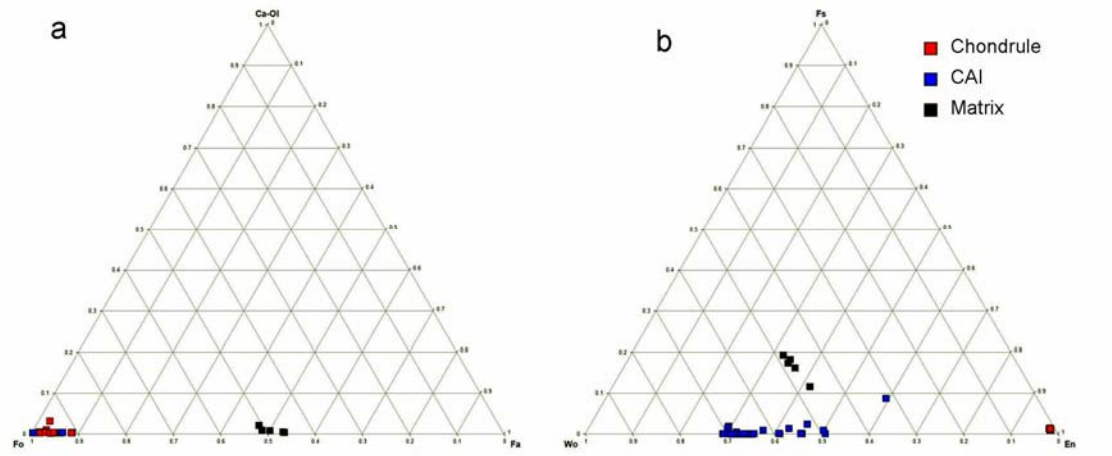

Figure 2.7: Ternary plots of a) Olivine and b) Pyroxene compositions in chondrules, CAIs and matrix.

2.4. GENERAL MINERALOGY AND CLASSIFICATION OF NWA 4502 CAI

Refractory inclusions studied so far in NWA 4502 are coarse-grained, igneous inclusions, up to ~1.5 cm in apparent diameter. They are classified as Type A and B inclusions following Grossman (1975), MacPherson and Grossman (1979), Wark and Lovering (1982), and MacPherson and Grossman (1984). CAI *6* and *7* are compact Type A (CTA) inclusions; CAI *4a* and *1* are Type B inclusions and CAI *5* is a Forsterite-bearing type B (FoB).

CAI *6* is large, with an ovoid shape truncated at both ends ('U' shaped). It has maximum dimensions up to ~1.5 cm (Figure 2.8). The inclusion is made up mainly of melilite (73 %) with subhedral to euhedral 100 µm grains of spinel (14 %) and 10-200 µm grains of pyroxene (12 %). Perovskite (0.4 %) grains are 3-10 µm in size and occur only along and in the rim sequence of the inclusion, and are not associated with phases in the core. The ~20-50 µm thick multi-layered Wark-Lovering (WL) rim surrounding this inclusion consists of phases that duplicate those in the core. The sequence from inside is made up of melilite, spinel mixed with minor perovskite, and pyroxene (Figure 2.9).

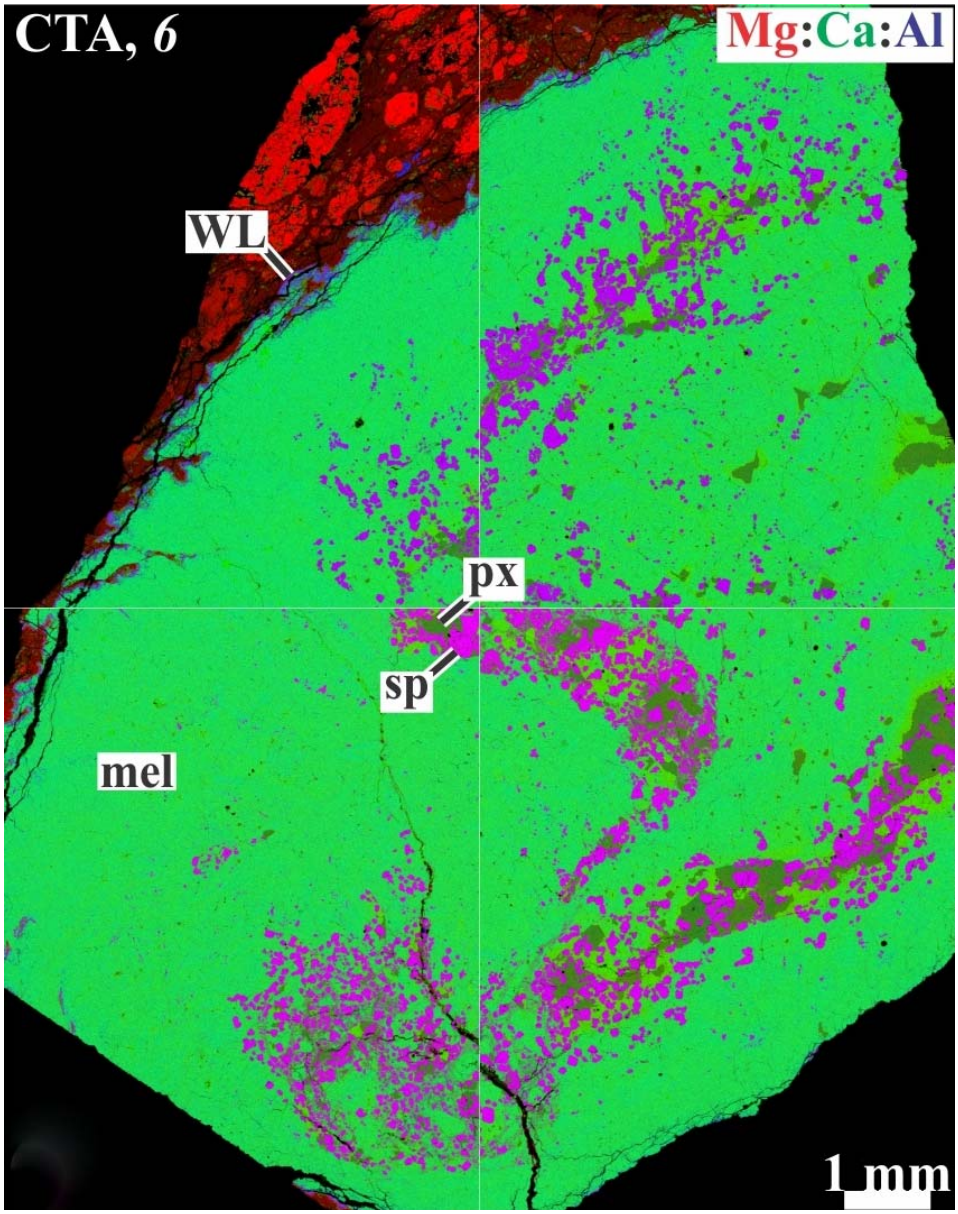

Figure 2.8: Combined elemental map in Mg (red): Ca (green): Al (blue) Kα of CAI *6* a compact Type A (CTA) CAI composed mainly of melilite (mel), pyroxene (px) and spinel (sp).

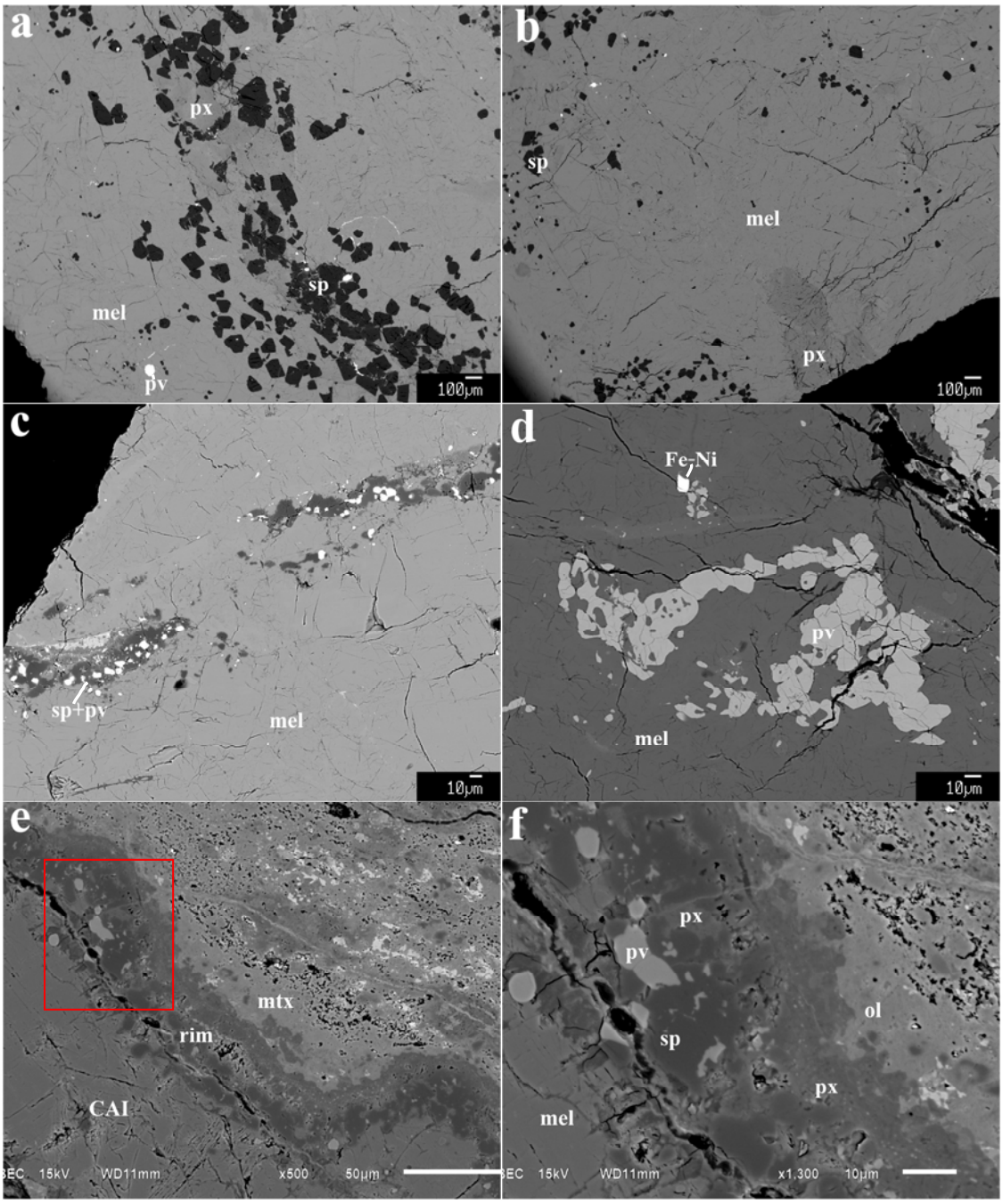

Figure 2.9: BSE images of typical mineral assemblages in the core (a-d) and rim (e, f) of CAI *6*, showing texture and association of mineral phases. The area of the rim sequence magnified in (f) is shown as red inset in (e). px: pyroxene, mel: melilite, sp: spinel, pv: perovskite, ol: olivine, Fe-Ni: Fe-Ni metal, mtx: matrix.

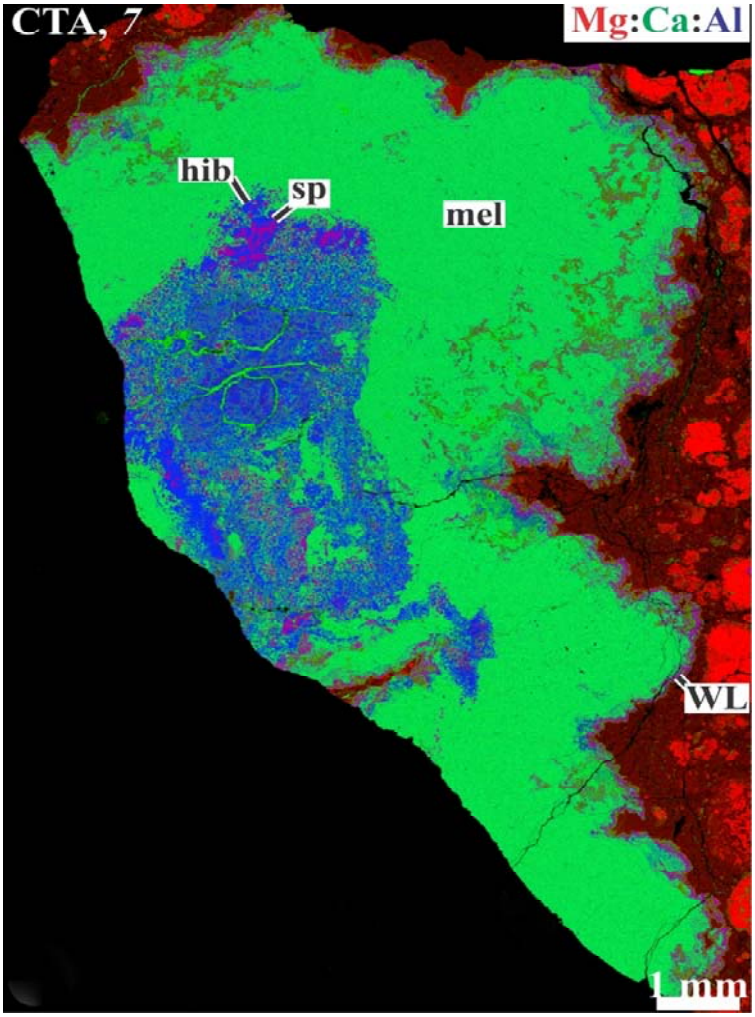

Figure 2.10: Combined elemental map in Mg (red): Ca (green): Al (blue) Kα of CAI *7* a compact Type A (CTA) CAI composed mainly of melilite (mel), hibonite (hib) and spinel (sp). It has a distinct core and mantle structure. The core is composed of an intergrowth of hibonite and spinel which is mantled by a thick layer of melilite.

CAI *7* has a more irregular structure (Figure 2.10) compared to the other NWA 4502 CAIs in this study, and has a generally ovoid shape. It is ~1.4 cm in maximum dimension. It is composed mainly of melilite (75 %), hibonite (12 %), spinel (8 %) and pyroxene + perovskite (5 %). This inclusion has a distinct core and mantle structure with the core made up of fine-grained (10-100 μm) intergrowths of subhedral to euhedral shaped spinel (~30 %) and irregular to lath shaped hibonite (~45 %), melilite (~25 %) and <1 % Fe-Ni metal. The core is mantled by a thick layer (up to 0.5 cm) of melilite associated with string-like assemblages of pyroxene,

spinel, hibonite and perovskite. The inclusion is enclosed by a WL rim about ~50-100 μm thick. The rim is made up of monomineralic and bimineralic layers. From the inside, layers are made up of melilite, spinel, a mixture of spinel and perovskite and pyroxene (Figure 2.11).

CAI *1* is an oval shaped inclusion approximately 1cm in maximum diameter (Figure 2.12). It is made up of melilite (57 %) enclosing coarse (100-500 μm) irregularly shaped pyroxene (20 %) and anorthite (15 %) as well as 20-100 μm euhedral spinel (8 %) grains peppered and poikilitically enclosed in other phases. The inclusion is bordered by a WL rim sequence of consistent thickness (~200 μm). The layers are monomineralic and consist of spinel, melilite, pyroxene, and spinel from inside out. Minor hibonite, Fe, Ni metal and nepheline are also present but rare. The rim is fractured in some areas (Figure 2.13).

CAI *4a* is oval in shape but slightly tapered at both ends with a maximum dimension of ~1 cm (Figure 2.14). It has a similar texture and composition as CAI *1*. Mineral abundances are melilite (47 %), pyroxene (29 %), anorthite (17 %) and spinel (7 %). Spinel grains apart from their poikilitic distribution also form concentric rings around pyroxene and anorthite grains. Also, anorthite is partly replaced by nepheline and sodalite at grain boundaries. The WL rim surrounding this inclusion is made up of monomineralic layers and has a thickness of ~50-80 μm. The layers consist of melilite, spinel, and pyroxene from inside out. Minor hibonite, anorthite and nepheline are present but rare. Fractures are also present at some areas (Figure 2.15).

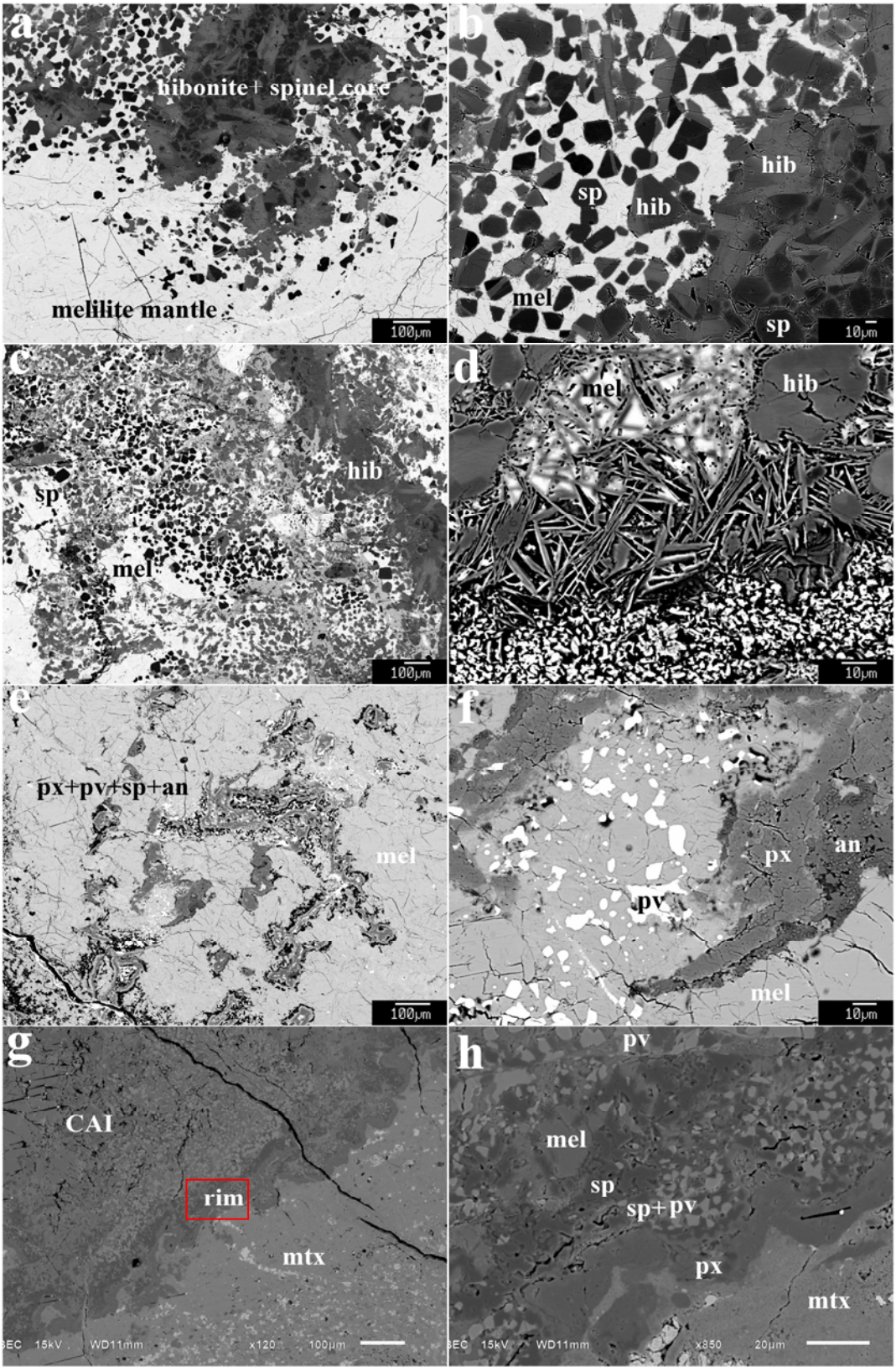

Figure 2.11: BSE images of typical mineral assemblages in the core (a-d), mantle (e, f) and rim (g, h) of CAI *7*, showing texture and association of mineral phases. The area of the rim sequence

magnified in (h) is shown as red inset in (g). px: pyroxene, mel: melilite, an: anorthite, sp: spinel, pv: perovskite, hib: hibonite, mtx: matrix.

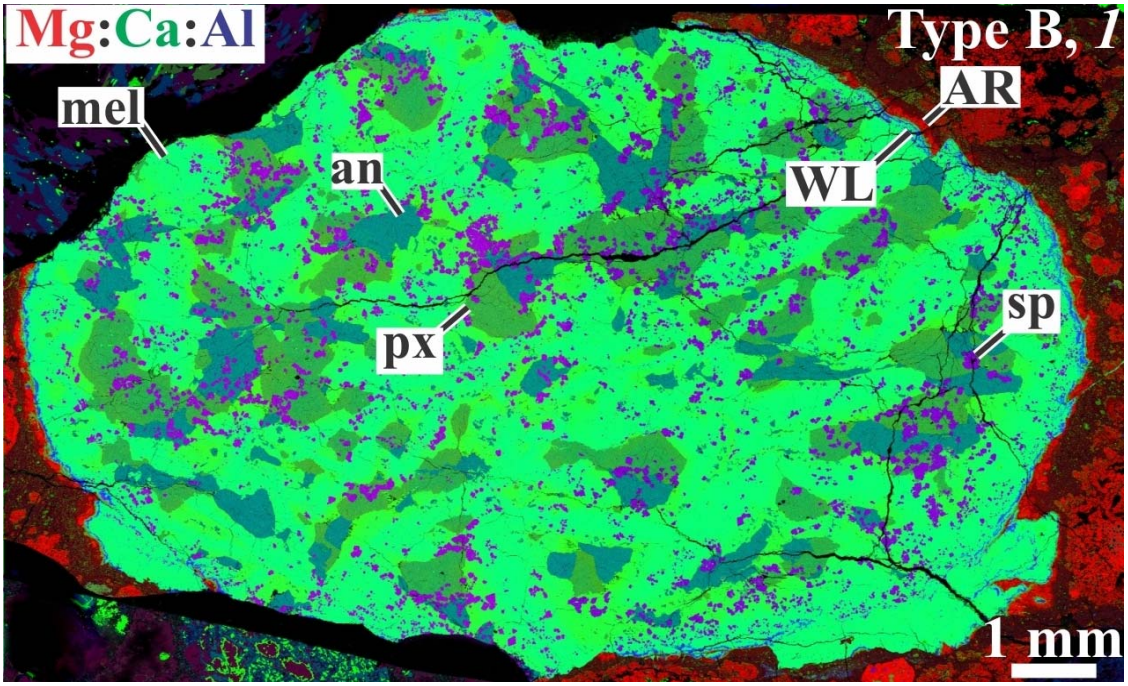

Figure 2.12: Combined elemental map in Mg (red): Ca (green): Al (blue) Kα of CAI *1* a Type B (B2) CAI composed of melilite (mel), pyroxene (px), anorthite (an) and spinel (sp). AR: Accretionary Rim.

CAI *5* is another ovoid object of about 0.7 cm in maximum dimension (Figure 2.16) and is composed of melilite (45 %), pyroxene (40 %), spinel (8 %), forsterite (2.5 %), anorthite + hibonite (4 %) and Fe,Ni-metal (<1 %). Distinct lithologies can be described in this inclusion. From the interior, 1) regions of very fine grained (<10 μm) melilite associated with very fine grains of pyroxene, spinel and Fe,Ni-metal, 2) regions of pyroxene ± melilite (60-80 %) poikilitically enclosing spinel (12-25 %) and forsterite (1-4 %) with variable but minor amounts of Fe-metal grains and 3) an outer < 2 mm mantle composed of coarse (100-500 μm) irregularly shaped melilite, pyroxene, and spinel. Overlying the entire inclusion is a ~50-100 μm thick WL rim. From the inside, the sequence is made up of melilite, a thicker layer of spinel associated with coarse grains of pyroxene and a thinner layer of pyroxene (Figure 2.17).

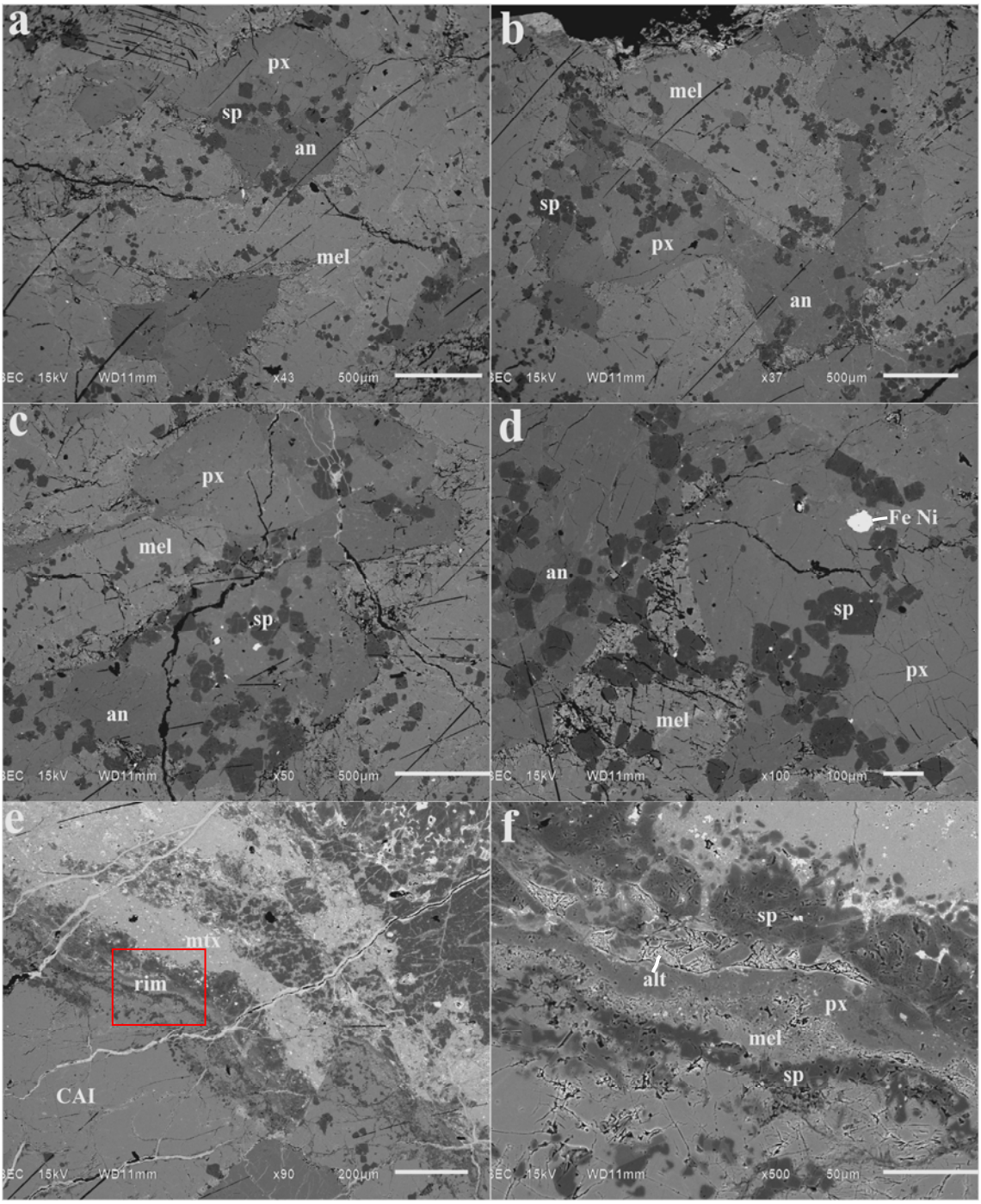

Figure 2.13: BSE images of mineral assemblages in the core (a-d) and rim (e, f) CAI *1*, showing texture and association of mineral phases. The area of the rim sequence magnified in (f) is shown as red inset in (e). px: pyroxene, mel: melilite, an: anorthite, sp: spinel, pv: perovskite, Fe-Ni: Fe-Ni metal, alt: altered material, mtx: matrix.

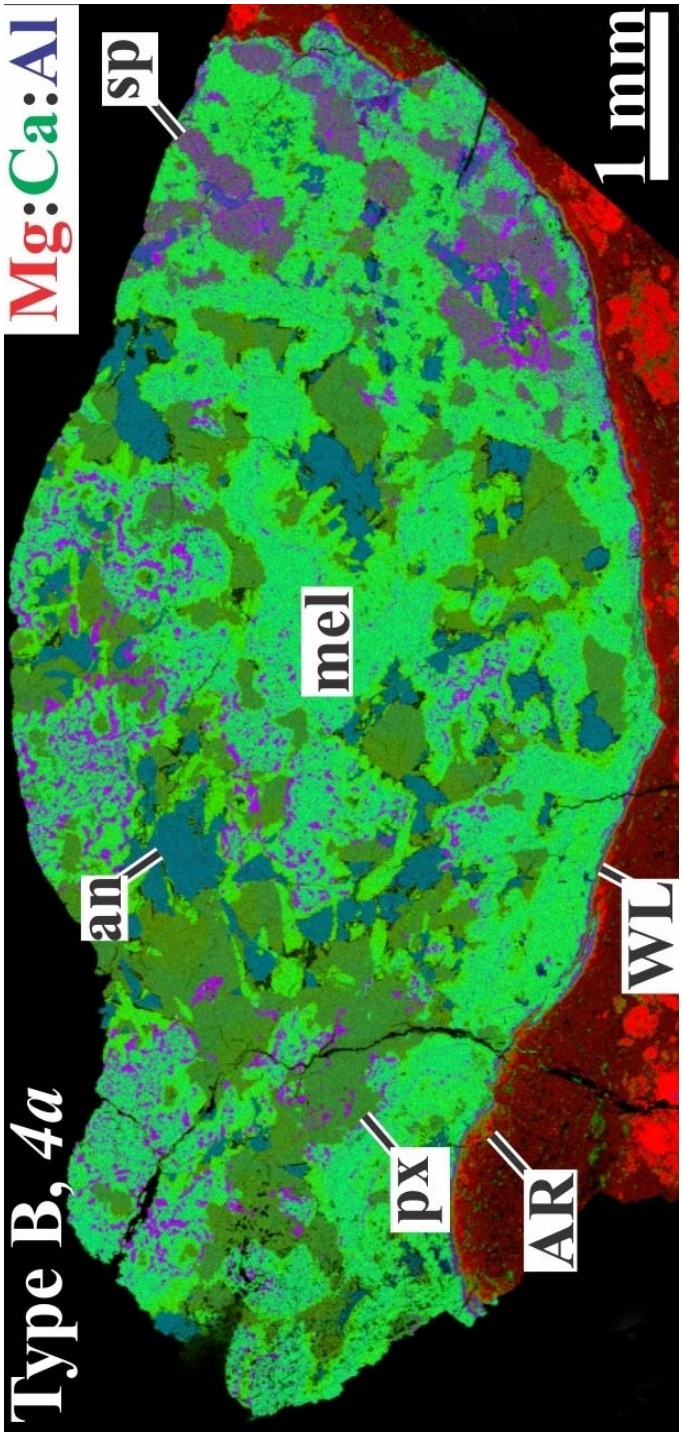

Figure 2.14: Combined elemental map in Mg (red): Ca (green): Al (blue) Kα of CAI *4a* a Type B (B2) CAI composed of melilite (mel), pyroxene (px), anorthite (an). AR: Accretionary Rim, WL: Wark-Lovering rim.

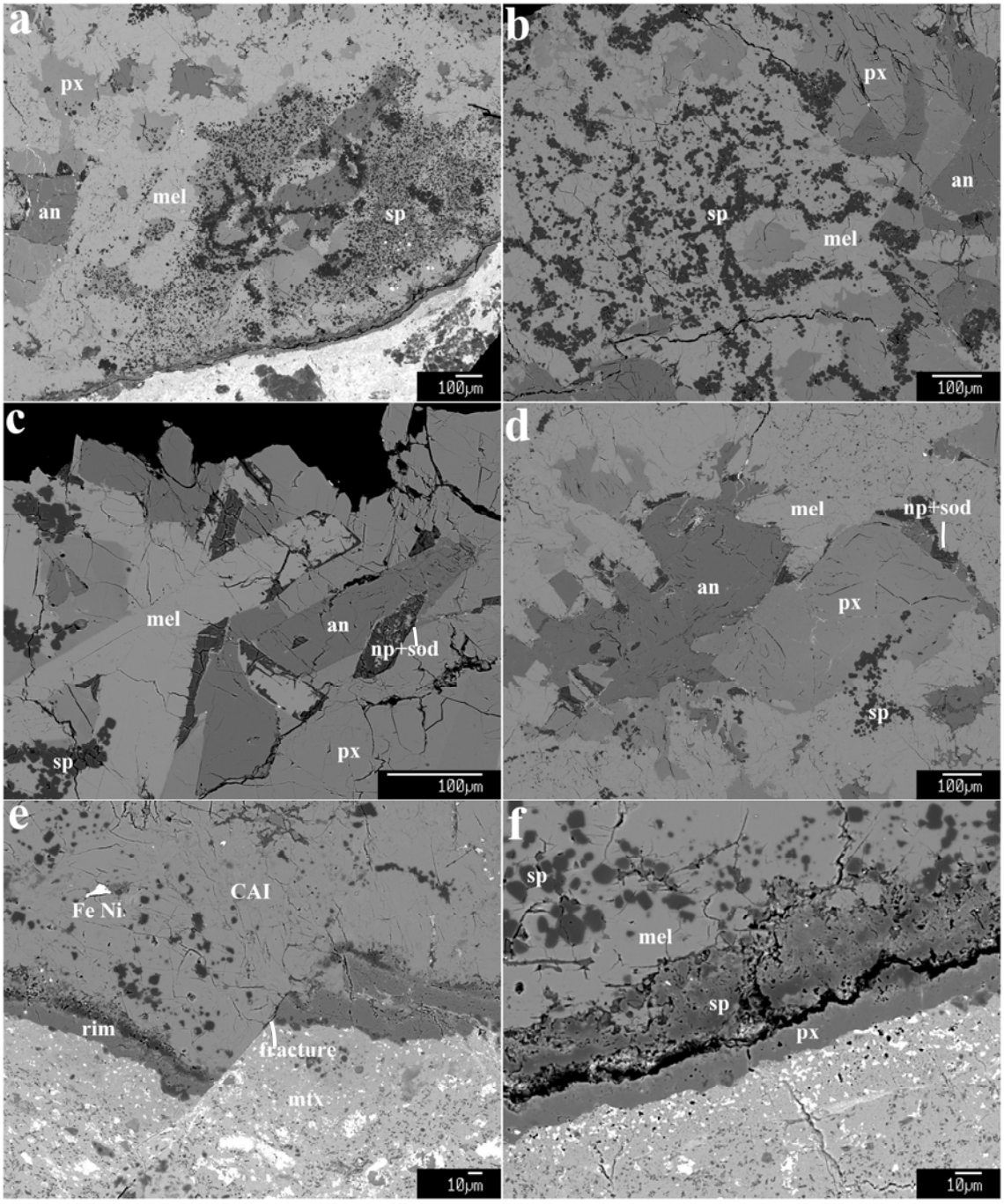

Figure 2.15: BSE images of mineral assemblages in the core (a-d) and rim (e, f) CAI *4a*, showing texture and association of mineral phases. px: pyroxene, mel: melilite, an: anorthite, sp: spinel, Fe-Ni: Fe-Ni metal, np: nephiline, sod: sodalite, mtx: matrix.

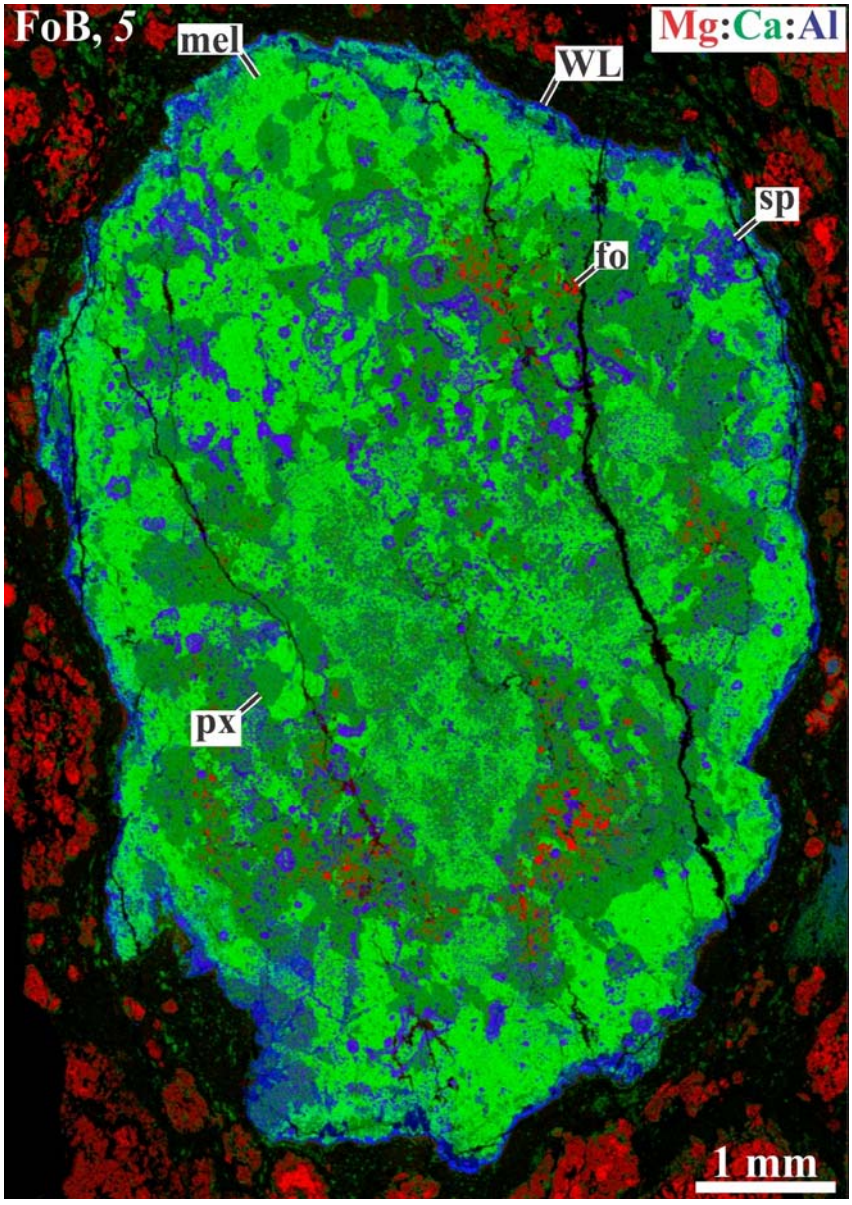

Figure 2.16: Combined elemental map in Mg (red): Ca (green): Al (blue) Kα of CAI 5 a Type B3 CAI also known as Fosterite bearing Type B (FoB) with fosterite (fo) as a main phase in addition to its Type B composition of melilite (mel), pyroxene (px), and spinel (sp).

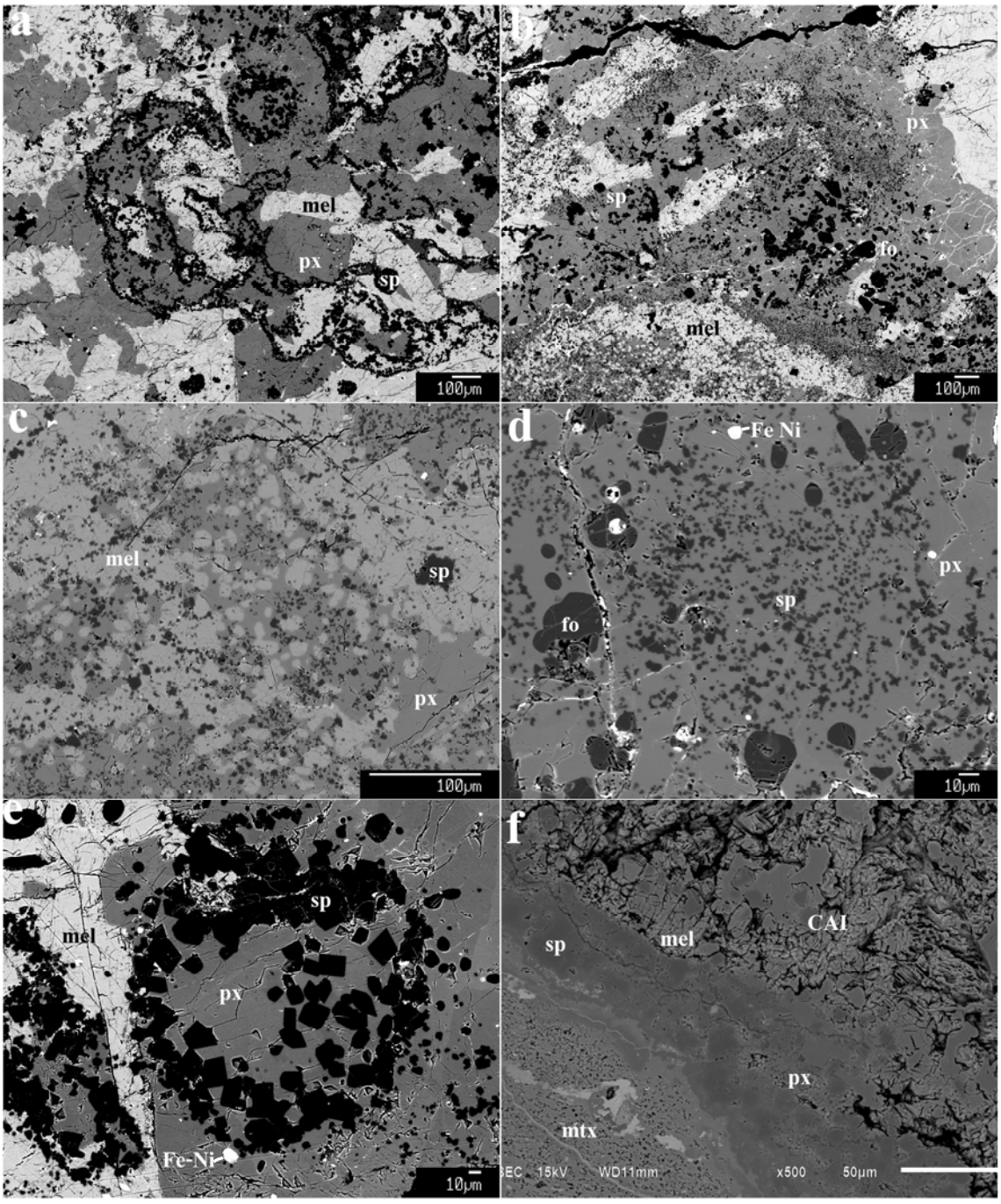

Figure 2.17: BSE images of mineral assemblages in the core (a-d) and rim (e, f) CAI 5, showing texture and association of mineral phases. px:pyroxene; mel:melilite; an:anorthite; sp:spinel; fo:forsterite; Fe-Ni: Fe-Ni metal; mtx:matrix.

2.5. CAI MINERAL CHEMISTRY

Major element compositions of mineral phases in the studied CAIs are summarised in Table 2.3 and plotted in Figures 2.18-2.22.

Pyroxene in all studied CAIs is an Al-Ti rich diopside ($En_{29-51,}$ $Fs_{0.02-8.8}$ and Wo_{32-71}) (Figure 2.19). There appears to be no significant compositional variations in the major element compositions within individual inclusions. The elemental concentrations in pyroxenes from CAI *6* are as follows; SiO_2 33-37 wt%, TiO_2 12-15 wt%, Al_2O_3 17-20 wt%, MgO 8-9 wt%, CaO ~24 wt%, and Cr_2O_3 0.03-0.07 wt%. FeO and MnO concentrations are between 0-0.04 wt% while Na_2O ranges between 0.002-0.02 wt%. The concentrations in CAI *7* range as follows; SiO_2 50-54 wt%, TiO_2 0.3-0.5 wt%, Al_2O_3 2-7 wt%, MgO 15-19 wt%, CaO 24-26 wt% and FeO 0.02-0.6 wt%. MnO and Cr_2O_3 concentrations are between 0.01-0.05 wt% while Na_2O and K_2O concentrations range between 0-0.01 wt%.

There are however compositional variations in average $TiO_{2,}$ $Al_2O_{3,}$ SiO_2 and MgO compositions. Pyroxenes in CAI *6* are more enriched in TiO_2 (14 wt%) and Al_2O_3 (18 wt%) compared to those in CAI *7* which has TiO_2 (0.4 wt%) and Al_2O_3 (5 wt%) respectively. CAI *7* pyroxenes are more enriched in SiO_2 (52 wt%) and MgO (17 wt%) compared to those in CAI *6* which has SiO_2 (35 wt%) and MgO (8 wt%).

The Type B CAIs *1* and *4a* and *5* show similar compositions in pyroxene for most of their major elements with no significant variations in compositions within each CAI. The variations in element content in pyroxene from CAIs *1* and *4a* are; SiO_2 36-40 wt%, TiO_2 6-10 wt%, Al_2O_3 19-22 wt%, MgO 8-10 wt%, CaO ~25 wt%, and Cr_2O_3 0.02-0.09 wt%. FeO and MnO concentrations are between 0-0.06 wt%. Na_2O and K_2O concentrations range between 0-0.02 wt%. The range of major element concentrations for pyroxene in FoB CAI *5* are; SiO_2 39-48 wt%, TiO_2 3-7 wt%, Al_2O_3 8-19 wt%, MgO 10-15 wt%, CaO 24-25 wt%, and Cr_2O_3 0.02-0.08 wt%. FeO is between 0.04-0.06 wt% while MnO, Na_2O and K_2O concentrations range between 0-0.05 wt%.

The average TiO_2 concentrations in pyroxenes for CAIs *1* and *4a* are 9 and 7 wt% respectively, and that in CAI *5* is slightly lower at 4 wt%. Average Al_2O_3 and MgO concentrations are ~21 and ~9 wt% respectively for CAIs *1* and *4a*, and 13 wt% for CAI *5*. The average FeO concentration is an order of magnitude higher in CAI *5* (0.20 wt%) compared to those in CAIs *1*

and *4a* (<0.05 wt%). There is a positive correlation between TiO_2 and Al_2O_3 abundances especially in the Type B CAIs (Figure 2.19 a,c).

Melilite in all the studied CAIs is gehlenitic in composition ($Åk_{2-30}$). Compositional variations within individual CAIs range from 2-4 and 6-24 mol% Åk for the type A CAIs *6* and *7* respectively, 4-16 and 11-20 mol% Å for the type B CAIs *1* and *4a* respectively and 24-30 mol% Åk for CAI *5* (Figure 2.20). Melilite in type A CAIs have slightly less magnesium ($Åk_{2-24}$) compared to those in the type B CAIs ($Åk_{4-30}$), with CAI *5* showing the most Åkermanitic compositions ($Åk_{24-30}$). Melilite composition histograms for all types of CAIs indicate a trend towards higher akermanite content in the type B CAIs (Figure 2.21). The studied CAIs are depleted in Na_2O (<0.5 wt%), and FeO (<0.1 wt%).

Table 2.3: Average major element composition of mineral constituents of NWA 4502 CAIs.

Name	Type	Mineral	SiO_2	TiO_2	Al_2O_3	Cr_20_3	FeO	MnO	MgO	CaO	Na_2O	K_2O	*n*
CAI *6*	**CTA**												
		Melilite	29.87	0.04	24.52	0.00	0.02	0.01	5.07	40.43	0.03	nd	13
		Pyroxene	35.21	13.86	18.14	0.05	0.01	0.01	8.31	24.40	0.01	nd	5
		Spinel	0.24	0.73	69.99	0.24	2.38	0.01	26.22	0.20	nd	nd	3
		Perovskite	0.13	58.43	0.71	0.02	0.14	0.02	0.13	40.40	0.01	nd	3
CAI *7*	**CTA**												
		Melilite	22.94	0.09	35.16	0.00	0.00	0.00	0.90	40.89	0.01	nd	4
		Pyroxene	52.33	0.37	4.91	0.03	0.22	0.01	17.24	24.89	nd	nd	3
		Spinel	0.07	0.20	70.49	0.14	2.35	0.02	26.39	0.33	0.01	nd	3
		Hibonite	0.09	4.83	84.15	0.05	0.09	0.01	2.33	8.44	0.01	nd	13
		Perovskite	0.33	56.85	1.85	0.01	0.04	0.00	0.07	40.85	nd	nd	2
CAI *1*	**B**												
		Melilite	27.58	0.04	27.99	0.00	0.05	0.01	3.74	40.58	0.02	nd	3
		Pyroxene	37.46	9.00	20.50	0.05	0.01	0.01	8.31	24.66	nd	nd	14
		Spinel	0.04	0.72	71.22	0.15	0.06	0.02	27.70	0.08	nd	nd	2
		Hibonite	0.44	1.89	87.89	0.03	0.26	0.03	1.24	8.20	nd	0.01	
		Anorthite	42.90	0.07	36.98	0.01	0.02	0.01	0.06	19.87	0.07	0.01	3
CAI *4a*	**B**												
		Melilite	29.54	0.02	24.22	0.01	0.10	0.00	5.11	40.84	0.15	nd	3
		Pyroxene	37.42	7.34	21.42	0.07	0.04	0.01	8.72	24.98	nd	nd	14
		Spinel	0.10	0.23	70.88	0.20	0.46	0.02	27.92	0.20	nd	nd	2
		Anorthite	42.91	0.08	36.66	0.01	0.03	0.01	0.17	20.02	0.10	nd	2
CAI *5*	**FoB**												
		Melilite	39.03	0.01	7.93	0.00	0.09	0.01	11.24	41.48	0.21	nd	18
		Pyroxene	44.40	4.08	13.22	0.05	0.20	0.01	13.07	24.95	0.01	nd	8
		Spinel	0.11	0.27	71.26	0.23	0.38	0.01	27.55	0.19	nd	nd	4
		Anorthite	43.13	0.04	36.66	0.01	0.09	0.00	0.12	19.84	0.12	nd	3
		Fosterite	42.36	0.04	0.11	0.02	0.22	0.00	55.89	1.37	nd	nd	2

nd - not detected

Spinel compositions in all the studied inclusions are near pure endmember $MgAl_2O_4$. Silica (SiO_2), TiO_2, Cr_2O_3, MnO, CaO, Na_2O and K_2O content in the CAIs is <1 %. The element concentrations in spinel from CAI *6* are; SiO_2 0-0.5 wt%, TiO_2 0.7-0.8 wt%, Al_2O_3 68-71 wt%, MgO 23-28 wt%, CaO 0-0.5 wt%, and Cr_2O_3 0.2-0.3 wt%, FeO 0.05-7 wt%. MnO 0-0.02 wt%, and Na_2O and K_2O concentrations are <0.1 wt%. Those in CAI *7* range as follows; SiO_2 0.004-0.2 wt%, TiO_2 0.01-0.6 wt%, Al_2O_3 70-71 wt%, MgO 25-27 wt%, CaO 0.2-0.6 wt%, Cr_2O_3 0.1-0.2 wt%, FeO 0.1-5 wt%, MnO 0.003-0.04 wt%, and Na_2O and K_2O concentrations are <0.02 wt%. The moderate enrichment in FeO in CAI *6* and *7* occur in single spinel grains found in their WL rim sequences.

The major element compositions in the Type B CAIs *1* and *4a* and *5* are comparable and consistent with those in the Type A CAIs. The element concentrations in spinel from CAIs *1* and *4a* range between: SiO_2 0.03-0.2 wt%, TiO_2 0.1-1.0 wt%, Al_2O_3 ~71 wt%, MgO ~28 wt%, CaO 0.1-0.3 wt%, and Cr_2O_3 ~0.2 wt%, FeO 0.1-0.7 wt%. MnO 0-0.04 wt%, and Na_2O and K_2O concentrations are <0.02 wt%. The concentrations in FoB CAI *5* are; SiO_2 ~0.01 wt%, TiO_2 0.2-0.4 wt%, Al_2O_3 ~71 wt%, MgO 27-28 wt%, CaO 0.1-0.3 wt%, Cr_2O_3 0.2-0.3 wt%, FeO 0.1-0.6 wt%, MnO 0-0.03, and Na_2O and K_2O concentrations s are < 0.03 wt%. The Cr_2O_3, TiO_2, FeO, and CaO contents are plotted in Figure 2.22.

Anorthite compositions in the Type B CAIs *1* and *4a* and *5* are nearly pure anorthite endmember $CaAl_2Si_2O_8$. There is no compositional variation within individual CAIs. All anorthite analysed have compositions around An_{99}. TiO_2, MgO, FeO, and Na_2O content in all studied CAIs is <0.1 wt% while Cr_2O_3 and MnO are <0.05wt% and K_2O is <0.01 wt%. SiO_2, Al_2O_3 and CaO concentrations are ~ 43, ~37 and ~20 wt% respectively.

Perovskite in the Type A CAIs *6* and *7* is essentially pure $CaTiO_3$. There are no substantial variations in element compositions within the individual inclusions. The concentrations of SiO_2, FeO, MgO, Cr_2O_3, MnO, Na_2O, and K_2O are < 0.5 wt% while Al_2O_3 is <2 wt%. The CaO and TiO_2 contents for CAI *6* are 40-41 wt% and 58-59 wt% respectively, and those for CAI *7* are ~41 wt% and ~57 wt% respectively.

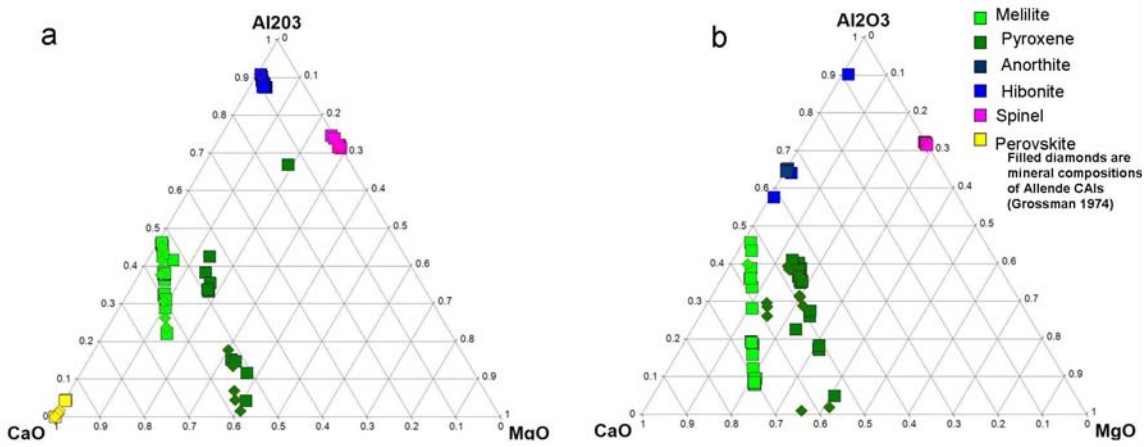

Figure 2.18: Ternary plots of a) Type A CAI and b) Type B CAI mineral compositions. Also plotted (filled diamonds) for comparison are compositions of the same minerals in Allende CAIs studied by Grossman 1974.

Hibonite grains analysed in the core of Type A CAI *7* and in the WL rim of Type B CAIs *1* show no significant variations in their major element compositions within the individual inclusions and between the two type inclusions. They contain SiO_2, FeO, and Cr_2O_3, <0.5 wt% and MnO, Na_2O, and K_2O <0.05 wt%. They however contain significant amounts of TiO_2 and MgO up to 8 and 4 wt% respectively indicating a coupled substitution of $Mg^{2+} + Ti^{4+}$ for $2Al^{3+}$.

Fosterite in the FoB CAI 5 is also nearly pure Mg_2SiO_4. Analysed grains contain ~56 and ~42 wt% MgO and SiO_2 respectively. TiO_2, and Cr_2O_3 content is <0.05 wt%, MnO, Na_2O, and K_2O are < 0.01 wt% while FeO content is <0.5 wt% and CaO is ~2 wt%.

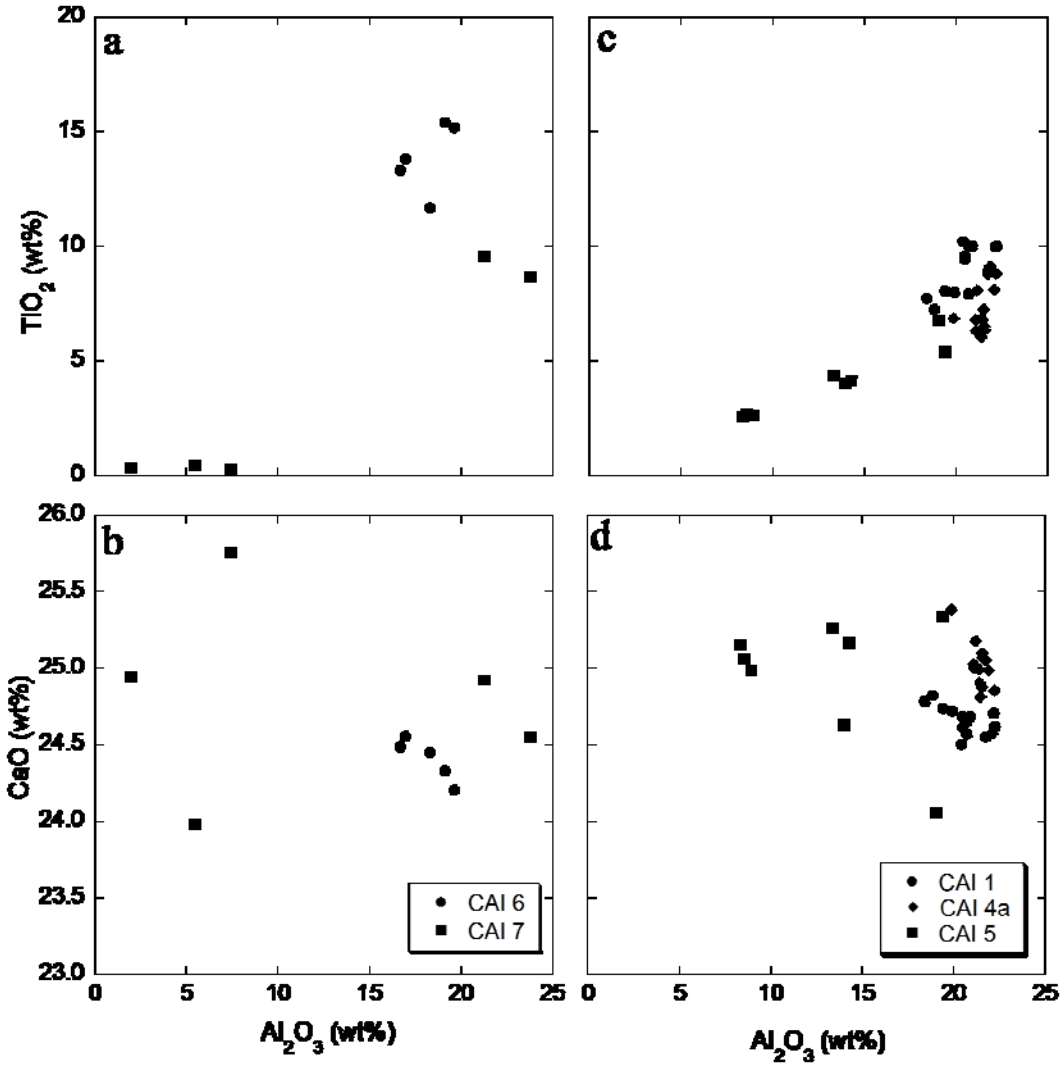

Figure 2.19: Pyroxene compositions represented by plots of TiO_2 and CaO vs Al_2O_3) for (a, b) Type A CAIs and (c, d) Type B CAIs. Pyroxene in Type A inclusions contain slightly higher TiO_2, CaO and Al_2O_3 concentrations.

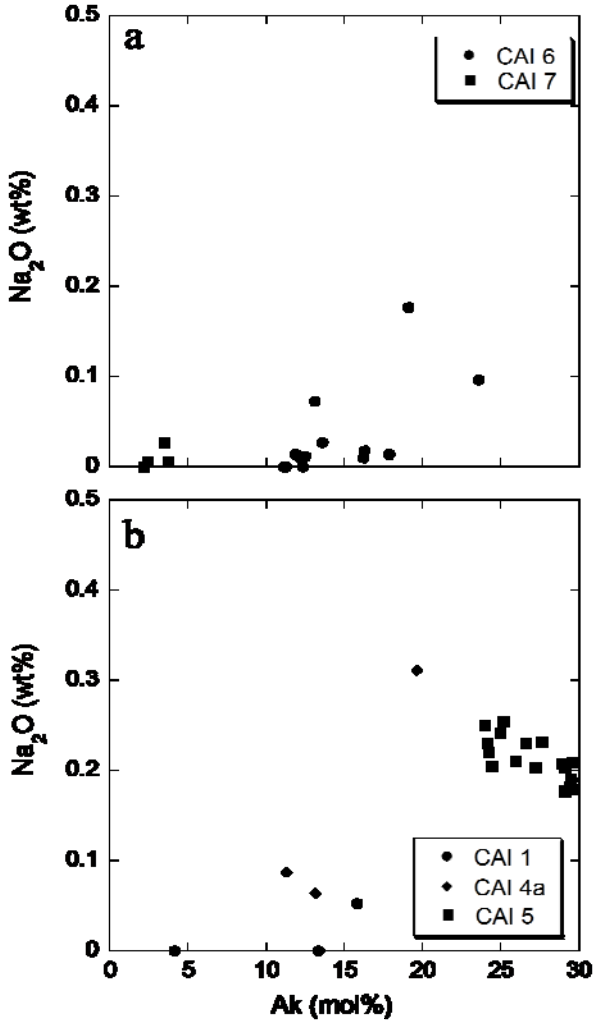

Figure 2.20: Melilite compositions represented by a plot of Na_2O vs Åk for (a) Type A and (b) Type B CAIs. Na_2O content in all CAIs is minor with the Type B inclusions having abundances up to 0.3 wt%.

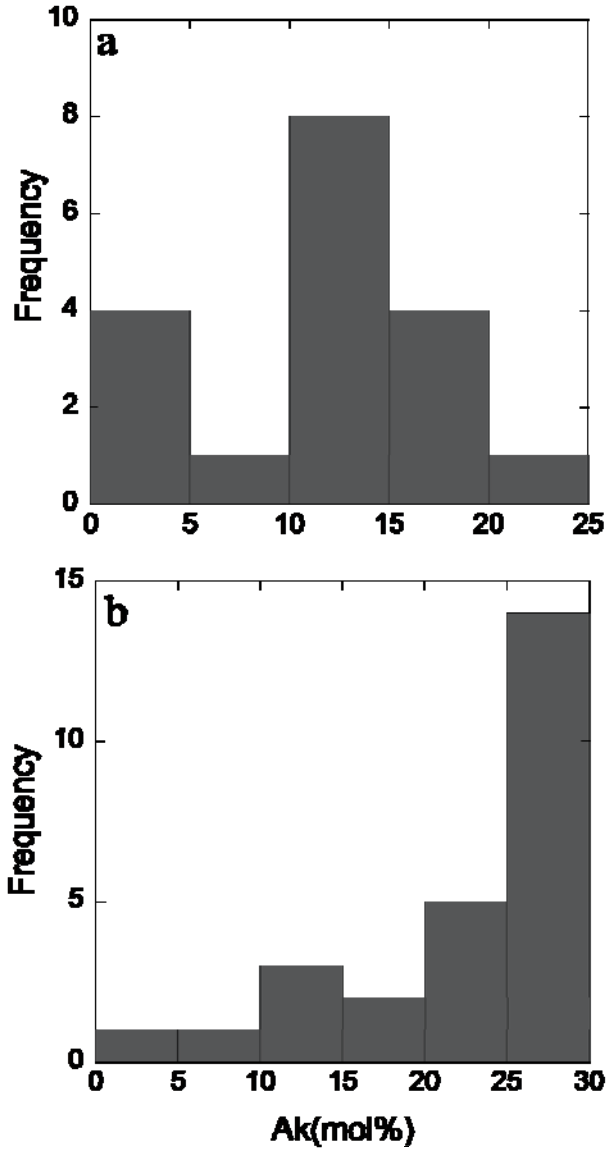

Figure 2.21: Melilite composition histograms for a) Type A and b) Type B inclusions. Type A melilite peaks in frequency between $Åk_{10}$ and $Åk_{15}$. The Type B melilite shows a distribution between $Åk_3$ and $Åk_{30}$, with the fosterite bearing type B peaking in frequency between $Åk_{20}$ and $Åk_{30}$. Type B inclusions have higher akermanite content, on the average, than that in Type A inclusion.

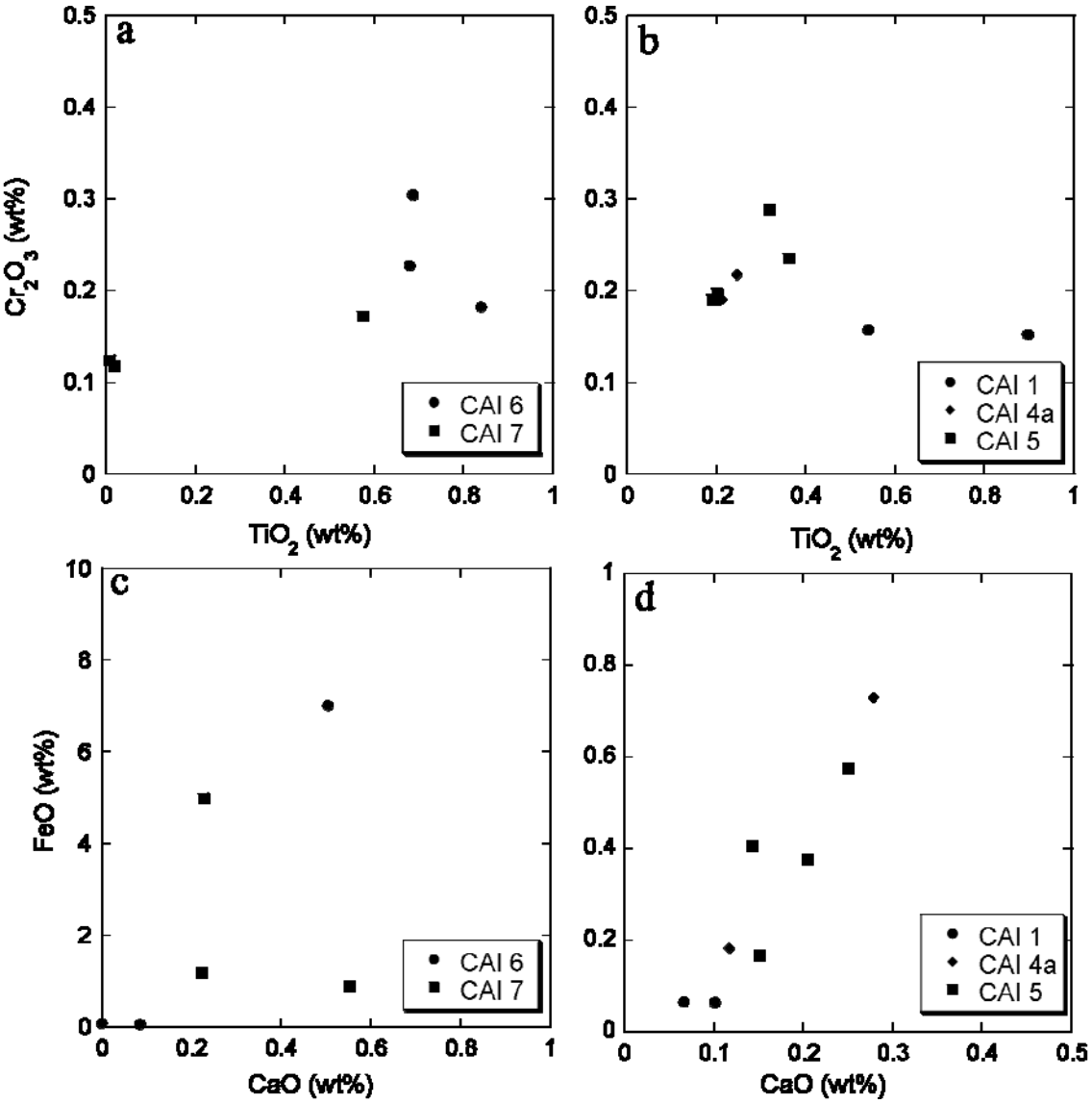

Figure 2.22: Cr_2O_3 vs TiO_2 and FeO vs CaO plots for spinel in (a, c) Type A and (b, d) Type B CAIs respectively. The spinels in these inclusions are close in composition to pure $MgAl_2O_4$, although FeO concentrations (c) in Type A CAIs sometimes exceed 1wt%. There is a positive correlation between FeO and CaO concentrations in Type B CAIs. Cr_2O_3 and TiO_2 contents of spinels in both type inclusions are comparable and <0.5 and 1 wt% respectively.

2.6. TRACE-ELEMENT ABUNDANCES

Trace-element abundances of constituent minerals (pyroxene, melilite spinel, anorthite and hibonite) from four NWA 4502 CAIs *1, 5, 6* and *7* were measured by LA-ICP-MS. Average enrichment values relative to CI chondrite were calculated using CI values from Anders and Grevesse (1989). Bulk element abundances were estimated using mean compositions and modal abundances of mineral phases. The data is summarised in Table 2.4 and plotted in Figure 2.23. Rare Earth Elements (REE) are plotted from left to right in order of decreasing ionic radius.

REE patterns in CAIs are the result of volatility-controlled fractionation processes. The volatility-controlled fractionations affecting the most refractory and most volatile elements are most useful in classifying REE patterns in groups (Mason and Taylor, 1982a; Ireland and Fegley, 2000). These groups are characterized by the relative abundances of the most volatile REE, Eu and Yb. While Eu and Yb anomalies represented as Eu/Eu* and Yb/Yb* respectively are expected to reflect volatility in bulk analysis, Eu/Eu* is subject to the possible fractionation of Eu^{2+} within Ca-bearing phases. As such, bulk REE patterns are identified for these studied CAIs based mainly on their Yb/Yb*. The anomalies are calculated as:

$$Eu/Eu^{*} = \frac{Eu_N}{\left(Sm_N \times Gd_N\right)^{0.5}} \quad \text{.....8}$$

$$Yb/Yb^{*} = \frac{Yb_N}{\left(Tm_N \times Lu_N\right)^{0.5}} \quad \text{.....9}$$

Eu* is an interpolated value between Sm and Gd and Yb* is interpolated between Tm and Lu and *N is* the chondrite-normalized value.

CAI *6* has REE abundances that are about an order of magnitude higher in pyroxene compared to melilite. The REE pattern in pyroxene shows a steady increasing enrichment from LREEs to HREEs. LREE abundances are ~15-25 x CI while HREE abundances are ~30-60 x CI, Eu/Eu* = 0.16 and Yb/Yb* = 0.78. The REE pattern for melilite has a slight steady decrease in REE abundances from LREEs to the HREEs. LREE abundances are ~8 x CI while HREE abundances are ~6 x CI. Eu and Yb are enriched relative to adjacent elements with Eu/Eu* = 1.97, and Yb/Yb* = 1.15. The bulk REE abundances for the Type A CAI *6* has a Group I pattern. REEs are unfractionated (~8-10 x CI) relative to each other with a positive Eu anomaly (Eu/Eu* = 1.24), and a small negative Yb anomaly (Yb/Yb* = 0.92).

CAI *7* has REE abundances in pyroxene 3-7 x CI (Eu/Eu* = 0.84; Yb/Yb* = 0.72), melilite 5-9 x CI (Eu/Eu* = 1.16; Yb/Yb* = 0.88) and hibonite ~3xCI (Eu/Eu* = 1.13; Yb/Yb* = 1.01). The bulk REE pattern is a more subdued Group I pattern. REEs are unfractionated (~5-8 x CI) relative to each other with a positive Eu anomaly (Eu/Eu* = 1.13), and a small negative Yb anomaly (Yb/Yb* = 0.85).

CAI *1* pyroxenes show progressive enrichment from the LREEs (10-20 x CI) to the HREEs (25-30 x CI). Europium and Yb are depleted relative to adjacent elements with Eu/Eu* = 0.13, and Yb/Yb* = 0.92. Melilite shows slight enrichment in LREE (10-15 x CI) relative to HREE (~10 x CI), with Eu/Eu* = 1.87, and Yb/Yb* = 1.10. Anorthite has a pattern similar to melilite, but with lower element abundances (0.1-1 x CI). The abundance of elements except for LREEs is below chondrite. Europium and Yb are enriched with a high Eu/Eu* = 30.7, and Yb/Yb* = 2.36. The REE abundances in spinel are below chondrite (~0.2-0.4 x CI) with Eu/Eu* = 0.70 and Yb/Yb* = 0.66.

Table 2.4: Trace element abundances (ppm) in studied CAIs.

CAI #	***6***	***6***	***6***	***7***	***7***	***7***	***7***	***1***	***1***	***1***	***1***	***1***	***4a***	***4a***	***4a***	***5***	***5***	***5***
Min.	**Px**	**Mel**	**B***	**Px**	**Mel**	**Hib**	**B***	**Px**	**Mel**	**An**	**Sp**	**B***	**Px**	**Mel**	**B***	**Px**	**Mel**	**B***
Elem/*n*	*5*	*24*		*8*	*23*	*8*		*9*	*17*	*3*	*2*		*11*	*18*		*10*	*11*	
La	14.6	8.31	7.85	3.89	6.76	2.71	5.76	8.10	15.4	1.34	0.349	10.6	10.7	12.5	9.29	6.14	10.9	7.53
Ce	16.3	7.92	7.79	3.33	7.02	3.03	5.89	10.8	14.2	1.02	0.292	10.5	14.2	11.1	9.64	7.03	9.90	7.44
Pr	20.3	7.74	8.11	3.83	7.90	2.91	6.61	13.8	13.5	0.928	0.151	10.7	16.0	9.69	9.43	7.69	8.31	6.97
Nd	23.0	7.51	8.28	4.00	8.44	2.97	7.04	17.0	12.4	0.737	0.228	10.6	18.5	8.83	9.71	8.61	7.57	7.01
Sm	25.6	7.10	8.28	4.30	8.65	3.23	7.25	22.4	11.1	0.495	0.174	11.0	21.9	7.05	9.83	9.94	6.26	6.95
Eu	4.21	13.0	10.0	3.56	9.71	3.31	7.94	2.92	18.5	13.1	0.139	13.1	6.29	21.9	14.5	5.07	27.2	14.5
Gd	28.1	6.09	7.84	4.19	8.11	2.65	6.81	24.4	8.89	0.367	0.228	10.1	21.9	5.45	9.03	10.4	5.39	6.72
Tb	30.6	5.71	7.87	4.25	7.52	2.72	6.37	24.5	8.45	0.309	0.202	9.85	21.6	4.64	8.56	10.1	4.74	6.32
Dy	35.9	6.19	8.85	4.87	7.83	2.80	6.69	27.5	8.98	0.218	0.199	10.8	24.5	4.70	9.41	11.2	5.23	6.99
Ho	37.8	5.83	8.81	4.79	6.96	2.58	6.02	26.0	8.61	0.253	0.167	10.2	22.9	3.79	8.53	10.3	4.71	6.37
Er	44.0	6.01	9.69	5.20	6.99	2.64	6.11	27.4	9.20	0.204	0.234	10.9	24.1	3.68	8.81	10.8	4.68	6.56
Tm	47.0	5.56	9.71	6.10	6.36	2.56	5.76	27.1	9.19	0.136	0.325	10.8	24.8	3.80	9.07	10.3	4.59	6.31
Yb	40.8	6.10	9.37	4.66	5.18	2.54	4.67	26.3	9.50	0.309	0.242	10.8	28.4	4.00	10.2	15.3	7.16	9.50
Lu	58.3	5.05	10.7	6.96	5.45	2.45	5.19	30.2	8.06	0.126	0.410	10.8	26.7	2.43	8.96	10.8	4.15	6.33
Eu/Eu*	0.16	1.97	1.24	0.84	1.16	1.13	1.13	0.13	1.87	30.7	0.70	1.24	0.29	3.54	1.54	0.50	4.67	2.12
Yb/Yb*	0.78	1.15	0.92	0.72	0.88	1.01	0.85	0.92	1.10	2.36	0.66	1.00	1.10	1.32	1.13	1.45	1.64	1.50
Hf	16.6	0.752	2.54	8.45	0.126	1.87	1.37	67.2	0.088	0.002	0.059	13.7	31.0	0.191	9.11	14.5	1.97	6.80
Lu	58.3	5.05	10.7	6.96	5.45	2.45	5.19	30.2	8.06	0.126	0.410	10.8	26.7	2.43	8.96	10.8	4.15	6.33
Zr	39.7	1.05	5.59	8.85	0.131	2.23	1.45	55.7	0.256	0.029	0.102	11.5	30.3	0.306	8.98	11.9	2.36	5.96
Y	34.5	5.38	8.12	4.55	6.50	2.32	5.63	23.8	8.25	0.204	0.204	9.6	20.8	3.43	7.72	9.30	4.28	5.79
Sc	15.6	1.22	2.82	10.4	1.07	4.06	2.46	89.5	0.177	0.188	0.071	18.3	41.1	0.399	12.2	18.7	2.16	8.67
Er	44.0	6.01	9.69	5.20	6.99	2.64	6.11	27.4	9.20	0.204	0.234	10.9	24.1	3.68	8.81	10.8	4.68	6.56
Ho	37.8	5.83	8.81	4.79	6.96	2.58	6.02	26.0	8.61	0.253	0.167	10.2	22.9	3.79	8.53	10.3	4.71	6.37
Dy	35.9	6.19	8.85	4.87	7.83	2.80	6.69	27.5	8.98	0.218	0.199	10.8	24.5	4.70	9.41	11.2	5.23	6.99
Tb	30.6	5.71	7.87	4.25	7.52	2.72	6.37	24.5	8.45	0.309	0.202	9.85	21.6	4.64	8.56	10.1	4.74	6.32
Gd	28.1	6.09	7.84	4.19	8.11	2.65	6.81	24.4	8.89	0.367	0.228	10.1	21.9	5.45	9.03	10.4	5.39	6.72
Tm	47.0	5.56	9.71	6.10	6.36	2.56	5.76	27.1	9.19	0.136	0.325	10.8	24.8	3.80	9.07	10.3	4.59	6.31
Th	49.1	3.44	8.42	3.41	1.27	2.22	1.60	14.0	7.99	0.655	1.70	7.63	13.2	6.77	7.28	7.23	3.88	4.75
U	15.5	2.34	3.57	8.37	0.732	3.00	1.92	33.5	5.99	5.67	1.53	11.2	14.9	10.6	10.4	5.94	3.38	4.04
Nd	23.0	7.51	8.28	4.00	8.44	2.97	7.04	17.0	12.4	0.737	0.228	10.6	18.5	8.83	9.71	8.61	7.57	7.01
Pr	20.3	7.74	8.11	3.83	7.90	2.91	6.61	13.8	13.5	0.928	0.151	10.7	16.0	9.69	9.43	7.69	8.31	6.97
Sm	25.6	7.10	8.28	4.30	8.65	3.23	7.25	22.4	11.1	0.495	0.174	11.0	21.9	7.05	9.83	9.94	6.26	6.95
La	14.6	8.31	7.85	3.89	6.76	2.71	5.76	8.10	15.4	1.34	0.349	10.6	10.7	12.5	9.29	6.14	10.9	7.53
Ce	16.3	7.92	7.79	3.33	7.02	3.03	5.89	10.8	14.2	1.02	0.292	10.5	14.2	11.1	9.64	7.03	9.90	7.44
Ba	3.55	11.8	9.90	33.9	6.49	10.2	10.2	6.79	28.3	27.7	2.42	21.8	20.0	49.6	34.2	2.10	12.7	7.49
Nb	30.4	1.84	5.08	5.84	0.224	4.45	1.28	7.38	2.24	0.054	2.32	2.97	23.3	5.35	9.47	9.13	6.70	6.92
Yb	40.8	6.10	9.37	4.66	5.18	2.54	4.67	26.3	9.50	0.309	0.242	10.8	28.4	4.00	10.2	15.3	7.16	9.50
Eu	4.21	13.0	10.0	3.56	9.71	3.31	7.94	2.92	18.53	13.1	0.139	13.1	6.29	21.9	14.5	5.07	27.2	14.5
Sr	7.58	15.3	17.3	9.54	12.0	7.78	10.9	4.59	19.78	18.5	4.62	15.3	6.36	27.5	18.4	4.52	25.6	16.7
V	15.0	1.09	60.9	3.42	0.232	9.21	1.34	33.8	0.232	0.054	7.23	7.58	13.2	0.324	4.46	6.32	1.91	37.6
Cd	0.039	0.005	0.01	0.087	0.018	0.028	0.028	0.021	0.006	0.042	0.012	0.015	0.030	0.050	0.041	0.014	0.032	0.022
In	0.014	0.015	0.01	1.10	0.012	0.009	0.165	0.014	0.008	0.004	0.026	0.010	0.015	0.058	0.034	0.023	0.170	0.087
Tl	0.025	0.011	0.01	0.423	0.000	0.064	0.062	0.021	0.010	0.051	nd	0.017	0.003	0.021	0.019	0.031	0.091	0.056
Bi	0.020	0.003	0.01	0.292	0.007	0.018	0.047	0.004	0.007	0.040	0.014	0.012	0.024	0.004	0.016	0.023	0.132	0.070
Pb	0.501	0.062	0.11	0.737	0.035	0.071	0.134	0.146	0.069	0.077	0.023	0.082	0.179	0.171	0.148	0.060	0.043	0.051

nd - not detected, An: Anorthite, Hib:Hibonite, Mel: Melilite, Px: Pyroxene and Sp: Spinel

B*: Bulk composition estimated from the mean mineral compostions and their modal abundances.

The bulk REE pattern is a Group V pattern. REEs are unfractionated (~10-11 x CI) relative to each other with a positive Eu anomaly (Eu/Eu* = 1.24), and no Yb anomaly (Yb/Yb* = 1.00).

CAI *4a* pyroxenes have a REE pattern with increasing abundances from LREE (11-22 x CI) to HREE (22-28 x CI). Europium is depleted (Eu/Eu* = 0.29) and Yb is enriched (Yb/Yb* = 1.10) relative to adjacent elements. Melilite shows enrichment in LREE (7-12 x CI) relative to HREE (2-5 x CI) and enrichment in both Eu and Yb (Eu/Eu* = 3.54; Yb/Yb* = 1.32). The bulk REE pattern is a Group VI pattern with unfractionated (~9-10xCI) abundances of elements relative to each other and enrichment in Eu and Yb (Eu/Eu* = 1.54; Yb/Yb* = 1.13) relative to adjacent elements.

CAI *5* pyroxene REE abundances are 5-10 x CI from LREEs to HREEs. This is superimposed with a depletion in Eu (Eu/Eu* = 0.50) and enrichment in Yb (Yb/Yb* = 1.45) relative to adjacent elements. Melilite has an REE pattern showing a decrease in REE abundances from the LREEs (6-10 x CI) to HREEs (~5 x CI). There is enrichment in Eu and Yb (Eu/Eu* = 4.67; Yb/Yb* = 1.64) relative to adjacent elements. The bulk REE pattern for CAI 5 is a Group VI with unfractionated (~6-8 x CI) abundances of elements relative to each other with enrichment in both Eu and Yb (Eu/Eu* = 2.12; Yb/Yb* = 1.50) relative to adjacent elements.

The REE abundances in pyroxenes of the studied inclusions are consistent with their trace element abundances where the depletion in the most volatile REEs Eu and Yb is complemented by the gradual depletion in the more volatile elements and less differentiation towards the more refractory elements. Melilite on the other hand shows enrichment in the most volatile REEs Eu and Yb consistent with increasing abundance of the more volatile elements and depletion in the more refractory elements.

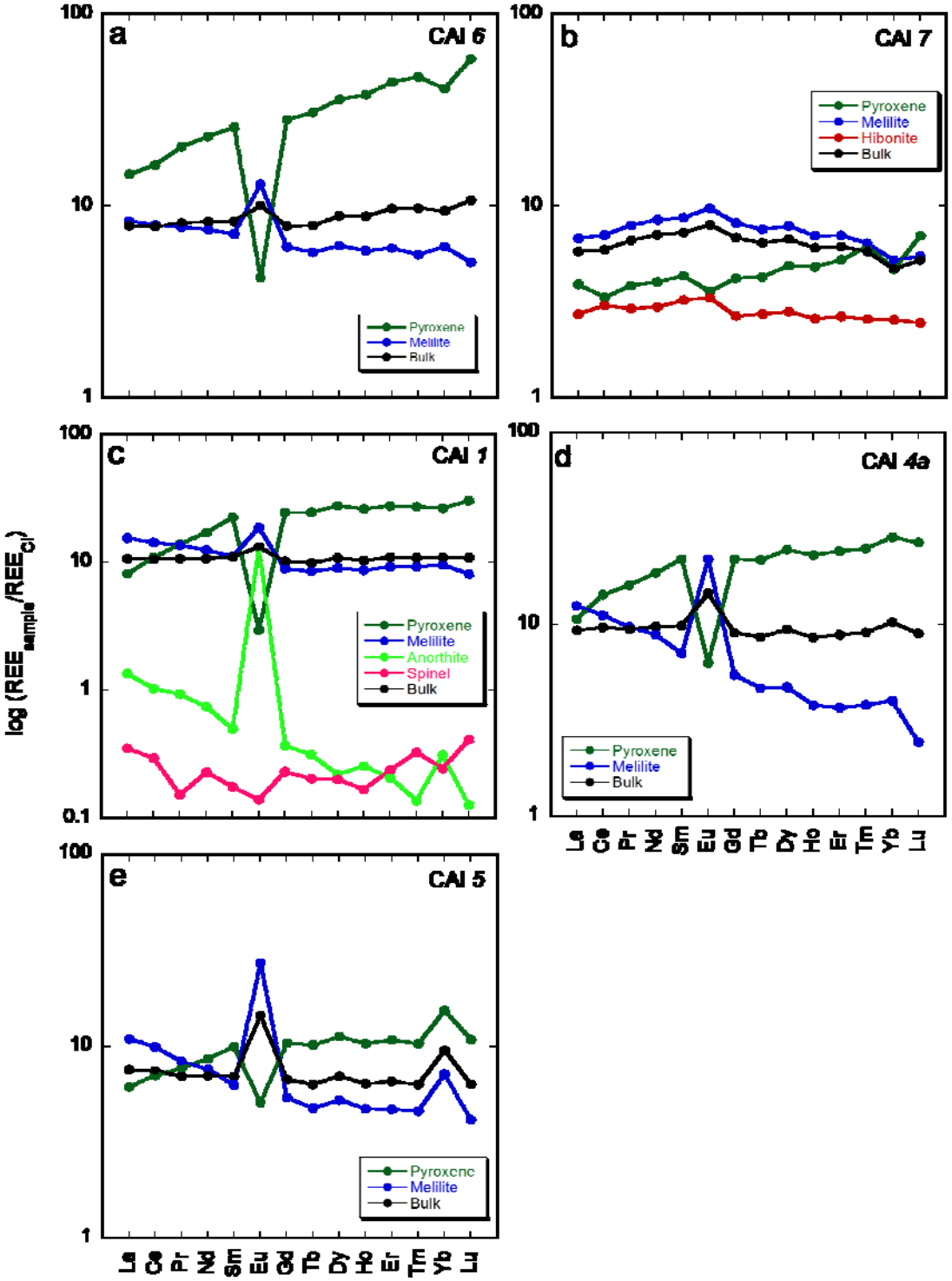

Figure 2.23: Rare Earth Element patterns of NWA 4502 CAIs.

2.7. SECONDARY ALTERATION

NWA 4502 is a meteorite found in a desert. As such it has been in contact with soil, and exposed to atmosphere and precipitation for an uncertain, and possibly long, period of time. During this time, it could have experienced chemical exchange with the terrestrial environment, which causes substitution of primary minerals with terrestrial weathering products. Terrestrial weathering effects on NWA 4502 are present but mineralogically minor. A Small amount of oxidation or rust is observed on surfaces of some hand specimens. More detailed inspection of thin sections shows low grade terrestrial weathering. Oxide rims around Fe, Ni metal and FeS grains as well as FeO rich veins are present but rare in the meteorite components. These features correspond to the weathering grade of this meteorite of W1.

Shock features such as strained grains, melt veins, brecciation and shock-mobilized materials, which are usually common in moderately shocked meteorites such as Efremovka, are absent. Mineral grains such as olivine and pyroxenes in matrix and chondrules mainly show sharp to undulatory extinctions. No planar fracturing was observed in mineral grains but some irregular fracturing is present in some crystals. The shock grade of this meteorite is S2.

The level of parent body alteration in this meteorite is also low compared to most other CV chondrites. The matrix of NWA 4502 contains fine-grained ferroan olivine, Fe-Ni sulphides, magnetite, Ni-rich metal, tiny nepheline crystals, and small irregularly-shaped regions of Ca, Fe-rich silicates (as shown in Figure 2.3). NWA 4502 CAIs show rare occurrences of secondary alteration products such as nepheline and sodalite. Occasional grains are present in WL rim sequences and along the grain boundaries of anorthite and sometimes in cavities or wedged between anorthite and pyroxene grains as shown in Figure 2.24. FeO-enrichment in spinel is moderate, 1-5 wt % in the Type A CAI *7* and up to 7 wt% in the peripheries of Type A CAI *6* and <0.5 wt% in the Type B CAIs *1 4a* and *5*. In contrast to Allende CAIs, secondary grossular, monticellite, anorthite, hedenbergite, andradite and Na-rich melilite are absent. Sodium maps showing the Na content of bulk NWA 4502 CAIs indicate low Na content of all CAIs even in their accretionary rims (Figure 2.25-2.29). The average Na_2O content in melilite is <0.05 wt% for all CAIs expect for CAI *4a* and *5* which have contents ~0.2 wt%. Na_2O content in anorthite does not exceed 0.1 wt%. Also, the forsterite composition of chondrule olivines and pyroxene phenocrysts ($Fa_{0.2\text{-}9}$ and $Fs_{0.9\text{-}1.4}$ $Wo_{0.9\text{-}1.2}$) indicates little evidence for Fe-Mg exchange with the surrounding matrix which contains mainly ferroan olivine ($Fa_{47\text{-}53}$) and salite-hedenbergite pyroxenes ($Fs_{12\text{-}19}$, $Wo_{47\text{-}49}$).

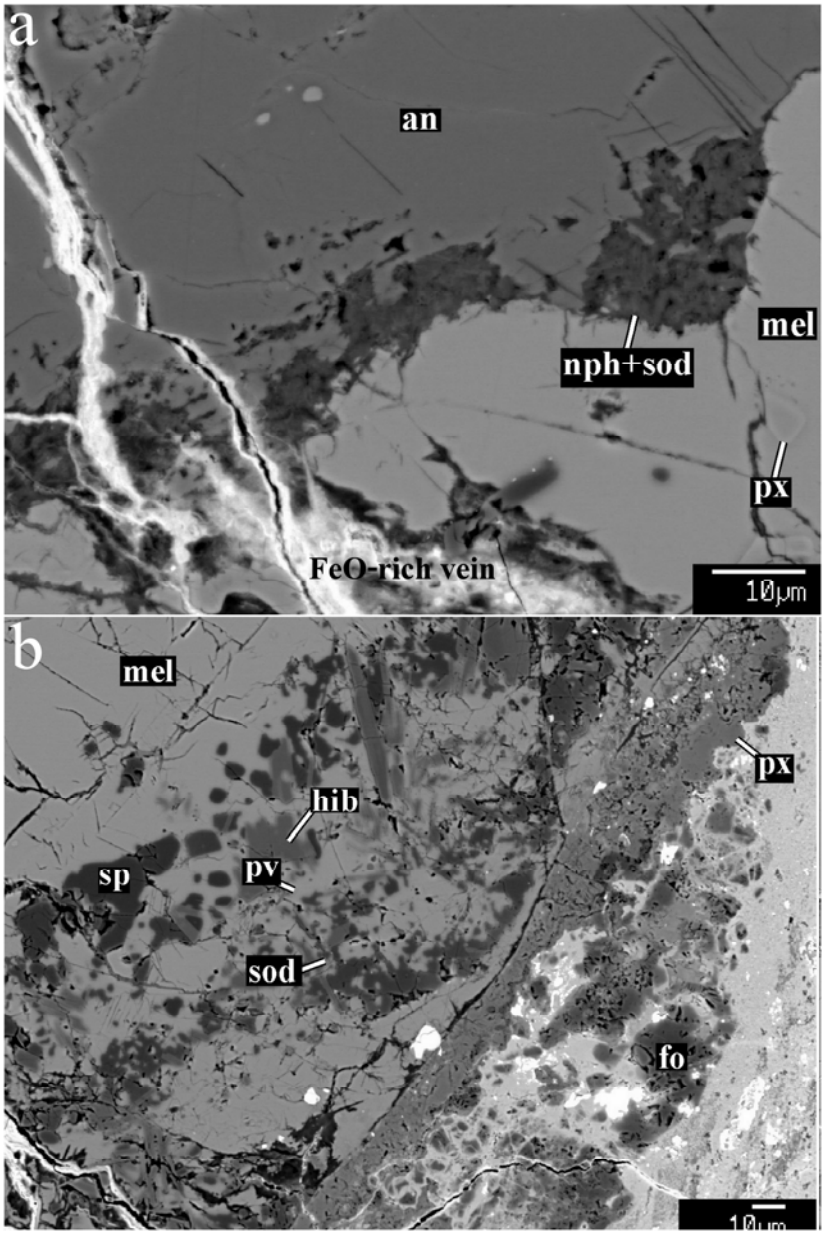

Figure 2.24: BSE images showing rare secondary alteration products in NWA 4502 CAI *1* (a) anorthite grain with a FeO-rich vein cutting across and nephiline and sodalite at grain boundary, (b) rim sequence with tiny sodalite grains. an: anorthite, fo: fosterite, hib: hibonite, mel: melilite, px: pyroxene, sod: sodalite; sp: spinel pv: perovskite.

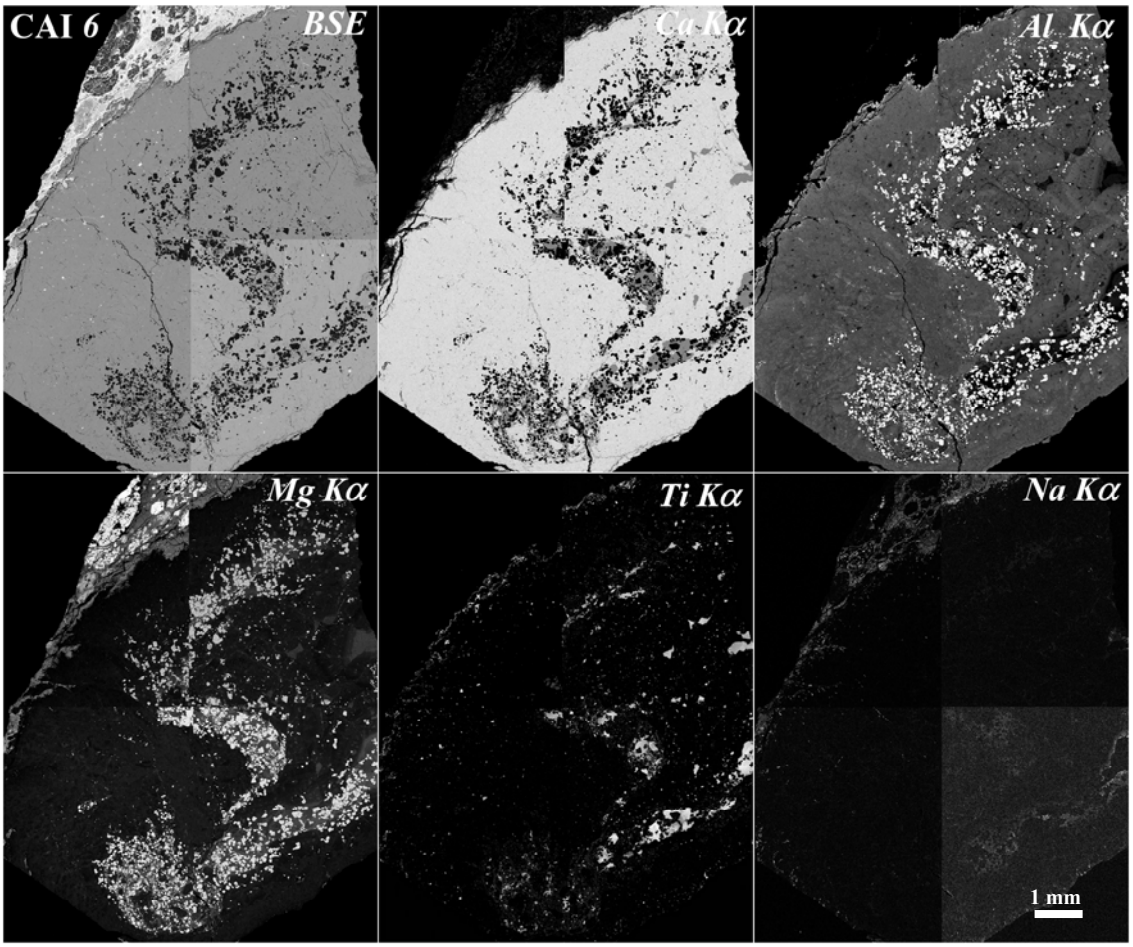

Figure 2.25: BSE image and X-ray maps of Ca, Al, Mg, Ti and Na (Kα) for CAI 6.

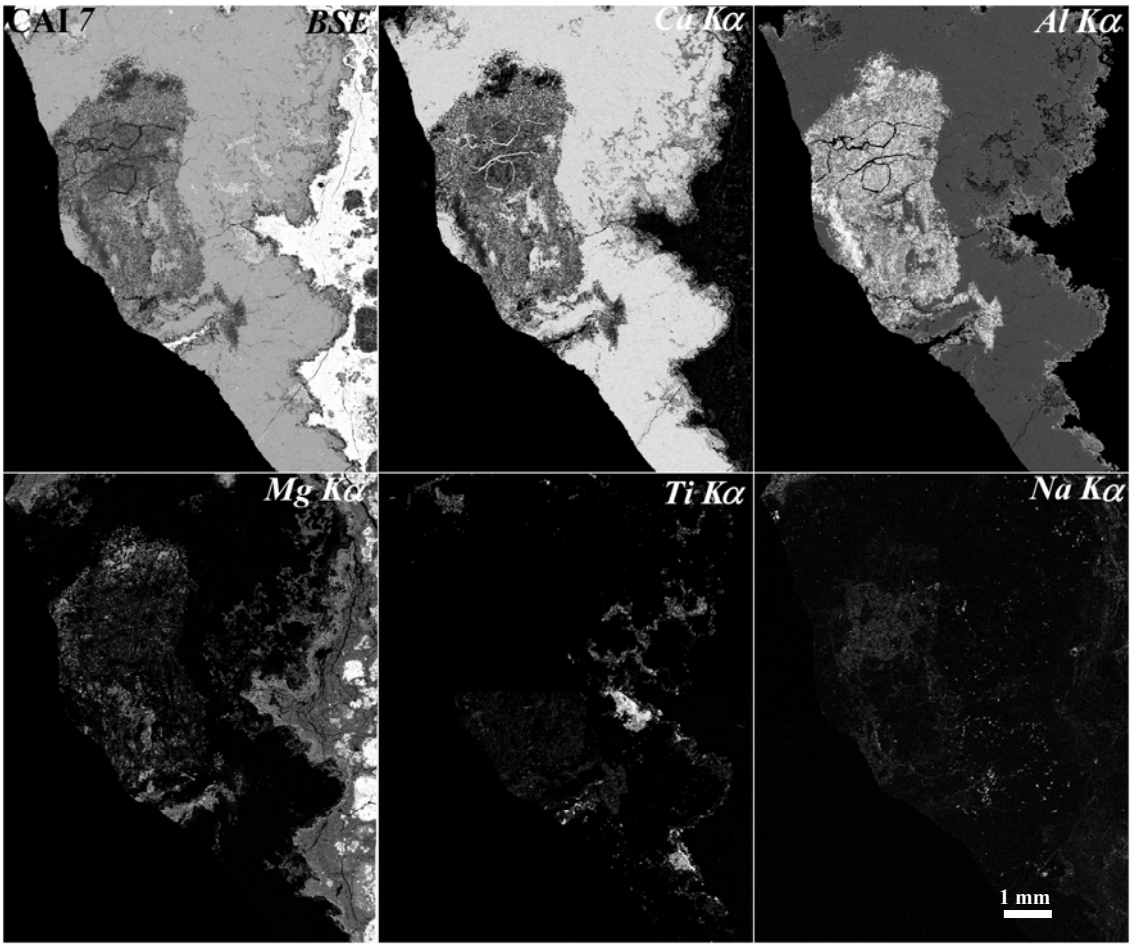

Figure 2.26: BSE image and X-ray maps of Ca, Al, Mg, Ti and Na (Kα) for CAI *7*.

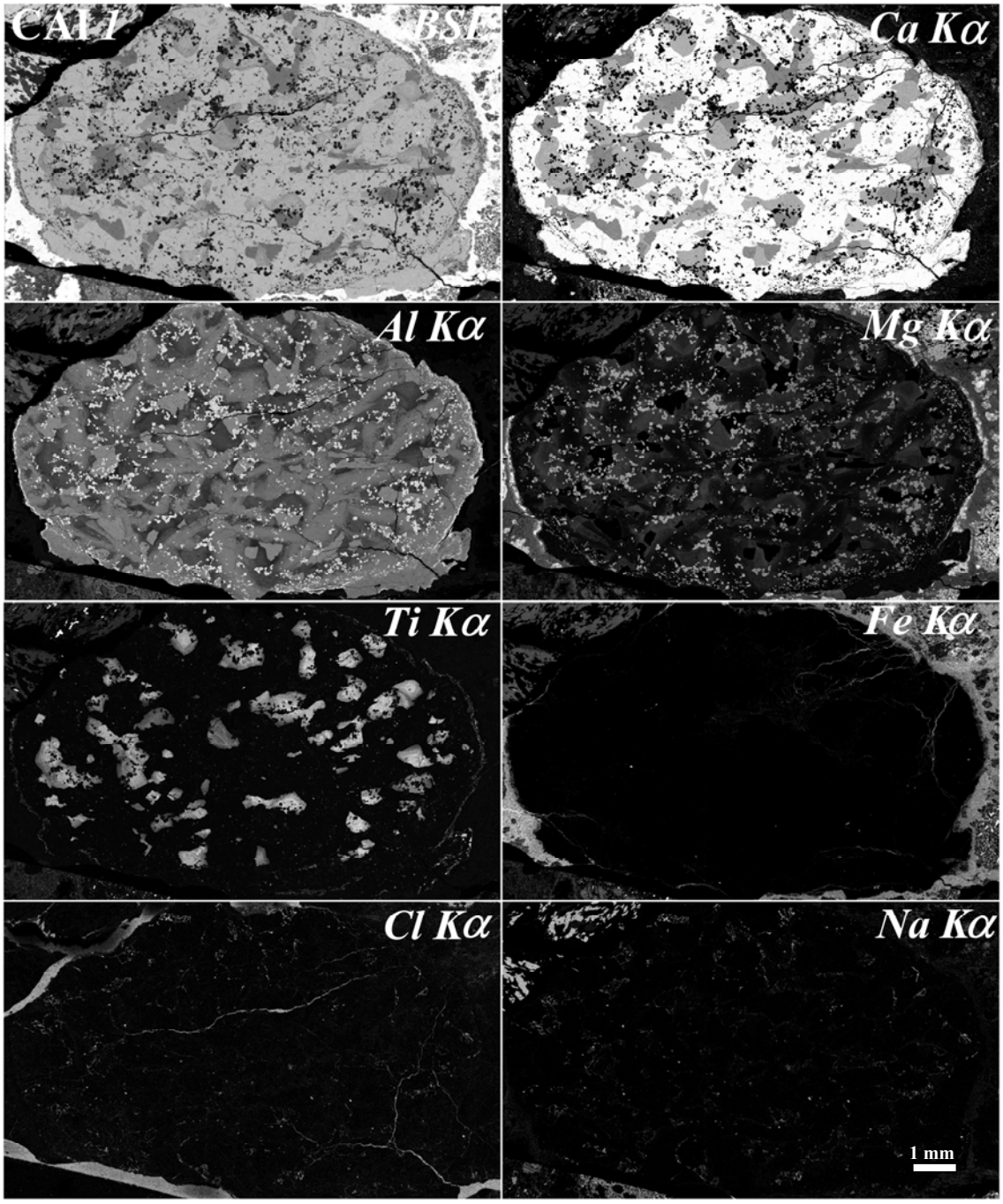

Figure 2.27: BSE image and X-ray maps of Ca, Al, Mg, Ti, Fe, Cl, and Na (Kα) for CAI *1*.

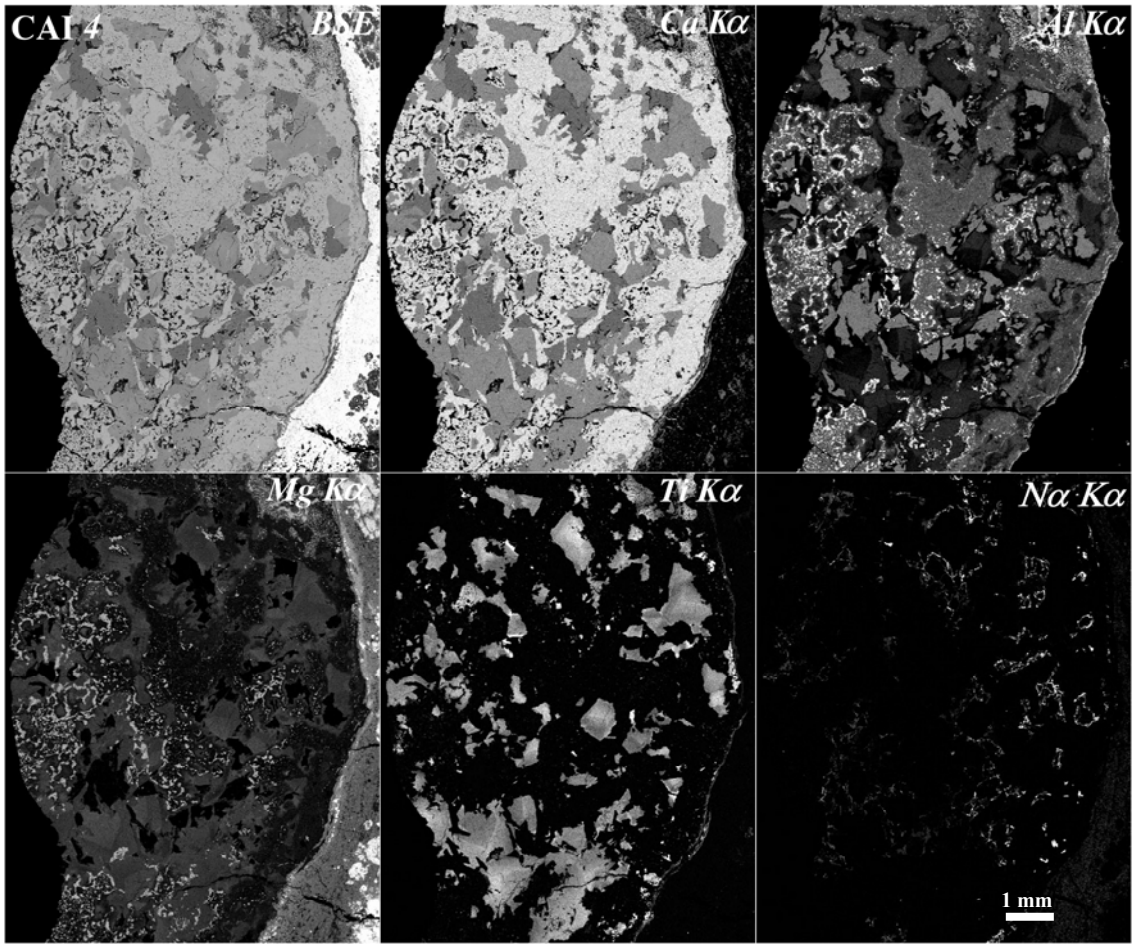

Figure 2.28: BSE image and X-ray maps of Ca, Al, Mg, Ti, and Na (Kα) for CAI *4a*.

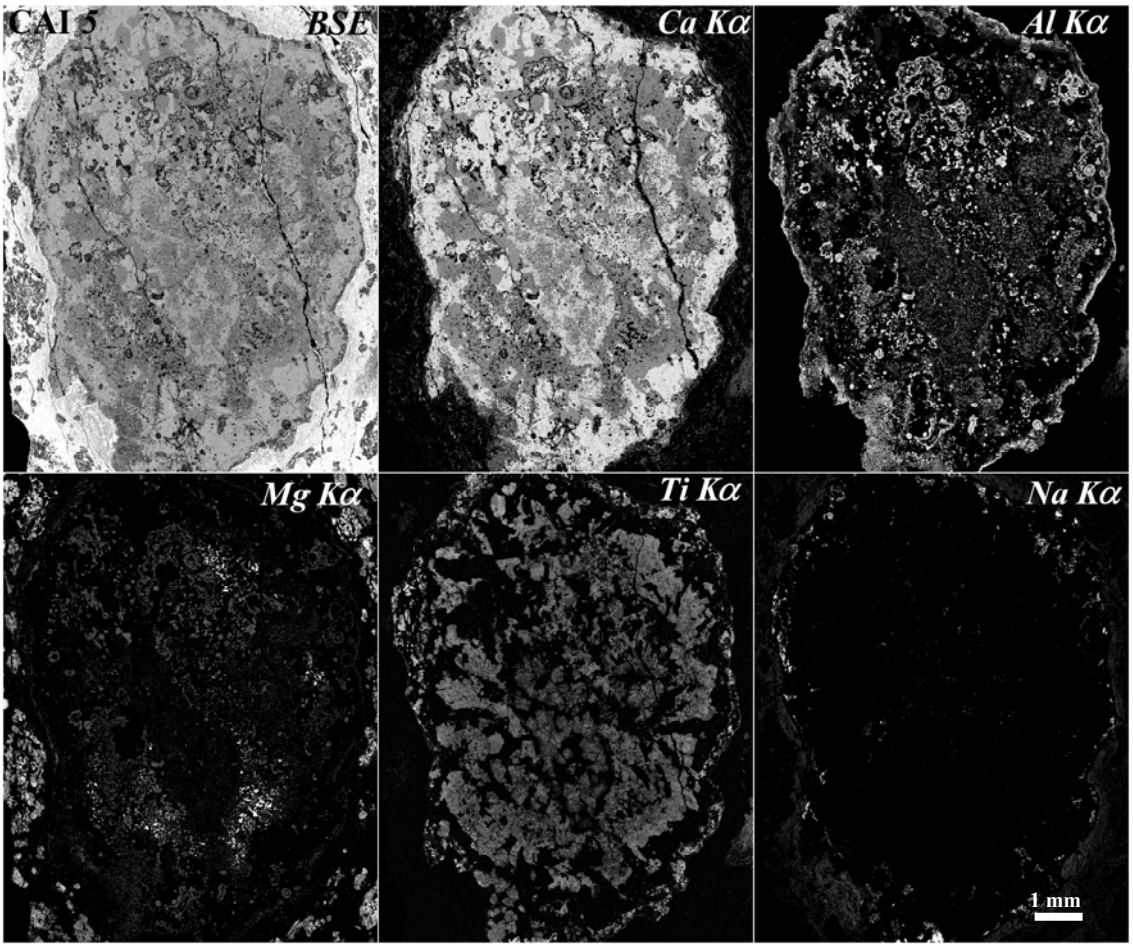

Figure 2.29: BSE image and X-ray maps of Ca, Al, Mg, Ti, and Na (Kα) for CAI 5.

2.8. DISCUSSION

NWA 4502 is an oxidized CV chondrite which shows many similarities to other CV chondrites. It is composed of well-defined chondrules and refractory inclusions. All the major types of refractory inclusions are present. These include coarse grained Type A (CTA), Type B and forsterite-bearing Type B (FoB). Evidence of igneous textures are present in the compact, regular shapes (ovoid to spheroidal) of the CAIs and the coarse, subhedral to euhedral shapes of mineral grains. These types of refractory inclusions are typical of CV chondrites and are comparable in mineral composition to those studied in Allende and other CV chondrites.

The CTA CAI 6 resembles typical CTA inclusions described in the literature (Grossman, 1975; Podosek et al., 1991; Simon et al., 1995; Simon et al., 1998; Simon et al., 1999). It is melilite (gehlenite)-rich, >60 vol% with Mg-Al spinel, minor Al-Ti pyroxene and traces of perovskite. Chondrite-normalized REE abundance patterns for melilite (flat at ~10 x CI with positive Eu and Yb anomalies) and pyroxene (slight HREE enrichment relative to LREE and negative Eu and Yb anomalies) are like those for their counterparts in Type B inclusions. CAIs *1* and *4a* are typical Type B2 (Wark and Lovering, 1982) inclusions which are structurally unzoned so that their major phases melilite, pyroxene, spinel and anorthite are not arranged in any obvious pattern as compared to Type B1 CAIs which are mineralogically concentrically zoned with a thick melilite mantle surrounding a core of pyroxene, anorthite and spinel.

Two of the studied CAIs (CTA CAI *7* and FoB CAI *5*) appear to be complex inclusions. CAI *7* has a unique texture and mineral composition. It has a distinct core composed mainly of spinel and hibonite, mantled by melilite which is the dominant phase. The unique spinel-hibonite core makes it different from other CTA CAIs. CTA CAIs in CV chondrites consist largely of melilite while hibonite appears mostly as a minor primary phase. In contrast to CAIs in CV chondrites, the mineralogy of CAIs in CM chondrites is dominated by the oxide minerals spinel, hibonite, and perovskite, while melilite and pyroxene are generally only minor constituents when present. These types of inclusions have been classified into three main groups based on their morphology and mineralogy: PLAty hibonite Crystal fragments (PLACs), Spinel-HIBonite-perovskite inclusions (SHIBs), and Blue hibonite AGgregates (BAGS) (Ireland et al., 1988a).

Hibonite is one of the most refractory minerals found in primitive meteorites and the widespread occurrence of hibonite in CM chondrites makes hibonite-bearing inclusions important because hibonite is only second in sequence, after corundum, of the minerals predicted to condense from a cooling gas of solar composition (Grossman, 1972; Grossman, 1980; Kornacki and Fegley, 1984; Geiger et al., 1988), as such, its origin is thought to be associated with high temperature processes. Hibonite-bearing inclusions like other CAIs are a source of information about the physical and chemical conditions that prevailed in the solar nebula. Some hibonite-bearing inclusions appear to contain condensate hibonite (MacPherson et al., 1984) while other inclusions probably crystallized from liquids (Beckett and Stolper, 1994). Hibonite can have a wide range of trace element abundances and large isotopic anomalies (Hinton et al., 1987; Hinton et al., 1988; Ireland et al., 1988a; Ireland, 1990; Ireland et al., 1991) which may reflect these different histories.

The core of CAI *7* is composed mainly of hibonite, spinel and melilite with minor Fe-Ni. It most closely resembles SHIBs (Ireland et al., 1988a; Ireland, 1990; Ireland et al., 1991) and spinel-hibonite inclusions (SH) from CM chondrites (MacPherson et al., 1983; MacPherson et al., 1984), and similar inclusions described in CH chondrite ALH85085 (Grossman et al., 1988; Kimura et al., 1993) and Allende (Allen et al., 1978) in texture and mineralogy.
Hibonites studied in hibonite-bearing inclusions (Allen et al., 1978; MacPherson et al., 1983; MacPherson et al., 1984; Ireland et al., 1988b; Ireland, 1990; Ireland et al., 1991; Kimura et al., 1993; Simon et al., 1997) display a range in their major element (MgO and TiO_2) contents. In this respect hibonite in CAI *7* resemble hibonites in spinel-hibonite inclusions from Murchison (MacPherson et al., 1983; MacPherson et al., 1984) and ALH85085 (Kimura et al., 1993) and in the CTA hibonite-bearing inclusion studied by Allen et al. (1978) with MgO and TiO_2 contents between 1-5 wt%. CAI *7* hibonites however differ from hibonites in SHIBs from Murchison (Ireland et al., 1988a; Ireland, 1990; Ireland et al., 1991; Simon et al., 1997) which have a wider range (0.07-10 wt%) in TiO_2 composition within individual inclusions.

In addition CAI *7* hibonite and spinel have very low (<0.1 wt%) FeO concentrations, indicating the low degree of alteration and oxidation of these CAIs compared to those in CV3 and CM2 chondrites. SHIBs in Murchison are usually dominated by depleted abundances of the ultrarefractory REEs, Gd to Er and Lu (Allende Group II pattern). Hibonite in CAI *7* on the other hand essentially shows unfractionated REE abundances, indicating they did not experience the complex condensation processes that result in the Allende Group II pattern.

Forsterite bearing Type B CAI are a relatively rare type of refractory inclusions and have so far only been identified in CV3 and CB carbonaceous chondrites (Grossman, 1975; Clayton and Mayeda, 1984; Krot et al., 2001; MacPherson et al., 2005). CAI *5* has textures and mineral composition comparable to those in the well studied Allende FoB inclusion SJ101 (Petaev and Jacobsen, 2009) and other CV FoBs (Bullock et al., 2012), with distinct forsterite-rich and forsterite-free lithologies. However, CAI *5* does not contain a mixture of secondary alteration products such andradite, hedenbergite, and diopside as observed in vesicles in the Allende FoBs ALVIN and TS35-F1.

Bullock et al. (2012) investigated melt evaporation and formation of fosterite-free mantles in FoBs and concluded that FoBs experienced an evolution from aggregated objects through to examples that have undergone extensive melting and evaporation (loss of MgO and SiO_2). This evolution is reflected in the texture (thickness of forsterite-free mantle), mineral chemistry

(melilite and pyroxene compositions) and oxygen isotope signature of each inclusion. It was demonstrated in this study that the least melted FoBs have textures inherited from their precursors and have undergone essentially no evaporative loss. Followed by more extensively melted inclusions that underwent moderate evaporation and developed thin but distinct forsterite-free mantles surrounding a core still containing abundant forsterite. Finally, some FoBs underwent extensive evaporation, which produced a thick forsterite-free mantle within which the aluminium-rich mineralogy (e.g., gehlenite-rich melilite) formed out of a melt that was incompatible with that from which the core minerals formed.

CAI *5* has a forsterite-free region up to ~1 mm in thickness surrounding a forsterite- rich core. Melilite is gehlenite-rich with a compositional range of $Åk_{7\text{-}30}$. Pyroxene is poor in TiO_2 compared to other Type B CAIs but comparable to other FoBs. However, there is an increase in Al_2O_3 and TiO_2 content suggesting Mg loss. Olivine in CAI *5* is forsteritic ($Fo_{93\text{-}100}$) with CaO abundances <2 wt% with most grains constantly containing CaO just over 1 wt%. Fosterite compositions are similar to those in other CV FoBs studied by Bullock et al. (2012). These characteristics of CAI *5* are comparable to those of other CV FoB inclusions that have undergone some melt evaporation.

NWA 4502 shows little evidence for secondary alteration processing. Mineralogy, chemistry and petrography of this chondrite indicate a low grade of terrestrial weathering as well as a smaller degree of hydrothermal alteration, thermal and shock metamorphism than those experienced by the well studied CV chondrite Allende. Even though some hand specimens appeared weathered, more detailed inspections of thin sections showed little or no evidence of extensive terrestrial contamination. There is little evidence for Fe-Mg exchange between chondrule olivine and pyroxene with the surrounding matrix.

Even though the compact texture of the matrix may be due to burial or some thermal processing on the parent body, it may possibly be as a result of weak shock metamorphism (S2) which is also evident in mineral optical characteristics and micro faulting at CAI rims and fracturing of chondrules.

Alteration in NWA 4502 CAIs resulted in the replacement of anorthite at CAI peripheries by minor nepheline and sodalite, moderate enrichment of spinel in FeO, and some micro fracturing. Melilite in the WL rims of CAIs show no evidence of replacement by either anorthite or secondary Na-rich minerals and are generally depleted in Na_2O and FeO as compared to those described in Allende CAIs by Grossman (1975). Enrichment in Na_2O and FeO content in

melilite grains in Allende CAIs have been interpreted as a result of close association with fine grained alteration materials which are absent in NWA 4502 CAIs. In addition, there is no evidence of common secondary alteration products such as grossular, monticellite, wollastonite, carbonates, phyllosilicates, magnetite, anorthite, forsterite, hedenbergite, andradite and ferroan olivine which are common secondary alteration products in Allende CAIs. The location and timing of secondary alteration in CAIs have been constrained using their mineral compositions and textures. Some studies favour a nebula or pre-accretionary alteration for CV CAIs based on the need for a high-temperature alteration event for the breakdown of melilite and anorthite to grossular and monticellite in Type B Allende CAIs (Hutcheon and Newton, 1981) and the occurrence of alkali-rich halos in the meteorite matrix surrounding some CAIs (Wark, 1981). Also, enrichment in Na of accretionary rims in Allende CAIs suggests CAIs became alkali-rich before accretion in the parent body. Well formed secondary minerals such as wollastonite, nepheline and grossular in CAI cavities are also indicative of condensation from a vapour, probably in the nebula. On the other hand, parent body alteration of CV CAIs (McSween Jr, 1977; Krot et al., 1995) and CM CAIs (Greenwood et al., 1994a) involves alkaline-rich fluids and is suggested to have affected the more oxidised CV meteorites, such as Allende, more than other CVs (McSween Jr, 1977). The more pristine nature of NWA 4502 CAIs evident in the absence of grossular and monticellite from the breakdown of melilite, alkali-rich halos surrounding CAIs and minor Na enrichment in accretionary rims of CAIs suggests secondary processing in a parent body environment possibly at a different fluid poor part of the CV chondrite parent body or even possibly, a different parent body.

Variations in the refractory trace element composition of CAIs provides a means of better understanding the physical and chemical conditions and processes in the earliest stages of solar system formation. Condensation, evaporation and partial melting are some of the processes CAIs are known to have undergone in their complex histories. The REE abundances in NWA 4502 CAIs are similar to those in other CAIs from other CV chondrites. NWA 4502 CAIs have the main fractionation REE patterns except the Group II REE pattern. The unfractionated Group I, III V and VI REE patterns are commonly found in CAIs from other CV chondrites such as Allende, Efremovka, Leoville, Vigarano and Axtell (Grossman, 1973; Mason and Taylor, 1982b; Mao et al., 1990; Sylvester et al., 1993; Simon et al., 1998; Srinivasan et al., 2000) and also in other carbonaceous chondrites (e.g., Fahey et al., 1987; Hinton et al., 1988; Ireland et al., 1988a; Ireland, 1990; Russell et al., 1998). The unfractionated characteristics of these patterns suggest they were produced due to complete condensation from a gas of solar composition. Of particular interest is the absence of the Group II REE pattern in these NWA 4502 CAIs. Group

II patterns are common among the fine-grained spinel-rich CAIs in the CV3 chondrites, and hibonite grains and inclusions in CM chondrites (e.g., Fahey et al., 1987; Ireland, 1990). The Group II pattern unlike Groups I, III, V, and VI, is highly fractionated indicating a more complex condensation history. This pattern is depleted in both the most refractory and most volatile elements except Eu and Yb, due to fractional condensation in which ultrarefractory REEs are first removed followed by condensation of the remaining REEs except the most volatile elements Eu and Yb.

Comparing NWA 4502 to the well studied Allende and Efremovka, apart from the similarities in availability as well as abundant and large CAIs, the main advantage of NWA 4502 over Allende and Efremovka is that it escaped the level of secondary processing experienced by these chondrites in their respective parent bodes. This detailed petrographic and mineralogical examination shows that at the mineralogical scale, this meteorite is less affected by parent body secondary alteration and terrestrial weathering.

CHAPTER 3

OXYGEN, Al-Mg, Rb-Sr AND URANIUM ISOTOPIC DATA

In order to extend the database of fully characterised CAIs from different CV chondrites and to better understand the isotopic systems in CAIs, oxygen, Al-Mg, Rb-Sr and uranium isotope systems were studied for CAIs from NWA 4502. The outcomes are reported in this chapter.

3.1 OXYGEN ISOTOPIC ANALYSIS

3.1.1 Introduction

On a three-isotope diagram, oxygen isotopic compositions of primitive meteorites (chondrites), chondritic components (chondrules, CAIs, matrix) and differentiated meteorites (derived from asteroids and Mars), deviate from the line along which nearly all terrestrial samples plot (Clayton et al., 1973). They demonstrated that the oxygen of anhydrous, high-temperature minerals in carbonaceous meteorites is strongly enriched in ^{16}O (Figure 3.1). Clayton and Mayeda (1977) showed in more detail that Allende CAIs and their constituent minerals disperse along the same mixing line defined by analysis of multiple whole CAIs (Figure 3.2). This was also shown to be true for CAIs from other CV chondrites such as Leoville and Vigarano (Clayton et al., 1986; Clayton et al., 1987). In general, spinel was found to be the most ^{16}O-rich phase while pyroxene, anorthite, and melilite have progressively lower enrichments in that order (Clayton et al., 1973; Clayton, 1993a; Yurimoto et al., 1998; McKeegan and Leshin, 2001; Aléon et al., 2002). This distribution suggests mixing between a ^{16}O-rich composition and a composition with more normal oxygen isotope values similar to planetary (terrestrial-like composition similar to bulk chondrites with $\Delta^{17}O \approx 0$) in composition.

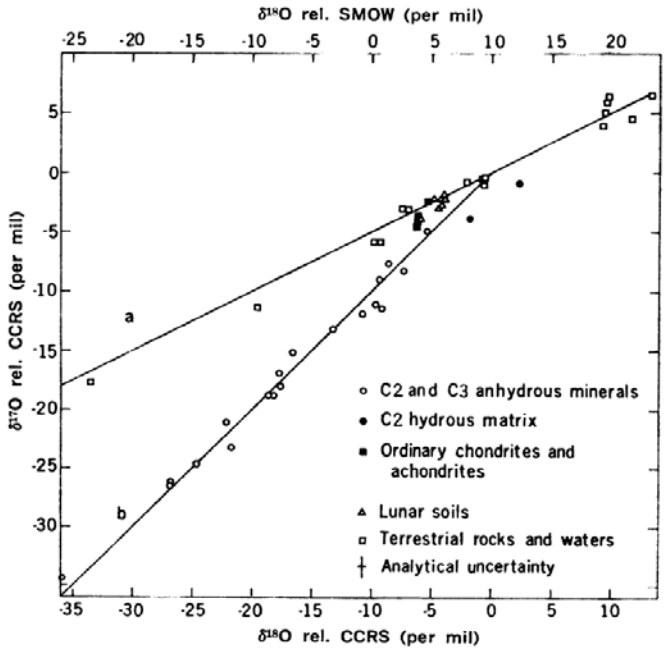

Figure 3.1: A plot from Clayton et al., 1973 showing the relationship between $^{17}O/^{16}O$ and $^{18}O/^{16}O$ variations for terrestrial, lunar, and meteoritic samples.

Various processes have been suggested to explain the distribution of oxygen isotopes in CV chondrite CAIs. They include 1) solid-gas exchange between an ^{16}O-rich solid and ^{16}O-poor gas (Clayton, 1993b), 2) Isotopic exchange between ^{16}O-rich solid and ^{16}O-poor gas during melting events (Yurimoto et al., 1998; Krot et al., 2006b) and, 3) late isotopic exchange during thermal metamorphism with a ^{16}O-poor fluid (Wasson et al., 2001).

Oxygen isotope compositions for CAIs from other carbonaceous chondrites are similar to those of CAIs from CV chondrites. Spinel and hibonite from CM are commonly ^{16}O-rich consistent with CV spinels and pyroxenes (Clayton et al., 1984; Fahey et al., 1987; Clayton and Mayeda, 1999). CO CAIs also have oxygen isotope compositions similar to CV CAIs with some less metamorphosed CO chondrites exhibiting ^{16}O-rich compositions in melilite and anorthite (Clayton and Mayeda, 1999; Wasson et al., 2001). Most CR chondrite CAIs also have ^{16}O-rich compositions (Aléon et al., 2002).

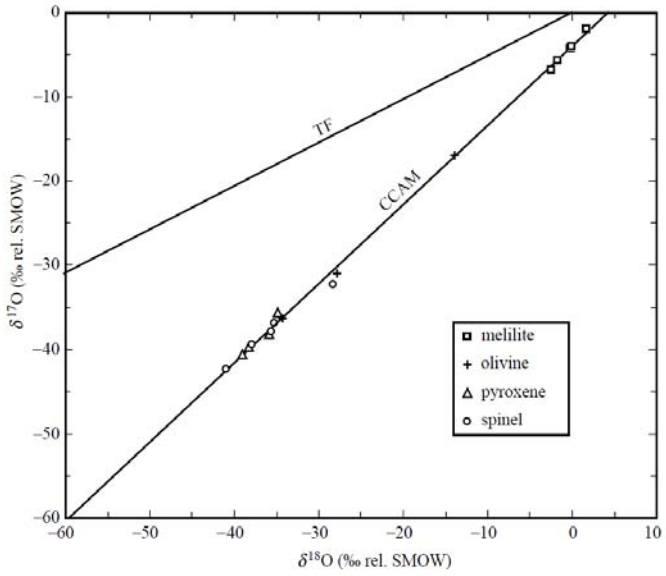

Figure 3.2: Oxygen isotopic compositions of mineral separates from Allende CAIs. These points were used to define the Carbonaceous Chondrite Anhydrous Mineral (CCAM) line (Clayton et al., 1977).

3.1.2 Oxygen isotope measurements by Sensitive High Resolution Ion Microprobe - Stable Isotope (SHRIMP-SI)

Oxygen isotopic compositions of NWA 4502 CAIs were measured using the SHRIMP-SI - an instrument designed for low-mass-range stable-isotope analysis. This is the first three-oxygen isotope analysis of CAIs by SHRIMP SI.

Polished and cleaned thick sections (epoxy resin mounts) of the studied CAIs *1*, *5*, *6* and *7*, a grain mount of 1-2 mm fragments of Allende FoB CAI SJ101 and a polished thin section of Efremovka Type B CAI E44 were measured. SJ101 and E44 have previously been described into detail Petaev and Jacobsen (2009) and Goswami et al. (1994) respectively. SJ101 and E44 have also been studied for oxygen isotopes by Petaev et al. (2010) and Dyl et al. (2008) respectively.

NWA 4502 CAI mounts were polished to 1 µm by diamond polishing and mapped with an automated Leica D6000 microscope in reflected light. The polished mounts were cleaned sequentially in ethanol, petroleum ether, HCl and deionised water with ultrasonic agitation, dried and coated with ca. 15 nm layer of Al for analysis. Al is used for the conductive coating in

preference to Au because of a much-reduced emission of $^{16}O^-$ from the electron beam impact (Ickert et al., 2008). After coating, the epoxy mounts were loaded into a steel holder for insertion into SHRIMP-SI. A new mount holder was used to remove edge effects related to proximity to the steel holder as previously observed in SHRIMP II (Ickert et al., 2008). BSE images were taken of analysed spots before and after SHRIMP-SI analysis. The analytical conditions are summarized in Table 3.1.

The SHRIMP-SI primary column consists of a Cs-ion source and three aperture einzel lenses with associated deflection plates that allow focusing and steering of the primary ion beam. Cesium ions are generated in a Kimball Physics IGS-4 alkali metal ion gun by heating a Cs zeolite cartridge and then extracting ions with an accelerating potential of 5 kV with an additional 10 kV acceleration provided by the immersion lens before the sample. A Cs^+ beam of ~10 nA is focused to sputter an area of around 20 μm, in diameter (Köhler illumination). An electron column is equipped with a low energy (Kimball Physics ELG-2) electron gun and is used to accelerate electrons to the target for charge neutralization. Electrons were delivered to the target surface with an energy of ~ -1.9 kV focused into a spot of ca. 200 μm in diameter. Negative secondary ions were accelerated to real ground from the −10 kV sample potential and focused by the quadrupole triplet lenses before passing through the source slit and entering the secondary mass analyzer. The source-slit width was set at 40 μm for all sessions. SHRIMP SI was operated with a 400 μm collector slit for $^{16}O^-$, 100 μm for $^{17}O^-$, and 300 μm for $^{18}O^-$. Mass resolution was sufficient to separate potential isobaric interferences of $^{16}OH^-$ from $^{17}O^-$ (at mass resolution 5,000, 1 % valley definition). Representative peak shapes are shown in Figure 3.3. Analyses were made in a static multicollector mode with $^{16}O^-$ measured with a 10^{11} Ω resistor (50 V range), and $^{17}O^-$ and $^{18}O^-$ on 10^{12} Ω resistors (5 V range). Each analysis took about 360 s and consisted of 120 s of presputtering, ~100 s of automated steering of secondary ions (i.e., adjustments of the secondary ion beam path in the Y and Z directions within the source chamber, prior to the electrostatic analyzer (ESA), so as to maximize secondary ion count rates), ~ 5s of automated centering of the secondary ions in the collector slits with magnet control, and 100 s of data collection. Data collection consisted of 5 subsets of 20 s, each subset comprised of 10 × 2 s acquisitions. The typical count rate for $^{16}O^-$ was approximately 10^9 c/s. The electron-induced secondary ion emission (EISIE) was assessed at the beginning and end of the analysis. Each EISIE measurement consisted of 20 s count time in which the electron gun was on, but Cs^+ beam was turned off. Count times were sufficient to produce internal precision in $\delta^{17}O$ better than 0.5 ‰, internal precision for $\delta^{18}O$ was typically better than 0.1 ‰. Reproducibility of $\delta^{18}O$

was approximately ±0.5 ‰. Examples of areas selected for analyses on each CAI and the analysed spots on minerals are shown in Figure 3.4.

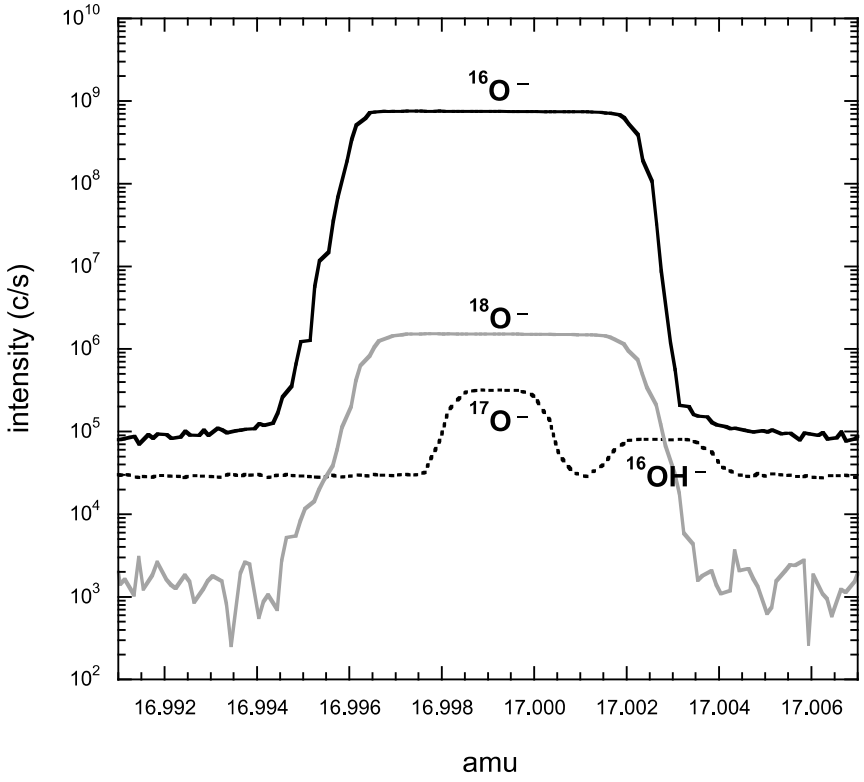

Figure 3.3: Mass spectra of the oxygen mass region. X-axis is determined by the ^{17}O mass position and is applicable to mass-17 only. Collector slit widths used: ^{16}O = 400 µm, ^{17}O = 100 µm, ^{18}O = 300 µm. The only interference observed was oxygen hydride at mass 17. With the appropriate collector slit width, the hydride peak is well resolved.

Data reduction was carried out with POXI MC Labview application, RSES-ANU in-house software. Corrections for instrumental mass fractionation (IMF), counting statistics, and uncertainty in standard compositions were applied. The IMF was monitored throughout the analytical sessions by analyzing pyroxene and plagioclase from Temora (samples derived from the Middledale Gabbroic Diorite (Wormald, 1993)) and FC1 (from the anorthositic series of the Duluth Complex Minnesota, USA) at the SHRIMP laboratory at ANU, From these analyses, FC1 pyroxenes appears to preserve more pristine domains. The plagioclase was variable in composition and this appears to be the result of late-stage deuteric alteration. The IMF corrections adopted were calculated from the entirety of analyses on the standard material FC1

over the course of an analytical session. Due to intensity fluctuations and fractionated isotopic composition, the electron-induced secondary ion emission (EISIE) effect has to be carefully monitored during SHRIMP measurements (Ickert et al., 2008). All SHRIMP oxygen isotopic ratios reported here were corrected for EISIE. The uncertainty associated with the EISIE fluctuations has very little effect on the overall uncertainty budget and were not propagated into the data reported here. Corrected oxygen isotopic ratios are expressed in conventional delta notation such that ratios are given as permil deviations (‰) from Standard Mean Ocean Water (SMOW) reference value.

$$\delta^{18}O_{SMOW} = \left[\frac{\left({}^{18}O/_{16}O \right)_{sample}}{\left({}^{18}O/_{16}O \right)_{reference}} - 1 \right] \times 1000 \quad \text{.....10}$$

$$\delta^{17}O_{SMOW} = \left[\frac{\left({}^{17}O/_{16}O \right)_{sample}}{\left({}^{17}O/_{16}O \right)_{reference}} - 1 \right] \times 1000 \quad \text{.....11}$$

Where $({}^{18}O/{}^{16}O)_{sample}$ and $({}^{17}O/{}^{16}O)_{sample}$ are the background, EISIE, and IMF corrected ${}^{18}O/{}^{16}O$ ratio, and $({}^{18}O/{}^{16}O)_{reference}$ and $({}^{17}O/{}^{16}O)_{reference}$ are the reference value of the reference material. The mass-independent enrichment of ${}^{16}O$ relative to SMOW is expressed as $\Delta^{17}O$:

$$\Delta^{17}O = \delta^{17}O_{SMOW} - 0.52 \times \delta^{18}O_{SMOW} \quad \text{.....12}$$

For reference, it is noted here that the end member CAI compositions of Clayton et al. (1973) have $\delta^{18}O \approx \delta^{17}O$ of approximately -40 ‰, and this corresponds to $\Delta^{17}O$ of -20 ‰. In comparison, the composition of solar wind measured and inferred by McKeegan et al. (2011) has $\delta^{18}O$ of ≈ -54 ‰ and $\Delta^{17}O$ of -27 ‰.

Following isotopic analyses, each CAI was examined by Scanning Electron Microscopy (SEM) to verify the locations of the sputtered craters and the mineralogy of the phases analysed and subsequently reject any analysis spots that included multi-mineral phases or cracks.

Table 3.1: SHRIMP-SI analytical conditions.

Analytical Conditions	
Primary beam (nA)	10
Source Slit (µm)	20
Collector Slit (µm), LMH	400
Collector Slit (µm), HMH	300
Electrometer, LMH	10^{11} Ω, 50V
Electrometer, HMH	10^{12} Ω, 5V
EG energy (kV)	-1.9
Background, Faraday LMH (median, cps)	36000
Background, Faraday HMH (median, cps)	7000
EISIE contribution (range, ‰)	2.4 - 5.4
EISIE fluctuation (median, ‰)	0.2
^{16}O cps (median)	1798222728
^{18}O cps (median)	3695621

3.1.3 Oxygen Isotope compositions

Oxygen isotope compositions in this study are reported as delta values relative to the deviations from the oxygen ratios measured from the Standard Mean Ocean Water (SMOW) standard (Baertschi, 1976; Li et al., 1988).

To verify consistency with other ion microprobe oxygen isotope measurements minerals from the Allende FoB SJ101 and Efremovka Type B E44 were analysed. SJ101 minerals show two clusters. Four pyroxene analyses are ^{16}O-enriched with δ^{17}O and δ^{18}O values clustered near -50 ‰ with an average Δ^{17}O of -25 ‰. Three points with intermediate ^{16}O-enrichment with δ^{17}O and δ^{18}O values between -11 to 18 ‰ and -8 to 15 ‰ respectively, (Δ^{17}O of -12 ‰) are melilite. These data are consistent with the results of oxygen isotope measurements using the University of Hawai‘i Cameca ims1280 by (Petaev et al., 2010) who reported ^{16}O-rich compositions for spinel, fosterite, and clinopyroxene and ^{16}O-poor compositions at varying degrees for melilite and anorthite (Figure 3.5a, b).

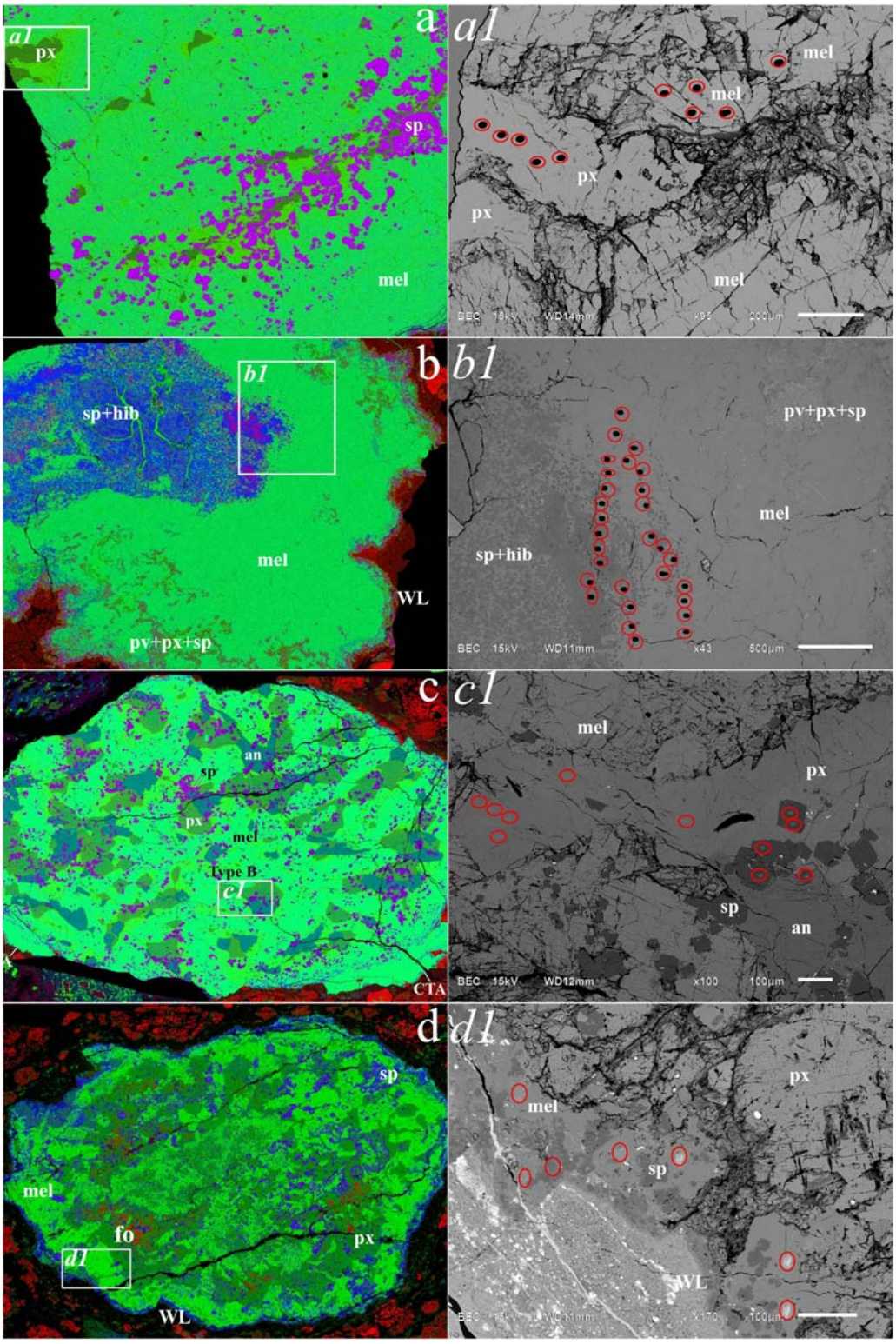

Figure 3.4: Combined element maps (Mg: red, Ca: green, Al: Blue) of NWA 4502 CAIs a) *6*, b)*7*, c)*1*, and d) *5* with areas selected (rectangular insets *a1, b1, c1* and *d1*) for analysis on

SHRIMP-SI. The SHRIMP-SI spots on minerals analysed are highlighted with red circles on the magnified BSE images.

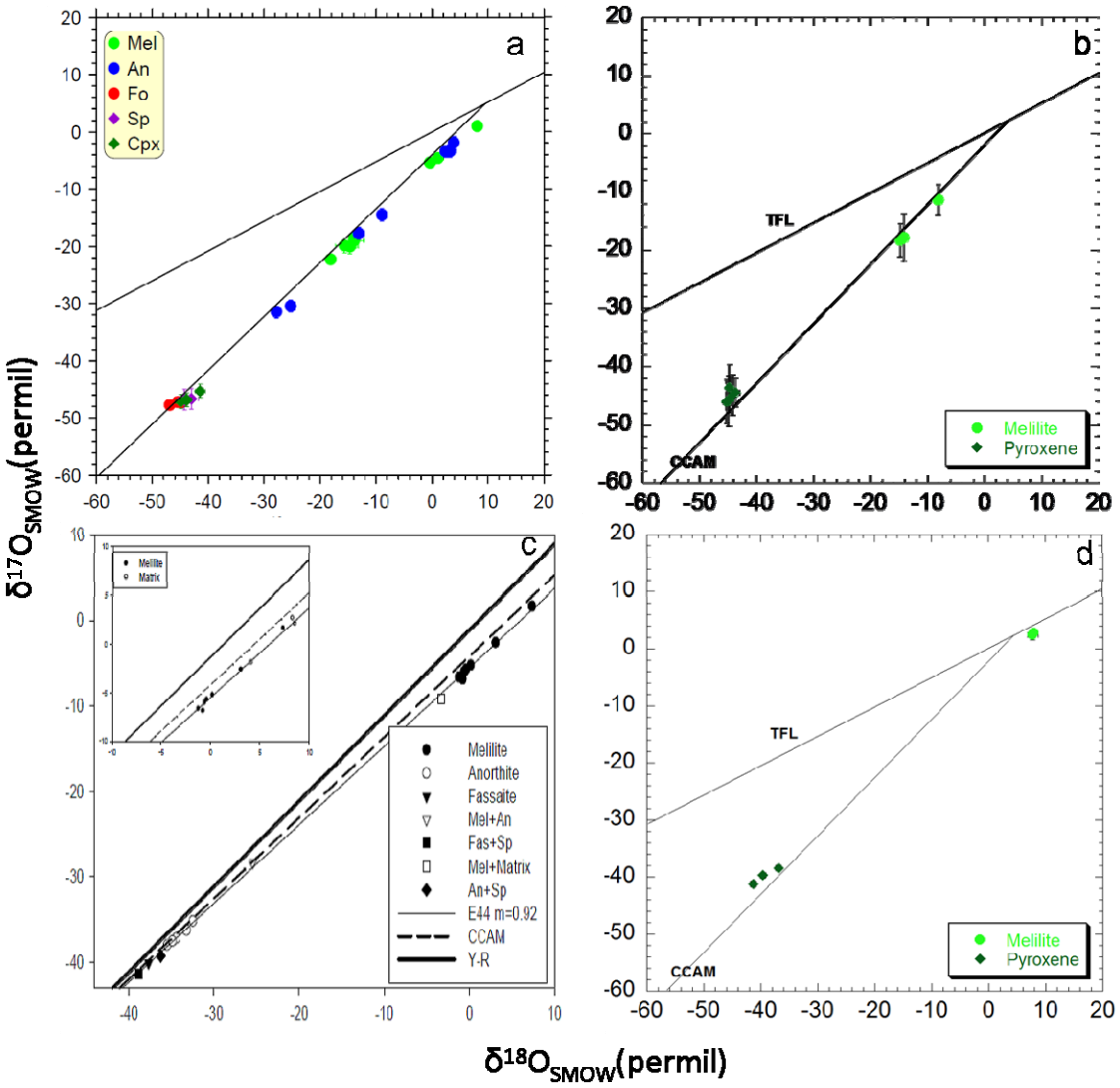

Figure 3.5: Oxygen isotope compositions of mineral phases in (a) Allende FoB SJ101 analysed by SIMS (Petaev et al., 2010), (b) SJ101 analysed by SHRIMP-SI in this study, (c) Efremovka CAI E44 analysed UV-laser fluorination (Dyl et al., 2008) and (d) E44 analysed by SHRIMP-SI in this study.

Pyroxenes in Efremovka Type B CAI E44 are ^{16}O-enriched with δ^{17}O and δ^{18}O near -40 ‰ and an average Δ^{17}O of −22 ‰. Melilite is ^{16}O-poor with δ^{17}O and δ^{18}O values at ~3 and ~8 ‰ respectively, (Δ^{17}O ~ −4 to −22 ‰). These data are consistent with UV-laser fluorination

analyses (Dyl et al., 2008) although pyroxene analyses in this study are slightly more ^{16}O-enriched possibly owing to some melilite contributing to the relatively large laser fluorination spots (Figure 3.5c,d).

Oxygen isotope compositions of the NWA 4502 CAIs are summarized in Table 3.2 and presented in Figure 3.6. Oxygen-isotope data were collected for major mineral phases (pyroxene, melilite, spinel, anorthite, hibonite) in each CAI. While minor contributions to spinel from other phases cannot be ruled out completely due to the sometimes small (<20 μm) sizes of spinel grains, the grain sizes of individual phases analysed in each inclusion are sufficiently large to confidently say these data are a good representation of the individual phases.

A total of 59 analyses spots were obtained for the CTA CAI *6* including 23 analyses for pyroxene, 21 for melilite and 15 for spinel (Figure 3.6a). Pyroxene in this inclusion has compositions ranging from ^{16}O-poor to ^{16}O-rich with the compositions becoming enriched towards the core of the inclusion. Pyroxenes analysed towards the periphery of the inclusion have $\delta^{17}O$ values ranging from -0.2 to 0.6 ‰ and $\delta^{18}O$ values ranging from -1.1 to 7.3 ‰. $\Delta^{17}O$ values range between -3.2 to -16.7 ‰. Core pyroxenes on the other hand are more ^{16}O-rich with $\delta^{17}O$ and $\delta^{18}O$ values ranging from -35 to -44 ‰ and -30 to -40 ‰ respectively, with $\Delta^{17}O$ varying between -18.9 to -23 ‰. The average $\Delta^{17}O$ value for all pyroxenes analysed in this inclusion is -12.3 ‰. Melilite in this CAI is consistently ^{16}O-poor. $\delta^{17}O$ values are between -0.1 to 3.0 ‰ while $\delta^{18}O$ values range from -2.0 to 8.7 ‰. $\Delta^{17}O$ is between -1.9 to -8.0 ‰ with the average $\Delta^{17}O$ value being -4.0 ‰. Spinel in this inclusion is ^{16}O-rich. $\delta^{17}O$ and $\delta^{18}O$ values are about -50 ‰ with $\Delta^{17}O \approx$ -24 ‰. A linear regression of values for all CAI 6 minerals yielded a slope of 0.916 ± 0.034.

For the CTA CAI *7*, a total of 69 spots were analysed including 31 analyses for melilite, 27 for hibonite and 11 for spinel (Figure 3.6b). Melilite in this CAI *7* show a large degree of isotopic heterogeneity with compositions ranging from ^{16}O-poor to ^{16}O-rich. Twenty-five of the 31 analyses are ^{16}O-rich with $\delta^{17}O$ values <-20 ‰. Their $\delta^{17}O$ values range between -20 to -47 ‰ and $\delta^{18}O$ values are between -17 to -44 ‰. The range of $\Delta^{17}O$ values is -11.8 to -23.9 ‰. The remaining less enriched melilite have $\delta^{17}O$ values between -3.5 to -17.4 ‰ and $\delta^{18}O$ values between -6.2 to 1.8 ‰, with a $\Delta^{17}O$ range of -4.5 to -10.3 ‰ . The average $\Delta^{17}O$ value for all melilite analysed is -16.7 ‰. Hibonite and spinel in this inclusion have ^{16}O-rich compositions. $\delta^{17}O$ values for both minerals range between -30 to -50 ‰ while $\delta^{18}O$ values are between -25 to -50 ‰ and $\Delta^{17}O$ values are between -15 to -24 ‰. Linear regression for all CAI *7* minerals yielded a slope of 0.9111 ± 0.0078.

Table 3.2: Oxygen isotope compositions.

	spot	$\delta^{17}O$	2σ	$\delta^{18}O$	2σ	$\Delta^{17}O$	2σ		spot	$\delta^{17}O$	2σ	$\delta^{18}O$	2σ	$\Delta^{17}O$	2σ
CAI *6*								**CAI *6***							
Mel	1	-2.1	0.34	5.0	0.15	-4.7	0.3	Sp	11	-51.2	0.48	-51.1	0.11	-24.7	0.1
Mel	2	-2.2	0.43	3.7	0.14	-4.1	0.3	Sp	12	-49.9	0.53	-49.5	0.14	-24.1	0.2
Mel	3	-2.6	0.44	3.6	0.18	-4.5	0.2	Sp	13	-50.0	0.44	-49.6	0.11	-24.2	0.2
Mel	4	-3.0	0.50	3.8	0.15	-5.0	0.2	Sp	14	-50.0	0.46	-49.8	0.13	-24.1	0.3
Mel	5	-9.8	0.46	-3.5	0.13	-8.0	0.3	Sp	15	-50.1	0.35	-49.5	0.13	-24.4	0.2
Mel	6	-0.7	0.40	6.2	0.12	-3.9	0.3	**CAI *7***							
Mel	7	-0.1	0.41	6.6	0.13	-3.5	0.3	Hib	1	-49.4	0.53	-48.9	0.14	-23.9	0.2
Mel	8	-0.3	0.36	6.0	0.12	-3.4	0.1	Hib	2	-48.8	0.58	-48.2	0.13	-23.8	0.2
Mel	9	0.2	0.45	6.4	0.12	-3.2	0.2	Hib	3	-49.1	0.47	-49.4	0.14	-23.4	0.2
Mel	10	0.4	0.47	7.0	0.12	-3.3	0.2	Hib	4	-44.8	0.31	-43.7	0.12	-22.1	0.2
Mel	11	1.8	0.46	8.4	0.11	-2.5	0.1	Hib	5	-42.7	0.48	-41.3	0.13	-21.2	0.3
Mel	12	0.7	0.50	7.4	0.11	-3.2	0.3	Hib	6	-46.2	0.39	-45.6	0.11	-22.5	0.2
Mel	13	1.1	0.40	7.3	0.13	-2.7	0.2	Hib	7	-49.0	0.43	-49.1	0.12	-23.5	0.2
Mel	14	-2.5	0.47	4.8	0.15	-5.0	0.3	Hib	8	-47.6	0.47	-46.5	0.14	-23.4	0.3
Mel	15	0.1	0.43	6.8	0.12	-3.5	0.2	Hib	9	-48.9	0.48	-48.0	0.16	-24.0	0.2
Mel	16	-3.4	0.46	3.9	0.15	-5.4	0.2	Hib	10	-46.7	0.45	-46.5	0.16	-22.5	0.2
Mel	17	-2.1	0.41	5.0	0.12	-4.7	0.4	Hib	11	-46.8	0.56	-46.1	0.13	-22.8	0.2
Mel	18	1.8	0.42	8.7	0.12	-2.7	0.1	Hib	12	-46.2	0.44	-46.1	0.14	-22.2	0.2
Mel	19	2.6	0.40	8.6	0.12	-1.9	0.3	Hib	13	-37.0	0.51	-34.8	0.15	-18.9	0.2
Mel	20	0.6	0.48	6.9	0.13	-3.0	0.1	Hib	14	-41.0	0.57	-40.2	0.15	-20.1	0.3
Mel	21	-7.5	0.34	-2.0	0.13	-6.5	0.1	Hib	15	-31.5	0.47	-30.7	0.12	-15.5	0.3
Px	1	-13.6	0.41	-8.0	0.11	-9.4	0.3	Hib	16	-38.8	0.43	-38.0	0.13	-19.0	0.2
Px	2	-14.9	0.34	-9.5	0.13	-10.0	0.3	Hib	17	-50.7	0.41	-51.5	0.11	-24.0	0.2
Px	3	0.6	0.36	7.3	0.12	-3.2	0.2	Hib	18	-49.7	0.48	-50.3	0.13	-23.6	0.2
Px	4	-5.9	0.45	-1.1	0.15	-5.4	0.1	Hib	19	-44.1	0.48	-43.9	0.14	-21.3	0.2
Px	5	-7.7	0.47	-2.5	0.15	-6.4	0.2	Hib	20	-33.5	0.56	-31.7	0.12	-17.0	0.1
Px	6	-23.5	0.51	-18.5	0.17	-13.9	0.3	Hib	21	-43.1	0.38	-42.3	0.14	-21.1	0.2
Px	7	-29.8	0.41	-25.2	0.12	-16.7	0.1	Hib	22	-36.0	0.51	-34.6	0.12	-18.0	0.2
Px	8	-16.1	0.41	-11.3	0.11	-10.2	0.2	Hib	23	-48.5	0.39	-47.4	0.13	-23.9	0.3
Px	9	-25.1	0.48	-20.1	0.15	-14.6	0.2	Hib	24	-48.8	0.35	-48.0	0.12	-23.9	0.2
Px	10	-26.6	0.40	-21.9	0.13	-15.3	0.2	Hib	25	-45.0	0.43	-44.9	0.13	-21.7	0.2
Px	11	-23.0	0.43	-17.9	0.15	-13.7	0.1	Hib	26	-46.2	0.38	-45.6	0.12	-22.5	0.1
Px	12	-0.2	0.39	6.7	0.17	-3.6	0.4	Hib	27	-28.5	0.43	-25.6	0.12	-15.2	0.2
Px	13	-4.6	0.32	0.5	0.14	-4.9	0.2	Mel	1	-38.6	0.44	-35.4	0.12	-20.2	0.2
Px	14	-6.3	0.49	0.3	0.12	-6.5	0.2	Mel	2	-38.4	0.43	-35.9	0.14	-19.7	0.2
Px	15	-17.3	0.35	-12.3	0.12	-10.9	0.2	Mel	3	-10.9	0.43	-6.2	0.11	-7.7	0.1
Px	16	-1.4	0.40	4.5	0.11	-3.8	0.1	Mel	4	-20.8	0.45	-17.4	0.10	-11.8	0.1
Px	17	-16.0	0.38	-9.6	0.10	-11.0	0.1	Mel	5	-46.9	0.42	-44.3	0.14	-23.9	0.2
Px (core)	18	-36.0	0.37	-32.2	0.14	-19.3	0.1	Mel	6	-45.5	0.44	-42.9	0.11	-23.2	0.3
Px (core)	19	-34.6	0.41	-30.2	0.13	-18.9	0.1	Mel	7	-3.5	0.44	1.8	0.12	-4.5	0.2
Px (core)	20	-38.2	0.47	-33.6	0.17	-20.7	0.2	Mel	8	-16.0	0.47	-11.0	0.15	-10.3	0.1
Px (core)	21	-37.8	0.44	-33.3	0.13	-20.5	0.2	Mel	9	-22.6	0.51	-18.5	0.13	-12.9	0.2
Px (core)	22	-43.6	0.52	-39.6	0.13	-23.0	0.3	Mel	10	-35.8	0.48	-32.8	0.15	-18.8	0.2
Px (core)	23	-42.2	0.38	-38.4	0.12	-22.2	0.2	Mel	11	-31.4	0.44	-27.8	0.11	-17.0	0.3
Sp	1	-49.8	0.54	-50.4	0.14	-23.6	0.1	Mel	12	-41.9	0.31	-38.5	0.14	-21.9	0.1
Sp	2	-49.9	0.49	-49.6	0.19	-24.1	0.2	Mel	13	-20.4	0.50	-15.6	0.15	-12.3	0.4
Sp	3	-49.9	0.47	-50.7	0.18	-23.5	0.2	Mel	14	-13.0	0.47	-8.7	0.13	-8.4	0.1
Sp	4	-50.6	0.44	-51.0	0.19	-24.1	0.2	Mel	15	-36.4	0.54	-34.1	0.13	-18.7	0.2
Sp	5	-50.0	0.41	-50.0	0.13	-24.1	0.1	Mel	16	-45.9	0.54	-44.7	0.14	-22.7	0.2
Sp	6	-50.4	0.54	-50.3	0.11	-24.2	0.2	Mel	17	-39.5	0.42	-37.1	0.12	-20.1	0.1
Sp	7	-50.5	0.74	-49.8	0.16	-24.6	0.3	Mel	18	-40.5	0.62	-38.3	0.13	-20.6	0.4
Sp	8	-49.8	0.54	-50.5	0.15	-23.5	0.4	Mel	19	-31.5	0.40	-27.8	0.12	-17.0	0.2
Sp	9	-50.6	0.46	-50.2	0.13	-24.5	0.1	Mel	20	-26.0	0.43	-21.3	0.14	-14.9	0.2
Sp	10	-50.2	0.39	-49.8	0.13	-24.2	0.2	Mel	21	-42.3	0.50	-39.6	0.12	-21.7	0.3

Table 3.2: Continued.

	spot	$\delta^{17}O$	2σ	$\delta^{18}O$	2σ	$\Delta^{17}O$	2σ		spot	$\delta^{17}O$	2σ	$\delta^{18}O$	2σ	$\Delta^{17}O$	2σ
CAI *7*								**CAI *1***							
Mel	22	-42.1	0.45	-39.5	0.13	-21.6	0.3	Mel	7.2	-14.8	0.65	-11.0	0.16	-9.1	0.3
Mel	23	-41.3	0.45	-38.9	0.15	-21.1	0.2	Px	1.1	-45.3	0.60	-41.7	0.13	-23.7	0.3
Mel	24	-34.8	0.43	-31.3	0.15	-18.5	0.2	Px	1.2	-46.0	0.46	-41.8	0.14	-24.2	0.2
Mel	25	-12.1	0.41	-6.6	0.13	-8.7	0.1	Px	1.3	-46.2	0.48	-42.4	0.12	-24.1	0.2
Mel	26	-22.5	0.40	-17.9	0.14	-13.2	0.2	Px	2.1	-45.6	0.42	-42.0	0.18	-23.8	0.4
Mel	27	-43.4	0.50	-41.2	0.13	-22.0	0.1	Px	2.2	-33.8	0.48	-29.1	0.13	-18.7	0.2
Mel	28	-34.7	0.48	-31.1	0.13	-18.6	0.2	Px	2.3	-45.2	0.42	-41.7	0.16	-23.6	0.2
Mel	29	-40.3	0.55	-36.9	0.12	-21.1	0.1	Sp	1	-48.9	0.71	-49.0	0.18	-23.4	0.3
Mel	30	-17.4	0.41	-13.5	0.14	-10.3	0.2	Sp	2	-48.5	0.51	-49.6	0.15	-22.7	0.1
Mel	31	-25.3	0.38	-20.9	0.14	-14.5	0.1	Sp	3	-50.8	0.52	-49.8	0.13	-24.9	0.2
Sp	1	-31.3	0.47	-27.1	0.12	-17.2	0.2	Sp	4	-49.1	0.57	-48.7	0.17	-23.7	0.4
Sp	2	-44.9	0.46	-43.7	0.13	-22.2	0.2	Sp	5	-48.0	0.52	-47.9	0.15	-23.1	0.3
Sp	3	-49.2	0.30	-48.6	0.14	-23.9	0.3	Sp	6	-42.6	0.59	-41.2	0.17	-21.2	0.3
Sp	4	-40.9	0.41	-39.8	0.12	-20.2	0.1	Sp	7	-48.6	0.68	-47.9	0.14	-23.7	0.1
Sp	5	-49.6	0.42	-49.6	0.14	-23.8	0.2	Sp	8	-49.4	0.57	-48.4	0.15	-24.2	0.2
Sp	6	-45.3	0.44	-45.1	0.12	-21.9	0.2	Sp	9	-49.1	0.48	-48.6	0.15	-23.8	0.2
Sp	7	-48.9	0.40	-49.0	0.14	-23.4	0.2	Sp	10	-47.6	0.52	-47.9	0.13	-22.6	0.2
Sp	8	-49.3	0.51	-48.8	0.13	-23.9	0.2	**CAI *5***							
Sp	9	-49.6	0.42	-48.7	0.13	-24.3	0.2	Mel	1	5.0	0.39	13.1	0.14	-1.8	0.3
Sp	10	-46.5	0.39	-46.4	0.13	-22.4	0.2	Mel	2	4.3	0.45	12.3	0.15	-2.1	0.3
Sp	11	-40.1	0.44	-39.0	0.13	-19.8	0.2	Mel	3	4.3	0.40	12.5	0.12	-2.2	0.1
CAI *1*								Mel	4	4.5	0.61	12.9	0.13	-2.2	0.2
An	1.1	-23.6	0.48	-20.4	0.12	-12.9	0.2	Mel	5	3.0	0.48	10.6	0.13	-2.6	0.2
An	1.2	-0.5	0.48	3.8	0.14	-2.5	0.2	Mel	6	2.8	0.39	10.0	0.12	-2.4	0.4
An	2.1	-5.4	0.49	-0.4	0.13	-5.2	0.2	Mel	7	0.0	0.36	6.0	0.11	-3.1	0.3
An	2.2	-40.6	0.57	-36.9	0.15	-21.4	0.2	Mel	8	-18.4	0.52	-13.5	0.14	-11.4	0.1
An	2.3	-27.9	0.36	-23.5	0.16	-15.7	0.2	Mel	9	-1.5	0.47	4.1	0.17	-3.6	0.5
An	3.1	-31.2	0.61	-27.4	0.14	-16.9	0.2	Mel	10	-8.1	0.40	-2.0	0.14	-7.1	0.2
An	3.2	-36.2	0.53	-33.1	0.14	-19.0	0.2	Mel	11	4.9	0.49	11.9	0.14	-1.3	0.2
An	4.1	-19.3	0.47	-15.0	0.16	-11.5	0.2	Mel	12	-2.2	0.44	5.2	0.13	-4.9	0.2
An	4.2	-21.6	0.49	-16.7	0.16	-12.9	0.1	Mel	13	2.0	0.41	9.6	0.15	-2.9	0.2
An	5.1	-17.7	0.52	-13.7	0.14	-10.6	0.3	Mel	14	6.2	0.36	14.2	0.14	-1.2	0.2
An	5.2	-37.8	0.51	-33.7	0.16	-20.2	0.3	Mel	15	5.8	0.46	14.4	0.13	-1.6	0.2
Hib	1.1	-22.1	0.66	-18.8	0.14	-12.3	0.3	Mel	16	0.6	0.54	6.4	0.15	-2.7	0.3
Hib	1.2	-38.2	0.48	-36.6	0.17	-19.2	0.2	Mel	17	-6.1	0.52	1.2	0.16	-6.7	0.2
Hib	1.3	-40.7	0.50	-39.0	0.14	-20.4	0.2	Mel	18	5.1	0.43	13.5	0.18	-1.9	0.2
Hib	2.1	-24.4	0.51	-21.6	0.13	-13.1	0.1	Mel	19	2.3	0.48	9.6	0.11	-2.7	0.2
Hib	2.2	-40.4	0.48	-39.3	0.16	-20.0	0.2	Mel	20	0.1	0.31	4.7	0.10	-2.4	0.1
Hib	2.3	-23.5	0.55	-19.4	0.16	-13.4	0.2	Px	1	-43.9	0.48	-40.0	0.13	-23.0	0.1
Mel	1.1	-6.7	0.44	-1.7	0.11	-5.8	0.3	Px	2	-42.0	0.45	-38.1	0.15	-22.2	0.3
Mel	1.2	-6.4	0.60	-1.2	0.13	-5.8	0.2	Px	3	-44.6	0.39	-41.0	0.19	-23.3	0.2
Mel	2.1	-4.3	0.45	-0.6	0.13	-4.0	0.3	Px	4	-43.2	0.53	-39.6	0.15	-22.5	0.2
Mel	2.2	-4.4	0.44	0.8	0.12	-4.8	0.3	Px	5	-46.4	0.54	-43.2	0.18	-23.9	0.2
Mel	3.1	-1.3	0.54	4.8	0.15	-3.8	0.2	Px	6	-46.8	0.51	-43.7	0.16	-24.0	0.2
Mel	3.2	-1.2	0.47	3.7	0.14	-3.2	0.2	Px	7	-45.5	0.45	-41.7	0.19	-23.8	0.4
Mel	4.1	-9.0	0.45	-3.9	0.16	-7.0	0.1	Px	8	-46.4	0.41	-43.5	0.18	-23.8	0.3
Mel	4.2	-7.6	0.38	-2.3	0.16	-6.4	0.2	Px	9	-42.8	0.57	-40.2	0.18	-21.9	0.2
Mel	5.1	-9.8	0.41	-5.6	0.14	-6.9	0.3	Px	10	-45.9	0.48	-43.2	0.19	-23.4	0.2
Mel	5.2	-9.2	0.54	-4.9	0.15	-6.7	0.1	Px	11	-46.6	0.53	-43.6	0.13	-24.0	0.1
Mel	5.3	-8.6	0.48	-3.6	0.15	-6.7	0.3	Px	12	-47.2	0.57	-43.8	0.16	-24.4	0.4
Mel	6.1	-6.6	0.53	-2.1	0.16	-5.5	0.2	Px	13	-46.4	0.49	-42.7	0.14	-24.2	0.3
Mel	6.2	-8.1	0.43	-3.3	0.15	-6.4	0.4	Px	14	-46.1	0.44	-42.6	0.14	-24.0	0.2
Mel	6.3	-7.1	0.41	-2.0	0.15	-6.1	0.2	Px	15	-45.2	0.51	-42.1	0.14	-23.4	0.1
Mel	7.1	-15.0	0.47	-10.3	0.15	-9.6	0.2	Px	16	-46.0	0.55	-43.0	0.13	-23.6	0.2

Table 3.2: Continued.

	spot	$\delta^{17}O$	2σ	$\delta^{18}O$	2σ	$\Delta^{17}O$	2σ
CAI *5*							
Px	17	-46.3	0.44	-43.2	0.11	-23.8	0.2
Px	18	-46.7	0.42	-44.1	0.13	-23.8	0.2
Px	19	-45.7	0.37	-43.3	0.13	-23.2	0.2
Px	20	-46.0	0.58	-42.4	0.14	-23.9	0.3
Px (rim)	1.1	-43.7	0.42	-40.4	0.11	-22.8	0.1
Px (rim)	1.2	-42.0	0.42	-37.7	0.11	-22.4	0.2
Px (rim)	1.3	-36.9	0.35	-32.3	0.12	-20.1	0.2
Px (rim)	1.4	-39.1	0.38	-34.9	0.12	-21.0	0.1
Sp	1	-39.2	0.48	-38.5	0.15	-19.1	0.1
Sp	2	-46.5	0.40	-47.3	0.18	-21.9	0.1
Sp	3	-45.7	0.50	-45.5	0.20	-22.0	0.2
Sp	4	-49.0	0.39	-50.3	0.14	-22.9	0.1
Sp	5	-49.3	0.46	-50.2	0.14	-23.2	0.2
Sp	6	-49.8	0.48	-49.8	0.15	-23.9	0.2
Sp	7	-49.8	0.54	-50.0	0.15	-23.9	0.2
Sp	8	-44.1	0.52	-41.8	0.14	-22.4	0.3
Sp	9	-49.2	0.49	-48.9	0.12	-23.8	0.2
Sp	10	-48.7	0.37	-49.0	0.12	-23.2	0.2
Sp	11	-43.2	0.38	-38.9	0.15	-22.9	0.3
Sp	12	-47.5	0.38	-46.0	0.15	-23.6	0.3
Sp	13	-36.2	0.62	-34.3	0.18	-18.4	0.2
Sp	14	-49.9	0.48	-49.4	0.14	-24.2	0.3
Sp	15	-30.1	0.47	-27.5	0.15	-15.8	0.2
Sp	16	-44.4	0.47	-43.8	0.15	-21.6	0.1
Sp	17	-48.2	0.53	-48.5	0.15	-23.0	0.3
Sp	18	-46.8	0.38	-46.8	0.13	-22.4	0.1
Sp	19	-34.9	0.50	-32.9	0.15	-17.8	0.3
Sp (rim)	1.1	-43.3	0.47	-42.3	0.21	-21.2	0.2
Sp (rim)	1.2	-34.6	0.32	-33.8	0.14	-17.0	0.1
Sp (rim)	1.3	-37.4	0.39	-36.0	0.13	-18.7	0.2
Sp (rim)	1.4	-43.1	0.50	-42.6	0.13	-20.9	0.3

	spot	$\delta^{17}O$	2σ	$\delta^{18}O$	2σ	$\Delta^{17}O$	2σ
SJ101							
Mel	15.2	-18.3	2.83	-14.8	0.78	-13.3	2.9
Mel	15.3	-17.8	4.03	-14.3	0.53	-13.0	4.1
Mel	15.4	-11.3	2.55	-8.2	0.69	-9.7	2.6
Px	1	-43.6	3.95	-44.8	0.55	-23.0	4.0
Px	2	-44.5	2.51	-43.8	0.72	-24.4	2.6
Px	3	-44.9	3.48	-44.2	0.54	-24.7	3.5
Px	4	-46	3.72	-45.3	0.71	-25.1	3.8
Px	15.1	-45.9	4.37	-45	0.51	-25.2	4.4
E44							
Mel	1	2.5	4.18	7.7	0.93	-4.2	4.3
Mel	2	2.8	3.51	7.9	0.41	-3.9	3.5
Px	3	-39.7	3.11	-39.6	0.48	-21.8	3.1
Px	4	-41.2	3.22	-41.3	0.54	-22.4	3.3
Px	5	-38.4	2.68	-36.9	0.5	-21.9	2.7

An: Anorthite, Hib:Hibonite, Mel: Melilite, Px: Pyroxene and Sp: Spinel.

Forty-nine analyses were obtained for the type B CAI *1*. Sixteen spots were analysed for melilite, 11 for spinel, 10 for anorthite, and 6 for pyroxene (Figure 3.6c). Pyroxene and spinel are ^{16}O-rich. Pyroxene has $\delta^{17}O$ and $\delta^{18}O$ values ranging from -33.8 to -46.2 ‰ and -29.1 to -42.4 ‰ respectively, and $\Delta^{17}O$ ranging between -18.7 to -24.2 ‰. Spinel values are between -42.6 to -50.8 ‰ and -41.2 to -49.8 ‰ for $\delta^{17}O$ and $\delta^{18}O$ respectively with $\Delta^{17}O$ between -22.6 to -24.9‰. Melilite is mainly ^{16}O-poor, with compositions ranging between -1.2 to -15.2 ‰ for $\delta^{17}O$, -0.6 to 4.8 ‰ for $\delta^{18}O$ and $\Delta^{17}O$ values between -3.2 to -9.1. Hibonite has intermediate to ^{16}O-rich compositions. Their $\delta^{17}O$ and $\delta^{18}O$ values range from -22.1 to -40.7 ‰ and -18.8 to -39.3 ‰ respectively, with $\Delta^{17}O$ values ranging between of -12.3 to -20.4 ‰. Anorthite in this CAI is also isotopically heterogeneous. It has ^{16}O-poor to ^{16}O -rich compositions. $\delta^{17}O$ values range between -0.5 to -40.6 ‰, while $\delta^{18}O$ values are between -0.4 to 3.8 ‰ and $\Delta^{17}O$ values

range between -2.5 to-21.4 ‰. The linear regression line through all minerals in the CAI *1* has a slope of 0.961 ± 0.041.

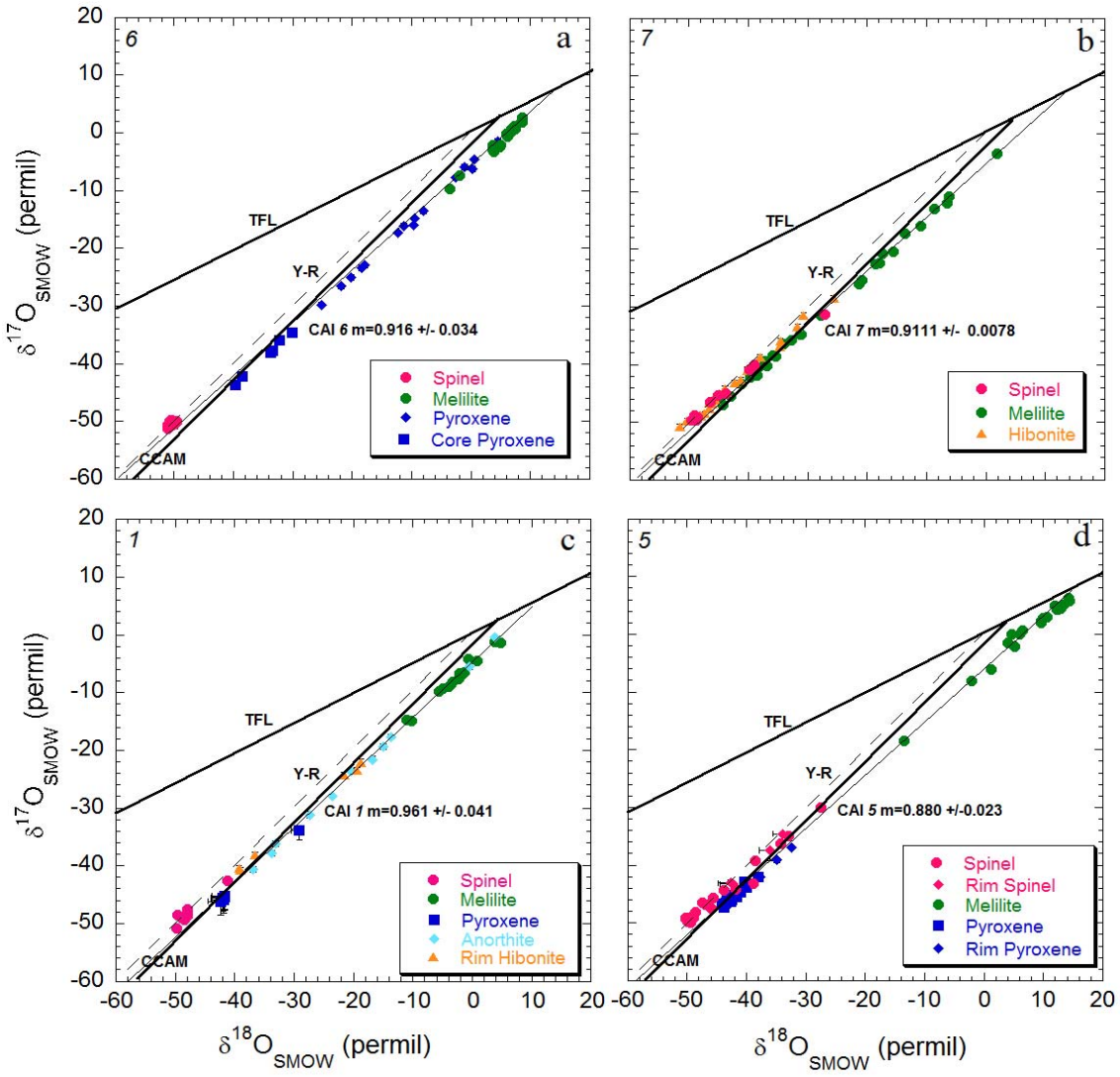

Figure 3.6: Oxygen isotope compositions of mineral phases in NWA 4502 CAIs a) *6*, b) *7*, c) *1*, d) *5*, measured by SHRIMP-SI. Thick solid lines are Terrestrial Fractionation line (TFL) and Carbonaceous Chondrite Anhydrous Mineral line (CCAM) dashed line is Young-Russell (Y-R) line and thin solid lines are regression lines for studied CAIs.

A total of 68 analyses were obtained for FoB CAI *5* including 20 analyses each for pyroxene, melilite and spinel. Four spots each were analysed for pyroxene and spinel in the WL rim sequence of this inclusion. The oxygen isotope compositions are similar to those from CAI *1*

although some melilite compositions are closer to the Terrestrial Fractionation Line (TFL) (Figure 3.6d). Pyroxene and spinel have ^{16}O-rich compositions. The δ^{17}O values for pyroxene are between -42.0 to -47.2 ‰ and -38.1 to -43.8 ‰ for δ^{18}O. The Δ^{17}O values are between -21.9 to -24.4 ‰. Spinel compositions range between -30.1 to -49.8 ‰ and -27.5 to -50.3 ‰ for δ^{17}O and δ^{18}O respectively. The Δ^{17}O values for spinel range between 15.8 to 23.9 ‰. The compositions of rim pyroxenes and spinels are similar and in within the compositional range of those in the core of the inclusion. All melilite analysed in this inclusion except one data point are ^{16}O-poor with δ^{17}O and δ^{18}O values ranging between -0.01 to 6.2 ‰ and -2.0 to 14 ‰ respectively, with Δ^{17}O ranging between -1.8 to -6.7 ‰. The remaining data point has an intermediate composition with δ^{17}O and δ^{18}O values of -18.4 ‰ and -13.5 ‰ respectively and a Δ^{17}O value of -11.4 ‰. The average Δ^{17}O of all melilite analysed in this CAI is -3.0 ‰. A linear regression line through all minerals in CAI 5 has a slope of 0.880 ± 0.023.

Melilite in CAIs *1, 5* and *6*, have ^{16}O-poor oxygen isotope compositions with average Δ^{17}O between -3 to -6 ‰, while spinel, pyroxene, hibonite and anorthite in the studied CAIs are more ^{16}O-rich (Δ^{17}O = -14 to -24 ‰). The oxygen isotopic compositions of minerals from NWA 4502 CAIs are generally comparable to those from Allende and Efremovka CAIs (Clayton et al., 1977; Young and Russell, 1998) and SJ101 this study, Efremovka (Aleon et al., 2005) and E44 this study) in terms of ^{16}O-enrichment in spinel, pyroxene, hibonite and isotopic heterogeneity in melilite and anorthite (Figure 3.7). Melilite in Allende inclusions appear to be slightly more ^{16}O- depleted (Δ^{17}O = -0.1 to -14) compared to those in Efremovka (Δ^{17}O = -4 to -26) and NWA 4502 (Δ^{17}O = -2 to -24) inclusions. Pyroxene has a large variation in Allende (Δ^{17}O = -0.03 to -26) compared to those in Efremovka (Δ^{17}O = -9 to -25) and NWA 4502 (Δ^{17}O = -4 to -24) which show comparable Δ^{17}O range. Spinel in Allende (Δ^{17}O = -18 to -21), Efremovka (Δ^{17}O = -12 to -21) and NWA 4502 (Δ^{17}O = -16 to -24) inclusions are ^{16}O-enriched. Anorthite compositions in NWA 4502 (Δ^{17}O = -3 to -21) and Efremovka (Δ^{17}O = -10 to -22) inclusions are very similar.

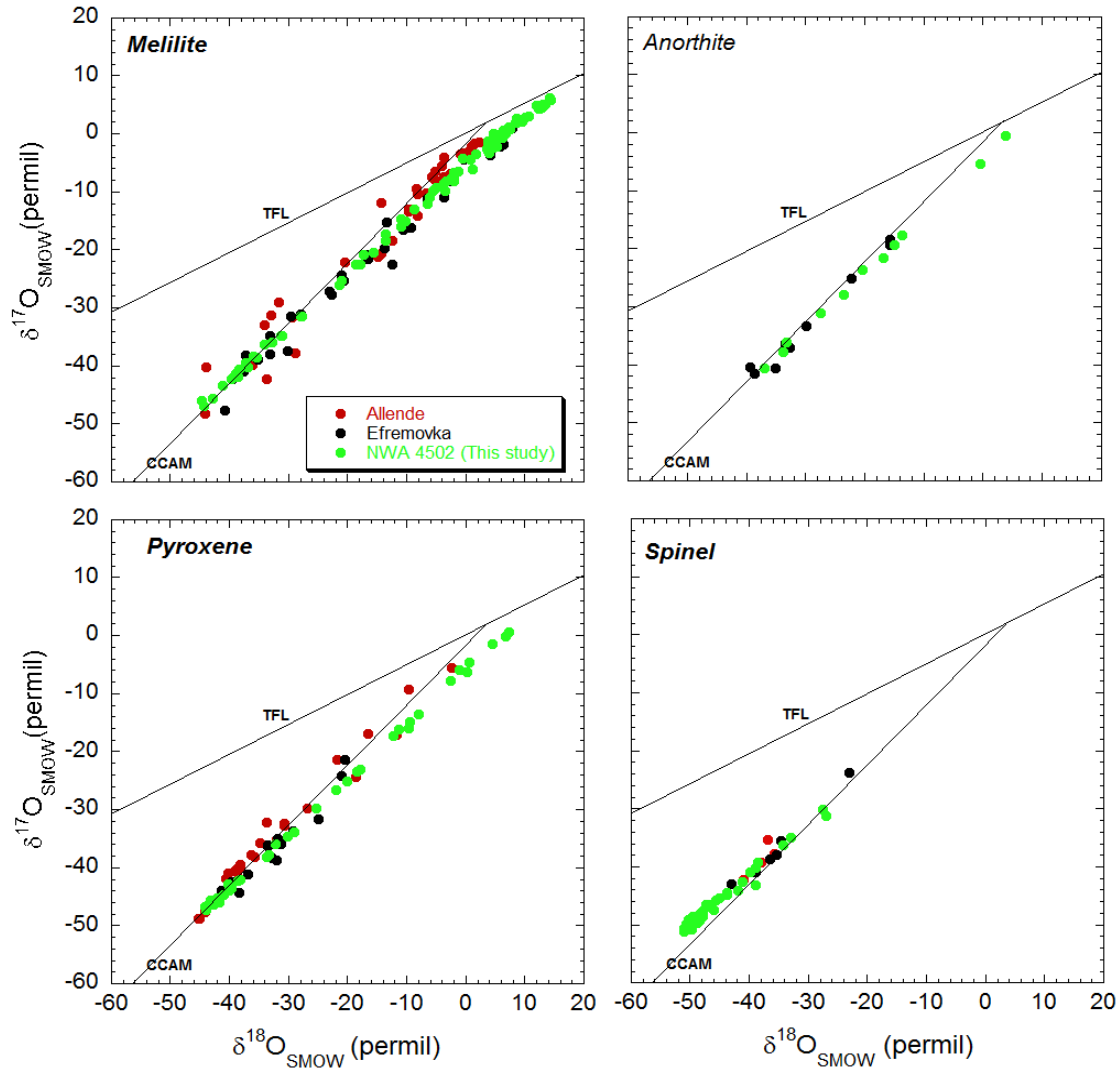

Figure 3.7: Oxygen isotopic compositions of NWA 4502 CAIs compared to other CV3 CAIs. Data obtained from Clayton and Mayeda (1977) and Young and Russell (1998) for Allende CAIs and from Aleon et al. (2005) for Efremovka CAIs.

3.1.4 Discussion

The first three-oxygen isotope analysis of CAIs by SHRIMP-SI produced results similar to those obtained by in-situ analysis using other SIMS instruments and the UV-laser ablation microprobe for UV-laser fluorination analyses.

The oxygen isotope compositions and their distribution between mineralogical phases are similar in all studied CAIs and also comparable to those found in other CV3 chondrites (Clayton and Mayeda, 1977; Young and Russell, 1998; Jones et al., 2014). There is no clear relationship between oxygen isotope composition of minerals and location except for pyroxene in CAI *6* which have more ^{16}O-depleted compositions towards the peripheries of the inclusion. Even though this SHRIMP-SI data set is consistent with general observations that the most ^{16}O-rich phases in CAIs are spinel and pyroxene while melilite and anorthite are less enriched, these data are also consistent with data reported by Yurimoto et al. (1998) who found rare ^{16}O-rich melilite ($Åk_{13-20}$) in the core portions of an Allende CAI 7R-19-1 whose texture and mineral compositions has been described to correspond to those of a coarse grained melilite-rich type B or a pyroxene-rich CTA CAI. Aléon et al. (2002), also reported oxygen isotope heterogeneity in core, mantle and rim melilite crystals in Efremovka Type A and B CAIs with ^{16}O-rich or ^{16}O-poor compositions sometimes occurring in the same CAI. Similar compositions were observed in this study to occur in the melilite crystals in CTA CAI *7* ($Åk_{2-4}$), FoB CAI 5 ($Åk_{24-30}$) and pyroxene in CTA CAI *7*. Even though there is no clear relationship between oxygen isotope composition of melilite crystals with mineral composition or type of inclusion. Melilite in CAIs can be ^{16}O-rich as demonstrated in these CAIs and other studies even though it is usually the most ^{16}O-poor phase.

There is no indication of variable mass-dependent oxygen fractionation within the NWA 4502 CAIs unlike FUN CAIs (Clayton and Mayeda, 1977; Wasserburg et al., 1977a) which show evidence of mass-dependent oxygen isotopic fractionation.

Several explanations were proposed for the processes responsible for the oxygen isotope compositions in CAIs. It has been suggested that most CAIs formed with ^{16}O-rich compositions but experienced varying levels of oxygen isotope exchange, which affected melilite and anorthite preferentially. The processes that change oxygen isotope composition include solid-gas exchange between a ^{16}O-rich solid and ^{16}O-poor gas (Clayton, 1993b), isotopic exchange between ^{16}O-rich solid and ^{16}O-poor gas during melting events (Yurimoto et al., 1998; Krot et al., 2006b) and late isotopic exchange during thermal metamorphism with a ^{16}O-poor fluid (Wasson et al., 2001). The oxygen isotope compositions in NWA 4502 CAIs agree with the suggestion that most CAIs started with ^{16}O-rich compositions however, the oxygen isotope variations cannot be simply explained due to the lack of significant mineralogical alteration and evidence of large degrees of melting.

The distribution of oxygen isotope composition of melilite in CAI *1* and *6* indicate complete resetting by oxygen isotope exchange while anorthite in CAI *1*, melilite in CAI *7*, and pyroxene in CAI 6 show partial resetting by exchange. Due to the low levels of hydrothermal alteration experienced by these CAIs, late isotopic exchange during thermal metamorphism with a ^{16}O-poor fluid can be ruled out. This leaves the options for solid-gas exchange between a ^{16}O-rich solid and ^{16}O-poor gas and isotopic exchange between ^{16}O-rich solid and ^{16}O-poor gas during melting events. The texture and structure of these inclusions indicate they are igneous and have undergone melting. Most of the mantle melilite in CAI *5* and *7* have a ^{16}O-rich composition. At the same time, the ^{16}O-depleted compositions are also found in the mantle. This suggests isotope exchange may have occurred along preferred paths such as fractures and mechanically strained or weakened zones.

The oxygen isotope data from the studied CAI phases fall along regression lines with slopes between 0.880-0961. The slope for CAIs *5* and *7* are lower than those of both the Carbonaceous Chondrite anhydrous Mineral (CCAM) line (slope = 0.94) and the Young and Russell (Y-R) line (slope = 1), those for CAI *6* are lower than the Y-R line but similar within uncertainty to CCAM line, while those for CAI *1* and *6* are similar within uncertainty to both the CCAM line and the Y-R line. Young and Russell (1998) suggested in their study that, a line with a slope of exactly 1.00 on a plot of δ^{17}O against δ^{18}O represents the primitive oxygen isotope reservoir of the early solar nebula. Most meteorites are enriched in ^{17}O and ^{18}O relative to this line, and their oxygen isotope ratios can be explained by mass fractionation or isotope exchange initiating from the primitive reservoir. The slopes of linear regression lines through minerals in the studied CAIs suggest mixing with a different end-member (^{16}O-poor environment) possibly followed by mass dependent fractionation induced by alteration in the minerals such as melilite. The similarity between the oxygen isotope systematics of NWA 4502 CAIs and Allende also demonstrates that the spread in oxygen isotope values is not due to partial alteration during parent body processing.

3.2. Al-Mg SYSTEMATICS

3.2.1. Introduction

Since the presence of live ^{26}Al was discovered in Allende (Lee et al., 1976; Lee et al., 1977) through the correlation of ^{26}Mg* (excess ^{26}Mg produced by radioactive decay) with Al/Mg in

refractory inclusions, other studies have shown widespread evidence of live ^{26}Al in a variety of chondritic material including CAIs and chondrules in carbonaceous, ordinary and enstatite chondrites (Fahey et al., 1987; Hutcheon and Hutchison, 1989; MacPherson et al., 1995; Huss et al., 2001; Kunihiro et al., 2004; Young et al., 2005; Thrane et al., 2006; Jacobsen et al., 2008; Larsen et al., 2011; MacPherson et al., 2012; Wasserburg et al., 2012; Kita et al., 2013; Bullock et al., 2015). Several studies over the years have revealed that most CAIs define a maximum initial $(^{26}Al/^{27}Al)_0$ value $[(^{26}Al/^{27}Al)_0]$ of ~5 x 10^{-5} (Lee et al., 1976; MacPherson et al., 1995) referred to as the solar "canonical" value which represents the ^{26}Al abundance in the early solar system. Many CAIs from carbonaceous chondrites have $(^{26}Al/^{27}Al)_0$ ratios that are very close to the canonical value. However, there are some inclusions which do not show the canonical value. Inferred Solar system $(^{26}Al/^{27}Al)_0$ values greater than the canonical value and referred to as the "supra-canonical" value (~5.857×10^{-5}) have been obtained for individual CAI minerals (Taylor et al., 2005; Young et al., 2005) and whole-rock CAIs (Bizzarro et al., 2004; Galy et al., 2004; Bizzarro et al., 2005; Thrane et al., 2006) from CV chondrites. A subsequent bulk CAI study by Jacobsen et al. (2008) did not support the supra-canonical value. Simon and Young (2011) using mass balance calculations to quantify the importance of open system isotopic exchange during CAI evolution have shown that both *in situ* canonical and *in situ* supra-canonical measurements can exist for an individual CAI.

It remains unclear as to whether these variations in $(^{26}Al/^{27}Al)_0$ in CV CAIs are as a result of Mg redistribution during high temperature processing in the solar nebula, or low temperature parent body processing on asteroidal bodies or whether it is due to initial ^{26}Al heterogeneity in the solar system or instrumental/analytical artefact. Due to the limited number of meteorites that contribute to the view of initial ^{26}Al heterogeneity in the solar system, the study of Al-Mg systematics in NWA 4502 CAIs may allow for a different view. Since the precise knowledge of the $(^{26}Al/^{27}Al)_0$ is important for the use of CAIs as the "time zero" age-anchor for the early Solar System, the difference between the canonical and supra-canonical values is problematic and discussions on this topic have concluded that claims of the Solar system $(^{26}Al/^{27}Al)_0$ being greater than ~5 x 10^{-5} are invalid.

3.2.2. Al-Mg measurements by Multiple Collector- Inductively Coupled Plasma- Mass Spectrometry (MC-ICP-MS)

The same CAIs from NWA 4502 that were studied for oxygen isotopes (i.e. *1, 5, 6* and *7*) were also studied for their ^{26}Al-^{26}Mg systematics. Sample preparation including mineral separation, cleaning and digestion was carried out under clean lab conditions at the Research School of Earth Sciences, Australian National University. Medium (100-275 μm) to coarse (>275 μm) sized minerals separates (1-3 mg) consisting of pure melilite, pyroxene and spinel-rich fractions, as well as less pure melilite ± anorthite ± pyroxene and spinel ± hibonite-rich fractions were repeatedly pre-cleaned in ethanol and deionised water and weighed into Savillex Teflon vials for dissolution. Samples were dissolved using a 2:1 solution of concentrated HF + HNO_3. To ensure the complete dissolution of spinel, further dissolution of spinel-rich fractions was later carried out using 3:1 solution of HF + HNO_3 in Parr acid digestion vessels. Dissolution, magnesium separation and analysis, were carried out in clean lab conditions under the supervision of Dr. Qin-Zhu Yin at the Geology Department of the University of California at Davis, following the procedure of Wasserburg et al. (2012). A 5 % aliquot of digested samples was saved for ^{27}Al-^{24}Mg measurements.

Magnesium was separated from sample matrix using Bio-Rad® AG50-x12 cation exchange resin. Mg isotopes and Al-Mg ratios were measured in solution using a Thermo Scientific Neptune Plus MC-ICP-MS. ^{27}Al/^{24}Mg ratios of CAI samples were obtained directly by measuring ^{27}Al and ^{24}Mg ion beams and calibrating them against five reference materials (BCR-2, BHVO-2, AGV-2, Peace River chondrite and San Carlos Olivine) with a well-known range of ^{27}Al/^{24}Mg ratios. Magnesium isotope ratios were bracketed against the DSM-3 standard solution with each sample solution. Mg isotope compositions are expressed as the permil deviation from the isotopic composition of the DSM-3 standard as follows:

$$\delta^{25}Mg = \left[\frac{\left({}^{25}Mg / {}^{24}Mg \right)_{sample}}{\left({}^{25}Mg / {}^{24}Mg \right)_{DSM-3}} - 1 \right] \times 1000 \quad \text{.....13}$$

$$\delta^{26}Mg = \left[\frac{\left({}^{26}Mg / {}^{24}Mg \right)_{sample}}{\left({}^{26}Mg / {}^{24}Mg \right)_{DSM-3}} - 1 \right] \times 1000 \quad \ldots\ldots 14$$

Reproducibility in terms of δ^{25}Mg and δ^{26}Mg for DSM-3 is <0.2 ‰ for each sample. Typical uncertainties on δ^{26}Mg* were <0.04 ‰. Seven to eight replicate analyses of Mg isotopic composition were carried out for 5-7 fractions from each CAI.

3.2.3. Al-Mg Isotope compositions

All data obtained on Al-Mg systematics analysed in CAIs 1, 5, 6 and 7 are summarised in Table 3.3. ^{27}Al/^{24}Mg is directly measured following the procedure described in the Methods Section. The columns labelled δ^{26}Mg and δ^{25}Mg are the permil (‰) differences in the measured values relative to the terrestrial standard DSM-3 with their associated errors. Mass dependent fractionation can be removed from the ^{26}Mg/^{24}Mg ratio assuming a functional relationship between ^{25}Mg/^{24}Mg and ^{26}Mg/^{24}Mg. For this work, a power law is used. The residual in the ^{26}Mg/^{24}Mg ratio is typically referred to as δ^{26}Mg* and this is typically related to excess ^{26}Mg (^{26}Mg*) derived from ^{26}Al decay.

Magnesium isotope compositions of mineral separates of all the studied CAIs are fractionated. Minerals in the studied CAIs are typically enriched in heavy magnesium isotopes with respect to the terrestrial standard DSM-3 (i.e. positive δ^{25}Mg). CAI *1* and *6* have consistent δ^{25}Mg values and lie within a restricted band between δ^{25}Mg of approximately 4.7 and 7.3 ‰. A notable feature of CAIs *5* and *7* is variable δ^{25}Mg between mineral fractions. CAI *5* shows values <-0.5 to 0.1 ‰ in some pyroxene and melilite-rich fractions (i.e. favouring lighter magnesium isotopes) to a spinel-rich fraction which are more enriched in heavier isotopes. CAI *7* has variations in δ^{25}Mg from ~ -0.2 ‰ in pyroxene-rich fractions to 13 ‰ in spinel ± hibonite-rich fraction. Typically, refractory inclusions have a limited internal range in Mg isotope fractionation (0.5-1 ‰ per a.m.u.), as shown in Figure 3.8 for CAIs *1, 5* and *6*. CAI *7* has an internal range of 14 ‰ per a.m.u and is quite unusual.

All CAIs contain excess ^{26}Mg (^{26}Mg*) that is correlated with ^{27}Al/^{24}Mg ratio. ^{26}Mg* of each CAI was measured to a precision of <0.04 ‰ (2σ). Melilite in CAI *1* has a ^{27}Al/^{24}Mg ratio of ~8 with δ^{26}Mg* of 3 ‰, whereas less pure melilite fractions (melilite ± anorthite ± pyroxene

±spinel) which have slightly lower $^{27}Al/^{24}Mg$ ratios of ~5 with $\delta^{26}Mg^*$ of ~2 ‰. Spinel-rich fractions have the lowest $^{27}Al/^{24}Mg$ ratios of ~3 in this inclusion with corresponding $\delta^{26}Mg^*$ of ~1 ‰.

Table 3.3: Al-Mg isotope compositions of NWA 4502 CAIs.

CAI	Fraction	$^{27}Al/^{24}Mg$	2σ	$\delta^{26}Mg$	2σ	$\delta^{25}Mg$	2σ	$\delta^{26}Mg^*$	2σ	*n*
6	Melilite	7.92	0.08	11.412	0.010	4.645	0.005	2.282	0.008	8
	Melilite	7.32	0.07	12.717	0.010	5.047	0.005	2.788	0.007	8
	Melilite	7.34	0.07	11.916	0.015	4.796	0.009	2.486	0.008	8
	Melilite>Pyroxene	5.60	0.06	10.811	0.007	4.508	0.004	1.953	0.010	8
	Melilite>Pyroxene>spinel	2.81	0.03	9.958	0.008	4.563	0.007	1.000	0.013	8
	Pyroxene	3.33	0.03	9.462	0.006	4.375	0.005	0.874	0.010	8
7	Melilite	31.18	0.31	17.635	0.008	2.794	0.005	12.094	0.007	8
	Melilite	33.15	0.33	18.535	0.006	3.026	0.006	12.530	0.009	8
	Melilite	30.93	0.31	20.297	0.006	4.462	0.004	11.446	0.008	8
	Spinel>hibonite	11.79	0.12	30.621	0.006	13.212	0.005	4.486	0.006	8
	Melilite>Pyroxene	6.23	0.06	0.389	0.008	-0.884	0.005	2.122	0.009	8
	Pyroxene	3.36	0.03	0.643	0.008	-0.197	0.005	1.030	0.010	8
1	Melilite	7.77	0.08	17.262	0.009	7.306	0.006	2.872	0.005	7
	Melilite>anorthite	5.54	0.06	16.404	0.021	7.319	0.010	2.001	0.006	7
	Melilite>Pyroxene	4.66	0.05	16.298	0.007	7.417	0.006	1.712	0.007	7
	Melilite>Spinel	5.57	0.06	16.545	0.014	7.381	0.007	2.024	0.006	7
	Spinel>Melilite	5.42	0.05	15.882	0.007	7.167	0.007	1.783	0.009	7
	Spinel	2.67	0.03	15.435	0.026	7.357	0.014	0.975	0.005	7
	Spinel	2.81	0.03	15.478	0.013	7.386	0.009	0.962	0.005	7
5	Melilite	1.70	0.02	0.615	0.014	0.042	0.007	0.533	0.010	7
	Melilite>Pyroxene	1.46	0.01	0.234	0.013	-0.140	0.008	0.492	0.013	7
	Melilite>Pyroxene	1.75	0.02	0.620	0.016	0.026	0.009	0.565	0.010	7
	Spinel	1.64	0.02	0.662	0.025	0.083	0.015	0.501	0.006	7
	Pyroxene	1.08	0.01	-0.276	0.011	-0.323	0.011	0.349	0.016	6

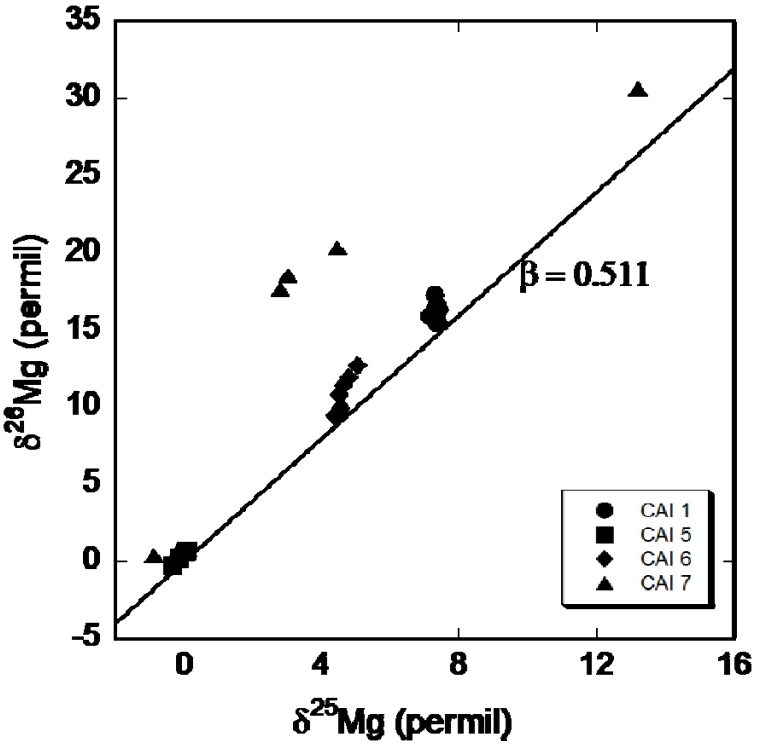

Figure 3.8: $\delta^{26}Mg$ vs $\delta^{25}Mg$ plot for NWA 4502 CAIs.

Melilite fractions in CAI *6* show $^{27}Al/^{24}Mg$ ratios values of 7-8 with $\delta^{26}Mg^*$ values of 2-3 ‰. Melilite ± pyroxene ± spinel fractions as well as pyroxene fractions have lower $^{27}Al/^{24}Mg$ ratios ranging from 3-6 with corresponding $\delta^{26}Mg^*$ values of 1-2 ‰. CAI *5* has the lowest $^{27}Al/^{24}Mg$ ratios (<2) for all mineral fractions. Their $\delta^{26}Mg^*$ values range between of ~0.3-0.6 ‰. Melilite in CAI *7* has relatively high $^{27}Al/^{24}Mg$ ratios compared to those in the other CAIs which is not unexpected given the abundance of hibonite in its core. $^{27}Al/^{24}Mg$ ratios are up to 33 and $\delta^{26}Mg^*$ values are between 11-13 ‰. Spinel ± hibonite fractions have $^{27}Al/^{24}Mg$ ratios of ~12 with $\delta^{26}Mg^*$ values ~4, while pyroxene fractions have $^{27}Al/^{24}Mg$ ratios of ~3 with a corresponding $\delta^{26}Mg^*$ of 1 ‰.

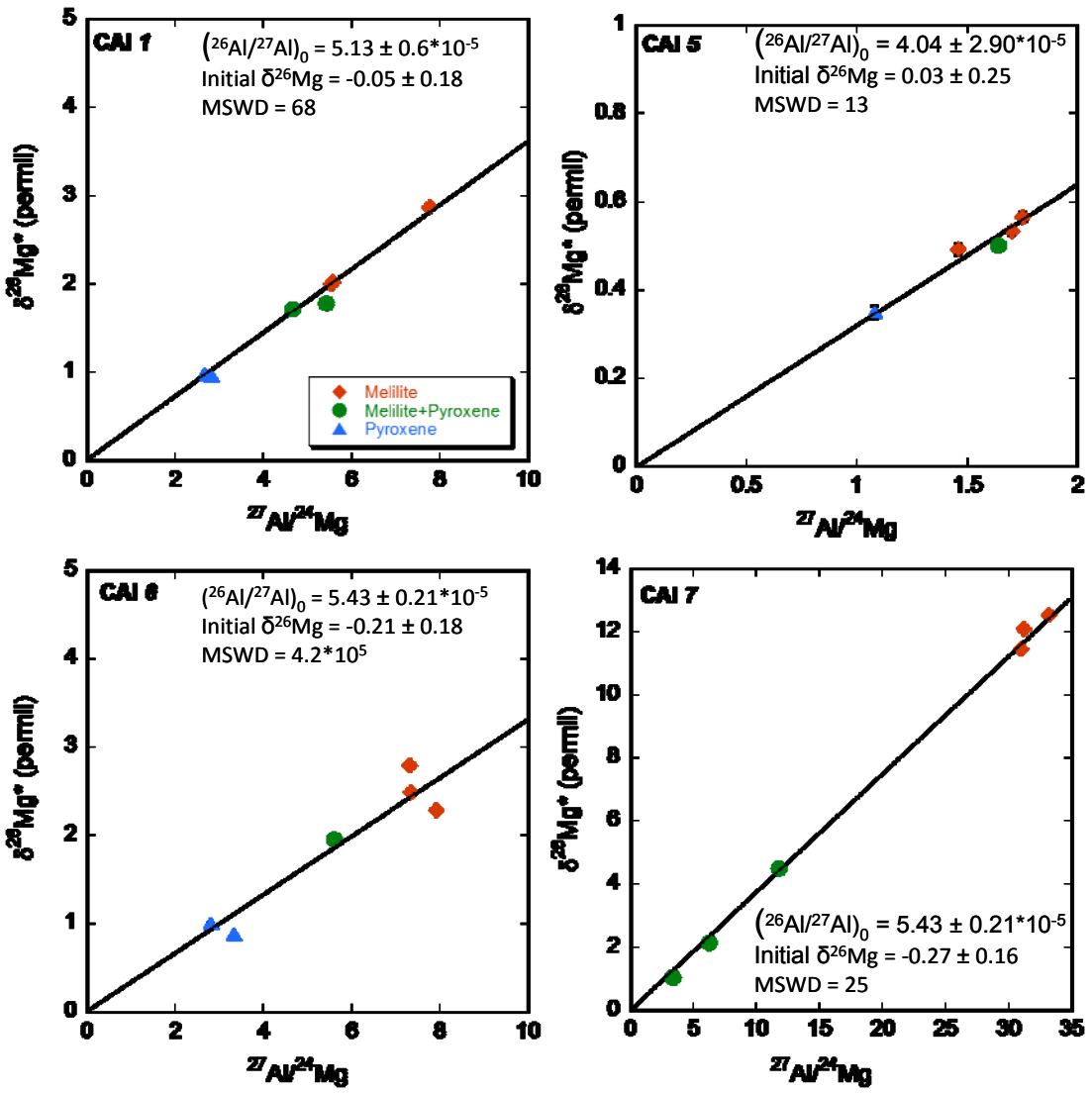

Figure 3.9: Plots of $\delta^{26}Mg^*$ against $^{27}Al/^{24}Mg$ for CAI *7*, *6*, *5* and *1*.

Internal isochron regressions for each CAI shows excess scattering (MSWD = 13-4.2x10^5; Figure 3.9). The degree of scattering varies between the CAIs and is most pronounced in CAI *6* to the extent that isochron regression with the available data appears impractical. The slope of a regression line through the data on a $^{26}Mg/^{24}Mg$ versus $^{27}Al/^{24}Mg$ plot gives the initial $^{26}Al/^{27}Al$ ratio, $(^{26}Al/^{27}Al)_0$, at the time the object formed. Isochrons for CAIs *1*, *5*, *6* and *7* yield initial $(^{26}Al/^{27}Al)_0$ of 5.13 ± 0.61 MSWD = 68, 4.04 ± 2.09 MSWD = 13, 5.43 ± 0.21 x 10^{-5} MSWD = 4.2x10^5 and 5.43 ± 0.37 x 10^{-5} MSWD = 25, respectively. The precision on the initial ratio for CAI *1* improves (5.24 ± 0.38 MSWD = 19) after the exclusion of one data point which falls

below the regression line. CAI *7* has an intercept (^{26}Mg*) that is resolvably negative at Al/Mg =0 with a value of -0.27 ± 0.16 ‰. This is similar to recently acquired data for the Allende CAI Egg-3 (Wasserburg et al., 2012).

3.2.4 Discussion

The search for evidence of live ^{26}Al has been carried out mainly on refractory inclusions from CV3 chondrites. Over the course of the years, data has been collected for refractory inclusions in Allende, Leoville, Vigarano, Efremovka, Grosnaja, and Ningqiang (Hsu et al., 2003; Taylor et al., 2005; Young et al., 2005; Jacobsen et al., 2008; Larsen et al., 2011; MacPherson et al., 2012; Wasserburg et al., 2012). From a review of these studies and others, Kita et al. (2013) demonstrated that high-precision bulk Al-Mg isotope measurements of CAIs from CV carbonaceous chondrites in several laboratories define a bulk ^{26}Al-^{26}Mg isochron with an $(^{26}Al/^{27}Al)_0$ of approximately 5.25×10^{-5} referred to as the canonical value and the internal isochrons of igneous CV CAIs show a range of $(^{26}Al/^{27}Al)_0$, $(4.2–5.2) \times 10^{-5}$.

Similar results were obtained for NWA 4502 CAIs. NWA 4502 CAIs contain levels of ^{26}Mg* that correspond to $(^{26}Al/^{27}Al)_0$, $(4.04 - 5.43) \times 10^{-5}$ consistent with the canonical value. The $(^{26}Al/^{27}Al)_0$ data obtained in this study provide no evidence of an initial ratio significantly greater than the canonical value (i.e., supra-canonical).

The excess scattering observed in the correlations between δ^{26}Mg* and ^{27}Al/^{24}Mg suggests that the Al-Mg isotope systematics in NWA 4502 CAIs may have been affected by secondary disturbance. In spite of the differences in the history of secondary processes both on the parent body and on the surface of the Earth, the consistency of $(^{26}Al/^{27}Al)_0$ in CAIs suggests broad-scale homogeneity in ^{26}Al in the CAI-forming region of the nebula. These data further supports the uniformity of the canonical ^{26}Al/^{27}Al value in CAIs from various CV chondrites.

3.3. Rb-Sr SYSTEMATICS

3.3.1. Introduction

The Rb-Sr isotopic system has been used to constrain the evolution of the early solar system since Papanastassiou and Wasserburg (1969) first applied it to basaltic achondrites. The Rb-Sr system as a geochronometer has since been applied to CAIs to better constrain the initial $^{87}Sr/^{86}Sr$ isotopic ratio which has significance both as a reference point for Sr isotope evolution in terrestrial materials and as a basis for model age determinations used for estimating the relative times of condensation of solar system bodies (Gray et al., 1973; Tatsumoto et al., 1976; Podosek et al., 1991; Halliday and Porcelli, 2001; Moynier et al., 2010; Moynier et al., 2012; Hans et al., 2013). The intercept value of the Rb-Sr isochron for Allende CAIs known as ALL (Gray et al., 1973) provides the lowest initial $^{87}Sr/^{86}Sr$ ratio (0.69877) so far of any solar system material. Other studies of Allende CAIs have subsequently turned out slightly higher ratios (Podosek et al., 1991; Hans et al., 2013). Nonetheless, the low initial $^{87}Sr/^{86}Sr$ ratios of CAIs are consistent with them being the oldest solar system objects. As such, strontium isotope compositions of CAIs are thought to approximate the initial $^{87}Sr/^{86}Sr$ of the solar system, and serve as a reference point in the models of Rb-Sr isotopic evolution of planetary reservoirs. There is evidence for isotopic disturbance of the Rb-Sr system in Allende CAIs (Gray et al., 1973; Tatsumoto et al., 1976; Moynier et al., 2010). This disturbance has been interpreted to reflect the effect of secondary processing occurring on the Allende parent body. Even though abundant data is available for Allende CAIs, little is known about CAIs from other CV chondrites with different histories of secondary processes.

CAIs exhibit clearly resolved positive $^{84}Sr/^{86}Sr$ anomalies relative to the Sr standard NBS 987, terrestrial rock standards eucrites and angrites (Moynier et al., 2012; Hans et al., 2013; Paton et al., 2013). The difference in $^{84}Sr/^{86}Sr$ between CV chondrites and terrestrial rocks allows for the use of this isotopic ratio as a tracer for Sr migration.

3.3.2. Rb-Sr measurements by Thermal Ionization Mass Spectrometry (TIMS)

Rb-Sr analysis was carried out on melilite and pyroxene-rich mineral separates (3-8 mg) of CAIs *1*, *5*, *6* and *7* prepared by repeated pre-cleaning in ethanol, acetone and water, and acid leaching in cold HNO_3 with sonication (W1) and hot HNO_3 and HCl (W2). Acid leached residues were dissolved in a concentrated HF-HNO_3 mixture at 110°C on a hotplate. After

digestion, Pb and U were extracted for U-Pb dating and the bulk solution that contained Rb and Sr was collected. The collected solutions were split into two aliquots, one of which was spiked with ^{85}Rb-^{84}Sr mixed tracer.

Rubidium and Sr were separated from both unspiked and spiked aliquots using 50 µl columns packed first with about 20 µl of pre-cleaned Eichrom pre-filter resin and then topped up with about 30 µl Eichrom Sr.Spec resin. Before samples were loaded onto the columns, Rb and Sr were sequentially washed off the column in 6M HCl, water and 0.02M HNO_3. Rubidium was washed off the column in 3M HNO_3. The bulk wash was collected and 10 µl aliquots were dried down with H_3PO_4 for Rb analysis by TIMS. Strontium was eluted in 0.02M HNO_3, and dried down with H_3PO_4 for analysis by TIMS.

Strontium was loaded on to single Re evaporation filaments previously outgassed at 4 A for 1.5 hours. Samples were mixed with Ta-phosphate activator solution (Charlier et al., 2006) and loaded on to a filament at 1.0 A. Samples were dried steadily at 0.1 A increments every 30 s to 2.0 A. The filament is flashed until a brief dull glow at >2.0 A. Rubidium is loaded by the same procedure using Sigma-Aldrich silica gel (Huyskens et al., 2012). Total procedure blank is 2.2 pg Sr and 0.15 pg Rb. Strontium was analysed by Triton Plus TIMS and Rb was analysed by the modified Finnigan MAT 261 TIMS at the Sensitive and Precise Isotopic Dating of Earth's and Extraterrestrial Rocks (SPIDE^{2}R) lab at the Research School of Earth Sciences, ANU. Results of repeated measurements of SRM 987 Sr isotope standard during analytical sessions are shown in Figure 3.10. The Sr data are normalised to ^{88}Sr/^{86}Sr=8.375209 and the ^{87}Sr/^{86}Sr values are reported relative to 0.71025 in the SRM 987 standard.

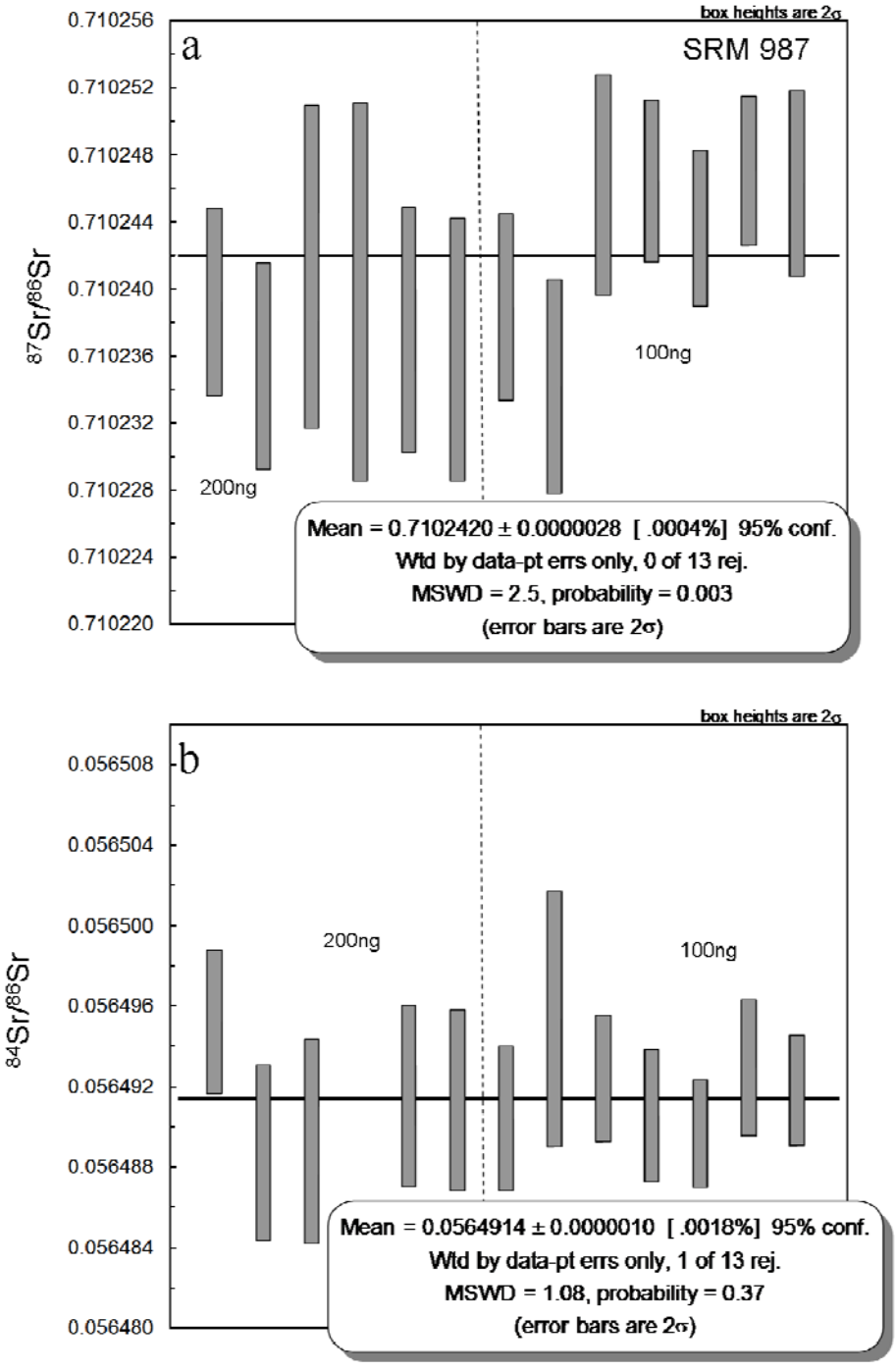

Figure 3.10: Weighted mean plots of $^{87}Sr/^{86}Sr$ and $^{84}Sr/^{86}Sr$ for repeated measurements of SRM 987 Sr isotope standard (n=13). The certified values for SRM 987 are $^{87}Sr/^{86}Sr$ = 0.71034 ± 0.00026 $^{84}Sr/^{86}Sr$ = 0.05655 ± 0.00014.

3.3.3 Rb-Sr Isotope compositions

^{87}Rb-^{87}Sr systematics

The Rb-Sr isotopic data for studied CAIs are listed in Table 3.4. Rubidium and Sr were easily extracted from the CAIs by mild leaching. The first cold acid leaching steps (W1) extracts 85-90 % of Sr with concentrations between 80-250 ppm. The second hot acid steps (W2) contain 6-8 % of Sr with concentrations between 2-16 ppm and residues contain only 3-7 % of total Sr concentrations between 0.6-9 ppm. Rb concentrations are between 0.8-12 ppb in the residues and 11-74 ppb in the washes. Total Sr concentrations in both melilite-rich and pyroxene–rich fractions of all studied CAIs are between 100-300 ppm while Rb concentrations are between 0.1-1.5 ppm.

For all the analysed samples, ^{87}Rb/^{86}Sr ratios are generally low and show limited variation both in the washes and in the residues. As such, no useful chronological constraints are to be expected from fitting isochrons to the data, especially considering the possibility of fractionation between Rb and Sr induced by leaching. The purpose of acid leaching of samples before sample dissolution is to preferentially dissolve relatively less-resistant phases (e.g., alteration phases such as nepheline and sodalite) that are expected to have higher Rb/Sr ratios, leaving in the residues the more resistant phases having lower Rb/Sr ratios and thus facilitating accurate determination of initial ^{87}Sr/^{86}Sr. It is indeed observed that, for all samples, the acid wash residues have comparably low Rb/Sr ratios as the leachates. ^{87}Rb/^{86}Sr ratios range from 0.0002-0.04 for washes and 0.001-0.05 for residues of melilite-rich fractions. Those for pyroxene-rich fractions are between 0.0004-0.03 for washes and 0.002-0.01 for residues.

A plot of measured ^{87}Sr/^{86}Sr against ^{87}Rb/^{86}Sr ratios reveals complex open system behaviour. The Rb-Sr data do not form a single linear array in the isochron coordinates. The ^{87}Sr/^{86}Sr ratios of all washes and two residues do not correlate with their ^{87}Rb/^{86}Sr (Figure 3.11). First washes (W1) have low ^{87}Rb/^{86}Sr and elevated ^{87}Sr/^{86}Sr ratios; second washes (W2) have higher ^{87}Rb/^{86}Sr but have a lot of scatter in ^{87}Sr/^{86}Sr ratios while residues have the highest ^{87}Rb/^{86}Sr and lowest ^{87}Sr/^{86}Sr ratios. The Rb-Sr system seems to be most disturbed in CAI *1* for which the leachate fractions W1 and W2 as well as one residue plot far from the isochron.

Table 3.4: Rb-Sr data for NWA 4502 CAIs.

Sample	Acid step	Rb ng	Sr ng	$^{87}Rb/^{86}Sr$	2σ	$^{87}Sr/^{86}Sr$	2σ	$(^{87}Sr/^{86}Sr)_0$	2σ
CAI *6* Pyroxene	W1	0.026	108.8	0.000696	0.000013	0.711522	0.000007	0.711476	0.000007
	Residue	0.015	6.0	0.007365	0.000410	0.699113	0.000014	0.698628	0.000056
CAI *6* Melilite	W1	0.015	289.9	0.000154	0.000004	0.703060	0.000006	0.703050	0.000007
	Residue	0.003	0.4	0.018413	0.003322	0.699063	0.000048	0.697851	0.000440
CAI *7* Pyroxene	W1	0.031	251.9	0.000357	0.000006	0.703227	0.000008	0.703204	0.000008
	Residue	0.004	1.7	0.006271	0.002668	0.699512	0.000022	0.699099	0.000352
CAI *7* Melilite	W1	0.077	115.4	0.001927	0.000019	0.710750	0.000007	0.710623	0.000008
	Residue	0.032	1.7	0.053803	0.001452	0.699143	0.000010	0.695601	0.000191
CAI *1* Pyroxene	W1	0.041	94.0	0.001261	0.000014	0.714030	0.000013	0.713947	0.000013
	W2	0.010	9.0	0.003175	0.000111	0.704421	0.000007	0.704212	0.000016
	Residue	0.008	11.9	0.001841	0.000269	0.698971	0.000011	0.698850	0.000037
CAI *1* Melilite	W1	0.122	404.0	0.000872	0.000007	0.700085	0.000015	0.700028	0.000015
	W2	0.020	26.2	0.002245	0.000034	0.699479	0.000008	0.699331	0.000009
	Residue	0.022	26.9	0.002409	0.000082	0.704689	0.000015	0.704531	0.000018
CAI *5* Pyroxene	W1	0.085	33.0	0.007468	0.000127	0.703565	0.000008	0.703074	0.000018
	W2	0.015	1.3	0.033376	0.000885	0.702669	0.000033	0.700472	0.000121
	Residue	0.006	9.3	0.001806	0.000200	0.698990	0.000011	0.698871	0.000029
CAI *5* Melilite	W1	0.091	114.6	0.002287	0.000020	0.700579	0.000008	0.700429	0.000008
	W2	0.018	1.4	0.036200	0.000984	0.700228	0.000019	0.697844	0.000131
	Residue	0.004	8.5	0.001321	0.000258	0.698969	0.000012	0.698882	0.000036

$^{87}Sr/^{86}Sr$: Measured ratios adjusted to the nominal value $^{87}Sr/^{86}Sr = 0.71025$ for SRM 987 standard (Hans et al., 2013).
$(^{87}Sr/^{86}Sr)_0$: Initial Sr values corrected for the insitu decay of ^{87}Rb.

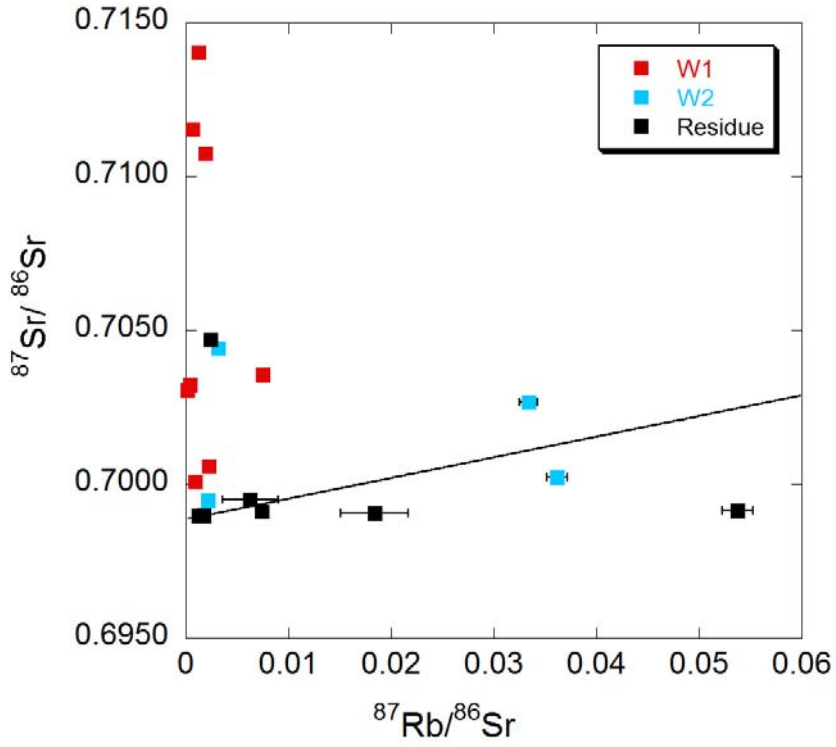

Figure 3.11: $^{87}Sr/^{86}Sr$ vs $^{87}Rb/^{86}Sr$ plot for leachates and residues of acid washed mineral separates from NWA 4502 CAIs. The black solid line is a 4.567 Ga reference isochron.

Initial $^{87}Sr/^{86}Sr$ ratios

The first acid leaching steps (W1) yields measured $^{87}Sr/^{86}Sr$ ratios between 0.700579 ± 0.000008 and 0.71403 ± 0.000013 while those of the second acid steps (W2) have $^{87}Sr/^{86}Sr$ values between 0.699479 ± 0.000008 and 0.704421 ± 0.000007. The residues have measured $^{87}Sr/^{86}Sr$ between 0.698969 ± 0.000012 and 0.704689 ± 0.000015.

In spite of the disturbance of the Rb-Sr system, the initial $^{87}Sr/^{86}Sr$ of NWA 4502 CAIs can be constrained with good precision using two of the CAIs due to low $^{87}Rb/^{86}Sr$ in some of the residues with the lowest measured $^{87}Sr/^{86}Sr$ (Figure 3.12).

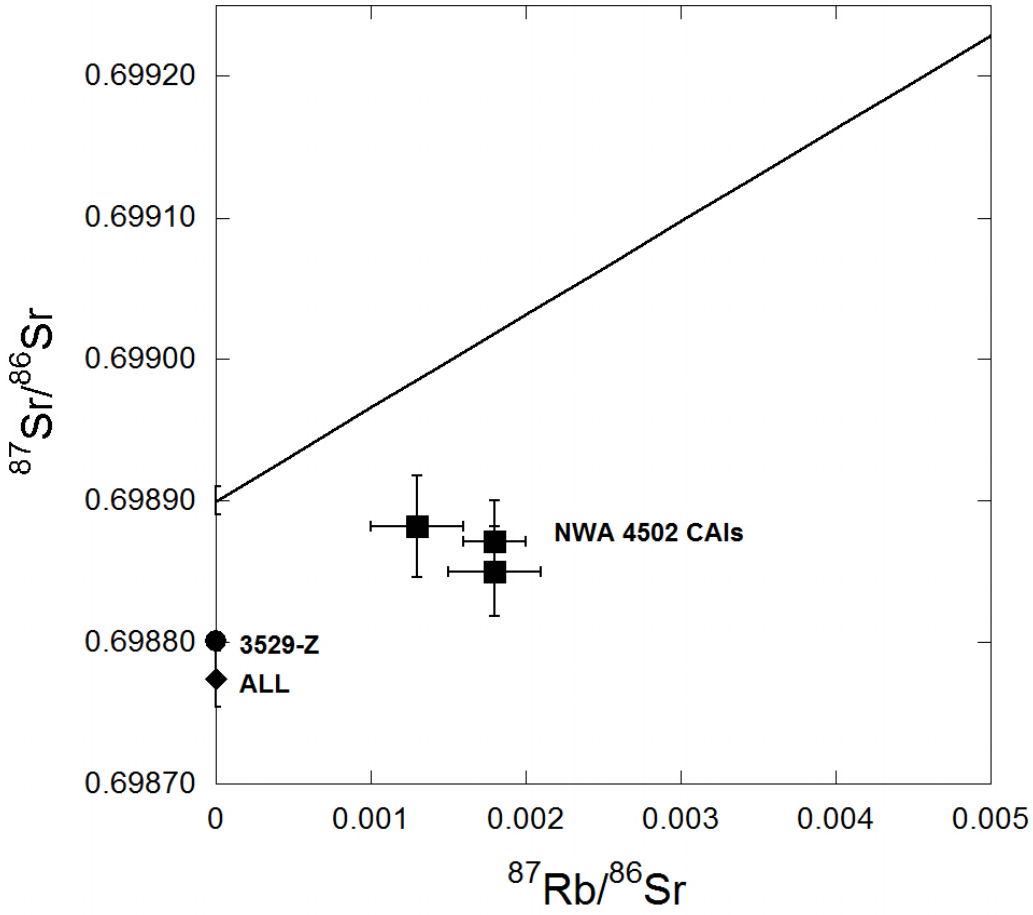

Figure 3.12: $^{87}Sr/^{86}Sr$ vs $^{87}Rb/^{86}Sr$ plot for three NWA 4502 CAI residues with the lowest initial $^{87}Sr/^{86}Sr$ compositions shown together with initial $^{87}Sr/^{86}Sr$ values from the previously published data for Allende CAIs; ALL (Gray et al., 1973) and 3529-Z (Podosek et al., 1991). The black solid line is a 4.567 Ga reference isochron, constrained to pass through $^{87}Sr/^{86}Sr$ of 0.69890 for reference.

The pyroxene-rich fraction from the type B CAI *1*, and both the melilite and pyroxene-rich fractions from forsterite-bearing type B CAI *5* have measured $^{87}Sr/^{86}Sr$ of 0.698969-0.698990, among the lowest values reported so far, and $^{87}Rb/^{86}Sr$ of 0.0013-0.0018. Values for initial $^{87}Sr/^{86}Sr$, corrected for in-situ growth by decay of Rb for CAI residues are summarized in Table 3.5. The initial $^{87}Sr/^{86}Sr$ of these fractions of 0.698850-0.698882 are slightly higher than the value (0.698774 ± 0.000022) reported for the Allende CAI D7 (Gray et al., 1973) and 0.698808 ± 0.000020 reported for the Allende CAI 3529-Z, (Podosek et al., 1991) but lower than the the

corrected values of 0.698930 ± 0.000014 for Efremovka CAI E38 (Nyquist et al., 2003) and 0.698935 ± 0.000009 for Allende and NWA 2364 CAIs (Hans et al., 2013) (Figure 3.13).

A linear regression of NWA 4502 data, calculated using IsoPlot plot on a reference isochron line, yielding an initial $^{87}Sr/^{86}Sr$ of 0.698886 ± 0.000026 which is comparable to $(^{87}Sr/^{86}Sr)_{ALL}$ = 0.698774 ± 0.000022.

Table 3.5: Comparison of $^{87}Sr/^{86}Sr$ data to results from previous studies.

Sample	$^{87}Sr/^{86}Sr$	2σ	$(^{87}Sr/^{86}Sr)_0$	2σ
This study				
CAI *1* Pyroxene	0.698971	0.000011	0.698850	0.000037
CAI *5* Pyroxene	0.698990	0.000011	0.698871	0.000029
CAI *5* Melilite	0.698969	0.000012	0.698882	0.000036
Other studies				
D7[a]	0.698882	0.000022	0.698774	0.000022
3529-Z[b]	0.698916	0.000020	0.698808	0.000020

a: Gray et al., 1973; b: Podosek et al,1991

$^{84}Sr/^{86}Sr$ ratios

The $^{84}Sr/^{86}Sr$ ratios of acid leachates and residues of studied CAIs are listed in Table 3.6. Figure 3.14 shows a plot of $\varepsilon^{84}Sr$ values of acid washed residues together with those for terrestrial samples, angrites and CAI data from Hans et al. (2013). CAIs show clearly resolved ^{84}Sr excesses compared to terrestrial samples and angrites. The average $^{84}Sr/^{86}Sr$ value in NWA 4502 CAIs corresponds to $\varepsilon^{84}Sr = +1.3 \pm 0.8$, consistent with those reported for other CAIs (Moynier et al., 2012; Hans et al., 2013; Paton et al., 2013). This value is didtinctly higher than those for angrites $\varepsilon^{84}Sr = 0.01 \pm 0.19$, eucrites $\varepsilon^{84}Sr = 0.01 \pm 0.12$ and terrestrial samples $\varepsilon^{84}Sr = -0.02 \pm 0.07$ reported by Hans et al. (2013). This indicates an apparent excess in ^{84}Sr for CAIs. The distinct $^{84}Sr/^{86}Sr$ isotope ratio of CAIs to that from other planetary materials and terrestrial samples offers a means of tracing Sr exchange between these environments.

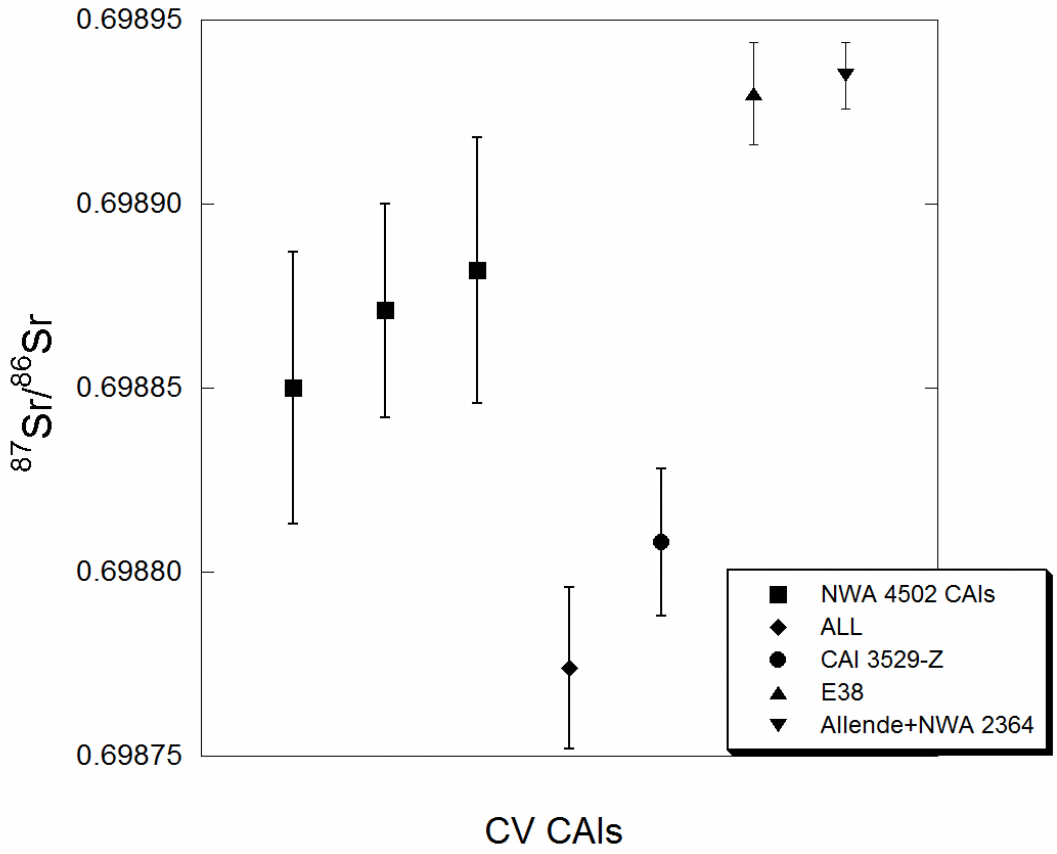

Figure 3.13: Initial $^{87}Sr/^{86}Sr$ plot comparing three NWA 4502 CAI residues with the lowest initial $^{87}Sr/^{86}Sr$ compositions with initial $^{87}Sr/^{86}Sr$ values from the previously published data for Allende CAIs; ALL (Gray et al., 1973), CAI 3529-Z (Podosek et al., 1991), Efremovka CAI E38 (Nyquist et al., 2003) and Allende CAI All-1-6 and NWA 2346 A-ZH-12 (Hans et al., 2013).

Table 3.6: $^{84}Sr/^{86}Sr$ data for NWA 4502 CAIs.

Sample description	Leaching step	$^{84}Sr/^{86}Sr$	2σ	ε ^{84}Sr	2σ
CAI *6* Pyroxene	W1	0.056494	0.000002	0.3	0.4
	Residue	0.056504	0.000007	2.1	1.3
CAI *6* Melilite	W1	0.056496	0.000002	0.7	0.3
	Residue	0.056508	0.000028	2.8	5.0
CAI *7* Pyroxene	W1	0.056498	0.000002	1.1	0.4
	Residue	0.056498	0.000021	1.1	3.7
CAI *7* Melilite	W1	0.056492	0.000003	0.002	0.533
	Residue	0.056499	0.000005	1.2	0.9
CAI *1* Pyroxene	W1	0.056498	0.000006	0.9	1.1
	W2	0.056499	0.000010	1.1	1.8
	Residue	0.056497	0.000004	0.8	0.8
CAI *1* Melilite	W1	0.056497	0.000003	0.8	0.5
	W2	0.056496	0.000004	0.7	0.6
	Residue	0.056495	0.000015	0.6	2.6
CAI *5* Pyroxene	W1	0.056497	0.000003	0.8	0.5
	W2	0.056487	0.000018	-0.9	3.2
	Residue	0.056500	0.000006	1.4	1.1
CAI *5* Melilite	W1	0.056499	0.000002	1.2	0.4
	W2	0.056503	0.000012	1.8	2.2
	Residue	0.056499	0.000008	1.1	1.4

For the first time, this study employs the $^{84}Sr/^{86}Sr$ isotopic variations as a means to investigate the cause of the open system behaviour observed in the Rb-Sr system. Figure 3.15a is a plot of $^{84}Sr/^{86}Sr$ against $^{87}Sr/^{86}Sr$ ratios for acid leachates and residues of studied CAIs. The $^{84}Sr/^{86}Sr$ values for the first leachates (W1) and second leachates (W2) are lower compared to those of the residues. First leachates have values ranging between 0.0564922 and 0.0564982 with an average $\varepsilon^{84}Sr = 0.73 \pm 0.28$. Second leachates have $^{84}Sr/^{86}Sr$ values between 0.0564870 and 0.0565025 with an average $\varepsilon^{84}Sr = 0.68 \pm 1.17$, while residues have the highest $^{84}Sr/^{86}Sr$ values

ranging between 0.0564982 and 0.0565082 with an average $\varepsilon^{84}Sr$ = 1.39 ± 0.52. Two first leachates (W1) of pyroxene-rich and melilite-rich fractions of CAIs 6 and 7 respectively and a second leachate (W2) of a pyroxene-rich fraction of CAI 5 have $\varepsilon^{84}Sr$ values of 0.3 ± 0.4 and 0.0 ± 0.5 and -0.9 ± 3.2 similar to, and within error of terrestrial $\varepsilon^{84}Sr$ values (Figure 3.15b). The data therefore indicate that the NWA 4502 CAIs have exchanged with the terrestrial environment.

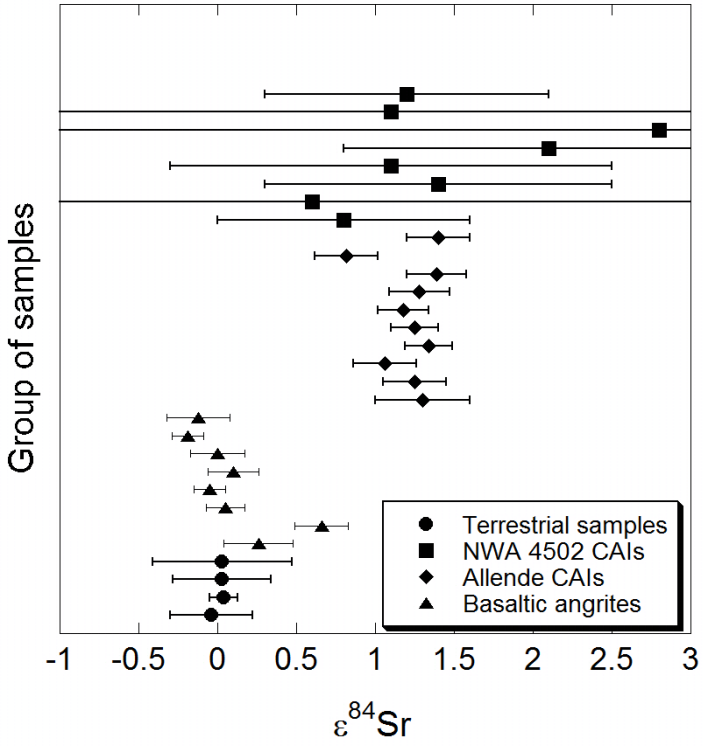

Figure 3.14: $\varepsilon^{84}Sr$ values of NWA 4502 CAIs plotted with terrestrial samples, basaltic angrites and Allende CAIs analysed by Hans et al. (2013). $\varepsilon^{84}Sr$ values were calculated relative to $^{84}Sr/^{86}Sr$ measured for the SRM 987 standard.

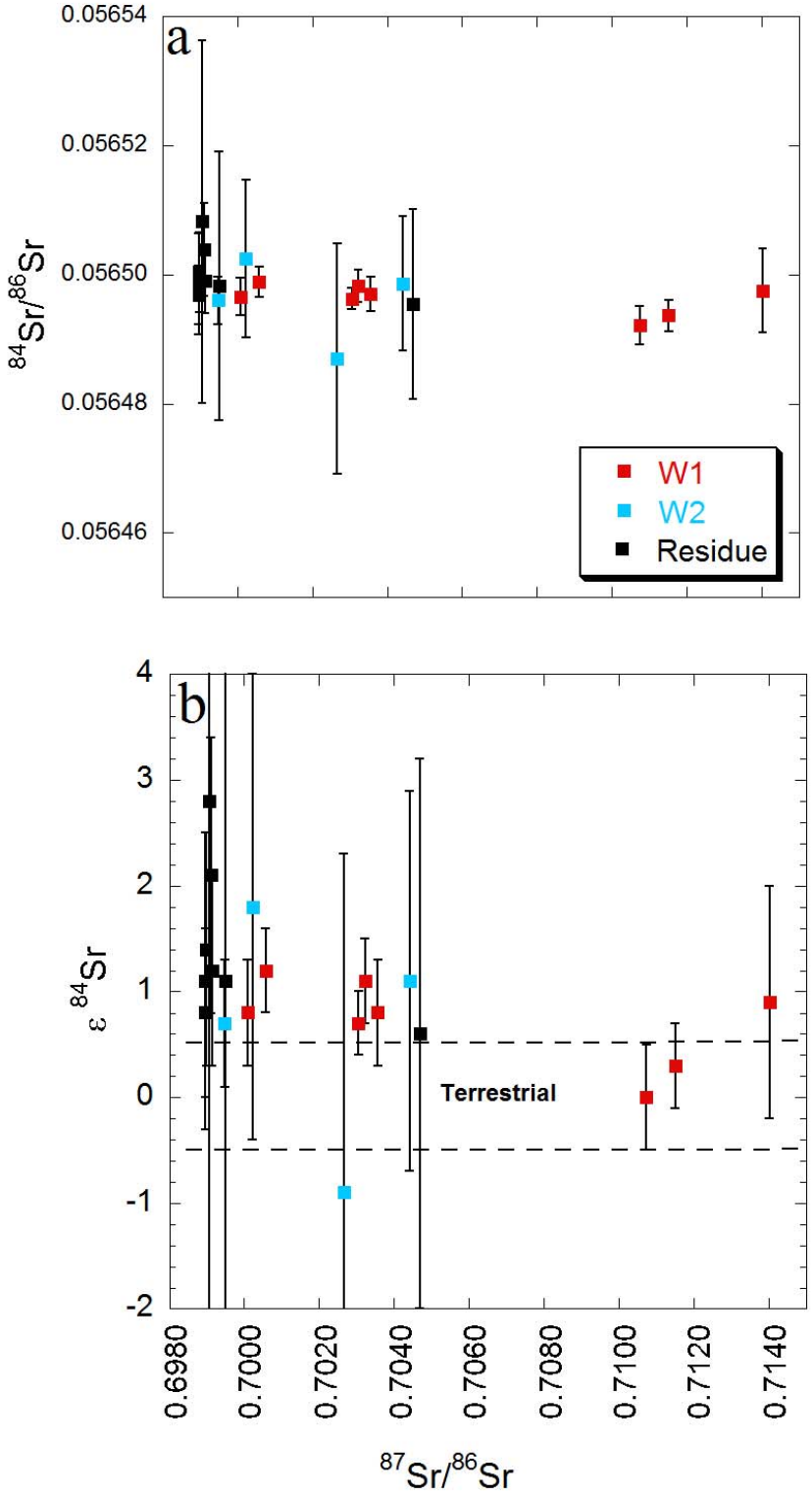

Figure 3.15: Plots of a) $^{84}Sr/^{86}Sr$ vs $^{87}Sr/^{86}Sr$, b) $\varepsilon^{84}Sr$ vs $^{87}Sr/^{86}Sr$ for all leachates and residues of NWA 4502 CAIs.

3.3.4 Discussion

The data reveal more complex open system behaviour of the Rb-Sr system in the NWA 4502 CAIs compared to Allende CAIs. The scatter observed in $^{87}Rb/^{86}Sr$ vs. $^{87}Sr/^{86}Sr$ plots for these inclusions indicate that inspite of acid washing not all sources of contamination could be removed. There is also the likelihood of parent-daughter fractionation during the acid washing steps such that points do not plot at their appropriate $^{87}Rb/^{86}Sr$ ratio for a given $^{87}Sr/^{86}Sr$ ratio. Given the amounts of Rb and Sr released in these steps, it seems unlikely that the parent/daughter ratio would be preserved.

Nevertheless, the initial $^{87}Sr/^{86}Sr$ values obtained for NWA 4502 CAIs are slightly higher than ALL (Gray et al., 1973), and lower than more recent estimates of initial Sr in CV CAIs (Nyquist et al., 2003; Hans et al., 2013).

NWA 4502 CAIs exhibit clearly resolved positive $^{84}Sr/^{86}Sr$ anomalies between 0.6 and 2.8 ε-units relative to the SRM 987 standard, and also relative to the $^{84}Sr/^{86}Sr$ of terrestrial rock standards and angrites. This anomaly is consistent with results from other recent ^{84}Sr studies (Moynier et al., 2012; Hans et al., 2013; Paton et al., 2013). The difference in $^{84}Sr/^{86}Sr$ between CAIs and terrestrial samples allows the differentiation of extraneous Sr of terrestrial origins. In this case, the comparable $\varepsilon^{84}Sr$ values in some acid leachates to those of terrestrial samples indicate these acid leaching steps were effective in removing terrestrial contamination from these samples.

Previous studies have shown that disturbed Rb-Sr systems in Allende CAIs are most likely related to alteration and thermal metamorphism on the Allende parent body (Gray et al., 1973; Podosek et al., 1991; Hans et al., 2013) and angrites may be disturbed by terrestrial weathering and may be affected by contamination with radiogenic terrestrial Sr as well as recent additions of Rb (Lugmair and Galer, 1992; Nyquist et al., 1994). Even though NWA 4502 CAIs have experienced lower levels of parent body alteration and metamorphism compared to CAIs in Allende and Efremovka, the Sr isotopic data suggest that these CAIs may have been affected by significant amounts of terrestrial weathering during their terrestrial residence period which is not readily obvious at the mineralogical level but can be detected in this isotope system.

3.4. URANIUM ISOTOPE SYSTEM

3.4.1. Introduction

The U-Pb and Pb-Pb method has been used for decades to date rocks on Earth, as well as meteorites. Obtaining an absolute age for solar system materials requires high-precision $^{207}Pb/^{206}Pb$ isotope measurements (Amelin, 2006). Until recently, it has been assumed that the modern $^{238}U/^{235}U$ ratio (137.88) required for Pb isotopic dating is invariant in meteoritic material. However, developments in modern analytical techniques and mass spectrometers now allow us to measure slight variations in isotope systems (Stirling et al., 2007; Weyer et al., 2008) long thought to be invariant. Brennecka et al. (2010) have demonstrated that the assumption of an invariant $^{238}U/^{235}U$ ratio in meteoritic material is invalid and that the age derived from CAIs is dependent on the $^{238}U/^{235}U$ ratio and if not addressed introduces significant additional uncertainties in calculation of CAI ages. As a result, reliable U-Pb CAI ages require a uranium isotope ratio precisely measured in the same inclusion.

3.4.2. $^{238}U/^{235}U$ analysis by MC-ICP-MS

Bulk samples consisting of two fragments, each for CAI *1, 4a, 5, 6* and *7*, as well as separated mineral fractions (melilite-rich) from CAIs *6* and *7* were chemically processed and analysed for uranium isotopic compositions. The analyses were carried out under clean lab conditions under the supervision of Dr. Claudine Sterling at the Community Trust of Otago Centre for Trace Element Analysis, Department of Chemistry, University of Otago following analytical procedures modified after Stirling et al. (2007) and Amelin et al. (2010).

Samples weighing ~16-150 mg for bulk samples to ~100 mg for mineral fractions were cleaned in ethanol and deionised water with ultrasonication, air dried and powdered. The powdered samples were transferred to clean Savillex Teflon vials for digestion using purified concentrated acids (1:10 concentrated HNO_3: HF, 7M HNO_3 and 6M HCl at 160°C). Centrifugation was carried out to separate residual undigested material followed by a second cycle of acid digestion to achieve complete dissolution of the samples. Samples were spiked with a high purity $^{236}U/^{233}U$ double spike for instrumental mass fractionation correction and equilibrated with the sample using HNO_3 + Optima® H_2O_2. Uranium was separated through a two-stage ion exchange protocol using Bio-Rad® AG 1-X4 and Eichrom® UTEVA ion exchange resins.

Uranium isotopic analysis was performed using a Nu Plasma MC-ICPMS (Nu Instruments, U.K.) coupled to a DSN-100 desolvating nebuliser. On-peak analysis was conducted over ~15-300 s depending on the sample size, using a signal integration period of 0.2 s. Signal intensities were measured simultaneously on an array of Faraday cups operating with 10^{11} Ω resistors. The measured isotope ratios were corrected for instrumental mass fractionation by normalization against the absolute $^{236}U/^{233}U$ of the mixed spike tracer (Richter et al., 2010) calibrated assuming CRM-145 has a $^{238}U/^{235}U$ value of 137.837 ± 0.015. Samples were bracketed with measurement of reference standard CRM 145 U metal (New Brunswick Laboratory, USA) and the USGS BHVO-2 terrestrial rock standard to monitor instrument accuracy. Fractions for $^{238}U/^{235}U$ determinations were analysed without acid leaching to prevent possible U isotopic fractionation.

3.4.3. Uranium Isotopic compositions

The uranium isotopic data that was obtained is summarised in Table 3.7 together with the uranium concentrations and Nd/U and Th/U ratios. Uranium concentrations range between ~40-200 ppb for all analysed samples. Higher concentrations (~70-200 ppb) occur in bulk CAI fragments while mineral fractions have concentrations between (~40-50 ppb). Terrestrial Basalt standards BHVO-2 and BCR-2 returned $^{238}U/^{235}U$ values of 137.789 ± 0.008 and 137.807 ± 0.005 respectively, consistent with measurements previously determined in the same laboratory, and are in excellent agreement with the average composition of 'bulk silicate earth' BSE at 137.795 ± 0.008 (Kaltenbach, 2013).

The uranium isotopic compositions of NWA 4502 CAIs range from 137.761 ± 0.018 to 137.857 ± 0.149. The measured $^{238}U/^{235}U$ ratios are uniform within error in all analysed fractions, except for two slightly disparate values (4a-P3 and 05-P4) (Figure 3.16). The weighted mean values are 137.795 ± 0.015, 137.807 ± 0.021, 137.840 ± 0.280, 137.785 ± 0.015 and 137.762 ± 0.017 for the CAIs *1, 4a, 5, 6* and *7* respectively. The average $^{238}U/^{235}U$ = 137.780 ± 0.044 for Type A CAIs 6 and 7 overlaps $^{238}U/^{235}U$ = 137.819 ± 0.046 for Type B CAIs 1, 4a and 5 within error. Because the precision of the $^{238}U/^{235}U$ varies substantially between the fractions due to the variations in sample sizes, the weighted average of 137.796 ± 0.019 (95% confidence interval with expansion to account for slight variability outside analytical uncertainties) is considered the best representation of the population value and the best estimate of the $^{238}U/^{235}U$ in the CAIs in NWA 4502. The CAI population in NWA 4502 has limited variation of U isotopic composition,

which differs markedly from variable $^{238}U/^{235}U$ in the CAI populations in Allende (Amelin et al., 2010; Brennecka et al., 2010) and Efremovka (Connelly et al., 2012). Plots of uranium isotopic composition against Nd/U and Th/U ratios (Figure 3.17) show no statistically resolvable correlation.

Table 3.7: Uranium isotopic compositions of NWA 4502 CAIs.

Name	^{238}U (ppb)	Nd/U	Th/U	$^{238/235}U$	2 σ	ε ^{235}U	2 σ
CAI *6*-P4	111.4	23.4	3.6	137.782	0.017	4.3	1.3
CAI *6*-P5	72.3	42.3	4.1	137.787	0.076	3.9	5.5
CAI *6*-mel	51.6	54.0	5.3	137.801	0.035	2.9	2.5
CAI *7*-P4	191.8	27.1	5.6	137.761	0.018	5.7	1.3
CAI *7*-mel	40.5	109.2	6.1	137.769	0.071	5.2	5.2
CAI *1*-P1	135.6	20.4	3.0	137.803	0.021	2.7	1.6
CAI *1*-P3	174.7	21.6	3.6	137.785	0.022	4.0	1.6
CAI *4a*-P2	188.6	23.3	3.7	137.806	0.022	2.5	1.6
CAI *4a*-P3	99.7	20.8	3.5	137.857	0.149	-1.1	10.8
CAI *5*-P4	114.5	22.9	3.9	137.856	0.022	-1.1	1.5
CAI *5*-P5	98.8	19.3	3.5	137.805	0.037	2.6	2.7

P: Piece or Fragment of a CAI, mel: melilite-rich fraction.

3.4.4. Discussion

It has become clear in the last few years that the $^{238}U/^{235}U$ composition of CAIs is variable (Amelin, et al. 2010; Brennecka, et al. 2010; Connelly, et al. 2012) and can vary largely even within the same meteorite. Uranium isotope variations in early solar system materials may be produced by many mechanisms, including natural variations in $^{238}U/^{235}U$ (Amelin, et al. 2010; Connelly, et al. 2012) or disturbances of the internal isotope systematics by alteration (Amelin and Krot, 2007; Connelly and Bizzarro, 2009) and the decay of extant ^{247}Cm to ^{235}U (Brennecka et al., 2010). Any or all of these mechanisms may play some role in $^{238}U/^{235}U$ variability in early solar system materials. However, because U has only two primordial isotopes, it is difficult to distinguish between these processes.

Large isotopic variations (>3.5 ‰, lowest $^{238}U/^{235}U$ and highest Nd/U and Th/U ratios) observed by Brennecka et al. (2010) occurred in fine-grained Allende CAIs classified as Group II by their REE patterns. Due to the lower condensation temperature of U relative to Nd and Th (Mason

and Taylor, 1982a), Brennecka et al. (2010) interpreted this observation as a likely result of the fractional condensation history that produced the characteristic Group II REE pattern to have produced the high Nd/U and Th/U ratios in these objects. Correlation of U isotopes with Th/U and Nd/U in all the Allende CAIs studied by Brennecka et al. (2010) suggested ^{247}Cm decay as being the dominant cause of the U isotope variation in these CAIs. Mane et al. (2014) studied the same Allende CAIs previously studied by Brennecka et al. (2010) to evaluate whether isotopic fractionation during the thermal processing (evaporation and condensation) of the CAIs is a primary driver for U isotopic variations using a correlation of their ^{238}U/^{235}U and ^{25}Mg/^{24}Mg ratios. Their study showed that coarse-grained CAIs, which have undergone melting and thermal processing, show a weak correlation between δ^{238}U and δ^{25}Mg suggesting that isotopic fractionation during thermal processing of these samples may have indeed contributed to the U isotope variation in this samples. Fine-grained CAIs, which did not undergo melting and have much larger range of U isotopic compositions than the coarse-grained CAIs, do not correlate with δ^{25}Mg suggesting that the U isotope variation in these samples is dominated by ^{247}Cm decay as demonstrated by Brennecka et al. (2010).

The uniformity (significantly narrower range) of U isotopic composition in NWA 4502 which differs noticeably from variable ^{238}U/^{235}U in the CAI populations in Allende (Amelin et al., 2010; Brennecka et al., 2010) and Efremovka (Connelly et al., 2012), together with identical average ^{238}U/^{235}U values in the NWA 4502 CAIs, unfractionated REE patterns and small range of Th/U and Nd/U compared to Allende CAIs (Brennecka et al., 2010), suggests that ^{238}U/^{235}U variability in CAIs observed in Amelin et al. (2010) and Connelly et al. (2012) may be a result of U isotopic fractionation induced by secondary alteration processes such as hydrothermal and shock metamorphism experienced by Allende and Efremovka. If this interpretation is correct, then the properties of CAIs (even an extensive and diverse population of CAIs) found in any particular CV chondrite cannot be considered representative for the entire range of CAIs. The Group II REE pattern has not been observed in NWA 4502 CAIs in this study. It would require a study of a much larger population of NWA 4502 CAIs to find out with more certainty whether Group II REE patterns do exist in this meteorite and if it corresponds to large U isotopic variations produced by ^{247}Cm decay.

Further studies involving the characterisation of CAIs into groups based on their degree of aqueous alteration and hydrothermal and shock metamorphism for CAIs from a range of CV chondrites will be useful to directly compare the processes leading to variable ^{238}U/^{235}U in CAIs.

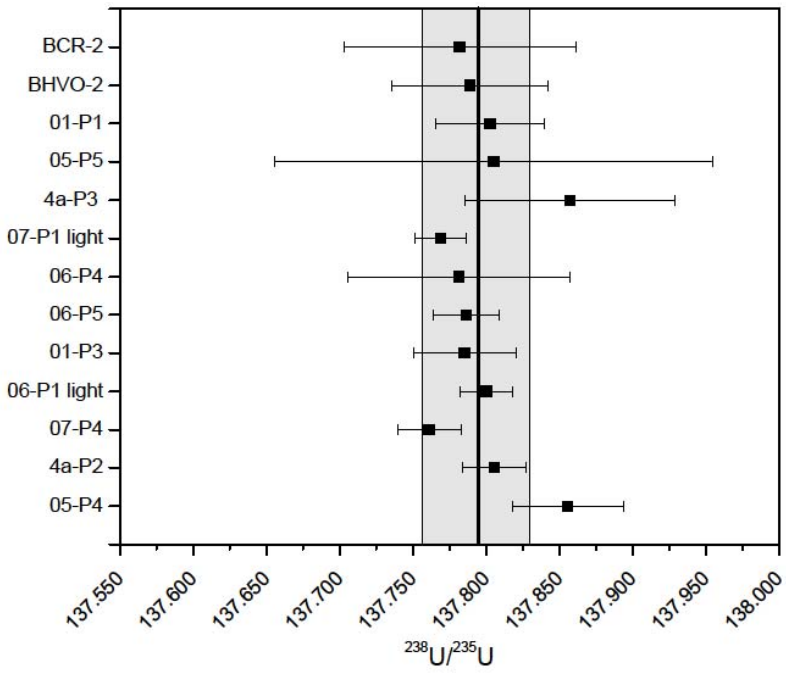

Figure 3.16: Plot of $^{238}U/^{235}U$ ratios for NWA 4502 CAIs and terrestrial standards BHVO-2 and BCR-2 with 2SE uncertainty. The average of all CAIs analysed (solid line) is given with the gray area representing the reproducibility of CRM-145 standard. Light: melilite-rich separates.

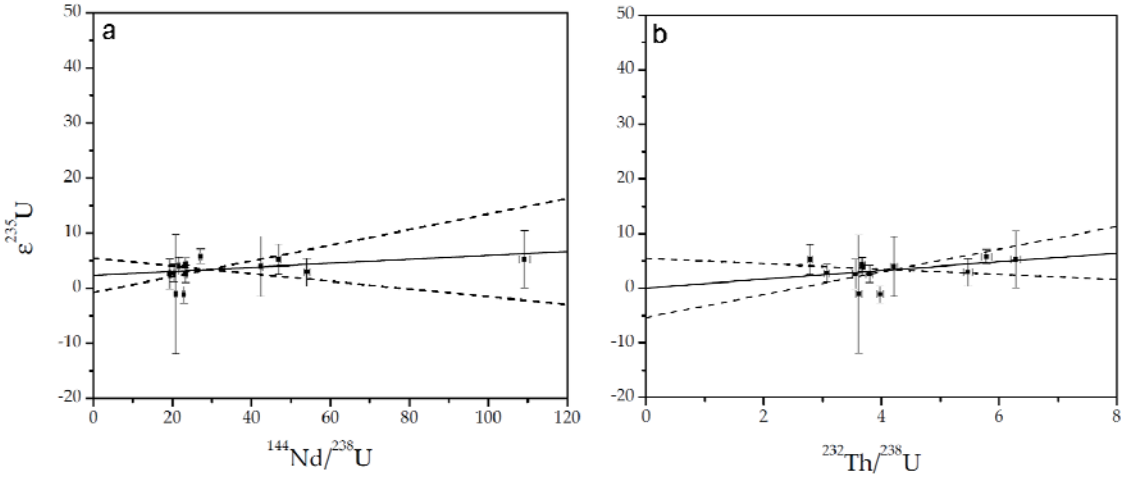

Figure 3.17: (a) Nd/U and (b) Th/U proxies for Cm/U plotted against $\varepsilon^{235}U$ variations. Weighted least squares regressions through the data yields the maximum possible slope (dashed lines) constraining the Cm-U chronometer. $\varepsilon^{235}U = [(^{235}U/^{238}U\text{sample}/^{235}U/^{238}U\text{standard})-1] \times 10{,}000$.

CHAPTER 4

U-Pb CHRONOLOGY

4.1. INTRODUCTION

The influence of secondary processes (asteroidal and terrestrial) and laboratory acid leaching processes on U-Pb systematics and Pb-Pb ages of NWA 4502 CAIs are reported in this chapter.

Being the oldest known objects in the solar system means that CAI ages make the best available proxy to the time of the beginning of formation of the Solar System. Acquiring precise and accurate ages of CAIs is thus important and requires precise isotopic analysis of uranium and radiogenic Pb from well preserved, undisturbed isotopic systems. At the current level of analytical sensitivity, CV chondrites are the only group of meteorites that contain CAIs that are sufficiently large to enable sufficiently precise U and Pb isotopic measurements. However, CV chondrites are not among the most pristine meteorites and are variably affected by hydrothermal alteration and metamorphism (Krot et al., 1995; Krot et al., 1998). Such secondary processing may lead to disturbance of the isotope systems.

The Pb-Pb ages determined for CAIs from the Allende, Efremovka, and NWA 2364 CV chondrites without the determination of their $^{238}U/^{235}U$ ratios vary between 4566.7 ± 0.2 and 4568.2 ± 0.2 Ma (Amelin et al., 2009; Bouvier and Wadhwa, 2010). However, this apparent ~1.5 Ma range of absolute ages is not consistent with a short formation interval of ≤300 ka for CAIs deduced from their ^{26}Al-^{26}Mg systematics (e.g., Jacobsen et al., 2008; MacPherson et al., 2010; Simon and Young, 2011). This range of CAI ages is more likely explained by secondary disturbance of Pb isotope systematics and/or variation in the U isotopic composition in these CAIs. Brennecka et al. (2010) discovered that uranium isotopic composition of CAIs is variable.

They showed U isotopic variations in Allende CAIs by as much as 0.35 % relative to the uranium standard NBS SRM 950 or CRM 145 that corresponds to corrections on Pb-Pb dates of +0.4 to -5 Ma. This means that accurate U-Pb dating of CAIs at the modern precision level requires $^{238}U/^{235}U$ analyses to account for possible variability of this ratio. The inconsistencies in CAI ages can have other possible causes besides $^{238}U/^{235}U$ variability, which should all be considered. Apparent ages can be influenced by secondary processing of the host meteorites, which may affect the U-Pb isotope systematics of CAIs. Acid leaching applied to remove contamination, weathering products and non-radiogenic Pb (Amelin, 2008; Connelly and Bizzarro, 2009) can also induce fractionation of radiogenic $^{207}Pb^*/^{206}Pb^*$ (Amelin et al., 2010).

Recent studies on CAI U-Pb chronology still show some age inconsistencies. While Allende and Efremovka CAIs recently measured using U-corrected Pb-Pb system gave consistent ages of 4567.18 ± 0.50 and 4567.3 ± 0.16 Ma respectively (Amelin et al., 2010; Connelly et al., 2012), a slightly older U-corrected Pb-Pb age, 4567.9 ± 0.3 Ma, was reported for a CAI from the CV chondrite NWA 6991 by Bouvier et al. (2011). The age of 4568.22 ± 0.17 Ma, reported by (Bouvier and Wadhwa, 2010) for a CAI from the CV chondrite NWA 2364, is about 1 Ma older and was determined without direct measurement of the $^{238}U/^{235}U$, but using instead the Th/U ratio as a proxy, on the basis of an empirical Th/U vs. $^{238}U/^{235}U$ correlation reported by (Brennecka et al., 2010). Even though the higher apparent age of the NWA 2364 CAI of Bouvier and Wadhwa (2010) may be due to the effects of variability of $^{238}U/^{235}U$ ratio in CAIs that is incompletely removed by the proxy correction, the apparent ages can also be influenced by secondary processing of the host meteorites, which may affect the U-Pb isotope systematics of CAIs. Since Bouvier and Wadhwa (2010) proposed that the older NWA 2364 CAI age is primary whereas the younger ages reported in earlier studies result from secondary disturbance, the matter of the CAI age variability requires close investigation.

The importance of the removal of non-radiogenic Pb to achieve a high radiogenic to nonradiogenic Pb ratio for precise and accurate Pb isotopic dating of meteorites and their components has been demonstrated (Lugmair and Galer, 1992; Göpel et al., 1994; Amelin et al., 2005; Amelin, 2006). This is important in Pb isotopic dating because it eliminates the major non-analytical uncertainty in $^{207}Pb/^{206}Pb$ age calculations. Phases rich in non-radiogenic Pb can be removed by a combination of ultrasonic agitation and acid leaching. However, intensive acid leaching for meteorite components such as CAIs and chondrules may result in Pb isotope fraction which affects the U-Pb system making accurate determination of $^{207}Pb/^{206}Pb$ age dates difficult (Tera et al., 1997; Amelin et al., 2009; Connelly and Bizzarro, 2009; Bouvier and

Wadhwa, 2010). Acid leaching also reduces the total amount of radiogenic Pb available for analysis in residues, and this affects precision. However, stepwise dissolution can be used to parse the radiogenic Pb into separate fractions with sufficient spread in Pb–Pb space to define an appropriate, well-constrained internal isochron that would characterize the isotopic composition of radiogenic Pb and, therefore, the age of a sample.

NWA 4502, as already described in previous chapters, has experienced less hydrothermal alteration and thermal metamorphism than Allende, and less shock metamorphism than Efremovka which are the most studied CV chondrites. U-Pb isotopic dating of NWA 4502 CAIs can therefore help to establish more reliably the age of the first solid formation in the solar system, resolve remaining age discrepancies, and understand the effects of metamorphism, alteration, and shock on the U-Pb isotopic dating of CAIs. Drawbacks of acid leaching such as the possible fractionation of radiogenic Pb can be possibly reduced by developing alternative, more selective leaching procedures, which would preferentially extract initial and contaminant Pb but preserve radiogenic Pb. The application of Citrate-Bicarbonate-Dithionite (CBD) treatment developed and proven effective in removing weathering products such as Fe oxides and hydroxides in soil studies (Mehra and Jackson, 1958; Hunt et al., 1995; Van Oorschot and Dekkers, 1999) and applied to extraterrestrial samples (Golden et al., 1993; Amelin and Sapah, 2012) may be useful in removing contamination and Fe hydroxides produced by terrestrial weathering.

4.2. METHODS

All sample preparation was carried out under clean lab conditions at the Research School of Earth Sciences, Australian National University, Canberra, Australia. The CAIs used in this study are the same CAIs from NWA 4502 that were studied for oxygen isotopes, ^{26}Al-^{26}Mg and Rb-Sr systematics (i.e., *1*, 5, *6* and *7*). Analysed samples consist of mixed mineral fractions and mineral separates obtained after disaggregation, cleaning and coarse crushing of CAI fragments. All fractions were pre-cleaned repeatedly with ultrasonic agitation in distilled acetone, ethanol and water and weighed into clean Savillex Teflon vials before acid leaching.

Acid leaching

To investigate the effects of different acids and acid strengths in stepwise dissolution of NWA 4502 CAI mineral components, three different procedures were applied to mineral fractions of different compositions and grain sizes. Table 4.1 shows a description of samples and the procedures used.

Table 4.1: Acid leaching procedures applied to NWA 4502 mineral fractions.

Leaching procedure	**Treatment**
1 ***(CAI 1, 5, 6 and 7 Melilite and Pyroxene fractions 100-275µm)***	
W1: 0.5 M HNO_3 x5	US 10 min
W2: 7M HNO_3 x2 and 6M HCl x2	HP 100°C, 1 hr each
Residue: 25M HF + 12M HNO_3	HP 100°C, >24 hr
2 ***(CAI 1 and 6 mixed/bulk fractions <100µm))***	
Cleaning with Citrate-Bicarbonate-Dithionite	
W1: 0.5M HNO_3	US 10 min
W2: 7M HNO_3 and 6M HCl	HP 100°C, 1 hr each
W3: 0.2M HF	US 10 min
W4: 1M HF	HP 100°C, 1 hr
Residue: 25M HF+12M HNO_3	HP 100°C, >24 hr
3 ***(CAI 1 Melilite and Pyroxene fractions <100->275µm)***	
L1: 0.3M HBr	HP 100°C, 6 hr, and US 15 min
L2: 0.5M HNO_3	HP 100°C, 6 hr, and US 15 min
L3: 2M HCl	HP 100°C, 6 hr, and US 15 min
L4: 6M HCl	HP 100°C, 6 hr, and US 15 min
L5: 6M HCl	HP 100°C, 6 hr, and US 15 min
L6: 1M HF	US 15 min
L7: 1M HF	HP 100°C, 6 hr, and US 15 min
Residue: 25M HF + 12M HNO_3	HP 100°C, >24 hr

W: Wash, L: Leachate, HP: Hot plate and US: Ultrasonic

Procedure 1: This is a mild acid leaching protocol following (Amelin, 2008). It was applied to 3-9 mg melilite and pyroxene concentrates (100-275 µm) from CAIs *1, 5, 6* and *7*. The first acid leaching step is an ultrasonic wash with 1ml of 0.5M HNO_3 with 10 min ultrasonic agitation,

repeated 5 times. All ultrasonic washes were collected as W1. This is followed by a 1 hour hot (110 °C) acid washing with 7M HNO_3 and 6M HCl two times each, combined as W2. All washes were collected after 10 minutes of centrifugation.

Procedure 2: This procedure was applied to two aliquots (~20 mg) each of cleaned mix fractions (<100 μm) of CAI *1* and *6*. One portion of each CAI was treated with CBD, the other was acid leached without CBD treatment. The CBD protocol used in this study was modified after (Van Oorschot and Dekkers, 1999). A solution of 40 ml sodium citrate and 5 ml sodium bicarbonate was added to samples and heated to 80°C. At this temperature, 0.5 g of sodium dithionite was added and stirred thoroughly. The samples were kept at a constant temperature (110 °C) for an hour with stirring every 15 min. The liquid was separated after cooling and the residue was thoroughly rinsed with ethanol and deionised water. The acid leaching procedure is slightly more intensive compared to procedure 1. It includes W1 and W2 as in procedure 1, followed by an additional 10 min ultrasonic wash in 0.2M HF collected as W3, and a 1 hour (110 °C) hot wash in 1M HF collected as W4.

Procedure 3: This procedure is usually referred to as progressive or stepwise dissolution. In this study, it is modified after Connelly and Bizzarro (2009) and Bouvier and Wadhwa (2010) and is the most intensive procedure in this study. It was applied to 20-30 mg of a mixed fraction (<100 μm), melilite and pyroxene-rich fractions (<100 μm to >275 μm) of CAI *1*. This acid leaching procedure consists of 7 steps of a combination of hot and ultrasonic washing in the following order: 1 ml 0.3M HBr, 1 ml 0.5M HNO_3, 1 ml 2M HCl, 1 ml 6M HCl, 1 ml 6M HCl (110 °C, 6 hr, and 15 min ultrasonication), 1 ml 1M HF (15 min), and 1M HF (110 °C, 6 hr, and 15 min ultrasonication). Washes are denoted as L1, L2…L7.

Element separation and Mass spectrometry

Residues were digested with a 2:1 solution of concentrated HF + HNO_3. All residues and washes were spiked with 5-10 μl of the ^{202}Pb-^{205}Pb-^{233}U-^{236}U mixed tracer. Samples were then converted to soluble forms by repeated evaporation with concentrated HNO_3, HCl and HBr and redissolved in dilute HBr or HCl.

Lead and U were separated following the procedures described in Amelin et al. (2002) and Amelin (2008). Lead separation was done using 50 µl columns of Eichrom® AG1x8 ion exchange resin. Matrix elements were removed sequentially from the columns using water, 0.3M HBr and 2.5M HCl. The Pb fractions were passed through the column twice for purification. In each pass, lead was eluted in 0.5M HNO_3 and after the second pass mixed with 0.02M H_3PO_4 to avoid complete dryness during final evaporation. Fractions containing uranium were collected as bulk wash fractions before Pb separation. The collected wash is evaporated and redissolved in 3M HNO_3 for U separation. 50 µl columns of Eichrom® UTEVA ion exchange resin cleaned sequentially with a mixture of 0.02M HNO_3 + 0.2M HF and 0.02M HNO_3 were used for uranium separation. Uranium was eluted in a solution of 0.02 HNO_3 + 0.2M HF, after eluting the matrix elements with 3M HNO_3+1% H_20_2 (hydrogen peroxide was added to assure complete removal of titanium).

Lead samples were loaded in Merck silica gel (Gerstenberger and Haase, 1997) or Aldrich silica gel (Huyskens et al., 2012) onto outgassed single evaporation filaments made of H.Cross zone refined rhenium. Samples were loaded on to a filament at 1.0 A, and dried steadily at 0.1 A increments every 30 s until 2.0 A. The filament is flashed (>2.0 A) to obtain a brief dull glow. Lead isotope ratios were measured on the Finnigan Triton Plus or MAT 261 thermal ionisation mass spectrometers (TIMS) at the Research School of Earth Science, ANU. To monitor reproducibility and accuracy of Pb-isotopic measurements, analysis of SRM 981 standards (~100-1000 pg loads) spiked with the same mixed tracer as the samples, was carried out in each analytical session. U-isotopic ratios were measured on the Thermo Scientific Neptune plus MC-ICPMS equipped with an Aridus desolvating nebulizer also at the Research School of Earth Science, ANU. Reproducibility and accuracy of U-isotopic measurements was monitored using a U-Th (^{238}U, ^{236}U, ^{233}U, ^{232}Th and ^{229}Th) standard solution.

Data reduction and evaluation

Measured isotope ratios, fractionation factors and ion yields are screened and calculated using Microsoft excel. The PBDAT software (Ludwig, 1980) operated on a DOS platform (Dosbox) was used to determine Pb-Pb ages after correcting for blank, spike and non-radiogenic Pb contributions as well instrumental mass fractionation. The initial Pb values used correspond to

the most primitive Pb isotopic composition known in the solar system (primordial Pb), as measured in a troilite inclusion from the Canyon Diablo iron meteorite (CDT Pb) (Tatsumoto et al., 1973). Isochrons were calculated using the model 1 regression of Isoplot *Ex* (Ludwig, 2003). This model assumes that the scattering of data points is mainly caused by the analytical uncertainties as assigned to the data points. Hence the points are weighted proportionally to the inverse square of these uncertainties. The 95%-confidence interval is calculated from the observed scatter as the product of the square root of the Mean Squared Weighted Deviates (MSWD) and a *priori* uncertainties. If the scatter of data points is exactly equivalent to the scatter predicted by analytical uncertainties, then MSWD is 1.

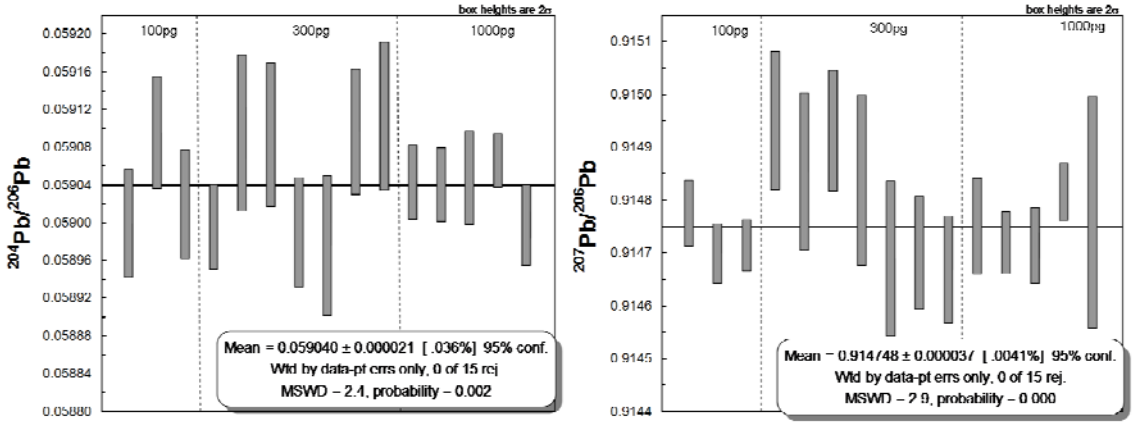

Figure 4.1: Weighted mean plots of $^{204}Pb/^{206}Pb$ and $^{207}Pb/^{206}Pb$ for repeated measurements of SRM 981 over the course of this study (n=15). The certified ratios for SRM 981 are $^{204}Pb/^{206}Pb = 0.059042 \pm 0.000037$ and $^{207}Pb/^{206}Pb = 0.91464 \pm 0.00033$.

Total procedure blanks consisting of washing, dissolution and chemistry blanks (measured separately and combined numerically) were determined with each batch of samples and are typically <1 pg for Pb and <0.1 pg for U in all three procedures. There is no significant difference in the blank levels between the three procedures. Correction for blank contribution with appropriate error magnification was carried out for all samples using the average Pb isotopic composition of the blank measured with each batch.

The reproducibility of all measurements was monitored using Pb standard SRM 981 analyses. The average $^{206}Pb/^{204}Pb$ and $^{207}Pb/^{206}Pb$ values for all standard analyses are 16.933 ± 0.027 and

0.91477 ± 0.00018 (n=15) respectively. Figure 4.1 shows the weighted mean of $^{207}Pb/^{206}Pb$ for all standard analyses. Ion yields for SRM 981 in all analytical sessions vary between ca. 2 and 7 %. Those for samples vary between ca. 0.2 and 9 %.

4.3. U-Pb CONCENTRATIONS AND Pb ISOTOPE COMPOSITIONS

Uranium and Pb data for each procedure used, including sample description, weight, concentrations, isotope ratios and model ages, are summarised in Tables 4.2-4.4.

Table 4.2: Fraction descriptions.

Sample	**Fraction**	**Weight (mg)**	**Acid Leaching procedure**
	100-275µm		1
CAI *6*	Pyroxene	4.95	
	Melilite	8.75	
CAI *7*	Pyroxene	6.08	
	Melilite	6.63	
CAI *1*	Pyroxene	3.34	
	Melilite	6.08	
CAI *5*	Pyroxene	2.97	
	Melilite	5.67	
	<100µm		2
CAI *6*	Bulk	15.93	
	Bulk (CBD)	8.40	
CAI *1*	Bulk	23.79	
	Bulk (CBD)	15.03	
CAI *1*	*<100->275 µm*		3
	Melilite (<100µm)	30.34	
	Melilite (100-275µm)	20.61	
	Melilite (>275µm)	19.99	
	Melilite (>275µm)	20.10	
	Pyroxene (>275µm)	7.35	
	Pyroxene ± Melilite (>275µm)	34.08	
	Melilite ± Pyroxene (>275µm)	7.39	

CBD: Samples treated with Citrate-Bicarbonate-Dithionite.
Bulk: Very fine fractions separated by suspension after coarse crushing.

Table 4.3: U-Pb isotopic data for acid-washed mineral fractions of NWA 4502 CAIs.

Sample description	Leaching step	U pg	Pb pg	$^{206}Pb^*/^{204}Pb^*$ corr.	$^{207}Pb^*/^{235}U$	$^{207}Pb^*/^{235}U$ % err.	$^{206}Pb^*/^{238}U$	$^{206}Pb^*/^{235}U$ % err.	Error corr. 6/8-7/5	$^{206}Pb^*/^{238}U$ date (Ma)	$^{207}Pb^*/^{206}Pb^*$ date (Ma)	U-Pb discord. %
100-275µm	Procedure 1											
CAI *6* Pyroxene	W1	283	4905	24.1	221.9	0.138	3.37	0.121	0.9977	9510.6	4172.0	-128
	R	66	238	393.4	108.3	0.283	1.29	0.285	0.9446	5329.8	4533.4	-18
CAI *6* Melilite	W1	114	2115	25.2	256.9	0.190	3.77	0.174	0.9565	10077.8	4222.2	-139
	R	60	170	436.0	94.6	0.370	1.10	0.357	0.9660	4782.8	4563.6	-5
CAI *7* Pyroxene	W1	106	990	23.1	117.2	0.281	1.64	0.265	0.9691	6259.6	4293.8	-46
	R	84	292	417.6	91.5	0.273	1.06	0.268	0.9826	4668.4	4565.5	-2
CAI *7* Melilite	W1	171	1399	20.1	90.2	0.232	1.31	0.206	0.9949	5405.5	4235.4	-28
	R	202	688	185.3	89.6	0.142	1.04	0.142	0.9617	4609.4	4560.9	-1
CAI *1* Pyroxene	W1	485	2634	21.2	65.7	0.306	0.93	0.205	0.9852	4230.2	4281.4	1
	W2	60	267	37.9	83.4	0.625	1.05	0.629	0.9984	4635.5	4445.3	-4
	R	60	208	450.0	94.3	0.345	1.10	0.346	0.8469	4769.8	4564.8	-4
CA *1* Melilite	W1	459	1865	32.1	69.4	0.162	0.87	0.154	0.9564	4042.1	4451.9	9
	W2	88	264	112.1	80.8	0.531	0.95	0.538	0.9966	4312.2	4545.6	5
	R	77	428	98.3	145.8	0.260	1.71	0.241	0.9759	6419.3	4554.5	-41
CAI *5* Pyroxene	W1	66	442	16.8	64.3	0.642	0.82	0.634	0.9906	3872.8	4422.9	12
	W2	28	146	31.2	96.5	1.170	1.17	1.190	0.9977	4993.1	4503.9	-11
	R	226	641	1295.1	95.0	0.138	1.10	0.137	0.9900	4789.6	4568.0	-5
CAI *5* Melilite	W1	119	507	29.8	76.6	0.410	0.92	0.408	0.9960	4194.6	4522.4	7
	W2	65	179	333.9	86.9	0.700	1.01	0.713	0.9979	4500.9	4565.2	1
	R	165	523.3	5883.8	104.9	0.150	1.22	0.151	0.9893	5132.4	4568.0	-12
<100µm	Procedure 2											
CAI *6*	W1	622592	45031	20.6	401.9	0.475	5.26	0.283	0.7191	11822.6	4392.6	-63
	W2	590671	8302	34.2	114.0	0.320	1.46	0.260	0.8784	5796.1	4426.4	-24
	W3	17356	6	43.1	113.1	0.874	1.31	0.866	0.9931	5390.1	4573.3	-15
	W4	30775	14	239.8	117.3	3.384	1.37	3.384	1.0000	5559.0	4559.3	-18
	R	162140	353	67.6	88.5	0.238	1.03	0.229	0.9714	4564.9	4563.3	0
CAI *6* CBD	W1	396502	34774	24.0	211.4	0.844	2.99	0.775	0.9398	8928.4	4275.8	-52
	W2	286004	3914	66.7	83.3	0.153	1.02	0.134	0.9141	4542.4	4485.6	-1
	W3	12172	9	74.6	102.7	2.115	1.21	2.113	0.9993	5105.1	4548.7	-11
	W4	14489	10	464.3	108.7	0.619	1.27	0.619	0.9992	5279.9	4559.5	-14
	R	101928	368	192.3	74.8	1.032	0.88	1.031	0.9998	4081.1	4542.6	11
CAI *1*	W1	2128738	38265	22.7	63.3	0.409	0.85	0.218	0.7118	3949.0	4363.2	10
	W2	1599607	24526	25.5	79.9	0.400	1.07	0.268	0.7920	4677.9	4363.4	-7
	W3	44020	10	67.1	72.6	0.224	0.85	0.213	0.9643	3972.7	4551.9	15
	W4	16271	7	338.9	402.6	1.900	4.68	1.900	1.0000	11200.4	4563.7	-59
	R	336448	617	245.5	84.0	0.187	0.98	0.186	0.9964	4403.1	4560.0	4
CAI *1* CBD	W1	1108115	25876	25.1	74.5	0.467	0.99	0.308	0.8274	4435.4	4370.8	-1
	W2	572098	5425	39.3	72.9	0.282	0.92	0.238	0.8974	4191.5	4452.4	6
	W3	30802	34	72.2	189.9	1.076	2.22	1.074	0.9988	7540.5	4556.1	-40
	W4	27795	19	327.7	154.6	5.125	1.80	5.125	1.0000	6640.0	4561.8	-31
	R	225169	638	404.8	78.4	0.332	0.91	0.332	0.9995	4187.9	4558.9	9

Table 4.3: Continued.

Sample description	Leaching step	U pg	Pb pg	$^{206}Pb^*/^{204}Pb^*$ corr	$^{207}Pb^*/^{235}U$	$^{207}Pb^*/^{235}U$ % err.	$^{206}Pb^*/^{238}U$	$^{206}Pb^*/^{235}U$ % err.	Error corr. 6/8-7/5	$^{206}Pb^*/^{238}U$ date (Ma)	$^{207}Pb^*/^{206}Pb^*$ date (Ma)	U-Pb discord. %
CAI *1* <100->275 µm	Procedure 3											
Melilite (<100µm)	L1	816	5903	21.1	92.7	0.278	1.20	0.165	0.9377	5090.9	4404.9	-16
	L2	630	1864	24.6	41.7	0.234	0.56	0.147	0.9216	2851.2	4364.8	35
	L3	783	3487	22.3	56.7	0.276	0.80	0.156	0.9249	3781.7	4285.1	12
	L4	94	894	24.0	131.3	0.272	1.80	0.183	0.9182	6637.6	4324.1	-54
	L5	375	1362	83.4	88.1	0.125	1.05	0.116	0.9609	4624.6	4529.2	-2
	L6	30	1738	21.2	763.1	0.406	9.55	0.345	0.9548	15186.2	4458.0	-241
	L7	76	59	43.9	16.1	0.834	0.19	0.832	0.9892	1134.2	4527.1	75
	R	62	643	52.1	228.4	0.194	2.71	0.183	0.9747	8457.9	4533.1	-87
Melilite (100-275µm)	L1	551	2813	24.2	72.4	0.231	0.94	0.147	0.9290	4269.2	4405.1	3
	L2	318	847	30.5	43.3	0.191	0.56	0.14	0.9239	2861.2	4413.5	35
	L3	386	1351	25.2	50.6	0.236	0.69	0.149	0.9176	3370.8	4337.9	22
	L4	46	278	29.4	100.9	0.33	1.31	0.294	0.9619	5411.1	4397.7	-23
	L5	250	828	122.8	85.7	0.237	1.01	0.209	0.9321	4501.2	4543.7	1
	L6	36	114	254.9	86.7	0.395	1.01	0.397	0.9933	4508.0	4558.4	1
	R	32	345	463.5	310.0	0.314	3.61	0.314	0.9970	9856.3	4560.7	-116
Melilite (>275µm)	L1	818	3253	32.1	66.6	0.172	0.85	0.127	0.9244	3970.8	4427.3	10
	L2	297	845	48.3	56.2	0.168	0.69	0.136	0.9384	3384.3	4484.2	25
	L3	405	1073	80.2	62.8	0.134	0.75	0.119	0.9568	3615.5	4522.3	20
	L4	98	286	148.7	84.3	0.198	0.99	0.197	0.9886	4435.2	4549.9	3
	L5	350	1011	452.4	84.1	0.123	0.98	0.12	0.9787	4396.9	4563.4	4
	L6	56	173	843.1	90.9	0.26	1.06	0.26	0.9901	4649.6	4564.3	-2
	R	7	274	895.3	1335.6	1.22	15.52	1.22	0.9996	18081.2	4564.8	-296
Melilite (>275µm)	L1	940	3654	30.9	63.3	0.215	0.82	0.175	0.9388	3861.4	4405.6	12
	L2	459	1306	43.6	53.5	0.302	0.66	0.292	0.9847	3286.4	4466.9	26
	L3	592	1601	50.8	54.5	0.246	0.67	0.238	0.9833	3302.9	4485.7	26
	L4	226	789	72.1	83.5	0.528	1.00	0.52	0.9939	4471.2	4519.9	1
	L5	566	1701	360.2	86.7	0.238	1.01	0.234	0.9894	4504.1	4560.5	1
	L6	47	164	635.8	102.8	2.39	1.20	2.39	0.9997	5069.5	4564.6	-11
	L7	50	56	178.9	32.1	3.43	0.37	3.48	0.9990	2049.2	4559.5	55
	R	79	671	537.1	271.2	1.39	3.16	1.39	0.9994	9193.1	4560.4	-102
Pyroxene (>275µm)	L1	390	2510	21.5	78.6	0.418	1.11	0.327	0.9324	4818.9	4279.2	-13
	L2	189	898	21.7	58.5	0.675	0.83	0.624	0.9725	3895.9	4272.5	9
	L3	442	3267	21.5	89.5	0.388	1.29	0.294	0.9232	5328.8	4255.4	-25
	L4	81	555	23.2	90.7	1.39	1.25	1.35	0.9893	5223.3	4317.6	-21
	L5	242	821	159.3	88.2	0.493	1.04	0.491	0.9968	4585.6	4548.8	-1
	L6	7	35	298.8	131.8	15.6	1.54	15.6	0.9999	6007.8	4557.5	-32
	L7	26	90	335.9	94.6	5.68	1.11	5.7	0.9998	4801.5	4556.5	-5
	R	73	291	355.6	106.0	1.58	1.24	1.59	0.9994	5192.8	4557.8	-14
Pyroxene ± Melilite (>275µm)	L1	977	4298	25.2	62.5	0.255	0.84	0.183	0.9225	3942.7	4347.7	9
	L2	734	2337	30.9	51.7	0.481	0.67	0.307	0.9417	3313.7	4403.2	25
	L3	1845	6974	28.4	59.0	0.29	0.78	0.203	0.8950	3708.5	4380.9	15
	L4	327	1587	31.1	83.2	0.429	1.07	0.405	0.9765	4699.8	4413.4	-6
	L5	773	2725	128.7	92.4	0.196	1.09	0.188	0.9809	4752.5	4543.3	-5
	L6	72	161	175.6	61.5	1.84	0.72	1.85	0.9988	3510.8	4546.4	23
	L7	49	87	301.5	49.3	2.8	0.58	2.83	0.9993	2934.5	4557.6	36
	R	190	1222	445.8	190.2	0.615	2.22	0.612	0.9950	7533.3	4560.2	-65
Melilite ± Pyroxene (>275µm)	L1	418	2096	24.5	69.3	0.379	0.93	0.325	0.9497	4248.3	4351.6	2
	L2	442	1643	26.7	54.2	0.38	0.73	0.33	0.9551	3525.8	4354.2	19
	L3	626	4971	22.6	100.6	0.381	1.43	0.281	0.9049	5735.6	4266.0	-34
	L4	144	946	25.5	95.8	1	1.30	0.836	0.9459	5379.7	4335.7	-24
	L5	287	927	168.0	87.7	0.478	1.03	0.468	0.9824	4564.0	4549.7	0
	L6	40	159	384.1	112.0	2.97	1.30	2.98	0.9994	5378.7	4563.1	-18
	L7	13	23	43.2	39.4	11.6	0.46	11.8	0.9991	2453.0	4549.8	46
	R	27	214	201.0	226.3	4.17	2.65	4.17	0.9999	8350.3	4552.8	-83

U and Pb concentrations are calculated using sample weights before leaching.
Isotopic ratios are corrected for fractionation, blank, and spike.
Errors are 2 sigma of the mean.
Isotopes marked with asterisk are "radiogenic": corrected for fractionation, spike, blank, and primordial Pb isotopic composition from Tatsumoto et al. (1973) as initial Pb.
Ages calculated using the primordial Pb isotopic composition from Tatsumoto et al. (1973).

Table 4.4: Pb isotopic data for acid-washed mineral fractions of NWA 4502 CAIs.

Sample description	Leaching step	$^{206}Pb/^{204}Pb$ tot.	$^{204}Pb/^{206}Pb$ tot.	$^{204}Pb/^{206}Pb$ % err.	$^{207}Pb/^{206}Pb$ tot.	$^{207}Pb/^{206}Pb$ % err.	Error corr. 4/6-7/6	$^{207}Pb^*/^{206}Pb^*$ date (Ma)	$^{207}Pb^*/^{206}Pb^*$ date err.
100-275µm	Procedure 1								
CAI *6* Pyroxene	W1	24.1	0.041	0.046	0.720	0.012	0.0820	4172.0	0.7
	R	393.4	0.003	4.100	0.622	0.069	0.9730	4533.4	0.3
CAI *6* Melilite	W1	25.2	0.040	0.060	0.720	0.017	0.2767	4222.2	0.7
	R	436.0	0.002	6.000	0.634	0.129	0.6065	4563.6	1.6
CAI *7* Pyroxene	W1	23.1	0.043	0.069	0.755	0.021	0.4760	4293.8	0.8
	R	417.6	0.002	4.140	0.635	0.087	0.6793	4565.5	1.0
CAI *7* Melilite	W1	20.1	0.050	0.050	0.780	0.015	0.0990	4235.4	1.0
	R	185.3	0.005	0.711	0.647	0.026	0.8753	4560.9	0.2
CAI *1* Pyroxene	W1	21.2	0.047	0.124	0.774	0.049	0.0070	4281.4	2.5
	W2	37.9	0.026	0.495	0.705	0.086	0.9722	4445.3	0.5
	R	450.0	0.002	6.020	0.634	0.098	0.8228	4564.8	0.9
CA *1* Melilite	W1	32.1	0.031	0.094	0.730	0.018	0.4410	4451.9	0.5
	W2	112.1	0.009	2.200	0.656	0.119	0.9640	4545.6	0.6
	R	98.3	0.010	0.722	0.666	0.061	0.3482	4554.5	1.1
CAI *5* Pyroxene	W1	16.8	0.060	0.070	0.866	0.024	0.3929	4422.9	1.3
	W2	31.2	0.032	0.593	0.750	0.099	0.9267	4503.9	1.2
	R	1295.1	0.001	4.800	0.629	0.029	0.7762	4568.0	0.3
CAI *5* Melilite	W1	29.8	0.034	0.230	0.762	0.031	0.7217	4522.4	0.9
	W2	333.9	0.003	9.990	0.638	0.182	0.9835	4565.2	0.7
	R	5883.8	0.000	27.400	0.626	0.031	0.9144	4568.0	0.2
<100µm	Procedure 2								
CAI *6*	W1	20.6	0.049	0.071	0.804	0.032	-0.0007	4392.6	4.9
	W2	34.2	0.029	0.145	0.714	0.054	-0.0001	4426.4	2.2
	W3	43.2	0.023	0.169	0.731	0.037	0.1933	4573.3	1.5
	W4	241.8	0.004	0.698	0.641	0.042	0.3622	4559.3	0.3
	R	67.6	0.015	0.075	0.690	0.023	0.0462	4563.3	0.8
CAI *6* CBD	W1	24.0	0.042	0.114	0.743	0.046	-0.0003	4275.8	4.3
	W2	66.7	0.015	0.112	0.663	0.050	0.0055	4485.6	0.9
	W3	75.0	0.013	0.523	0.678	0.063	0.4167	4548.7	1.1
	W4	482.6	0.002	3.234	0.631	0.052	0.7623	4559.5	0.4
	R	192.8	0.005	0.284	0.638	0.036	0.1728	4542.6	0.3
CAI *1*	W1	22.7	0.044	0.112	0.775	0.052	-0.0003	4363.2	4.3
	W2	25.5	0.039	0.139	0.749	0.064	-0.0002	4363.4	3.6
	W3	67.2	0.015	0.177	0.686	0.032	0.2912	4551.9	0.9
	W4	341.1	0.003	0.581	0.637	0.039	0.2146	4563.7	0.2
	R	245.7	0.004	0.259	0.640	0.063	0.0106	4560.0	0.2
CAI *1* CBD	W1	25.1	0.040	0.222	0.754	0.050	-0.0001	4370.8	4.0
	W2	39.3	0.025	0.148	0.703	0.072	0.0001	4452.4	1.8
	W3	72.3	0.014	0.121	0.683	0.026	0.1828	4556.1	0.8
	W4	330.8	0.003	0.823	0.637	0.040	0.3290	4561.8	0.2
	R	405.9	0.002	0.370	0.633	0.042	0.0528	4558.9	0.1

Table 4.4: Continued.

Sample description	Leaching step	$^{206}Pb/^{204}Pb$ tot.	$^{204}Pb/^{206}Pb$ tot.	$^{204}Pb/^{206}Pb$ % err.	$^{207}Pb/^{206}Pb$ tot.	$^{207}Pb/^{206}Pb$ % err.	Error corr. 4/6-7/6	$^{207}Pb^*/^{206}Pb^*$ date (Ma)	$^{207}Pb^*/^{206}Pb^*$ date err.
CAI *1 <100->275 µm*	Procedure 3								
Melilite (<100µm)	L1	21.1	0.047	0.161	0.800	0.022	0.0001	4404.9	2.0
	L2	24.6	0.041	0.163	0.756	0.023	0.0030	4364.8	1.7
	L3	22.3	0.045	0.162	0.762	0.022	0.0005	4285.1	2.1
	L4	24.0	0.042	0.167	0.753	0.023	0.0180	4324.1	1.9
	L5	83.4	0.012	0.219	0.664	0.025	0.1730	4529.2	0.5
	L6	21.2	0.047	0.163	0.811	0.022	0.0004	4458.0	1.9
	L7	43.9	0.023	1.020	0.714	0.123	0.8382	4527.1	1.8
	R	52.1	0.019	0.192	0.699	0.024	0.1660	4533.1	0.6
Melilite	L1	24.2	0.041	0.162	0.770	0.021	0.0010	4405.1	1.6
(100-275µm)	L2	30.5	0.033	0.168	0.728	0.023	0.0440	4413.5	1.2
	L3	25.2	0.040	0.166	0.745	0.023	0.0070	4337.9	1.7
	L4	29.4	0.034	0.198	0.730	0.031	0.2923	4397.7	1.4
	L5	122.8	0.008	0.756	0.652	0.066	0.0880	4543.7	1.3
	L6	254.9	0.004	3.390	0.639	0.090	0.8908	4558.4	0.7
	R	463.5	0.002	2.010	0.632	0.035	0.7506	4560.7	0.4
Melilite (>275µm)	L1	32.1	0.031	0.162	0.724	0.021	0.0040	4427.3	1.1
	L2	48.3	0.021	0.253	0.690	0.026	0.0960	4484.2	0.9
	L3	80.2	0.012	0.293	0.664	0.023	0.1210	4522.3	0.6
	L4	148.7	0.007	0.913	0.648	0.044	0.8106	4549.9	0.4
	L5	452.4	0.002	1.000	0.633	0.027	0.4645	4563.4	0.4
	L6	843.1	0.001	7.600	0.629	0.062	0.8402	4564.3	0.5
	R	895.3	0.001	4.330	0.629	0.044	0.6554	4564.8	0.5
Melilite (>275µm)	L1	30.9	0.032	0.164	0.724	0.022	0.0500	4405.6	1.2
	L2	43.6	0.023	0.236	0.695	0.033	0.5181	4466.9	0.8
	L3	50.8	0.020	0.240	0.685	0.030	0.4960	4485.7	0.7
	L4	72.1	0.014	0.663	0.670	0.050	0.6999	4519.9	0.8
	L5	360.2	0.003	1.810	0.635	0.036	0.5746	4560.5	0.5
	L6	635.8	0.002	27.500	0.631	0.265	0.9912	4564.6	0.8
	L7	178.9	0.006	20.800	0.647	0.693	0.9930	4559.5	2.3
	R	537.1	0.002	5.320	0.630	0.076	0.7820	4560.4	0.7
Pyroxene (>275µm)	L1	21.5	0.047	0.173	0.770	0.023	0.0130	4279.2	2.4
	L2	21.7	0.046	0.170	0.766	0.029	0.0900	4272.5	2.4
	L3	21.5	0.047	0.164	0.765	0.024	0.0080	4255.4	2.4
	L4	23.2	0.043	0.267	0.759	0.041	0.1740	4317.6	3.0
	L5	159.3	0.006	1.470	0.646	0.056	0.8380	4548.8	0.6
	L6	298.8	0.003	63.700	0.636	1.300	0.9977	4557.5	3.6
	L7	335.9	0.003	28.000	0.634	0.514	0.9928	4556.5	1.6
	R	355.6	0.003	9.380	0.634	0.167	0.9632	4557.8	0.8
Pyroxene ± Melilite	L1	25.2	0.040	0.162	0.748	0.022	0.0150	4347.7	1.6
(>275µm)	L2	30.9	0.032	0.496	0.723	0.033	0.0270	4403.2	3.2
	L3	28.4	0.035	0.218	0.732	0.046	0.0040	4380.9	2.1
	L4	31.1	0.032	0.190	0.725	0.034	0.1380	4413.4	1.4
	L5	128.7	0.008	0.512	0.650	0.029	0.3036	4543.3	0.6
	L6	175.6	0.006	7.360	0.642	0.262	0.9655	4546.4	1.3
	L7	301.5	0.003	24.700	0.636	0.502	0.9919	4557.6	1.6
	R	445.8	0.002	2.750	0.632	0.066	0.4831	4560.2	0.9
Melilite ± Pyroxene	L1	24.5	0.041	0.171	0.755	0.027	0.0410	4351.6	1.8
(>275µm)	L2	26.7	0.037	0.191	0.738	0.028	0.0980	4354.2	1.7
	L3	22.6	0.044	0.176	0.755	0.039	0.0030	4266.0	2.6
	L4	25.5	0.039	0.511	0.742	0.067	0.0350	4335.7	5.0
	L5	168.0	0.006	1.410	0.645	0.087	0.4401	4549.7	1.3
	L6	384.1	0.003	17.400	0.635	0.286	0.9548	4563.1	1.5
	L7	43.2	0.023	8.590	0.723	0.975	0.9801	4549.8	7.7
	R	201.0	0.005	6.360	0.641	0.195	0.9814	4552.8	0.8
	$^{206}Pb/^{204}Pb$	% error	$^{207}Pb/^{206}Pb$	% error					
SRM 981 (*n* =15)	16.9332	0.0279	0.91477	0.00018					

The total amounts of U and Pb in acid leached mineral fractions calculated using sample weights before leaching vary from ~0.01-2 ng and ~0.01-18 ng respectively. Uranium and Pb are preferentially extracted during the early stages of acid leaching, so the U and Pb quantities in the successive leaching steps decrease as acid leaching progresses (Figure 4.2). The abundance ratio of non-radiogenic Pb to radiogenic Pb is generally higher in leachates than in the residues of the same fraction. This indicates that initial and contaminant Pb was preferentially removed during acid leaching processes. The radiogenic Pb isotopic compositions in the various mineral fractions for each procedure are plotted in Figure 4.3.

Procedure 1 yielded U and Pb concentrations varying between 20-150 ppb and 200-1000 ppb respectively in first ultrasonic washes in HNO_3 (W1). The U and Pb concentrations in hot HNO_3 and HCl washes (W2) and residues are generally lower than those of the W1. Uranium and Pb content range from 10-20 ppb and 30-80 ppb respectively in W2 and from 10-80 ppb and 50-200 ppb respectively in residues (Figure 4.2a).

The isotopic ratios in CAIs *1, 5, 6* and *7* mineral fractions are variably radiogenic (Figure 4.3a). In general, the isotopic composition of the Pb extracted in progressively stronger HNO_3 becomes more radiogenic. The most radiogenic signatures occur in some second leachates (W2) of melilite-rich fractions and in all final residues. The measured $^{206}Pb/^{204}Pb$ after correction for fractionation, spike, and analytical blank are between 17-32 (W1), 38-334 (W2) and 98–5884 (Residues). The total $^{206}Pb/^{204}Pb$ calculated recombining washes and residues for melilite-rich fractions in CAIs *1, 5, 6* and *7* are 40, 77, 28 and 29 respectively.

These values in pyroxene-rich fractions in the same CAIs *1, 5* and *6* are 24, 47, and 25, respectively, and in hibonite-rich fractions in CAI *7* is 30. This shows that mineral fractions from the FoB CAI *5* contain the most radiogenic Pb. All other CAIs have similar amounts of radiogenic Pb in both their pyroxene-rich and melilite-rich fractions. All the first acid steps (W1) and a couple of the second leachates (W2) plot below the primordial Pb tie line (Tatsumoto et al., 1973) and on or close to the average modern terrestrial Pb tie line (Stacey and Kramers, 1975), while all residues and two second leachates plot on and close to the primordial Pb tie line (Figure 4.4a).

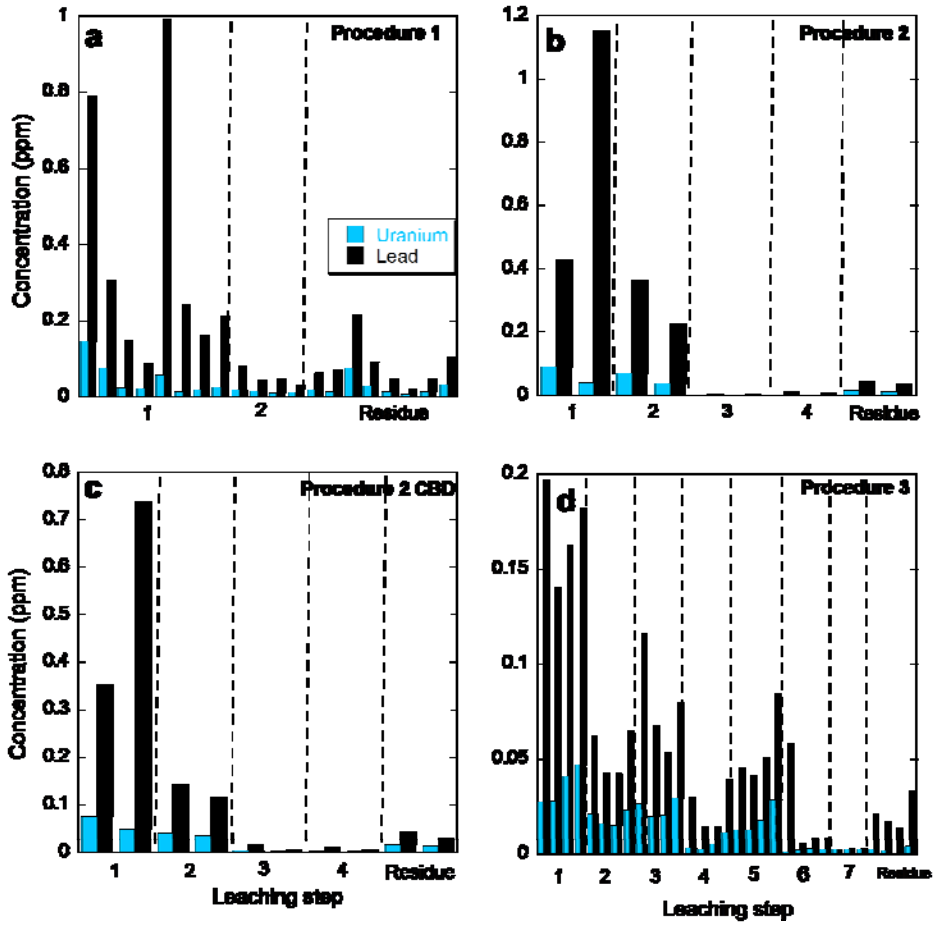

Figure 4.2: Plots of U and Pb concentrations in leachates and residues for (a) procedure 1(b) procedure 2 (c) procedure 2 with CBD treatment and (d) procedure 3.

Procedure 2 produced comparable U and Pb concentrations in leachates and residues for both CBD-treated and untreated samples (Figure 4.2b, c). The U content ranges from 40-70 ppb and 40-90 ppb for treated and untreated samples respectively in W1. Pb content is between 400-700 ppb and 400-1200 ppb for treated and untreated samples respectively. U and Pb concentrations in W2 are slightly lower than those in W1. While uranium contents range from 30-40 ppb and 40-70 ppb for treated and untreated samples respectively, Pb concentrations are ~100 ppb and 200-400 ppb for treated and untreated samples respectively. The U concentrations in third (W3) and fourth (W4) leachates as well as residues are an order of magnitude lower compared to W1 and W2 at ~1-2 ppb while Pb values are ~10-40 ppb for both CBD-treated and untreated samples of both CAI *1* and *6*.

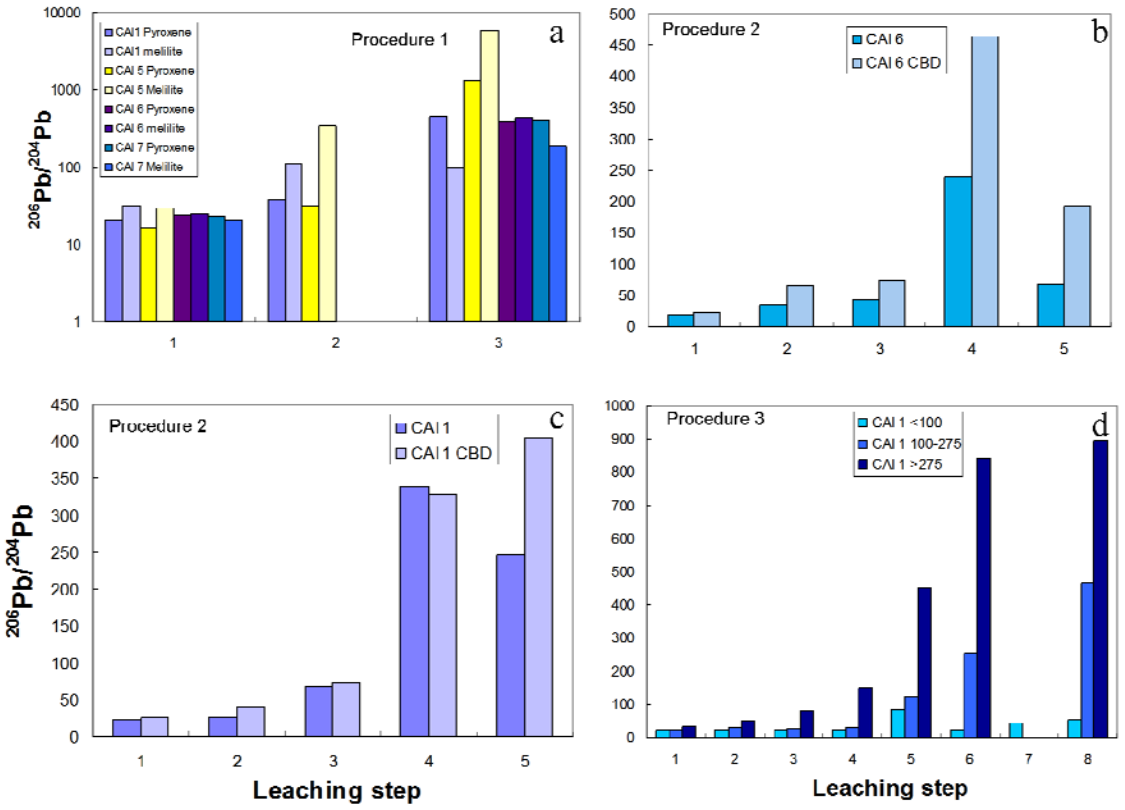

Figure 4.3: Plots of $^{206}Pb/^{204}Pb$ ratios (radiogenic Pb isotopic compositions) for mineral fractions in acid leaching steps.

Pb isotopic ratios in both CBD- treated and untreated mineral fractions from CAI *1* and *6* are progressively more radiogenic, CBD-treated samples are consistently more radiogenic than untreated samples (Figure 4.3b, c). This indicates that CBD treatment helps to remove terrestrial contamination. The first application of HF yielded Pb slightly more radiogenic than the previous HNO_3 and HCl steps. A second application of HF liberates Pb that is still more radiogenic. The $^{206}Pb/^{204}Pb$ ratios are between 24-464 (W1-R) for CBD-treated samples and 20-250 (W1-R) for untreated samples. In both CBD-treated and untreated samples, the first acid steps (W1 and W2) plot below the primordial Pb tie line along the modern terrestrial tie line. Third and fourth washes (W3 and W4) as well as residues plot on the primordial Pb tie line (Figure 4.4b, c)

Procedure 3, the progressive dissolution protocol yielded U and Pb concentrations in the first three leachates (L1-3) between 20-50 ppb and 40-200 ppb respectively. Leachates 4 and 5 gave

concentrations between 2-30 ppb and 10-80 ppb of U and Pb. Leachates from 6 and 7 produced lower concentrations than previous leachates. Uranium content in these leachates is ~1-3 ppb while Pb values range between 2-60 ppb. In residues, concentrations are also low and range between 0.3-4 ppb for U and 10 -30 ppb for Pb (Figure 4.2d).

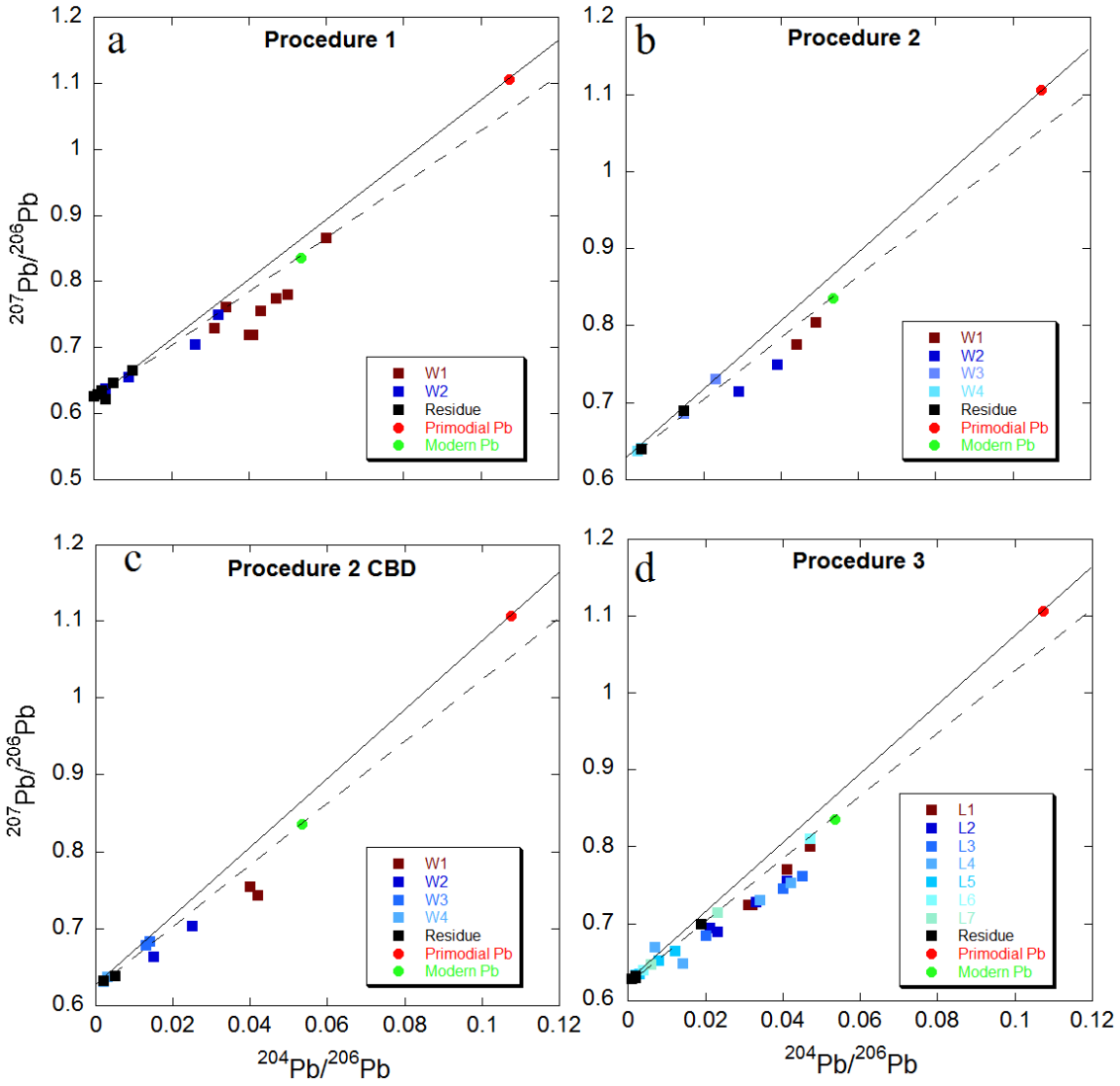

Figure 4.4: $^{207}Pb/^{206}Pb$ vs $^{204}Pb/^{206}Pb$ plots for leachates and residues of mineral fractions in each acid leaching procedure.

Pb isotopic ratios in leachates become progressively more radiogenic from L1-R especially for coarse (>275 μm) grained fractions (Figure 4.3d). $^{206}Pb/^{204}Pb$ ratios range from 21-83 (<100 μm mixed fraction), 24-464 (<100 μm melilite-rich fraction) and 32- 895 (>275 μm melilite-rich fraction).

The first leaching steps with weak HBr and HNO_3 (L1-L2) removes non-radiogenic Pb but did not extract significant quantities of radiogenic Pb ($^{206}Pb/^{204}Pb$ = 20-58). Subsequent steps (L3-L5) of progressively stronger HCl extracted progressively more radiogenic Pb ($^{206}Pb/^{204}Pb$ = 22-450). Application of HF liberates Pb more radiogenic than previous steps ($^{206}Pb/^{204}Pb$ = 43-843), and final residues contain the most radiogenic Pb ($^{206}Pb/^{204}Pb$ = 201-895). Mixed fractions <100 μm depart from this pattern where pre-HF steps have more radiogenic signatures. The HNO_3 and HCl steps (L2-L4) contain slightly more radiogenic Pb ($^{206}Pb/^{204}Pb$ = 22-25) than the subsequent HF step (L6) ($^{206}Pb/^{204}Pb$ = 21) which is the same as the first HBr step L1, but less radiogenic than the second HF step (L7) ($^{206}Pb/^{204}Pb$ = 44) and the final residue ($^{206}Pb/^{204}Pb$ = 52). The most radiogenic signature occurs in the second concentrated HCl step (L5) ($^{206}Pb/^{204}Pb$ = 83).

The Pb isotopic ratios of acid steps (L1-L5) for both coarse and fine grained fractions plot below the primordial Pb tie line and along the same line as the average modern terrestrial value (Figure 4.4d). The most radiogenic leachates (L6-L7) and the final residues plot on the primordial Pb tie line. The least radiogenic leachates of fine grained fractions plot closer to the average modern terrestrial value compared to coarse grained fractions. This implies that an ultrasonic wash in HF after concentrated HCl does not have an effect on radiogenic phases as demonstrated for coarser grained fractions but attacks phases containing non-radiogenic Pb that was not affected by earlier steps of HNO_3 and HCl.

Coarse grained fractions of different mineral compositions from the same CAI *1* show a range of $^{206}Pb/^{204}Pb$ values from L1-R for melilite-rich coarse fraction (31-636), pyroxene-rich coarse fraction (22-356), melilite ± pyroxene-rich coarse fraction (25-446) and melilite ± spinel-rich fraction (23-384). Recombined $^{206}Pb/^{204}Pb$ values for melilite, pyroxene, and melilite ± pyroxene and melilite ± spinel coarse fractions are 153, 52, 70 and 47 respectively. This indicates melilite maybe the dominant carrier phase of radiogenic Pb.

Comparing the degree to which the final residues of mineral fractions from CAI *1* are radiogenic in all three procedures, melilite and pyroxene-rich fractions in procedure 1 yielded $^{206}Pb/^{204}Pb$ of ~98 and 450 respectively. Mix fraction residues in procedure 2 not treated with CBD have a $^{206}Pb/^{204}Pb$ value of 245 while CBD treated samples have a $^{206}Pb/^{204}Pb$ value of 405. Mix fraction residues in procedure 3 produced a $^{206}Pb/^{204}Pb$ of 52 about 5 times lower compared to those in procedure 1. Melilite-rich fractions yielded the most radiogenic CAI *1* residues with values from 463-895.

4.4. U-Pb AGES OF NWA 4502 CAI

Radiogenic $^{206}Pb/^{207}Pb$ ages calculated assuming the $^{238}U/^{235}U$ value of 137.88 yielded a Pb-Pb internal isochron regression line with an intercept of 0.62552 ± 0.00024, corresponding to an age of 4568.41 ± 0.55Ma (MSWD = 7.5) for seven residue analyses (excluding one analytically suspect data point) of all four NWA 4502 CAIs in procedure 1. Excluding one data point that plots slightly above the isochron, increases precision of the intercept to 0.625407 ± 0.000077, correlating to an age of 4568.16 ± 0.18 Ma (MSWD = 2.0). The Pb-Pb isochron plots for the most radiogenic fractions (W4 and residues) in procedure 2 samples without CBD treatment gives a regression line with an intercept of 0.6227 ± 0.0037 corresponding to an age of 4561.8 ± 8.6 Ma (MSWD = 5.2) and CBD-treated samples give an intercept value of 0.629 ± 0.011 which corresponds to an age of 4575 ± 25 Ma (MSWD = 161). Isochron plots for the most radiogenic fractions L7 and residues of coarse melilite-rich fractions in procedure 3 yielded a regression line with an intercept of 0.62535 ± 0.00054 corresponding to an age of 4568.0 ± 1.3 Ma (MSWD = 1.4).

These ages are assigned no real age meaning in this study but useful for direct comparison with the Pb-Pb ages reported before Brennecka et al. (2010). See Appendix C Table C1.

Recalculating the isochron ages above by applying the weighted mean $^{238}U/^{235}U$ value of 137.796 for NWA 4502 CAIs, with the additional age uncertainty due to $^{238}U/^{235}U$ uncertainty yielded Pb-Pb ages of 4574 ± 25 Ma and 4561.0 ± 8.6 Ma respectively for the last leachates W4 and residues of CBD-treated and untreated samples in procedure 2 (Figure 4.5 a, b). The last leachates L7 and residues of coarse melilite-rich fractions in procedure 3 give a more precise

age of 4567.24 ± 1.32 Ma (Figure 4.5c), while residue analyses of all four studied CAIs in procedure 1 yielded the most precise Pb-Pb age of 4567.40 ± 0.27 Ma (Figure 4.5d).

U-Pb dates and the concordance of the U-Pb system are presented for leachates and residues of melilite, pyroxene and bulk fractions as presented in Table 4.3. The data are plotted in Figures 4.6 and 4.7 in a conventional (Wetherill-type) concordia diagram, for visual evaluation of discordance. The U-Pb ages of the washes and acid-washed residues are variably discordant in all procedures. Most early washes show substantial normal discordance, suggesting that uranium is extracted during acid leaching more easily than radiogenic Pb. The U-Pb discordance of acid-washed residues for most fractions are less than 10% for the less aggressive procedures 1 and 2 (Figure 4.6 a, b and c). The U-Pb systems in acid-washed residues in procedure 3 (Figure 4.6 d, e) appear to be less stable and show variable discordance up to 100 %. This indicates that the isotopic systems were better preserved in procedure 1 and 2 but more disturbed in procedure 3 due to the more intense leaching.

Upper concordia intercepts, calculated from the fractions containing less non radiogenic Pb yield 4564.5 ± 7.6 Ma (MSWD = 6.1) for acid washed residues in procedure 1, 4560.0 ± 4.0 Ma (MSWD = 92) and 4559.4 ± 4.1 Ma (MSWD = 28) for last leachates and residues of untreated and CBD-treated samples respectively in procedure 2 and 4563.7 ± 1.4 Ma (MSWD = 10) for last leachates and residues in procedure 3 (Figure 4.7). These dates are similar within uncertainty to the weighted averages of $^{207}Pb^*/^{206}Pb^*$ dates for the same fractions (Figure 4.8).

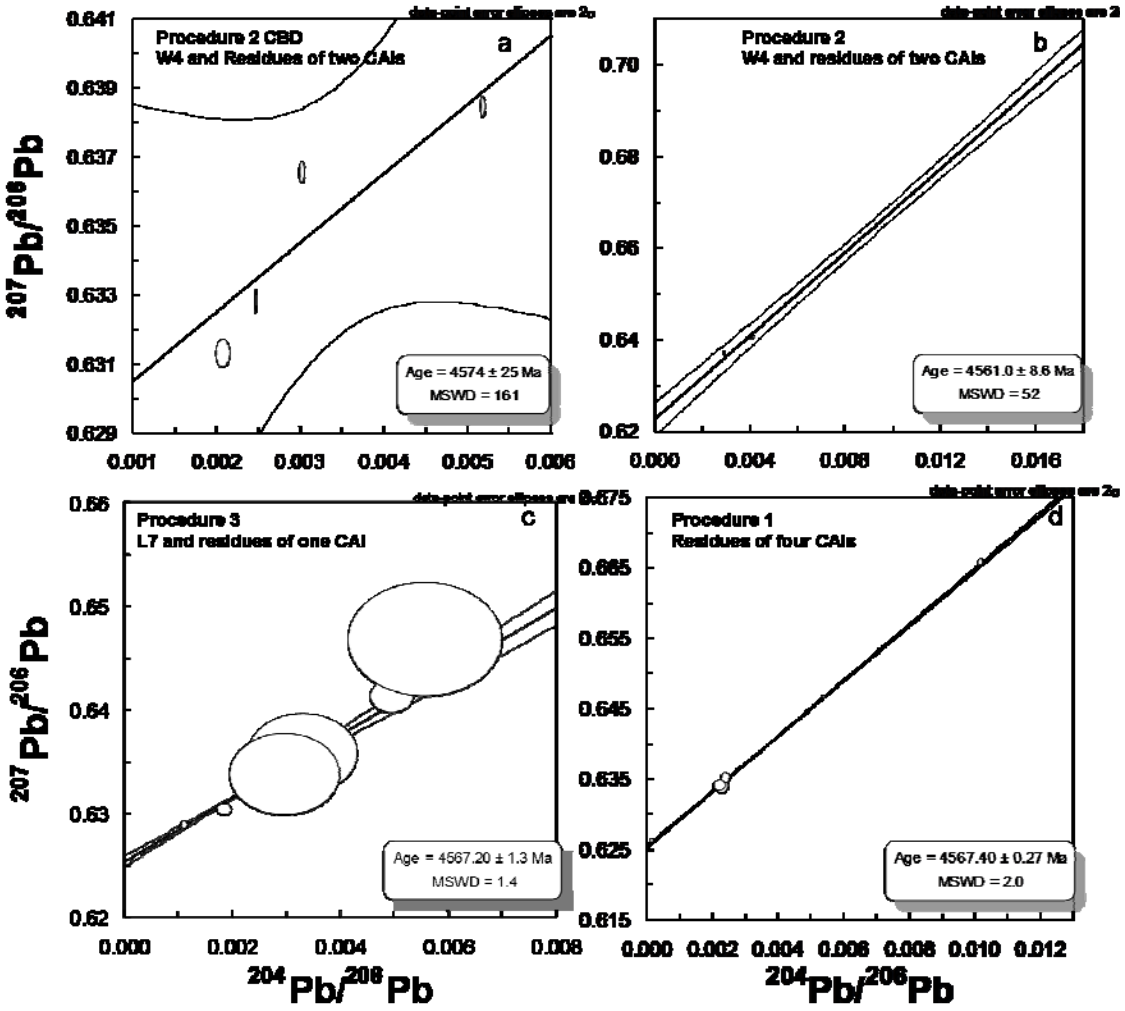

Figure 4.5: Pb-Pb isochron plots for (a) CBD-treated final HF leachates (W4) and acid washed residues (procedure 2) of CAI *1* and *6* (b) the final HF leachates (W4) and acid washed residues (procedure 2) of CAI *1* and *6* (c) the most radiogenic fractions, L7 and acid washed residues (procedure 3) of coarse melilite-rich fractions in CAI *1*(d) acid washed residues (procedure 1) of the four studied CAIs *1, 5 , 6* and *7.*

.

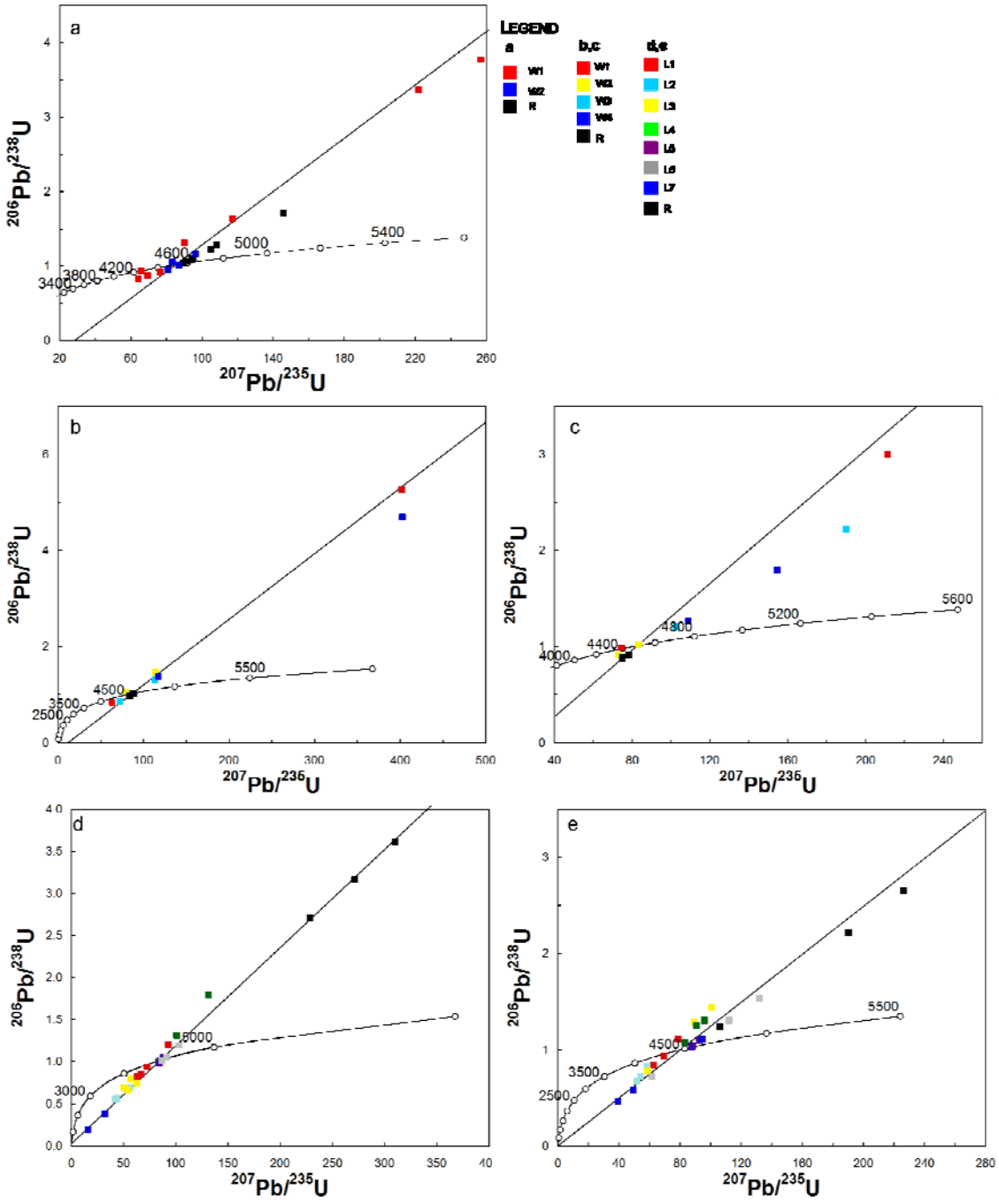

Figure 4.6: U-Pb concordia plots for NWA 4502 CAIs showing all acid washes and residues (a) CAIs *1*, *5*, *6* and *7* melilite and pyroxene fractions (procedure 1), (b) CAI *1* and *6* bulk fractions (procedure 2), (c) CBD-treated bulk fractions from CAI *1* and *6* from (procedure 2), (d) CAI *1* melilite fractions (procedure 3) and (e) CAI *1* pyroxene fractions (procedure 3).

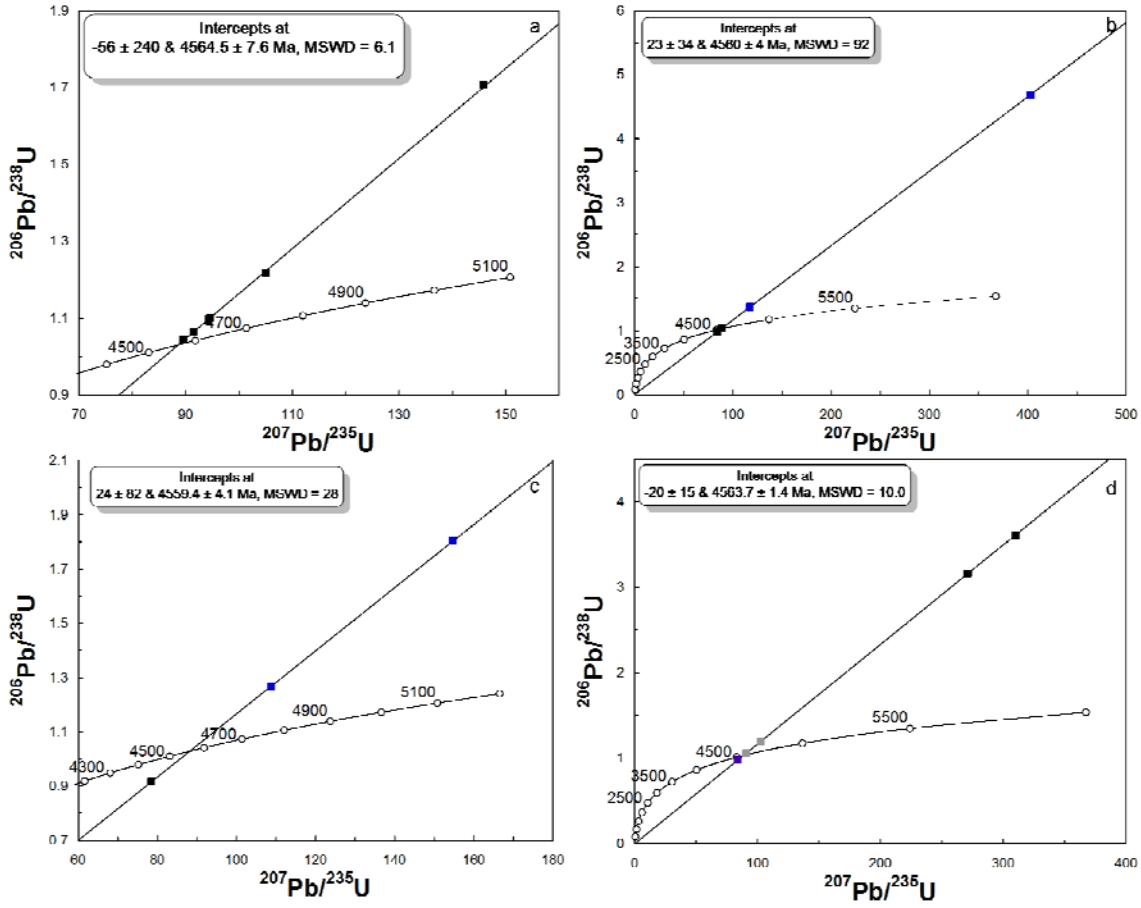

Figure 4.7: U-Pb concordia plots for NWA 4502 CAIs showing (a) residues of CAIs *1*, *5*, *6* and *7* melilite and pyroxene fractions (procedure 1), (b) late leachates, W4 and residues of CAI *1* and *6* bulk fractions (procedure 2), (c) CBD-treated late leachates, W4 and residues of CAI *1* and *6* bulk fractions (procedure 2) and (d) late leachates L5, L6 and residues of CAI *1* melilite fractions (procedure 3). Symbols are same as in Figure 4.6.

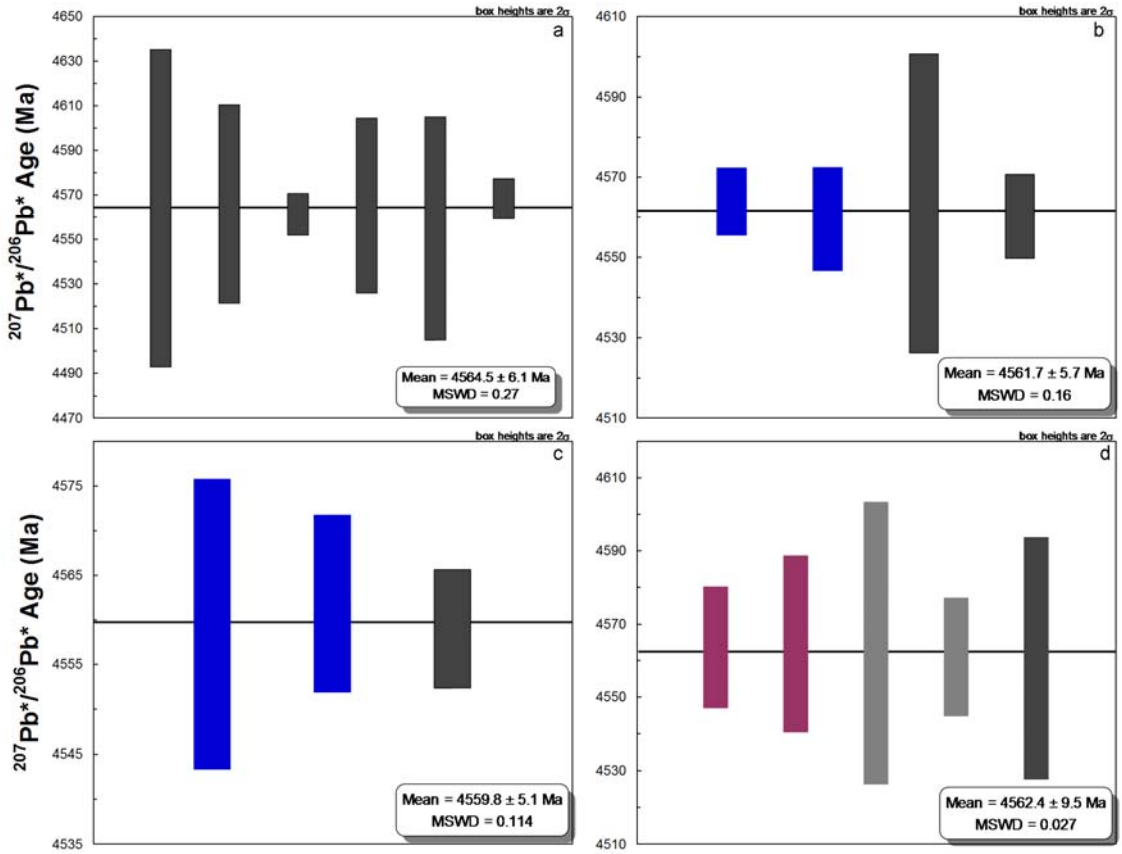

Figure 4.8: Weighted mean plots for $^{207}Pb^*/^{206}Pb^*$ ages showing fractions selected for U-Pb concordia diagrams. Data points selected are the same as those in Figures 4.7.

4.5. DISCUSSION

4.5.1. Effect of acid leaching on U-Pb systems of NWA 4502 CAIs

The U and Pb contents in residues and washes varies between fractions, but are broadly similar to the concentration levels previously reported for Allende, Efremovka and NWA 2364 CAIs. In all three procedures, acid leached residues plot on the primordial Pb tie line indicating that repeated pre-cleaning by ultrasonication in distilled ethanol, acetone and water is useful to remove some common Pb from the samples analysed as reported in other studies (Amelin, 2008; Connelly and Bizzarro, 2009). Non-radiogenic Pb was preferentially removed during acid leaching processes. Procedure 2 shows that additional cleaning with CBD helps in further removing non-radiogenic Pb and terrestrial contamination. Procedure 1 produces variably

radiogenic leaching steps compared to procedure 2 and 3 which gave progressively enriched radiogenic Pb through the leaching steps.

Leaching with HNO_3 usually separates the least radiogenic component of the dissolution series. However, increasing concentrations of HNO_3 and HCl with longer and higher temperature also intensifies dissolution of radiogenic Pb. HF is most effective in liberating radiogenic signatures. This has been previously observed for CV chondrite chondrules (Connelly and Bizzarro, 2009).

An important point to note is that at least the repeated treatment of samples with hot (100°C) concentrated 7M HN03 and 6M HCl for 1 hour each, does not seem to fractionate the radiogenic Pb since this procedure resulted in the preferred Pb-Pb age obtained for NWA 4502 CAIs with radiogenic residual Pb composition.

No systematic differences in the contents of U, radiogenic and non-radiogenic Pb were observed between mineralogically distinct fractions. It is not clear which mineral phase is the dominant U and radiogenic Pb carrier in these CAIs. Both melilite and pyroxene contain comparable amounts of radiogenic Pb and are suitable for U-Pb dating. The more aggressive procedure 3 significantly reduces the total amount of radiogenic Pb analysed compared to the other procedures. Also, variable radiogenic Pb isotopic compositions obtained for fine fractions compared to coarse fractions in procedure 3 may indicate that the mineral that hosts non-radiogenic Pb is more readily removed from coarse grained fractions.

The difference in the level to which the final residues are radiogenic represent compositional variations between CAIs, grain size, the effectiveness of removing contamination and the aggressiveness of acid leaching prior to the application of HF. While U and Pb were highly and variably fractionated during procedures 2 and 3, the residues of CAIs obtained with procedure 1 gave the most accurate and precise Pb-Pb age for NWA 4502 CAIs so far.

4.5.2. Chronological consistency and the effect of secondary processes on CV CAI ages.

The most precise Pb-Pb isochron age of 4567.40 ± 0.27 Ma obtained for (with the uncertainty including U uncertainty for 6 residues at least one for each studied CAI using procedure 1) NWA 4502 CAIs using the measured $^{238}U/^{235}U$ ratio (Figure 4.9), is identical to four recently

dated CAIs from the CV chondrite Allende and Efremovka also using measured $^{238}U/^{235}U$ ratio which gave ages of 4567.18 ± 0.50 and 4567.3 ± 0.16 Ma respectively (Amelin et al., 2010; Connelly et al., 2012). A slightly older U-corrected Pb-Pb age, 4567.9 ± 0.3 Ma, was reported for a CAI from the CV chondrite North West Africa 6991 by Bouvier et al. (2011). A younger age was obtained for NWA 4502 CAIs after U-correction (from 4568.16 ± 0.18 Ma to 4567.40 ± 0.27 Ma). This shows the importance of U-correction to precise determination of CAI ages.

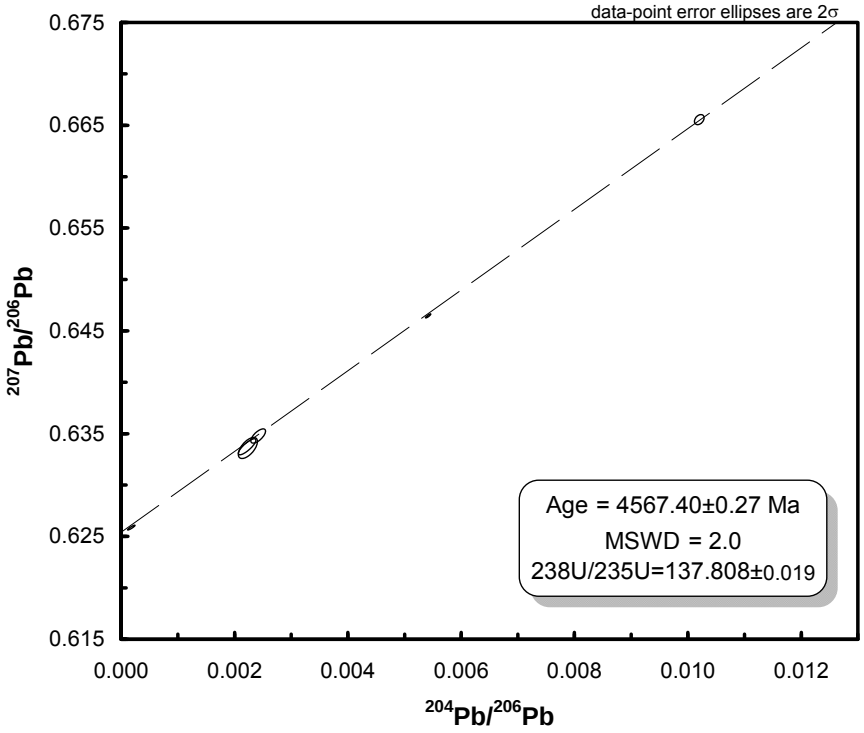

Figure 4.9: Pb-Pb isochron plot showing the preferred age obtained for four NWA 4502 CAIs.

This result indicates that alteration and thermal metamorphism in Allende, and shock metamorphism in Efremovka, did not measurably affect the U-Pb isotopic system of the CAIs. Considering the possibility that the CAI ages of all these meteorites, with different histories of secondary processes, were reset to the same degree is low, as such the difference between the much older CAI age in NWA 2364 of 4568.22 ± 0.17 Ma reported by Bouvier and Wadhwa (2010) is likely to be a result of the use of the Th/U vs. $^{238}U/^{235}U$ proxy instead of directly

measured $^{238}U/^{235}U$ ratios. Without this direct measurement of $^{238}U/^{235}U$, this age must be suspect. This conclusion can be directly checked by $^{238}U/^{235}U$ analysis of an aliquot of the CAI dated in Bouvier and Wadhwa (2010).

CHAPTER 5

SYNTHESIS AND CONCLUSIONS

This thesis is the first study of refractory inclusions in the oxidized CV chondrite NWA 4502. It demonstrates the importance of expanding the population of well-characterized refractory inclusions from a wider variety of CV chondrites. The properties of the studied refractory inclusions including availability, size and the nature and level of secondary processing provide a unique opportunity to better understand secondary processing in both extraterrestrial and terrestrial environments.

We obtained detailed petrographic, mineralogical and chemical data that show that NWA 4502 and its components experienced much less secondary alteration on the CV chondrite parent body. Comparison between these results and the data for CAIs from other CV chondrites such as Allende and Efremovka shows that all studied NWA 4502 CAI types have low levels of secondary hydrothermal alteration, thermal as well as shock metamorphism that affected CAIs in the other CV chondrites. Even though NWA 4502 shows pristine parent body characteristics, complexities discovered in some of the isotope systems, especially Rb-Sr gave an indication of a significant imprint of terrestrial weathering even though the extent of the effects of terrestrial contamination were not obvious on a macro scale and at the mineralogical level.

Initial $(^{26}Al/^{27}Al)_0$ values obtained for the studied CAIs are consistent with those of other CV CAIs and support the canonical value of ~5×10^{-5}. Correlated $^{26}Mg^*$ and $^{27}Al/^{24}Mg$ in the studied CAIs indicates their Al-Mg systematics were not significantly disturbed by secondary metamorphism. This further supports the pristine nature of NWA 4502 CAIs and the difference in secondary processing of the NWA 4502 parent body. The cause of excess scattering on isochron regressions of NWA 4502 CAIs is not clear, but it may be related to terrestrial

weathering. Further studies are required to investigate this possibility. One way to achieve this is through *in situ* analyses of minerals with different proximity to fractures and abundance of elements that are mobile in terrestrial surface environments. Regardless of the differences in the history of secondary processes both on the parent body and on the surface of the Earth, there is a consistency of initial $(^{26}Al/^{27}Al)_0$ in CV CAIs. We interpret this as a result of broad-scale homogeneity in ^{26}Al in the CV-CAI-forming region of the nebula.

NWA 4502 CAIs show clear signs of a disturbed Rb-Sr system. In spite of this, initial $^{87}Sr/^{86}Sr$ values corrected for *in situ* growth by decay of Rb were obtained from fractions from two CAIs; the type B CAI *1*, and forsterite-bearing type B CAI *5* are identical to initial $^{87}Sr/^{86}Sr$ in the Allende CAI D7 (Gray et al., 1973). Using the stable $^{84}Sr/^{86}Sr$ ratios of the studied CAIs gave a clearer indication of the role of terrestrial contamination in these CAIs. It has been shown (e.g., Moynier et al., 2012; Hans et al., 2013) that there is a difference between the measured $^{84}Sr/^{86}Sr$ ratios of CAIs and terrestrial rocks. This difference allows us to use this isotopic ratio for the first time as a tracer of Sr migration. The early acid leachates of NWA 4502 CAIs contain significant amounts of radiogenic $^{87}Sr/^{86}Sr$ and terrestrial $^{84}Sr/^{86}Sr$. These data are in contrast with the data obtained for Allende CAI A63 (Amelin et al., 2015) using the same procedures under the same laboratory conditions where initial $^{87}Sr/^{86}Sr$ between the first washes and residues are consistent indicating that the CAI did not exchange Sr with the matrix, chondrules, or with any terrestrial environment. This gives an insight into the effects of terrestrial contamination on Rb-Sr systems of NWA 4502 inclusions. Further study is necessary to better understand the difference terrestrial weathering makes to the chemistry of CAIs particularly to the alkaline earth elements.

In spite of the complexities encountered in other isotope systems, we are still able to access the primary age of these inclusions by evaluating various acid leaching procedures aimed at removing weathering products and terrestrial contamination. Even though this study has provided some insights into the effects of acid leaching on U-Pb isotope systems of NWA 4502 CAIs, further studies are required because there is still much to be understood. It is still unclear at this stage whether or not aggressive acid leaching methods play a major role in inducing fractionation of radiogenic $^{207}Pb^*/^{206}Pb^*$, however, as observed in the results of procedure 1 repeated treatment of samples with concentrated acids (7M HN03 and 6M HCl) at high temperature (100°C) for a long duration (1 hour each) does not seem to fractionate the

radiogenic residual Pb composition. This study has shown that one of the most important factors in U-Pb dating is that the analysis of the most radiogenic material can be achieved using less aggressive acid leaching methods.

We obtained a high-precision Pb-Pb isochron age with measured U isotope compositions for the studied inclusions. This age is identical to that of CV CAIs that experienced different secondary processing and leads us to the new finding that secondary processing has not substantially affected the U-Pb isotopic system of the CAIs from CV chondrites. It is highly unlikely that the CAI ages of all these meteorites, having different histories of secondary processes, were reset to the same degree.

The preferred interpretation therefore of the discrepancy between the CAI ages in NWA 2364 (Bouvier and Wadhwa, 2010) and Allende, Efremovka (Amelin et al., 2010; Connelly et al., 2012) and NWA 4502 is that the Th/U vs. $^{235}U/^{238}U$ proxy used in Bouvier and Wadhwa (2010) is not universal, and can yield an inaccurate age adjustment. This suggestion can be directly checked by $^{238}U/^{235}U$ analysis of an aliquot of the CAI dated in Bouvier and Wadhwa (2010). However, the Pb-Pb age of the Allende CAI SJ-101 (using its measured U isotope composition) is 4567.18 ± 0.50 Ma (Amelin et al., 2010) is resolvably younger than the age of 4567.90 ± 0.30 Ma (with its measured U isotope composition) reported for NWA 6991 CAI B4 by Bouvier et al. (2011). Therefore, even after accounting for possible U isotopic variations, the apparent range of Pb-Pb ages of CAIs still extends over ~0.7 Ma. Pb isotopic fractionation following CAI formation, either during late parent body processes, or possibly even during leaching in the laboratory cannot be ruled out as possible explanations for this.

CAIs have been through a lot of events throughout their history especially regarding secondary processing on parent body and in terrestrial environments. The complexities encountered with some of the isotope systems of NWA 4502 CAIs were unexpected because the cause was terrestrial contamination and this was not obvious following the initial examination. This reveals a problem concerning our limited knowledge of the effects of terrestrial contamination on carbonaceous chondrites and their components. There is therefore the need for a detailed study highlighting the effects of terrestrial contamination on carbonaceous chondrites and their components. Considerable work has been done regarding parent body alteration in meteorites and their components but not much is known about terrestrial weathering. Some work has been

done to understand the effects of cold and hot desert weathering in ordinary chondrites (Lee and Bland, 2004). A similar study for carbonaceous chondrites would be very useful.

In conclusion, CAIs are fantastic objects that date the earliest solar system. Most researchers agree that solid precursors of CAIs were melted during rapid heating events in the solar nebula then the molten droplets cooled rapidly. Some CAIs appear to have gone through this cycle more than once. CAIs subsequently experienced secondary alteration processes both in the nebula and on parent bodies. Notwithstanding alteration effects, we can see through this to a singular episode in the formation of our solar system. Combined constraints from U-Pb, Al-Mg and Sr isotopes all point to this being a brief, high-temperature episode likely a result of rapid in fall of material in to the Sun.

REFERENCES

Aléon J., Krot A. N. and McKeegan K. D. (2002) Calcium-Aluminum-rich inclusions and amoeboid olivine aggregates from the CR carbonaceous chondrites. *Meteorit. Planet. Sci.* **37,** 1729-1755.

Aleon J., Krot A. N., McKeegan K. D., MacPherson G. J. and Ulyanov A. A. (2005) Fine - grained, spinel - rich inclusions from the reduced CV chondrite Efremovka: II. Oxygen isotopic compositions. *Meteorit. Planet. Sci.* **40,** 1043-1058.

Allen J. M., Grossman L., Davis A. M. and Hutcheon I. D. (1978) Mineralogy, textures and mode of formation of a hibonite-bearing Allende inclusion. *Lunar Planet. Sci.* **9,** 1209-1233.

Amelin Y. (2006) The prospect of high-precision Pb isotopic dating of meteorites. *Meteoritics & Planetary Science* **41,** 7-17.

Amelin Y. (2008) U–Pb ages of angrites. *Geochimica et Cosmochimica Acta* **72,** 221-232.

Amelin Y., Connelly J., Zartman R., Chen J., Göpel C. and Neymark L. (2009) Modern U–Pb chronometry of meteorites: Advancing to higher time resolution reveals new problems. *Geochim. Cosmochim. Acta* **73,** 5212-5223.

Amelin Y., Ghosh A. and Rotenberg E. (2005) Unraveling the evolution of chondrite parent asteroids by precise U-Pb dating and thermal modeling. *Geochimica et Cosmochimica Acta* **69,** 505-518.

Amelin Y., Kaltenbach A., Iizuka T., Stirling C. H., Ireland T. R., Petaev M. and Jacobsen S. B. (2010) U–Pb chronology of the Solar System's oldest solids with variable $^{238}U/^{235}U$. *Earth Planet. Sci. Lett.* **300,** 343-350.

Amelin Y., Koefoed P., Yin Q. Z. and Yamashita K. (2015) Sr Isotope Systematics of the Allende CAIs A63 and SJ101. *Annual Meeting of the Meteoritical Society* **78,** Abstract #5388.

Amelin Y. and Krot A. (2007) Pb isotopic age of the Allende chondrules. *Meteoritics & Planetary Science* **42,** 1321-1335.

Amelin Y., Krot A. N., Hutcheon I. D. and Ulyanov A. A. (2002) Lead isotopic ages of chondrules and calcium-aluminum-rich inclusions. *Science* **297,** 1678-1683.

Amelin Y. and Sapah M. (2012) Cooling rates of plutonic angrites from pyroxene-phosphate U-Pb chronology. *Annual Meeting of the Meteorical Society* **75,** Abstract #5199.

Anders E. and Ebihara M. (1982) Solar-system abundances of the elements. *Geochimica et Cosmochimica Acta* **46,** 2363-2380.

Anders E. and Grevesse N. (1989) Abundances of the elements: Meteoritic and solar. *Geochim. Cosmochim. Acta* **53,** 197-214.

Ashworth J. and Barber D. (1975) Electron petrography of shock-deformed olivine in stony meteorites. *Earth and Planetary Science Letters* **27,** 43-50.

Baertschi P. (1976) Absolute ^{18}O content of standard mean ocean water. *Earth Planet. Sci. Lett.* **31,** 341-344.

Baker J., Bizzarro M., Wittig N., Connelly J. and Haack H. (2005) Early planetesimal melting from an age of 4.5662 Gyr for differentiated meteorites. *Nature* **436,** 1127-1131.

Bally J. and Langer W. (1982) Isotope-selective photodestruction of carbon monoxide. *The Astrophysical Journal* **255,** 143-148.

Beckett J. and Stolper E. (1994) The stability of hibonite, melilite and other aluminous phases in silicate melts: Implications for the origin of hibonite-bearing inclusions from carbonaceous chondrites. *Meteoritics* **29,** 41-65.

Beckett J. R. and Grossman L. (1988) The origin of type C inclusions from carbonaceous chondrites. *Earth and Planetary Science Letters* **89,** 1-14.

Bizzarro M., Baker J. A. and Haack H. (2004) Mg isotope evidence for contemporaneous formation of chondrules and refractory inclusions. *Nature* **431,** 275-278.

Bizzarro M., Baker J. A. and Haack H. (2005) Corrigendum: Mg isotope evidence for contemporaneous formation of chondrules and refractory inclusions. *Nature* **435,** 1280-1280.

Bland P., Berry F. and Pillinger C. (1998a) Rapid weathering in Holbrook: An iron - 57 Mössbauer spectroscopy study. *Meteoritics & Planetary Science* **33,** 127-129.

Bland P., Berry F., Smith T., Skinner S. and Pillinger C. (1996) The flux of meteorites to the Earth and weathering in hot desert ordinary chondrite finds. *Geochimica et Cosmochimica Acta* **60,** 2053-2059.

Bland P., Cressey G. and Menzies O. (2004) Modal mineralogy of carbonaceous chondrites by X-ray diffraction and Mossbauer spectroscopy. *Meteoritics & Planetary Science* **39,** 3–16.

Bland P., Sexton A., Jull A., Bevan A., Berry F., Thornley D., Astin T., Britt D. and Pillinger C. (1998b) Climate and rock weathering: A study of terrestrial age dated ordinary chondritic meteorites from hot desert regions. *Geochimica et Cosmochimica Acta* **62,** 3169-3184.

Bland P., Zolensky M., Benedix G. and Sephton M. (2006) Weathering of chondritic meteorites. *Meteorites and the early solar system II* **1,** 853-867.

Blander M. and Fuchs L. H. (1975) Calcium-aluminum-rich inclusions in the Allende meteorite: evidence for a liquid origin. *Geochimica et Cosmochimica Acta* **39,** 1605-1619.

Bouvier A., Blichert-Toft J., Moynier F., Vervoort J. D. and Albarède F. (2007) Pb–Pb dating constraints on the accretion and cooling history of chondrites. *Geochimica et Cosmochimica Acta* **71,** 1583-1604.

Bouvier A., Brennecka G. A. and Wadhwa M. (2011) Absolute chronology of the first solids in the Solar System. *LPI Contrib.* **1639,** 9054.

Bouvier A. and Wadhwa M. (2010) The age of the Solar System redefined by the oldest Pb–Pb age of a meteoritic inclusion. *Nature Geosci.* **3,** 637-641.

Boynton W., Frazier R. and Macdougall J. (1980) Identification of an ultra-refractory component in the Murchison meteorite. *Lunar and Planetary Science Conference* **11,** 103-105.

Boynton W. V. (1975) Fractionation in the solar nebula: condensation of yttrium and the rare earth elements. *Geochimica et Cosmochimica Acta* **39,** 569-584.

Brearley A. (2003) Nebular versus parent-body processing. *Treatise on Geochemistry* **1,** 247-268.

Brearley A. J. (1993) Matrix and fine-grained rims in the unequilibrated CO3 chondrite, ALHA77307: Origins and evidence for diverse, primitive nebular dust components. *Geochimica et Cosmochimica Acta* **57,** 1521-1550.

Brearley A. J. and Krot A. N. (2013) Metasomatism in the early solar system: The record from chondritic meteorites. *In Metasomatism and the Chemical Transformation of Rock-Lecture notes in Earth Systems Sciences* (eds. Harlov D. E. and Austrheim H.), 659-789. Springer.

Brennecka G., Weyer S., Wadhwa M., Janney P., Zipfel J. and Anbar A. (2010) $^{238}U/^{235}U$ variations in meteorites: Extant ^{247}Cm and implications for Pb-Pb dating. *Science* **327,** 449-451.

Bullock E., Nakashima D., Tenner T., Kita N., MacPherson G., Ivanova M., Krot A., Petaev M. and Jacobsen S. (2015) High precision Al-Mg systematics in Forsterite bearing Type B CAIs. *Lunar and Planetary Science Conference* **46,** Abstract #1971.

Bullock E. S., MacPHERSON G. J., Nagashima K., Krot A. N., Petaev M. I., Jacobsen S. B. and Ulyanov A. A. (2012) Forsterite - bearing type B refractory inclusions from CV3 chondrites: From aggregates to volatilized melt droplets. *Meteorit. Planet. Sci.* **47,** 2128-2147.

Charlier B., Ginibre C., Morgan D., Nowell G., Pearson D., Davidson J. and Ottley C. (2006) Methods for the microsampling and high-precision analysis of strontium and rubidium isotopes at single crystal scale for petrological and geochronological applications. *Chemical Geology* **232,** 114-133.

Chaumard N., Devouard B., Bouvier A. and Wadhwa M. (2014) Metamorphosed calcium - aluminum - rich inclusions in CK carbonaceous chondrites. *Meteoritics & Planetary Science* **49,** 419-452.

Chen J. and Tilton G. (1976) Isotopic lead investigations on the Allende carbonaceous chondrite. *Geochim.Cosmochim. Acta* **40,** 635-643.

Chen J. and Wasserburg G. (1980) A search for isotopic anomalies in uranium. *Geophysical Research Letters* **7,** 275-278.

Chen J. and Wasserburg G. (1981) The isotopic composition of uranium and lead in Allende inclusions and meteoritic phosphates. *Earth Planet. Sci. Lett.* **52,** 1-15.

Christophe Michel-Lévy M. (1968) Un chondre exceptionnel dans la météorite de Vigarano. *Bull. Soc. Fr. Minéral. Cristallogr.* **91,** 212-214.

Clayton R., Hinton R. and Davis A. (1988) Isotopic variations in the rock-forming elements in meteorites. *Philosophical Transactions of the Royal Society of London. Series A, Mathematical and Physical Sciences* **325,** 483-501.

Clayton R., Mayeda T., MacPherson G. and Grossman L. (1987) Oxygen and silicon isotopes in inclusions and chondrules from Vigarano. *Lunar and Planetary Science Conference* **18,** 185.

Clayton R., Mayeda T., Palme H. and Laughlin J. (1986) Oxygen, silicon, and magnesium isotopes in Leoville refractory inclusions. *Lunar and Planetary Science Conference* **17,** 139-140.

Clayton R. N. (1978) Isotopic anomalies in the early solar system. *Annual Review of Nuclear and Particle Science* **28,** 501-522.

Clayton R. N. (1993a) Oxygen isotopes in meteorites. *Annual Review of Earth and Planetary Sciences* **21,** 115-149.

Clayton R. N. (1993b) Oxygen isotopes in meteorites. *Annual Rev. Earth Plane. Sci.* **21,** 115-149.

Clayton R. N. (2002) Solar system: Self-shielding in the solar nebula. *Nature* **415,** 860-861.

Clayton R. N., Grossman L. and Mayeda T. K. (1973) A component of primitive nuclear composition in carbonaceous meteorites. *Science* **182,** 485-488.

Clayton R. N. and Mayeda T. K. (1977) Correlated oxygen and magnesium isotope anomalies in Allende inclusions, I: Oxygen. *Geophys. Res. Lett.* **4,** 295-298.

Clayton R. N. and Mayeda T. K. (1984) The oxygen isotope record in Murchison and other carbonaceous chondrites. *Earth Planet. Sci. Lett.* **67,** 151-161.

Clayton R. N. and Mayeda T. K. (1999) Oxygen isotope studies of carbonaceous chondrites. *Geochimica et Cosmochimica Acta* **63,** 2089-2104.

Clayton R. N., Mayeda T. K. and Rubin A. E. (1984) Oxygen isotopic compositions of enstatite chondrites and aubrites. *Journal of Geophysical Research: Solid Earth (1978–2012)* **89,** C245-C249.

Clayton R. N., Onuma N., Grossman L. and Mayeda T. K. (1977) Distribution of the pre-solar component in Allende and other carbonaceous chondrites. *Earth Planet. Sci. Lett.* **34,** 209-224.

Connelly J. N., Amelin Y., Krot A. N. and Bizzarro M. (2008) Chronology of the Solar System's oldest solids. *The Astrophysical Journal Letters* **675,** L121.

Connelly J. N. and Bizzarro M. (2009) Pb–Pb dating of chondrules from CV chondrites by progressive dissolution. *Chemical Geology* **259,** 143-151.

Connelly J. N., Bizzarro M., Krot A. N., Nordlund Å., Wielandt D. and Ivanova M. A. (2012) The absolute chronology and thermal processing of solids in the solar protoplanetary disk. *Science* **338,** 651-655.

Davis A. M. (1984) A scandalously refractory inclusion in Ornans. *LPI Contributions* **537,** 49.

Davis A. M. (1985) Refractory Inclusions in the Ornans C3O Chondrite. *Lunar and Planetary Science Conference* **16,** 1084.

Davis A. M. (1991) Ultrarefractory inclusions and the nature of the group II REE fractionation. *Meteoritics* **26,** 330.

Davis A. M. and Grossman L. (1979) Condensation and fractionation of rare earths in the solar nebula. *Geochimica et Cosmochimica Acta* **43,** 1611-1632.

Devouard B., Ferriere L., Zanda B. and Messaoudi M. (2006) Mineralogy and petrology of TAN057 (C4) and comparison to the CV and CK groups. *Meteorit. Planet. Sci.* **41,** A203.

Dyl K. A., Young E. D. and Krot A. N. (2008) In-Situ UV-Laser Fluorination Oxygen Isotopic Analyses of an Efremovka CAI and Matrix: Implications for Oxygen Isotopic Exchange in the Solar Nebula. *Lunar Planet. Sci.* **39,** Abstract #2486.

El Goresy A., Zinner E., Matsunami S., Palme H., Spettel B., Lin Y. and Nazarov M. (2002) Efremovka 101.1: A CAI with ultrarefractory REE patterns and enormous enrichments of Sc, Zr, and Y in fassaite and perovskite. *Geochimica et Cosmochimica Acta* **66,** 1459-1491.

Fagan T., Guan Y. and MacPherson G. (2007) Al - Mg isotopic evidence for episodic alteration of Ca-Al-rich inclusions from Allende. *Meteorit. Planet. Sci.* **42,** 1221-1240.

Fahey A., Goswami J., McKeegan K. and Zinner E. (1987) ^{26}Al, ^{244}Pu, ^{50}Ti, REE, and trace element abundances in hibonite grains from CM and CV meteorites. *Geochimica et Cosmochimica Acta* **51,** 329-350.

Fegley Jr B. (1999) Chemical and physical processing of presolar materials in the solar nebula and the implications for preservation of presolar materials in comets. *In Composition and Origin of Cometary Materials* (eds., 239-252. Springer.

Ford R. and Brearley A. (2007a) Phyllosilicates in two coarse-grained Allende CAIs: evidence for advanced hydration. *Lunar and Planetary Science Conference* **38,** Abstract #2411.

Ford R. and Brearley A. (2007b) Timing and Location of CAI Alteration in Allende: Evidence from CAI-Matrix Interactions. *Workshop on Chronology of Meteorites* **1,** 60-61.

Ford R. and Brearley A. (2008) Element exchange between matrix and CAIs in the Allende meteorite *Lunar Planet. Sci.* **39,** Abstract #2399.

Ford R. and Brearley A. (2010) Discovery of vesuvianite and kaolinite formed during the alteration of melilite in an Allende Type A CAI: characterization by FIB/TEM. *Lunar Planet. Sci.* **41,** Abstract #1402.

Galy A., Hutcheon I. and Grossman L. (2004) $(^{26}Al/^{27}Al)_0$ of the Solar Nebula Inferred from Al-Mg Systematic in Bulk CAIs from CV3 Chondrites. *Lunar and Planetary Science Conference* **35,** Abstract #1790.

Gao Y. Q. and Marcus R. (2002) On the theory of the strange and unconventional isotopic effects in ozone formation. *The Journal of chemical physics* **116,** 137-154.

Geiger C., Kleppa O., Mysen B., Lattimer J. and Grossman L. (1988) Enthalpies of formation of $CaAl_4O_7$ and $CaAl_{12}O_{19}$ (hibonite) by high temperature, alkali borate solution calorimetry. *Geochim. Cosmochim. Acta* **52,** 1729-1736.

Geiger T. and Bischoff A. (1995) Formation of opaque minerals in CK chondrites. *Planetary and Space Science* **43,** 485-498.

Gerstenberger H. and Haase G. (1997) A highly effective emitter substance for mass spectrometric Pb isotope ratio determinations. *Chemical Geology* **136,** 309-312.

Golden D., Morris R., DW M. and Lauer H. J. (1993) Location of Nanophase Fe-oxides in palagonitic soils: Implications for Martian pigments. *Workshop on Chemical Weathering on Mars* **2,** 14-15.

Göpel C., Manhes G. and Allegre C. J. (1994) U-Pb systematics of phosphates from equilibrated ordinary chondrites. *Earth and Planetary Science Letters* **121,** 153-171.

Goswami J., Srinivasan G. and Ulyanov A. (1994) Ion microprobe studies of Efremovka CAIs: I. Magnesium isotope composition. *Geochim. Cosmochim. Acta* **58,** 431-447.

Gounelle M. and Zolensky M. E. (2001) A terrestrial origin for sulfate veins in CI1 chondrites. *Meteoritics & Planetary Science* **36,** 1321-1329.

Gray C. and Compston W. (1974) Excess ^{26}Mg in the Allende meteorite. *Nature* **251,** 495–497.

Gray C., Papanastassiou D. and Wasserburg G. (1973) The identification of early condensates from the solar nebula. *Icarus* **20,** 213-239.

Greenwood R., Franchi I., Kearsley A. and Alard O. (2004) The relationship between CK and CV chondrites: a single parent body source? *Lunar and Planetary Science Conference* **35,** Abstract #1664.

Greenwood R., Franchi I., Kearsley A. and Alard O. (2010) The relationship between CK and CV chondrites. *Geochimica et Cosmochimica Acta* **74,** 1684-1705.

Greenwood R., Hutchison R., Huss G. and Hutcheon I. (1992) CAIs in CO3 meteorites: parent body or nebular alteration? *Meteoritics* **27,** 229.

Greenwood R., Kearsley A. and Franchi I. (2003) Are CK chondrites really a distinct group or just equilibrated CVs? *Meteorit. Planet. Sci.* **38** A96.

Greenwood R. C., Franchi I. A., Jambon A. and Buchanan P. C. (2005) Widespread magma oceans on asteroidal bodies in the early solar system. *Nature* **435,** 916-918.

Greenwood R. C., Lee M. R., Hutchison R. and Barber D. J. (1994a) Formation and alteration of CAIs in Cold Bokkeveld (CM2). *Geochim. Cosmochim. Acta* **58,** 1913-1935.

Greenwood R. C., Lee M. R., Hutchison R. and Barber D. J. (1994b) Formation and alteration of CAIs in Cold Bokkeveld (CM2). *Geochimica et Cosmochimica Acta* **58,** 1913-1935.

Grossman J. N., Rubin A. E. and MacPherson G. J. (1988) ALH85085: A unique volatile-poor carbonaceous chondrite with possible implications for nebular fractionation processes. *Earth Planet. Sci. Lett.* **91,** 33-54.

Grossman L. (1972) Condensation in the primitive solar nebula. *Geochim. Cosmochim. Acta* **36,** 597-619.

Grossman L. (1973) Refractory trace elements in Ca-Al-rich inclusions in the Allende meteorite. *Geochim. Cosmochim. Acta* **37,** 1119-1140.

Grossman L. (1975) Petrography and mineral chemistry of Ca-rich inclusions in the Allende meteorite. *Geochim. Cosmochim. Acta* **39,** 433-454.

Grossman L. (1980) Refractory inclusions in the Allende meteorite. *Annual Rev. Earth Planet. Sci.* **8,** 559-608.

Grossman L. and Ganapathy R. (1976) Trace elements in the Allende meteorite—II. Fine-grained. Ca-rich inclusions. *Geochim. Cosmochim. Acta* **40,** 967-977.

Grossman L. and Steele I. M. (1976) Amoeboid olivine aggregates in the Allende meteorite. *Geochimica et Cosmochimica Acta* **40,** 149-155.

Halliday A. and Porcelli D. (2001) In search of lost planets–the paleocosmochemistry of the inner solar system. *Earth and Planetary Science Letters* **192,** 545-559.

Hammond S. J., Bland P. A., Gordon S. H. and Rogers N. W. (2008) ICP-MS Analysis of a Suite of Carbonaceous Chondrites. *Lunar and Planetary Science Conference* **38,** Abstract #1786.

Hans U., Kleine T. and Bourdon B. (2013) Rb–Sr chronology of volatile depletion in differentiated protoplanets: BABI, ADOR and ALL revisited. *Earth and Planetary Science Letters* **374,** 204-214.

Hashimoto A. and Grossman L. (1987) Alteration of Al-rich inclusions inside amoeboid olivine aggregates in the Allende meteorite. *Geochimica et Cosmochimica Acta* **51,** 1685-1704.

Heidenreich III J. E. and Thiemens M. H. (1986) A non - mass - dependent oxygen isotope effect in the production of ozone from molecular oxygen: The role of molecular symmetry in isotope chemistry. *The Journal of chemical physics* **84,** 2129-2136.

Heydegger H., Foster J. and Compston W. (1979) Evidence of a new isotopic anomaly from titanium isotopic ratios in meteoric materials. *Nature* **278,** 704-707.

Hezel D. C., Russell S. S., Ross A. J. and Kearsley A. T. (2008) Modal abundances of CAIs: Implications for bulk chondrite element abundances and fractionations. *Meteoritics & Planetary Science* **43,** 1879-1894.

Hinton R. W., Davis A. M. and Scatena-Wachel D. E. (1987) Large negative Ti-50 anomalies in refractory inclusions from the Murchison carbonaceous chondrite-Evidence for

incomplete mixing of neutron-rich supernova ejecta into the solar system. *Astrophys. J.* **313,** 420-428.

Hinton R. W., Davis A. M., Scatena-Wachel D. E., Grossman L. and Draus R. J. (1988) A chemical and isotopic study of hibonite-rich refractory inclusions in primitive meteorites. *Geochim. Cosmochim. Acta* **52,** 2573-2598.

Hoffman E., Bland P., Seifu D. and Oliver F. (2000) Ferric Ion Phases in Mössbauer Spectra of "Oxidized" and "Reduced"CV3 Chondrites. *Meteoritics and Planetary Science Supplement* **35,** 75.

Hoffman E., Housley R. M., Bland P. A., Seifu D. and Oliver F. W. (2001) Fe-rich Pentlandite in Allende Bulk Samples and Separates: Mössbauer Spectroscopic Analysis. *Lunar and Planetary Science Conference* **32,** Abstract #2116.

Hoffman E. and Seifu D. (2000) Axtell and Allende: A Mössbauer spectroscopic study. *Meteoritics & Planetary Science* **35,** 431-434.

Holmes A. (1946) An estimate of the age of the earth. *Nature* **157,** 680.

Houdek G. and Gough D. (2011) On the seismic age and heavy-element abundance of the Sun. *Monthly Notices of the Royal Astronomical Society* **418,** 1217-1230.

Houtermans F. (1946) The isotope ratios in natural lead and the age of uranium. *Naturwissenschaften* **33,** 185-186.

Hsu W., Huss G. R. and Wasserburg G. (2003) Al - Mg systematics of CAIs, POI, and ferromagnesian chondrules from Ningqiang. *Meteoritics & Planetary Science* **38,** 35-48.

Hunt C. P., Singer M. J., Kletetschka G., TenPas J. and Verosub K. L. (1995) Effect of citrate-bicarbonate-dithionite treatment on fine-grained magnetite and maghemite. *Earth and Planetary Science Letters* **130,** 87-94.

Huss G. R. (1988) The role of presolar dust in the formation of the solar system. *Earth, moon, and planets* **40,** 165-211.

Huss G. R., MacPherson G. J., Wasserburg G., Russell S. S. and Srinivasan G. (2001) Aluminum - 26 in calcium - aluminum - rich inclusions and chondrules from unequilibrated ordinary chondrites. *Meteoritics & Planetary Science* **36,** 975-997.

Hutcheon I. and Hutchison R. (1989) Evidence from the Semarkona ordinary chondrite for ^{26}Al heating of small planets. *Nature* **337,** 238.

Hutcheon I. and Newton R. (1981) Mg isotopes, mineralogy and mode of formation of secondary phases in C3 refractory inclusions. *Lunar Planet. Sci.* **12,** 491-493.

Hutchison R. (2004) Meteorites: A petrologic, chemical and isotopic synthesis.

Huyskens M. H., Iizuka T. and Amelin Y. (2012) Evaluation of colloidal silicagels for lead isotopic measurements using thermal ionisation mass spectrometry. *Journal of Analytical Atomic Spectrometry* **27,** 1439-1446.

Ickert R., Hiess J., Williams I., Holden P., Ireland T., Lanc P., Schram N., Foster J. and Clement S. (2008) Determining high precision, in situ, oxygen isotope ratios with a SHRIMP II: Analyses of MPI-DING silicate-glass reference materials and zircon from contrasting granites. *Chem. Geol.* **257,** 114-128.

Ireland T. (2012) Oxygen isotope tracing of the Solar System. *Australian Journal of Earth Sciences* **59,** 225-236.

Ireland T., Compston W. and Heydegger H. (1985) Titanium isotopic anomalies in hibonites from the Murchison carbonaceous chondrite. *Geochimica et Cosmochimica Acta* **49,** 1989-1993.

Ireland T., Fahey A. and Zinner E. (1991) Hibonite-bearing microspherules: A new type of refractory inclusions with large isotopic anomalies. *Geochim. Cosmochim. Acta* **55,** 367-379.

Ireland T. R. (1990) Presolar isotopic and chemical signatures in hibonite-bearing refractory inclusions from the Murchison carbonaceous chondrite. *Geochim. Cosmochim. Acta* **54,** 3219-3237.

Ireland T. R., Fahey A. and Zinner E. (1988a) Trace-element abundances in hibonites from the Murchison carbonaceous chondrite: Constraints on high-temperature processes in the solar nebula. *Geochim. Cosmochim. Acta* **52,** 2841-2854.

Ireland T. R., Fahey A. and Zinner E. (1988b) Trace-element abundances in hibonites from the Murchison carbonaceous chondrite: Constraints on high-temperature processes in the solar nebula. *Geochimica et Cosmochimica Acta* **52,** 2841-2854.

Ireland T. R. and Fegley B. (2000) The solar system's earliest chemistry: Systematics of refractory inclusions. *Int. Geol. Rev.* **42,** 865-894.

Itoh S., Kojima H. and Yurimoto H. (2004) Petrography and oxygen isotopic compositions in refractory inclusions from CO chondrites. *Geochimica et Cosmochimica Acta* **68,** 183-194.

Jacobsen B., Matzel J., Hutcheon I. D., Krot A. N., Yin Q.-Z., Nagashima K., Ramon E. C., Weber P. K., Ishii H. A. and Ciesla F. J. (2011) Formation of the short-lived radionuclide 36Cl in the protoplanetary disk during late-stage irradiation of a volatile-rich reservoir. *The Astrophysical Journal Letters* **731,** L28.

Jacobsen B., Yin Q.-z., Moynier F., Amelin Y., Krot A. N., Nagashima K., Hutcheon I. D. and Palme H. (2008) ^{26}Al-^{26}Mg and ^{207}Pb-^{206}Pb systematics of Allende CAIs: Canonical solar initial ^{26}Al/^{27}Al ratio reinstated. *Earth and Planetary Science Letters* **272,** 353-364.

Jaffey A., Flynn K., Glendenin L., Bentley W. t. and Essling A. (1971) Precision measurement of half-lives and specific activities of U 235 and U 238. *Physical Review C* **4,** 1889.

Jones R. H., Rudraswami N. G. and Ziegler K. (2014) Primary Oxygen Isotope Distribution in Chondrules and Refractory Inclusions from CV Carbonaceous Chondrites. *Lunar Planet. Sci.* **45,** Abstract #1512.

Kallemeyn G. W., Rubin A. E. and Wasson J. T. (1996) The compositional classification of chondrites: VII. The R chondrite group. *Geochimica et Cosmochimica Acta* **60,** 2243-2256.

Kaltenbach A. (2013) Uranium isotopic analysis of terrestrial and extraterrestrial samples. *Unpublished PhD Thesis* University of Otago.

Keller L. P., Thomas K. L., Clayton R. N., Mayeda T. K., DeHart J. M. and McKay D. S. (1994) Aqueous alteration of the Bali CV3 chondrite: Evidence from mineralogy, mineral chemistry, and oxygen isotopic compositions. *Geochimica et Cosmochimica Acta* **58,** 5589-5598.

Kimura M., El Goresy A., Palme H. and Zinner E. (1993) Ca-Al-rich inclusions in the unique chondrite ALH85085: Petrology, chemistry and isotopic compositions. *Geochim. Cosmochim. Acta* **57,** 2329-2359.

Kita N., Huss G., Tachibana S., Amelin Y., Nyquist L. and Hutcheon I. (2005) Constraints on the origin of chondrules and CAIs from short-lived and long-lived radionuclides. *ASP Conf. Ser Chondrites and the Protoplanetary disk* **341,** 558.

Kita N. T., Yin Q. Z., MacPherson G. J., Ushikubo T., Jacobsen B., Nagashima K., Kurahashi E., Krot A. N. and Jacobsen S. B. (2013) ^{26}Al - ^{26}Mg isotope systematics of the first solids in the early solar system. *Meteoritics & Planetary Science* **48,** 1383-1400.

Kleine T., Münker C., Mezger K. and Palme H. (2002) Rapid accretion and early core formation on asteroids and the terrestrial planets from Hf–W chronometry. *Nature* **418,** 952-955.

Kojima T., Yada S. and Tomeoka K. (1995) Ca-Al-rich inclusions in three Antarctic CO3 chondrites, Yamato-81020 Yamato-82050 and Yamato-790992: Record of lowtemperature alteration. *Antarctic Meteorite Research* **8,** 79.

Kornacki A. S. and Fegley B. (1984) Origin of spinel - rich chondrules and inclusions in carbonaceous and ordinary chondrites. *J. Geophys. Res.: Solid Earth (1978–2012)* **89,** B588-B596.

Kornacki A. S. and Fegley B. (1986) The abundance and relative volatility of refractory trace elements in Allende Ca, Al-rich inclusions: implications for chemical and physical processes in the solar nebula. *Earth and Planetary Science Letters* **79,** 217-234.

Krot A., Nagashima K., Hutcheon I., Ishii H., Jacobsen B., Yin Q.-Z., Davis A. and Simon S. (2010) Mineralogy, petrography, oxygen and magnesium isotopic compositions and formation age of grossular-bearing assemblages in the Allende CAIs. *Lunar Planet. Sci.* **41,** Abstract #1406.

Krot A., Yurimoto H., Petaev M., Hutcheon I., Wark D., Libourel G., Tissandier L. and Paque J. (2005) Coarse-grained Anorthite-rich (Type C) CAIs in Carbonaceous Chondrites: Evidence for a Complex Formation History. *Meteoritics and Planetary Science Supplement* **40,** 5256.

Krot A. N. and Bizzarro M. (2009) Chronology of meteorites and the early solar system. *Geochimica et Cosmochimica Acta* **73,** 4919-4921.

Krot A. N., Hutcheon I. D., Brearley A. J., Pravdivtseva O. V., Petaev M. I. and Hohenberg C. M. (2006a) Timescales and settings for alteration of chondritic meteorites. *Meteorites and the early solar system II* **1,** 525-553.

Krot A. N., McKeegan K. D., Huss G. R., Liffman K., Sahijpal S., Hutcheon I. D., Srinivasan G., Bischoff A. and Keil K. (2006b) Aluminum-magnesium and oxygen isotope study of relict Ca-Al-rich inclusions in chondrules. *Astrophys. J.* **639,** 1227.

Krot A. N., McKeegan K. D., Russell S. S., Meibom A., Weisberg M. K., Zipfel J., Krot T. V., Fagan T. J. and Keil K. (2001) Refractory calcium-aluminum-rich inclusions and aluminum - diopside - rich chondrules in the metal - rich chondrites Hammadah al Hamra 237 and Queen Alexandra Range 94411. *Meteorit. Planet. Sci.* **36,** 1189-1216.

Krot A. N., Nagashima K., Bizzarro M., Huss G. R., Davis A. M., Meyer B. S. and Ulyanov A. A. (2008) Multiple generations of refractory inclusions in the metal-rich carbonaceous chondrites Acfer 182/214 and Isheyevo. *The Astrophysical Journal* **672,** 713.

Krot A. N., Petaev M. I., Russell S. S., Itoh S., Fagan T. J., Yurimoto H., Chizmadia L., Weisberg M. K., Komatsu M. and Ulyanov A. A. (2004) Amoeboid olivine aggregates and related objects in carbonaceous chondrites: records of nebular and asteroid processes. *Chemie der Erde-Geochemistry* **64,** 185-239.

Krot A. N., Petaev M. I., Scott E. R., Choi B. G., Zolensky M. E. and Keil K. (1998) Progressive alteration in CV3 chondrites: More evidence for asteroidal alteration. *Meteorit. Planet. Sci.* **33,** 1065-1085.

Krot A. N., Scott E. R. and Zolensky M. E. (1995) Mineralogical and chemical modification of components in CV3 chondrites: nebular or asteroidal processing? *Meteoritics* **30,** 748-775.

Krot A. N., Yurimoto H., Hutcheon I. D., Libourel G., Chaussidon M., Tissandier L., Petaev M. I., MacPherson G. J., Paque-Heather J. and Wark D. (2007) Type C Ca, Al-rich inclusions from Allende: Evidence for multistage formation. *Geochimica et Cosmochimica Acta* **71,** 4342-4364.

Kunihiro T., Rubin A. E., McKeegan K. D. and Wasson J. T. (2004) Initial $^{26}Al/^{27}Al$ in carbonaceous-chondrite chondrules: too little ^{26}Al to melt asteroids. *Geochimica et Cosmochimica Acta* **68,** 2947-2957.

Larimer J. W. (1967) Chemical fractionations in meteorites—I. Condensation of the elements. *Geochimica et Cosmochimica Acta* **31,** 1215-1238.

Larsen K. K., Trinquier A., Paton C., Schiller M., Wielandt D., Ivanova M. A., Connelly J. N., Nordlund Å., Krot A. N. and Bizzarro M. (2011) Evidence for magnesium isotope heterogeneity in the solar protoplanetary disk. *The Astrophysical Journal Letters* **735,** L37.

Le Roux L. and Glendenin L. (1963) Half-life of ^{232}Th. *Proceedings of the National Meeting on Nuclear Energy* **83.**

Lee D.-C., Halliday A. N., Snyder G. A. and Taylor L. A. (1997) Age and origin of the Moon. *Science* **278,** 1098-1103.

Lee M. R. and Bland P. A. (2004) Mechanisms of weathering of meteorites recovered from hot and cold deserts and the formation of phyllosilicates. *Geochimica et Cosmochimica Acta* **68,** 893-916.

Lee T. (1979) New isotopic clues to solar system formation. *Reviews of Geophysics* **17,** 1591-1611.

Lee T. (1988) Implications of isotopic anomalies for nucleosynthesis. *Meteorites and the early solar system* **1,** 1063-1089.

Lee T., Papanastassiou D. and Wasserburg G. (1976) Correction to "Demonstration of ^{26}Mg excess in Allende and evidence for ^{26}Al". *Geophysical Research Letters* **3,** 109-112.

Lee T., Papanastassiou D. and Wasserburg G. (1977) Aluminum-26 in the early solar system-Fossil or fuel. *The Astrophysical Journal* **211,** L107-L110.

Li W., Ni B., Jin D. and Zhang Q. (1988) Measurement of the absolute abundance of Oxygen-17 in V-SMOW. *Sci. Bull.* **19,** 008.

Lord III H. C. (1965) Molecular equilibria and condensation in a solar nebula and cool stellar atmospheres. *Icarus* **4,** 279-288.

Ludwig K. R. (1980) Calculation of uncertainties of U-Pb isotope data. *Earth and Planetary Science Letters* **46,** 212-220.

Ludwig K. R. (2003) User's manual for Isoplot 3.00: a geochronological toolkit for Microsoft Excel.

Lugmair G. and Galer S. (1992) Age and isotopic relationships among the angrites Lewis Cliff 86010 and Angra dos Reis. *Geochimica et Cosmochimica Acta* **56,** 1673-1694.

Lyons J. and Young E. (2005) CO self-shielding as the origin of oxygen isotope anomalies in the early solar nebula. *Nature* **435,** 317-320.

Macdougall J. and Goswami J. (1981) Windows to early solar system processes: Refractory inclusions in the CV and CM chondrites. *Proceedings of the Indian Academy of Sciences-Earth and Planetary Sciences* **90,** 1-26.

MacPherson G., Bullock E., Janney P., Kita N., Ushikubo T., Davis A., Wadhwa M. and Krot A. (2010) Early solar nebula condensates with canonical, not supracanonical, initial ^{26}Al/^{27}Al ratios. *The Astrophysical Journal Letters* **711,** L117.

MacPherson G. and Grossman L. (1979) Melted and Non-Melted Coarse-Grained Ca-Al-Rich Inclusions in Allende. *Meteoritics* **14,** 479.

MacPherson G., Kita N., Ushikubo T., Bullock E. and Davis A. (2012) Well-resolved variations in the formation ages for Ca–Al-rich inclusions in the early Solar System. *Earth and Planetary Science Letters* **331,** 43-54.

MacPherson G., Simon S., Davis A., Grossman L. and Krot A. (2005) Calcium-aluminum-rich inclusions: Major unanswered questions. *In Chondrites and the Protoplanetary disk* (eds. Krot A. N., Scott E. R. D. and Reipurth B.), ASP Conf. Ser. 341 225-250.

MacPherson G. J., Bar-Matthews M., Tanaka T., Olsen E. and Lawrence G. (1983) Refractory inclusions in the Murchison meteorite. *Geochim. Cosmochim. Acta* **47,** 823-839.

MacPherson G. J., Davis A. M. and Zinner E. K. (1995) The distribution of aluminum - 26 in the early Solar System—A reappraisal. *Meteoritics* **30,** 365-386.

MacPherson G. J. and Grossman L. (1984) "Fluffy" Type A Ca-, Al-rich inclusions in the Allende meteorite. *Geochim. Cosmochim. Acta* **48,** 29-46.

MacPherson G. J., Grossman L., Hashimoto A., Bar - Matthews M. and Tanaka T. (1984) Petrographic studies of refractory inclusions from the Murchison meteorite. *J. Geophys. Res.: Solid Earth (1978–2012)* **89,** C299-C312.

MacPherson G. J., Wark D. and Armstrong J. T. (1988) Primitive material surviving in chondrites-Refractory inclusions. *Meteorites and the early solar system* **1,** 746-807.

Mane P., Brennecka G. A., Romaniello S. J. and Wadhwa M. (2014) Mg and U Isotopic Systematics in Allende CAIs: Implications for the Origin of Uranium Isotopic Variation in Refractory Inclusions. *Lunar and Planetary Science Conference* **45,** Abstract #1685.

Mao X.-Y., Ward B. J., Grossman L. and MacPherson G. J. (1990) Chemical compositions of refractory inclusions from the Vigarano and Leoville carbonaceous chondrites. *Geochim.Cosmochim. Acta* **54,** 2121-2132.

Marcus R. (2004) Mass-independent isotope effect in the earliest processed solids in the solar system: A possible chemical mechanism. *The Journal of chemical physics* **121,** 8201-8211.

Martin P. M. and Mason B. (1974) Major and trace elements in the Allende meteorite. *Nature geoscience* **249** 333–334.

Mason B. and Martin P. M. (1977) Geochemical differences among components of the Allende meteorite. *Smithson. Contrib. Earth Sci* **19,** 84-95.

Mason B. and Taylor S. R. (1982a) Inclusions in the Allende meteorite. *Smithsonian Contrib. Earth Sci.* **1,** 30.

Mason B. and Taylor S. R. (1982b) Inclusions in the Allende meteorite. *Smithsonian Contributions to the Earth Sciences* **1,** 30.

Matsuda H. (1974) Double focusing mass spectrometers of second order. *International Journal of Mass Spectrometry and Ion Physics* **14,** 219-233.

Mauersberger K., Morton J., Schueler B., Stehr J. and Anderson S. (1993) Multi - isotope study of ozone: Implications for the heavy ozone anomaly. *Geophysical Research Letters* **20,** 1031-1034.

McKeegan K., Kallio A., Heber V., Jarzebinski G., Mao P., Coath C., Kunihiro T., Wiens R., Nordholt J. and Moses R. (2011) The oxygen isotopic composition of the Sun inferred from captured solar wind. *Science* **332,** 1528-1532.

McKeegan K. D. and Leshin L. A. (2001) Stable isotope variations in extraterrestrial materials. *Reviews in Mineralogy and Geochemistry* **43,** 279-318.

McSween Jr H. Y. (1977) Petrographic variations among carbonaceous chondrites of the Vigarano type. *Geochim. Cosmochim. Acta* **41,** 1777-1790.

McSween Jr H. Y. and Labotka T. C. (1993) Oxidation during metamorphism of the ordinary chondrites. *Geochimica et Cosmochimica Acta* **57,** 1105-1114.

Meeker G., Wasserburg G. and Armstrong J. (1983) Replacement textures in CAI and implications regarding planetary metamorphism. *Geochim. Cosmochim. Acta* **47,** 707-721.

Mehra O. and Jackson M. (1958) Iron-oxide removalfrom soils and clays by Dithionite-Citrate system buffered with Sodium Bicarbonate. *National Conference on Clays and Clay Minerals* **7,** 317-327.

Montmerle T., Augereau J.-C., Chaussidon M., Gounelle M., Marty B. and Morbidelli A. (2006) Solar system formation and early evolution: the first 100 million years. *From Suns to Life: A Chronological Approach to the History of Life on Earth,* 39-95.

Moynier F., Agranier A., Hezel D. C. and Bouvier A. (2010) Sr stable isotope composition of Earth, the Moon, Mars, Vesta and meteorites. *Earth and Planetary Science Letters* **300,** 359-366.

Moynier F., Day J. M., Okui W., Yokoyama T., Bouvier A., Walker R. J. and Podosek F. A. (2012) Planetary-scale strontium isotopic heterogeneity and the age of volatile depletion of early solar system materials. *The Astrophysical Journal* **758,** 45.

Navon O. and Wasserburg G. (1985) Self-shielding in O_2—a possible explanation for oxygen isotopic anomalies in meteorites? *Earth and Planetary Science Letters* **73,** 1-16.

Nebel O., Scherer E. E. and Mezger K. (2011) Evaluation of the 87 Rb decay constant by age comparison against the U–Pb system. *Earth and Planetary Science Letters* **301,** 1-8.

Neumann W. and Huster E. (1974) The half-life of ^{87}Rb measured as difference between the isotopes ^{87}Rb and ^{85}Rb. *Zeitschrift für Physik* **270,** 121-127.

Niemeyer S. and Lugmair G. (1981) Ubiquitous isotopic anomalies in Ti from normal Allende inclusions. *Earth and Planetary Science Letters* **53,** 211-225.

Niemeyer S. and Lugmair G. (1984) Titanium isotopic anomalies in meteorites. *Geochimica et Cosmochimica Acta* **48,** 1401-1416.

Norris T., Gancarz A., Rokop D. and Thomas K. (1983) Half - life of ^{26}Al. *Journal of Geophysical Research: Solid Earth (1978–2012)* **88,** B331-B333.

Nyquist L., Bansal B., Wiesmann H. and Shih C. Y. (1994) Neodymium, strontium and chromium isotopic studies of the LEW86010 and Angra dos Reis meteorites and the chronology of the angrite parent body. *Meteoritics* **29,** 872-885.

Nyquist L., Shih C., Wiesmann H. and Mikouchi T. (2003) Fossil ^{26}Al and ^{53}Mn in D'Orbigny and Sahara 99555 and the Timescale for Angrite Magmatism. *Lunar and Planetary Institute Science Conference Abstracts* **34,** Abstract #1388.

Palme H., Wlotzka F., Nagel K. and El Goresy A. (1982) An ultra-refractory inclusion from the Ornans carbonaceous chondrite. *Earth and Planetary Science Letters* **61,** 1-12.

Papanastassiou D., Wasserburg G. and Bogdanovski O. (2005) The ^{53}Mn-^{53}Cr system in CAIs: An update. *Lunar Planet. Sci.* **36,** Abstract #2198.

Papanastassiou D. A. and Wasserburg G. (1969) Initial strontium isotopic abundances and the resolution of small time differences in the formation of planetary objects. *Earth Planet. Sci. Lett.* **5,** 361-376.

Paton C., Schiller M. and Bizzarro M. (2013) Identification of an ^{84}Sr-depleted Carrier in Primitive Meteorites and Implications for Thermal Processing in the Solar Protoplanetary Disk. *The Astrophysical Journal Letters* **763,** L40.

Patterson C., Tilton G. and Inghram M. (1955) Age of the earth. *Science* **121,** 69-75.

Petaev M. I. and Jacobsen S. B. (2009) Petrologic study of SJ101, a new forsterite-bearing CAI from the Allende CV3 chondrite. *Geochim. Cosmochim. Acta* **73,** 5100-5114.

Petaev M. I., Nagashima K., Krot A. N. and Jacobsen S. B. (2010) Oxygen Isotopic Compositions of the Allende FoB CAI SJ101. *Lunar Planet. Sci.* **41,** Abstract #1818.

Podosek F. A. (1978) Isotopic structures in solar system materials. *Annual Review of Astronomy and Astrophysics* **16,** 293-334.

Podosek F. A., Zinner E. K., Macpherson G. J., Lundberg L. L., Brannon J. C. and Fahey A. J. (1991) Correlated study of initial ^{87}Sr/^{86}Sr and Al-Mg isotopic systematics and petrologic properties in a suite of refractory inclusions from the Allende meteorite. *Geochim. Cosmochim. Acta* **55,** 1083-1110.

Reynolds J. H. (1967) Isotopic abundance anomalies in the solar system. *Annual Review of Nuclear Science* **17,** 253-316.

Richter S., Eykens R., Kühn H., Aregbe Y., Verbruggen A. and Weyer S. (2010) New average values for the ^{238}U/^{235}U isotope ratios of natural uranium standards. *International Journal of Mass Spectrometry* **295,** 94-97.

Rollinson H. R. (2009). *Early Earth systems: a geochemical approach*, John Wiley & Sons.

Rubin A. E. and Krot A. N. (1996) Multiple Heating of Chondrules. *In Chondrules and the protoplanetary disk* (eds.), 173.

Rumble D., Miller M. F., Franchi I. and Greenwood R. (2007) Oxygen three-isotope fractionation lines in terrestrial silicate minerals: An inter-laboratory comparison of hydrothermal quartz and eclogitic garnet. *Geochimica et Cosmochimica Acta* **71,** 3592-3600.

Russell S., Huss G., Fahey A., Greenwood R., Hutchison R. and Wasserburg G. (1998) An isotopic and petrologic study of calcium-aluminum-rich inclusions from CO3 meteorites. *Geochimica et Cosmochimica Acta* **62,** 689-714.

Sapah M. S. and Krot A. N. (2013) NWA 4502. *in Meteoritical Bulletin* **101** 19-20 (September 2015).

Schoene B. (2014) U–Th–Pb Geochronology. *Treatise on Geochemistry,* 341-378.

Scott E. and Krot A. (2003) Chondrites and their components. *Treatise on Geochemistry* **1,** 143-200.

Scott E. and Krot A. Chondritic meteorites and the high-temperature nebular origins of their components. Chondrites and the protoplanetary disk, 2005. 15.

Scott E. R. (2007) Chondrites and the protoplanetary disk. *Annu. Rev. Earth Planet. Sci.* **35,** 577-620.

Scott E. R. and Jones R. H. (1990) Disentangling nebular and asteroidal features of C03 carbonaceous chondrite meteorites. *Geochimica et Cosmochimica Acta* **54,** 2485-2502.

Scott E. R., Keil K. and Stoeffler D. (1992) Shock metamorphism of carbonaceous chondrites. *Geochim. Cosmochim. Acta* **56,** 4281-4293.

Searle M., Noble S., Cottle J., Waters D., Mitchell A., Hlaing T. and Horstwood M. (2007) Tectonic evolution of the Mogok metamorphic belt, Burma (Myanmar) constrained by U - Th - Pb dating of metamorphic and magmatic rocks. *Tectonics* **26.**

Simon J. I. and Young E. D. (2011) Resetting, errorchrons and the meaning of canonical CAI initial $^{26}Al/^{27}Al$ values. *Earth and Planetary Science Letters* **304,** 468-482.

Simon S., Davis A. and Grossman L. (1999) Origin of compact type A refractory inclusions from CV3 carbonaceous chondrites. *Geochimi. Cosmochim. Acta* **63,** 1233-1248.

Simon S., Grossman L., Casanova I., Symes S., Benoit P., Sears D. and Wacker J. (1995) Axtell, a new CV3 chondrite find from Texas. *Meteoritics* **30,** 42-46.

Simon S. B., Davis A. M. and Grossman L. (1996) A unique ultrarefractory inclusion from the Murchison meteorite. *Meteoritics & Planetary Science* **31,** 106-115.

Simon S. B., Davis A. M. and Grossman L. (1998) Formation of an unusual compact Type A refractory inclusion from Allende. *Meteorit. Planet. Sci.* **33,** 115-126.

Simon S. B., Grossman L. and Davis A. M. (1997) Multiple generations of hibonite in spinel - hibonite inclusions from Murchison. *Meteorit. Planet. Sci.* **32,** 259-269.

Srinivasan G., Huss G. and Wasserburg G. (2000) A petrographic, chemical, and isotopic study of calcium - aluminum - rich inclusions and aluminum - rich chondrules from the Axtell (CV3) chondrite. *Meteorit. Planet. Sci.* **35,** 1333-1354.

Stacey J. t. and Kramers J. (1975) Approximation of terrestrial lead isotope evolution by a two-stage model. *Earth and Planetary Science Letters* **26,** 207-221.

Steiger R. H. and Jäger E. (1977) Subcommission on geochronology: convention on the use of decay constants in geo-and cosmochronology. *Earth and Planetary Science Letters* **36,** 359-362.

Steiger R. H. and Wasserburg G. (1966) Systematics in the Pb^{208} - Th^{232} , Pb^{207} - U^{235}, and Pb^{206} - U^{238} Systems. *Journal of Geophysical Research* **71,** 6065-6090.

Stirling C. H., Andersen M. B., Potter E.-K. and Halliday A. N. (2007) Low-temperature isotopic fractionation of uranium. *Earth and Planetary Science Letters* **264,** 208-225.

Sylvester P. J., Simon S. B. and Grossman L. (1993) Refractory inclusions from the Leoville, Efremovka, and Vigarano C3V chondrites: Major element differences between Types A and B, and extraordinary refractory siderophile element compositions. *Geochim. Cosmochim. Acta* **57,** 3763-3784.

Tanaka T. and Masuda A. (1973) Rare-earth elements in matrix, inclusions, and chondrules of the Allende meteorite. *Icarus* **19,** 523-530.

Tatsumoto M., Knight R. J. and Allegre C. J. (1973) Time differences in the formation of meteorites as determined from the ratio of lead-207 to lead-206. *Science* **180,** 1279-1283.

Tatsumoto M., Unruh D. M. and Desborough G. A. (1976) U-Th-Pb and Rb-Sr systematics of Allende and U-Th-Pb systematics of Orgueil. *Geochim. Cosmochim. Acta* **40,** 617-634.

Taylor D., McKeegan K. and Krot A. (2005) High resolution 26Al chronology: resolved time interval between rim and interior of a highly fractionated compact Type A CAI from Efremovka. *Lunar and Planetary Science Conference* **36,** Abstract #2121.

Tera F., Carlson R. W. and Boctor N. Z. (1997) Radiometric ages of basaltic achondrites and their relation to the early history of the solar system. *Geochimica et Cosmochimica Acta* **61,** 1713-1731.

Tera F., Papanastassiou D. and Wasserburg G. (1974) Isotopic evidence for a terminal lunar cataclysm. *Earth and Planetary Science Letters* **22,** 1-21.

Tera F. and Wasserburg G. (1972a) U-Th-Pb systematics in lunar highland samples from the Lunar 20 and Apollo 16 missions. *Earth and Planetary Science Letters* **17,** 36-51.

Tera F. and Wasserburg G. (1972b) U-Th-Pb systematics in three Apollo 14 basalts and the problem of initial Pb in lunar rocks. *Earth and Planetary Science Letters* **14,** 281-304.

Thiemens M. H. and Heidenreich J. E. (1983) The mass-independent fractionation of oxygen: A novel isotope effect and its possible cosmochemical implications. *Science* **219,** 1073-1075.

Thrane K., Bizzarro M. and Baker J. A. (2006) Extremely brief formation interval for refractory inclusions and uniform distribution of ^{26}Al in the early solar system. *The Astrophysical Journal Letters* **646,** L159.

Ushikubo T., Guan Y., Hiyagon H., Sugiura N. and Leshin L. A. (2007) ^{36}Cl, ^{26}Al, and O isotopes in an Allende type B2 CAI: Implications for multiple secondary alteration events in the early solar system. *Meteorit. Planet. Sci.* **42,** 1267-1279.

van Dishoeck E. F. and Black J. H. (1988) The photodissociation and chemistry of interstellar CO. *The Astrophysical Journal* **334,** 771-802.

Van Oorschot I. and Dekkers M. (1999) Dissolution behaviour of fine-grained magnetite and maghemite in the citrate–bicarbonate–dithionite extraction method. *Earth and Planetary Science Letters* **167,** 283-295.

Villeneuve M., Sandeman H. A. and Davis W. J. (2000) A method for intercalibration of U-Th-Pb and 40Ar-39Ar ages in the Phanerozoic. *Geochimica et Cosmochimica Acta* **64,** 4017-4030.

Wadhwa M., Amelin Y., Bogdanovski O., Shukolyukov A., Lugmair G. and Janney P. (2009) Ancient relative and absolute ages for a basaltic meteorite: Implications for timescales of planetesimal accretion and differentiation. *Geochimica et Cosmochimica Acta* **73,** 5189-5201.

Wark D. (1981) Alteration and metasomatism of Allende Ca-Al materials. *Lunar Planet. Sci.* **12,** 1145-1147.

Wark D. (1987) Plagioclase-rich inclusions in carbonaceous chondrite meteorites: liquid condensates? *Geochimica et Cosmochimica Acta* **51,** 221-242.

Wark D. and Lovering J. (1978) Refractory/platinum metals and other opaque phases in Allende Ca-Al inclusions. *Lunar and Planetary Science Conference* **9,** 1214-1216.

Wark D. and Lovering J. (1982) The nature and origin of type B1 and B2 Ca-Al-rich inclusions in the Allende meteorite. *Geochim. Cosmochim. Acta* **46,** 2581-2594.

Wark D. and Wasserburg G. Anomalous mineral chemistry of Allende FUN inclusions Cl, EK-141 and Egg 3. Lunar and Planetary Science Conference, 1980. 1214-1216.

Wasserburg G. and Arnould M. (1987) A possible relationship between extinct ^{26}Al and ^{53}Mn in meteorites and early solar activity. *Nuclear Astrophysics,* 262-276.

Wasserburg G., Lee T. and Papanastassiou D. (1977a) Correlated O and Mg isotopic anomalies in Allende inclusions: II. Magnesium. *Geophys. Res. Lett.* **4,** 299-302.

Wasserburg G., Tera F., Papanastassiou D. and Huneke J. (1977b) Isotopic and chemical investigations on Angra dos Reis. *Earth and Planetary Science Letters* **35,** 294-316.

Wasserburg G., Wimpenny J. and Yin Q. Z. (2012) Mg isotopic heterogeneity, Al - Mg isochrons, and canonical ^{26}Al/^{27}Al in the early solar system. *Meteoritics & Planetary Science* **47,** 1980-1997.

Wasson J. T., Yurimoto H. and Russell S. S. (2001) ^{16}O-rich melilite in CO3. 0 chondrites: possible formation of common, ^{16}O-poor melilite by aqueous alteration. *Geochim. Cosmochim. Acta* **65,** 4539-4549.

Weber D., Zinner E. and Bischoff A. (1995) Trace element abundances and magnesium, calcium, and titanium isotopic compositions of grossite-containing inclusions from the carbonaceous chondrite Acfer 182. *Geochimica et Cosmochimica Acta* **59,** 803-823.

Weidenschilling S. and Ruzmaikina T. (1994) Coagulation of grains in static and collapsing protostellar clouds. *The Astrophysical Journal* **430,** 713-726.

Weisberg M. K. and Prinz M. (1998) Fayalitic olivine in CV3 chondrite matrix and dark inclusions: A nebular origin. *Meteoritics & Planetary Science* **33,** 1087-1099.

Wetherill G. W. (1956) Discordant uranium - lead ages, I. *Eos, Transactions American Geophysical Union* **37,** 320-326.

Weyer S., Anbar A., Gerdes A., Gordon G., Algeo T. and Boyle E. (2008) Natural fractionation of $^{238}U/^{235}U$. *Geochimica et Cosmochimica Acta* **72,** 345-359.

Williams J. P. (2010) The astrophysical environment of the solar birthplace. *Contemporary Physics* **51,** 381-396.

Wood J. A. (2004) Formation of chondritic refractory inclusions: The astrophysical setting. *Geochimica et Cosmochimica Acta* **68,** 4007-4021.

Woolfson M. (1993) The solar-origin and evolution. *Quarterly Journal of the Royal Astronomical Society* **34,** 1-20.

Wormald R. J. 1993. *The petrology and geochemistry of mid to late Palaeozoic magmatism in the Temora region, New South Wales.*, La Trobe University.

Yoneda S. and Grossman L. (1995) Condensation of $CaOMgOAl_2O_3SiO_2$ liquids from cosmic gases. *Geochimica et Cosmochimica Acta* **59,** 3413-3444.

Young E. D. and Russell S. S. (1998) Oxygen reservoirs in the early solar nebula inferred from an Allende CAI. *Science* **282,** 452-455.

Young E. D., Simon J. I., Galy A., Russell S. S., Tonui E. and Lovera O. (2005) Supra-canonical $^{26}Al/^{27}Al$ and the residence time of CAIs in the solar protoplanetary disk. *Science* **308,** 223-227.

Yurimoto H., Ito M. and Nagasawa H. (1998) Oxygen isotope exchange between refractory inclusion in Allende and solar nebula gas. *Science* **282,** 1874-1877.

APPENDIX A

This appendix contains images of NWA 4502 CAIs after extraction from matrix and coarse crushing. Also presented here are the normalized major element compositions of mineral phases in NWA 4502 CAIs.

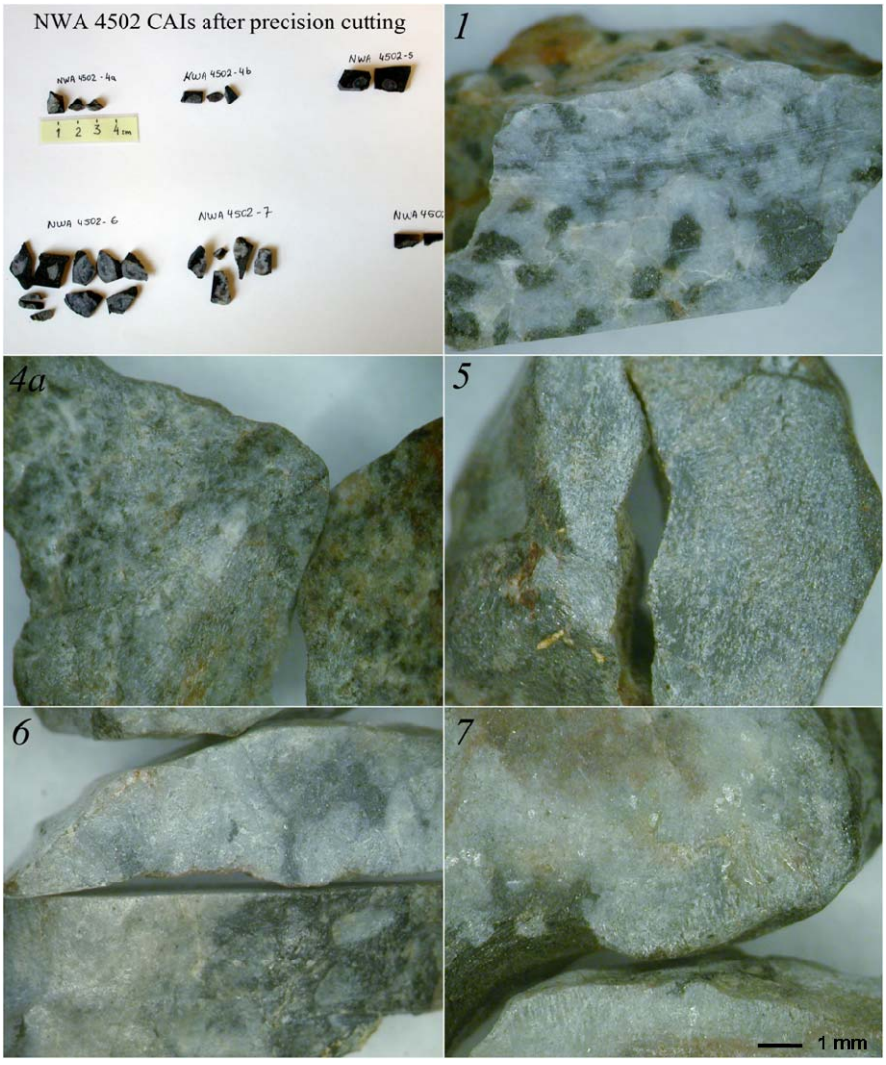

Figure A1: Images of NWA 4502 CAIs *1, 4a, 5, 6* and *7* after precision cutting and extraction from the host meteorite matrix.

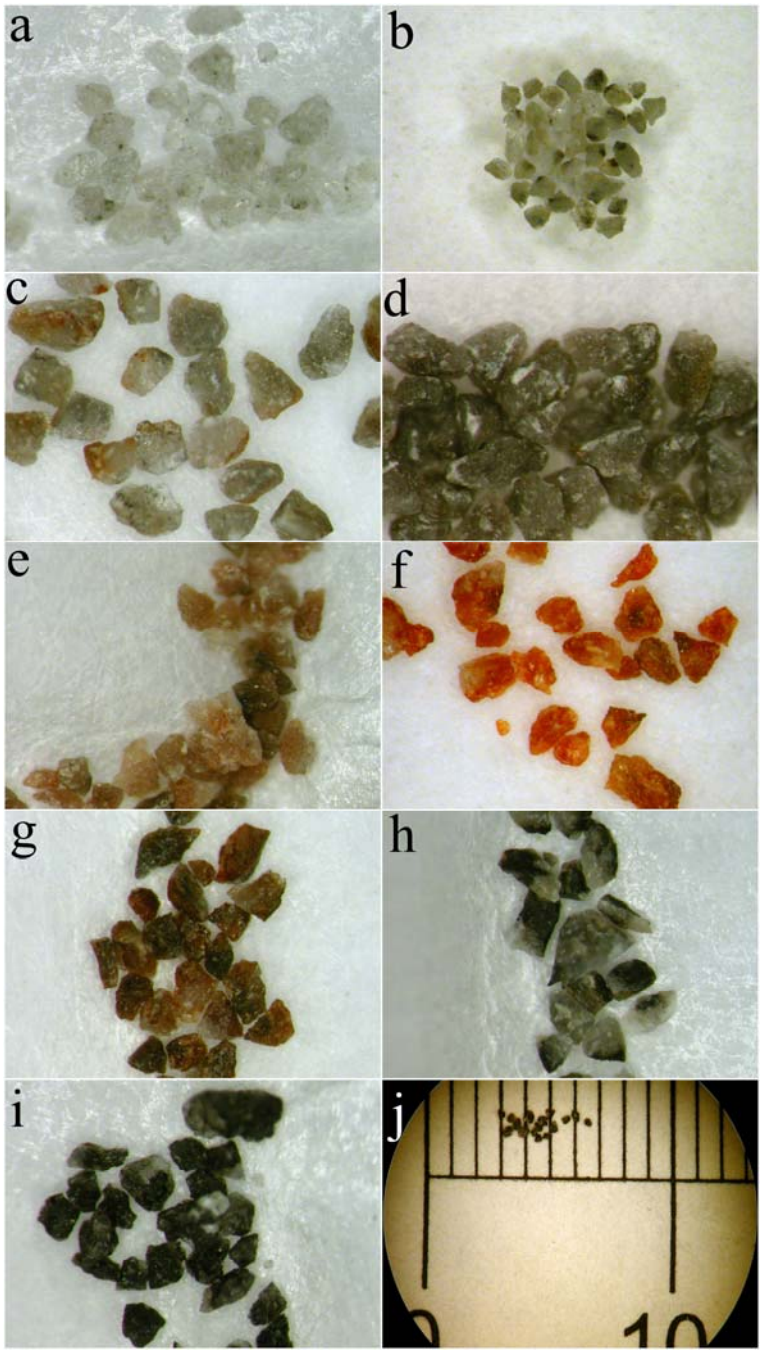

Figure A2: Images of hand picked (a-d) melilite-rich, (e-h) mixed: (e-f) melilite + spinel, (g) melilite + spinel + pyroxene, h) melilite + pyroxene and (I, j) pyroxene-rich mineral separates. Grain sizes are 100-275µm.

Table A1: Major element composition of pyroxenes in NWA 4502 CAIs.

Oxide	SiO_2	TiO_2	Al_2O3	Cr_20_3	FeO	MnO	MgO	CaO	Na_2O	K_2O
CAI *6*										
	36.56	13.31	16.67	0.05	nd	nd	8.92	24.48	0.005	nd
	33.33	15.17	19.64	0.07	0.01	0.02	7.55	24.20	0.01	nd
	33.59	15.39	19.12	0.04	0.01	nd	7.51	24.33	0.002	nd
	36.67	11.66	18.30	0.04	0.04	0.03	8.81	24.45	0.02	nd
	35.89	13.79	16.95	0.03	0.01	nd	8.75	24.55	0.02	nd
CAI *7*										
	50.87	0.26	7.38	0.05	0.02	0.02	15.66	25.75	nd	nd
	54.15	0.35	1.94	0.02	0.06	0.01	18.52	24.94	0.005	nd
	51.98	0.49	5.40	0.03	0.59	nd	17.52	23.98	nd	nd
CAI *1*										
	37.04	9.57	20.50	0.08	nd	0.01	8.13	24.68	nd	0.001
	39.35	7.72	18.42	0.07	nd	0.00	9.65	24.78	nd	nd
	35.74	9.98	22.17	0.04	0.04	0.03	7.28	24.70	0.003	0.01
	35.77	10.00	22.24	0.06	0.01	nd	7.31	24.61	nd	nd
	36.83	8.89	21.75	0.09	nd	nd	7.89	24.55	nd	0.003
	37.90	7.90	20.68	0.07	nd	nd	8.79	24.64	nd	0.01
	38.73	8.06	19.42	0.05	0.01	0.01	8.97	24.74	nd	0.001
	39.61	7.24	18.83	0.03	nd	0.00	9.47	24.82	nd	nd
	36.78	10.02	20.71	0.04	0.001	0.02	7.85	24.57	nd	0.001
	36.60	10.00	20.91	0.05	nd	0.01	7.74	24.68	0.001	0.01
	37.31	9.43	20.50	0.05	nd	0.02	8.08	24.61	nd	nd
	36.89	10.21	20.41	0.03	nd	0.00	7.95	24.50	0.01	nd
	38.42	8.00	19.90	0.02	0.01	0.02	8.89	24.72	0.01	0.01
	54.19	0.20	2.18	0.02	0.78	0.03	18.31	24.29	nd	nd
CAI *4a*										
	36.26	8.77	21.73	0.07	0.01	nd	8.10	25.05	nd	0.002
	37.02	8.08	21.18	0.05	0.000	0.01	8.48	25.18	nd	0.002
	38.10	6.86	19.86	0.07	0.04	0.003	9.67	25.38	0.02	nd
	35.95	9.14	21.88	0.08	0.05	nd	7.92	24.99	ndd	nd
	36.01	8.80	22.20	0.09	0.01	0.04	7.99	24.85	0.01	nd
	36.74	8.11	22.10	0.07	0.04	0.01	8.33	24.57	0.01	nd
	37.72	7.25	21.50	0.04	0.22	0.001	8.37	24.87	0.02	0.01
	38.36	6.04	21.36	0.06	0.03	0.01	9.16	24.99	nd	nd
	37.89	6.36	21.57	0.08	0.03	nd	9.02	25.07	nd	nd
	38.30	6.31	21.09	0.09	nd	0.01	9.20	25.00	0.002	nd
	37.85	6.81	21.43	0.06	0.06	0.03	8.95	24.81	0.0004	nd
	38.05	6.80	21.07	0.06	nd	0.01	8.96	25.02	0.004	0.002
	37.70	6.84	21.39	0.07	0.04	0.002	9.06	24.90	0.01	nd
	37.94	6.51	21.55	0.05	0.01	0.005	8.84	25.10	nd	nd
CAI *5*										
	44.20	4.35	13.33	0.08	0.04	0.02	12.70	25.26	0.01	nd
	39.66	5.40	19.38	0.08	0.04	nd	10.11	25.34	nd	nd
	39.23	6.77	19.03	0.02	0.47	nd	10.37	24.06	0.04	nd
	43.20	4.03	13.96	0.06	0.78	nd	13.35	24.63	nd	nd
	43.71	4.15	14.28	0.06	0.09	nd	12.53	25.16	0.004	0.01
	48.45	2.67	8.56	0.04	0.08	nd	15.13	25.06	nd	0.01
	48.53	2.58	8.32	0.07	0.06	nd	15.30	25.15	nd	nd
	48.21	2.67	8.93	0.02	0.06	0.05	15.07	24.99	nd	nd

nd:not detected

Table A2: Major element composition of melilites in NWA 4502 CAIs.

Oxide	SiO_2	TiO_2	Al_2O3	Cr_20_3	FeO	MnO	MgO	CaO	Na_2O	K_2O
CAI *6*										
	30.54	0.03	22.45	nd	0.03	nd	5.73	41.21	0.01	nd
	30.61	0.004	22.64	nd	0.02	0.04	5.73	40.95	0.02	nd
	32.70	0.16	19.34	0.01	0.01	0.03	6.90	40.67	0.18	nd
	28.94	0.03	25.76	nd	0.02	0.02	4.59	40.62	0.03	nd
	27.34	0.06	27.91	0.01	0.02	0.003	3.73	40.94	nd	nd
	27.61	0.03	27.39	nd	0.01	nd	3.95	40.99	0.01	nd
	27.86	0.03	27.10	nd	0.03	nd	4.07	40.89	0.01	0.01
	32.18	0.08	28.14	nd	0.01	0.02	3.86	35.62	0.07	nd
	27.38	nd	27.97	nd	0.05	nd	3.67	40.93	nd	nd
	27.84	0.05	27.26	nd	nd	0.003	4.16	40.65	0.011	nd
	27.67	0.05	27.48	nd	nd	nd	4.11	40.69	nd	0.002
	31.71	nd	21.31	0.01	nd	nd	6.35	40.62	0.01	nd
	35.88	0.03	14.05	nd	0.05	nd	9.06	40.84	0.10	nd
CAI *7*										
	22.99	0.08	34.95	nd	nd	0.01	1.08	40.85	0.03	0.01
	23.14	0.08	35.17	nd	nd	0.005	0.73	40.86	0.01	nd
	23.20	0.11	34.65	nd	nd	nd	1.14	40.89	0.01	nd
	22.40	0.09	35.86	0.001	0.01	0.002	0.66	40.98	nd	nd
CAI *1*										
	30.35	nd	23.50	nd	nd	0.02	5.47	40.61	0.05	0.01
	28.94	0.04	25.63	nd	0.01	nd	4.52	40.86	nd	nd
	23.44	0.07	34.84	0.003	0.14	0.01	1.24	40.26	nd	nd
CAI *4a*										
	27.06	0.04	28.22	0.02	0.05	nd	3.73	40.80	0.09	nd
	28.51	0.01	25.77	nd	0.02	nd	4.47	41.14	0.06	0.01
	33.06	0.02	18.68	nd	0.22	nd	7.13	40.58	0.31	0.004
CAI *5*										
	40.76	nd	5.60	nd	0.12	0.01	12.33	41.00	0.18	nd
	36.69	nd	11.63	0.0004	0.14	nd	9.91	41.39	0.24	nd
	36.25	0.001	12.28	nd	0.05	0.003	9.47	41.69	0.25	nd
	36.25	0.02	12.15	0.002	0.02	nd	9.56	41.77	0.23	nd
	36.58	0.04	11.89	nd	0.04	0.03	9.67	41.54	0.20	0.01
	39.36	0.01	7.33	0.003	0.05	nd	11.42	41.60	0.23	nd
	40.57	0.03	5.21	nd	0.05	nd	12.31	41.62	0.20	0.002
	40.87	nd	4.79	nd	0.03	0.002	12.58	41.55	0.18	nd
	41.09	0.01	4.62	nd	0.08	0.01	12.46	41.54	0.18	nd
	41.29	0.02	4.56	nd	0.07	0.04	12.49	41.32	0.21	nd
	40.98	0.01	4.80	0.002	0.04	0.003	12.48	41.50	0.19	nd
	40.40	0.01	5.27	nd	0.10	0.01	12.23	41.76	0.21	nd
	40.38	0.02	5.63	nd	0.12	nd	12.25	41.43	0.18	nd
	38.10	0.001	9.71	nd	0.08	nd	10.46	41.44	0.21	0.0003
	41.02	0.01	4.93	nd	0.09	nd	12.42	41.33	0.19	nd
	38.98	0.02	8.29	0.0004	0.07	0.02	11.11	41.30	0.20	0.002
	38.62	0.03	9.11	0.01	0.07	0.04	10.75	41.15	0.23	nd
	37.15	0.03	10.79	0.01	0.22	nd	10.05	41.50	0.25	nd
	36.21	0.000	12.06	0.01	0.22	nd	9.59	41.70	0.22	nd

nd:not detected

Table A3: Major element composition of spinels in NWA 4502 CAIs.

Oxide	SiO_2	TiO_2	Al_2O3	Cr_20_3	FeO	MnO	MgO	CaO	Na_2O	K_2O
CAI *6*										
	nd	0.84	71.22	0.18	0.08	nd	27.68	nd	nd	0.0001
	0.20	0.68	70.50	0.23	0.05	nd	28.25	0.08	nd	nd
	0.51	0.69	68.24	0.30	7.01	0.02	22.72	0.50	0.01	nd
CAI *7*										
	0.004	0.02	70.05	0.12	4.98	0.03	24.54	0.23	0.01	0.01
	0.04	0.01	71.17	0.12	1.18	0.003	27.24	0.22	0.003	0.002
	0.17	0.57	70.24	0.17	0.88	0.01	27.39	0.55	0.01	0.003
CAI *1*										
	0.03	0.90	71.28	0.15	0.06	0.02	27.49	0.07	nd	0.01
	0.05	0.54	71.16	0.16	0.06	0.01	27.91	0.10	nd	0.002
CAI *4a*										
	0.05	0.25	71.18	0.22	0.18	0.04	27.97	0.12	0.01	0.01
	0.15	0.21	70.58	0.19	0.73	nd	27.87	0.28	nd	0.001
CAI *5*										
	0.18	0.36	71.31	0.24	0.57	0.003	27.08	0.25	0.01	nd
	0.15	0.32	71.38	0.29	0.38	0.01	27.28	0.20	nd	nd
	0.05	0.19	71.31	0.19	0.41	0.03	27.68	0.14	nd	0.002
	0.07	0.20	71.03	0.20	0.17	nd	28.17	0.15	0.01	nd

nd:not detected

Table A4: Major element composition of hibonites in NWA 4502 CAIs.

Oxide	SiO_2	TiO_2	Al_2O3	Cr_20_3	FeO	MnO	MgO	CaO	Na_2O	K_2O
CAI *7*										
	nd	8.05	80.46	0.04	0.02	0.02	3.27	8.15	nd	nd
	nd	7.82	80.40	0.06	0.06	0.01	3.52	8.13	0.01	nd
	0.14	2.33	87.91	0.03	0.03	0.02	1.36	8.16	nd	0.01
	0.31	0.65	89.89	0.04	0.11	0.01	0.74	8.24	0.01	0.002
	nd	8.10	80.29	0.02	0.001	nd	3.20	8.38	0.001	nd
	0.17	3.54	85.54	0.05	0.005	0.04	2.06	8.59	0.005	nd
	0.00	3.58	86.03	0.05	0.11	0.01	1.75	8.46	nd	0.001
	0.01	5.77	82.67	0.03	0.11	0.00	2.95	8.47	0.002	0.003
	0.19	4.17	84.73	0.04	0.10	0.03	2.21	8.53	0.005	0.003
	0.10	3.79	85.54	0.04	0.09	nd	1.94	8.50	0.0001	nd
	nd	4.30	84.92	0.06	0.07	nd	2.11	8.54	0.004	nd
	0.08	4.95	83.72	0.06	0.13	nd	2.48	8.57	0.01	nd
	0.20	5.81	81.82	0.10	0.37	nd	2.73	8.95	0.03	nd
	0.13	4.83	84.15	0.05	0.09	0.02	2.33	8.44	0.01	0.003
CAI *1*										
	0.44	1.89	87.89	0.03	0.26	0.03	1.24	8.20	nd	0.01

nd:not detected

Table A5: Major element composition of anorthite in NWA 4502 CAIs.

Oxide	SiO_2	TiO_2	Al_2O3	Cr_20_3	FeO	MnO	MgO	CaO	Na_2O	K_2O
CAI *1*										
	42.9	0.05	37.10	nd	nd	nd	0.04	19.84	0.03	0.01
	42.9	0.09	36.85	0.03	0.07	nd	0.04	19.89	0.08	0.01
	42.8	0.06	36.99	nd	nd	0.02	0.09	19.89	0.09	0.01
	42.9	0.07	36.98	0.03	0.07	0.02	0.06	19.87	0.07	0.01
CAI *4a*	42.6	0.08	37.08	0.02	0.03	nd	0.20	19.87	0.11	nd
	43.2	0.08	36.37	0.01	0.02	0.03	0.15	20.03	0.12	nd
	42.9	0.08	36.55	nd	0.03	0.01	0.16	20.17	0.09	nd
CAI *5*	42.9	0.04	37.06	0.01	0.07	nd	0.13	19.64	0.13	nd
	43.3	0.03	36.40	0.02	0.13	nd	0.10	19.91	0.11	nd
	43.2	0.05	36.51	nd	0.08	nd	0.12	19.98	0.11	nd
	43.1	0.04	36.66	0.02	0.09	nd	0.12	19.84	0.12	nd

nd:not detected

Table A5: Major element composition of anorthite in NWA 4502 CAIs.

Oxide	SiO_2	TiO_2	Al_2O3	Cr_20_3	FeO	MnO	MgO	CaO	Na_2O	K_2O
CAI *7*										
	0.33	56.80	1.89	nd	0.04	nd	0.10	40.84	nd	nd
	0.34	56.90	1.81	0.03	0.03	nd	0.04	40.86	nd	nd
CAI *6*										
	0.18	58.58	0.49	nd	0.18	nd	0.25	40.30	0.02	nd
	0.00	59.00	0.38	nd	0.00	0.02	0.04	40.55	0.01	0.01
	0.21	57.72	1.28	0.05	0.23	0.03	0.11	40.35	nd	nd

nd:not detected

Table A6: Major element composition of fosterite in NWA 4502 CAIs.

Oxide	SiO_2	TiO_2	Al_2O3	Cr_20_3	FeO	MnO	MgO	CaO	Na_2O	K_2O
CAI *5*										
	42.26	0.05	0.11	0.03	0.17	nd	55.90	1.48	0.001	0.0003
	42.47	0.05	0.14	0.01	0.35	nd	55.73	1.26	nd	nd
	42.34	0.02	0.07	0.01	0.13	0.01	56.03	1.39	0.002	nd

nd:not detected

APPENDIX B

The components of the SHRIMP-SI and their functions describes into more detail in this appendix. The RSES, ANU SHRIMP SI is designed to facilitate stable isotope measurements alone. It includes some elements of previous models SHRIMP I and SHRIMP II. The features from SHRIMP I include the sample-stage motors being mounted externally to the vacuum chamber, and the intermediate extraction lens to produce a crossover in the secondary extraction. Like SHRIMP-II, SHRIMP-SI is a high mass resolution double-focusing mass spectrometer that combines an electrostatic analyzer (ESA), an electrostatic quadrupole lens, and a magnet as the essential ion-optical elements (Matsuda, 1974). Typical of SHRIMP instruments have large magnets needed to achieve high mass resolution without compromising sensitivity, primary beam incident at 45°, normal secondary ion extraction, and a 45° incident angle electron gun.

In spite of the similarities with other SHRIMP instruments, SHRIMP SI includes a fully redesigned primary column consisting of a Cs-ion source, three aperture einzel lenses and deflection plates that allow focusing and steering of the primary ion beam. The beam transport is based around Kohler illumination for spot analysis, but also has a critical illumination capability for submicron illumination.

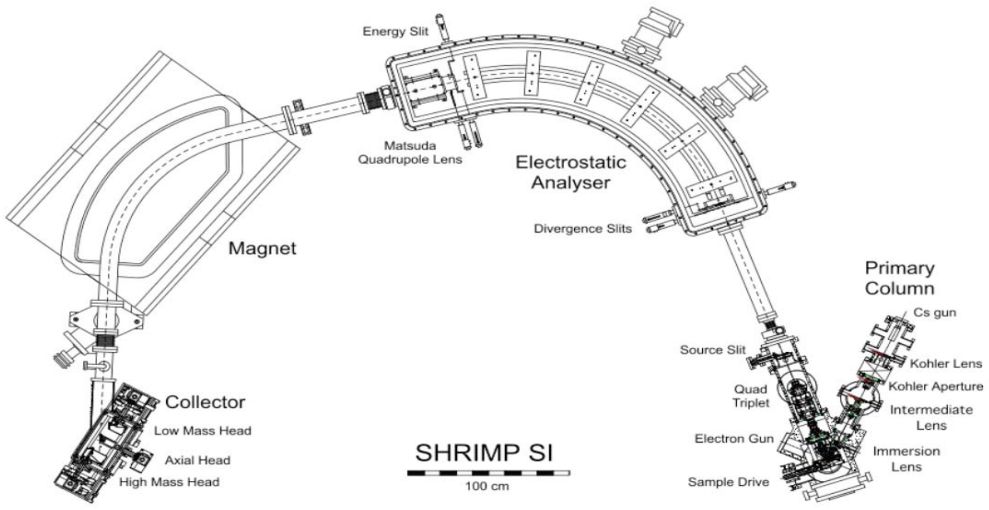

Figure B1: Schematic layout of SHRIMP-SI showing its main components.

SHRIMP-SI source chamber was specifically designed to improve vacuum pressure in the target region through compartmentalized space and differential pumping between sub-chambers.

The electron column is equipped with a Kimball Physics ELG-2 electron gun, which is used to accelerate electrons to the target for charge neutralization of insulating samples. The multiple-collector for SHRIMP SI is designed for low mass. This means that unit mass spacing is further apart and allows the use of standard ETP multipliers in the multiple collector, with fully shielded containers for each multiplier. In measuring stable isotopes, there is little variation in the collector set up and so the design has been simplified with fewer control systems in the chamber. The collector heads can be configured with either Faraday cups or electron multipliers. For this work, secondary ion signals are collected in Faraday cups and ion currents measured by electrometers with high-ohmic ($10^{10} – 10^{12}$ Ω) resistors (i.e., in current mode). On SHRIMP SI, the resistors can be replaced by capacitors where charge is accumulated on the capacitor due to the arrival of ions into the Faraday cup; the signal is measured as a discharge voltage (i.e., charge mode).

These modifications were specially designed to optimize instrument performance for measurements of stable isotopes in both insulating and conducting phases.

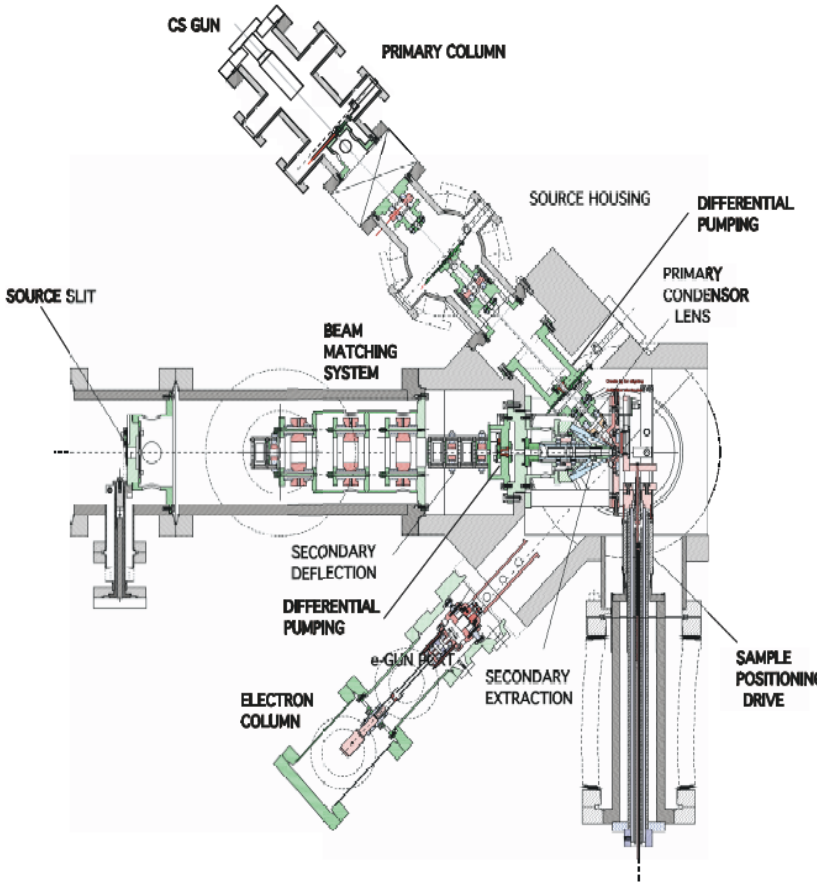

Figure B2: Schematic layout of the primary column of SHRIMP-SI showing its main components.

APPENDIX C

Table C1 and Figure C1 are used to illustrate the progress made in U-Pb dating of CV CAIs over the last few decades. Our understanding of CAIs ages has improved with the increase in amount of information overtime and improvements in analytical techniques.

Table C1: Summary of Pb isotopic ages published after 1995 (Amelin et al., 2009)

#	Meteorite	CAI name	Type	207Pb/206Pb isochron age	2σ err	MSWD	$^{206}Pb/^{204}Pb$ meas max	Technique	Normalization	Comments	References
1	Allende	F2	B2	4568.59	0.61	0.29	687	TIMS	External	3-point isochron Px + Mel + Plag	Connelly et al. (2008)
2	Allende	TS32	CTA	4567.81	0.79	0.94	1011	TIMS	External	3-point isochron Px + Mel + Plag	Connelly et al. (2008)
3	Allende	TS33	B1	4570.70	1.10	0.87	403	TIMS	External	3-point isochron Px + Mel + Plag	Connelly et al. (2008)
4	Allende	F2 + TS32 + TS33		4567.72	0.93	1.60	1011	TIMS	External	6-point isochron Px + Melilite	Connelly et al. (2008)
5	Allende	AJEF	B	4567.60	0.36	1.60	1823	TIMS	^{202}Pb–^{205}Pb DS	3 residues + one leachate	Jacobsen et al. (2008)
6	Allende	A43	B	4567.50	1.40	0.60	2034	TIMS	^{202}Pb–^{205}Pb DS	4 residues	Jacobsen et al. (2008)
7	Allende	AJEF + A43		4567.44	0.34	1.40	2034	TIMS	^{202}Pb–^{205}Pb DS	8-point isochron	Jacobsen et al. (2008)
8	Allende	Not reported	B[a]	4567.59	0.10	0.18	3457[b]	MC-ICPMS	Tl	3 residues + one leachate	Bouvier et al. (2008)
9	Efremovka	E49	CTA	4567.17	0.70	0.68	1263	TIMS	External	6 residues	Amelin et al. (2002)
10	Efremovka	E60	Fo-b B	4567.40	1.10	1.09	548	TIMS	External	12 residues	Amelin et al. (2002)
11	Efremovka	E60	Fo-b B	4567.11	0.16	1.00	2261	TIMS	External + DS	19 residues	Amelin et al. (2002, 2006) and this study
12	Efremovka	E60	Fo-b B	4569.50	0.40	1.70	548	TIMS	External	12 residues + 2 washes	Data of Amelin et al. (2002), reinterpreted by Baker et al. (2005)
13	All + Efr	E60 + Allende CAIs		4568.50	0.50	0.90	454	TIMS+ICP	Various	7 E60 + 3 UCLA	Data of Amelin et al. (2002) and Bouvier et al. (2007), interpreted together by Bouvier et al. (2007)
14	Allende	multiple CAIs		4568.00	9.40	0.076	76	MC-ICPMS	Tl	3 residues UCLA sample	Bouvier et al. (2007)

[a] A. Bouvier, personal communication 2008.
[b] Blank-corrected value.

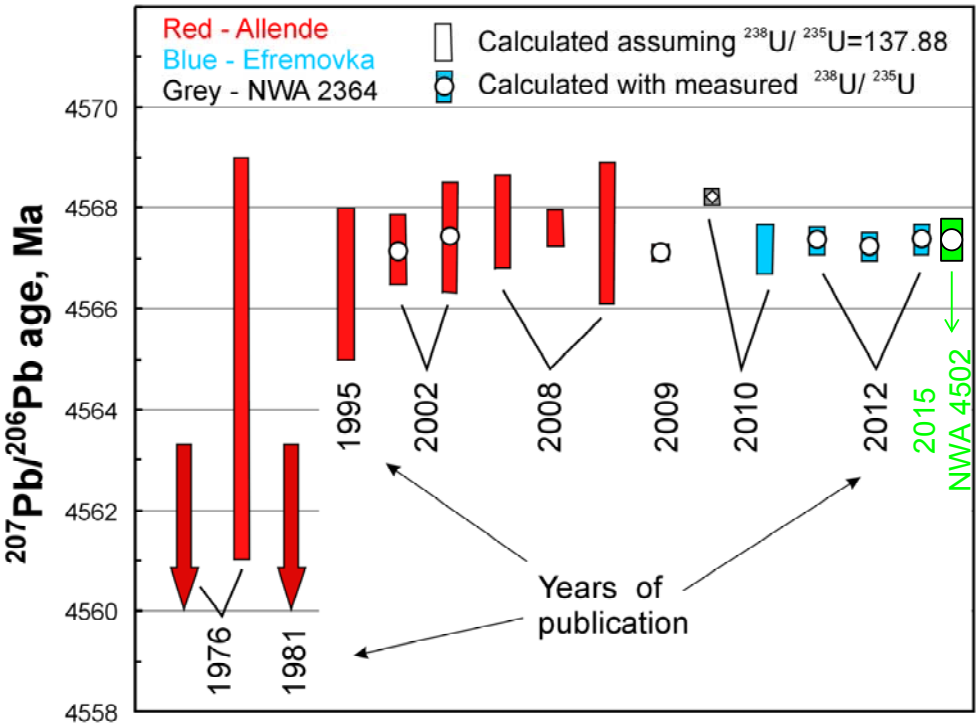

Figure C1: $^{207}Pb/^{206}Pb$ ages of CV CAIs analysed over the last few decades.

APPENDIX D

LIST OF PUBLICATIONS

1. Amelin Y. and **Sapah M. S.** (2012) Cooling rates of Plutonic Angrites from Pyroxene-Phosphate U-Pb chronology: Abstract #5199. *75th Meteoritical society conference*.

2. **Sapah M. S.,** Krot A. N. and Amelin Y. (2013) Mineralogy and Petrography of refractory inclusions in North West Africa 4502, oxidized CV chondrite: Abstract #1036. *44th Lunar and Planetary Science Conference*.

3. Amelin Y., **Sapah M. S.,** Cooke I., Stirling C. H. and Kaltenbach A. (2013) U-Th-Pb Systematics of CAIs from CV Chondrite Northwest Africa 4502: Abstract #2690. *44th Lunar and Planetary Science Conference*.

4. Cooke I., **Sapah M. S.,** Kaltenbach A., Stirling C. H. and Amelin Y. (2013) Uranium Isotopic Composition and Trace Element Abundances of CAIs from CV Chondrite Northwest Africa 4502: Abstract #1709. *44th Lunar and Planetary Science Conference*.

5. **Sapah M. S.,** Amelin Y., Wimpenny J., Yin Q. and Ireland T. (2013). Al-Mg Isotopic Systematics of Refractory Inclusions from the CV3 chondrite NWA 4502: Abstract #5156. *76th* Meteoritical society conference.

6. Ireland T. R., **Sapah M. S.,** Ávila J. N., Holden P., Amelin Y., Krot A. N. and Yin Q.(2014).Oxygen Isotope Compositions of CAI from NWA 4502 CV3 chondrite. Abstract #1671. *45th Lunar and Planetary Science Conference*.

7. **Sapah M. S.,** Ireland T. R., Ávila J. N., Amelin Y. and Krot A. N. (2014). Oxygen Isotope Compositions of CAIs from CV3 chondrite NWA 4502. Abstract #5203. *77th* Meteoritical society conference.

8. Amelin Y., **Sapah M. S**., Ireland T. R. and Yin Q.Z. (2014). Sr Isotope Systematics of CAIs from the CV3 chondrite NWA 4502. Abstract #5244. 77th *Meteoritical society conference*.

9. Wimpenny J., Sanborn M., Yin Q.Z., Yamakawa A., **Sapah M.,** Amelin Y., Ireland T., Stirling C., Cooke I. and Krot A. N. (2014). Al-Mg and Mn-Cr Systematics in CAIs from NWA 4502. Abstract #2722. *Goldschmidt* conference.

10. **Sapah M. S.,** Amelin Y. and Ireland T. (2015). Investigating the effects of acid leaching on the U-Th-Pb system in CAIs from the CV chondrite NWA 4502. Abstract #1859. *46th Lunar and Planetary Science Conference*.